Searching for Penguin Footprints

Towards High Precision *CP* Violation Measurements in the *B* Meson Systems

Kristof De Bruyn

Searching for Penguin Footprints

Towards High Precision *CP* Violation Measurements in the *B* Meson Systems

Kristof Antoon Maria De Bruyn

Reading Committee:

prof.dr. Daniel Boer	[Rijksuniversiteteit Groningen]
prof.dr. Nicolo de Groot	[Radboud Universiteit Nijmegen]
prof.dr. Olivier Leroy	[CPPM/CNRS & Aix Marseille Université]
prof.dr. Thomas Mannel	[Universität Siegen]
prof.dr. Piet Mulders	[Vrije Universiteit Amsterdam]
prof.dr. Gerhard Raven	[Vrije Universiteit Amsterdam]

Cover Illustration: Jan Mariën, 2015 – Oil on cardboard

ISBN: 978-94-6233-034-4
Printed by: Gildeprint – www.gildeprint.nl
Published by: Gildeprint – www.gildeprint.nl

Nikhef FOM NWO

Netherlands Organisation for Scientific Research

This work is part of the research programme of the Foundation for Fundamental Research of Matter (FOM), which is part of The Netherlands Organisation for Scientific Research (NWO).

VRIJE UNIVERSITEIT

Searching for Penguin Footprints

Towards High Precision *CP* Violation Measurements in the *B* Meson Systems

ACADEMISCH PROEFSCHRIFT

ter verkrijging van de graad Doctor aan
de Vrije Universiteit Amsterdam,
op gezag van de rector magnificus
prof.dr. F.A. van der Duyn Schouten,
in het openbaar te verdedigen
ten overstaan van de promotiecommissie
van de Faculteit der Exacte Wetenschappen
op donderdag 8 oktober 2015 om 11.45 uur
in de aula van de universiteit,
De Boelelaan 1105

door

Kristof Antoon Maria De Bruyn

geboren te Mortsel, België

promotor: prof.dr. R. Fleischer
copromotor: dr. P. Koppenburg

Contents

Publications

This thesis discusses the following publications and analysis notes:
Chapter 4

- K. De Bruyn, R. Fleischer, R. Knegjens, P. Koppenburg, M. Merk and N. Tuning, *Branching Ratio Measurements of B_s Decays*, Phys. Rev. **D86** (2012) 014027, arXiv:1204.1735.
- K. De Bruyn, R. Fleischer, R. Knegjens, P. Koppenburg, M. Merk, A. Pellegrino and N. Tuning, *Probing New Physics via the $B_s^0 \to \mu^+\mu^-$ Effective Lifetime*, Phys. Rev. Lett. **109** (2012) 041801, arXiv:1204.1737.

Chapter 5

- K. De Bruyn and R. Fleischer, *A Roadmap to Control Penguin Effects in $B^0 \to J/\psi K_S^0$ and $B_s^0 \to J/\psi \phi$*, JHEP **1503** (2015) 145, arXiv:1412.6834.

Chapter 7

- LHCb collaboration, R. Aaij *et al.*, *Measurement of the $B_s^0 \to J/\psi K_S^0$ Branching Fraction*, Phys. Lett. **B713** (2012) 172, arXiv:1205.0934.
- LHCb collaboration, R. Aaij *et al.*, *Measurement of the Effective $B_s^0 \to J/\psi K_S^0$ Lifetime*, Nucl. Phys. **B873** (2013) 275, arXiv:1304.4500.
- LHCb collaboration, R. Aaij *et al.*, *Measurement of the Time-Dependent CP Asymmetries in $B_s^0 \to J/\psi K_S^0$*, JHEP **1506** (2015) 131, arXiv:1503.07055.
- K. De Bruyn and P. Koppenburg, *Measurement of the $B_s^0 \to J/\psi K_S^0$ Branching Fraction*, LHCb Analysis Note (2012), LHCb-ANA-2011-093.
- K. De Bruyn and P. Koppenburg, *Measurement of the $B_s^0 \to J/\psi K_S^0$ Effective Lifetime*, LHCb Analysis Note (2013), LHCb-ANA-2012-049.
- K. De Bruyn *et al.*, *Measurement of the Time-Dependent CP Asymmetries in $B_s^0 \to J/\psi K_S^0$*, LHCb Analysis Note (2015), LHCb-ANA-2013-011.

Other publications and proceedings contributions:

- K. De Bruyn, R. Fleischer and P. Koppenburg, *Extracting Gamma and Penguin Topologies through CP Violation in $B_s^0 \to J/\psi K_S^0$*, Eur. Phys. J. **C70** (2010) 1025, arXiv:1010.0089.
- K. De Bruyn, R. Fleischer, R. Knegjens, M. Merk, M. Schiller and N. Tuning, *Exploring $B_s^0 \to D_s^{(*)\pm} K^{\mp}$ Decays in the Presence of Sizable Width Difference $\Delta\Gamma_s$*, Nucl. Phys. **B868** (2013) 351, arXiv:1208.6463.
- L. Bel, K. De Bruyn, R. Fleischer, M. Mulder and N. Tuning, *Anatomy of $B \to D\overline{D}$ Decays*, (2015), arXiv:1505.01361.
- K. De Bruyn, R. Fleischer and P. Koppenburg, *Extracting Gamma and Penguin Parameters from $B_s^0 \to J/\psi K_S^0$*, Proceedings of the 6th International Workshop on the CKM Unitarity Triangle (2010), arXiv:1012.0840
- K. De Bruyn, *Measurements of CP Violation in the B_s^0 System*, Proceedings of the XI International Conference on Hyperons, Charm and Beauty Hadrons (2014), LHCb-PROC-2014-039

1 Introduction

Our knowledge about the most basic building blocks of the Universe and their interactions is summarised in a single theory: *the Standard Model of elementary particle physics* [1, 2, 3]. It provides a successful description for three out of the four identified fundamental forces in Nature: the strong, weak, and electromagnetic interaction. But although the experimental data and the corresponding Standard Model predictions have so far been remarkably consistent, the Standard Model is not considered to be a complete theory of particle physics. There are several arguments for posing this conjecture. First of all, the fourth fundamental force, gravity, is not included in this framework[a]. Secondly, the Standard Model cannot explain the origin or nature of experimentally firmly established observations like neutrino masses [5], the matter–antimatter asymmetry of our Universe [6], or *dark matter* [7] and *dark energy* [8]. Likewise, there are a number of puzzling theoretical questions to which the Standard Model does not provide a satisfactory answer. Examples include the hierarchy problem [9], the strong *CP* problem [10], and the family and flavour structures of the Standard Model. The associated experimental results need to be taken at face-value within the Standard Model paradigm. Because of these shortcomings, the Standard Model is commonly interpreted as a low-energy effective description of a more complete, but unknown, theory of particle physics. Observing phenomena like new fundamental particles, new types of interactions, or modified Standard Model couplings, which all go under the general name of *new physics*, would provide insights into the properties of this more complete theory.

To help solve some of the above raised problems by searching for further experimental evidence of new physics, high energy particle accelerators are built. The latest and most powerful accelerator taking up this task is the Large Hadron Collider (LHC). It operated at centre-of-mass energies of 7 and 8 TeV in 2010–2011 and 2012, respectively, and is expected to reach 13 TeV later this year (2015). The data collected during its first three years of operation, between 2010 and 2012, has already resulted in many interesting new measurements. Undoubtedly the most significant highlight is the discovery of a Higgs-like particle by the Atlas [11] and

[a] A successful description of gravity on macroscopic length scales is provided by Einstein's *General Relativity* [4]. But physicists have not yet succeeded to incorporate it into the quantum mechanical framework of the Standard Model.

CMS [12] collaborations in July 2012. Further measurements, performed with all data collected during the first run period of the LHC, indicate that its properties match that of the Standard Model Higgs boson, thereby completing the Standard Model theory. But with exception of the Higgs particle, all direct searches for new, heavy fundamental particles, commonly referred to as the *high energy frontier*, have so far been unsuccessful [13]. Instead, the results of these searches constrain the parameter space of many new physics models.

Complementary to the direct searches is the *high precision frontier*. Although mostly associated with the flavour sector of the Standard Model, this strategy applies equally well to the high precision measurements of the Higgs properties, among others. It focuses on indirectly probing the energy scales at which new physics manifests itself, and which can well be out of reach for the direct production at currently available particle accelerators. Observables like cross-sections, branching ratios and asymmetry parameters can be affected by new physics contributions appearing as modified couplings or new degrees of freedom in virtual loop interactions. Instead of resonance searches based on global event properties, indirect detection methods therefore study the properties of well-known decay channels and compare those to their Standard Model predictions.

One of the main LHC highlights in the high precision frontier is the first observation of the rare decay $B_s^0 \to \mu^+\mu^-$ and the discovery of its partner mode $B^0 \to \mu^+\mu^-$ by the LHCb and CMS collaborations [14]. The branching fractions of these two decay modes put stringent constraints on many new physics models based on weak scale supersymmetry [15]. It is therefore important to have accurate predictions for the Standard Model values. We contributed to this effort by pointing out that there are subtleties involved in comparing the experimentally measured branching fractions, which are time-integrated quantities, with their decay-time-independent theoretical counterparts [16]. The non-zero decay width difference of the B_s^0 meson system introduces a non-trivial correction factor between both branching ratio concepts. Due to the nature of the Standard Model interaction, this factor is maximal for the $B_s^0 \to \mu^+\mu^-$ decay [17], and can thus have a large impact on new physics searches. Because of this caveat, both papers received a lot of attention in the community, and are highly cited. Taking into account the differences between both branching ratio definitions, the Standard Model calculations are consistent with the measured $B_s^0 \to \mu^+\mu^-$ and $B^0 \to \mu^+\mu^-$ branching fractions.

Another important cornerstone of flavour physics, complementing the rare decay measurements, is the study of flavour-changing processes. These weak transitions can violate the Charge–Parity (CP) symmetry between particles and antiparticles, which among others, is a necessary condition to explain the matter–antimatter asymmetry of our Universe [18]. CP violation was first discovered in 1964 with the observation of long-lived neutral kaons decaying into two pions

[19]. This observation came as a big surprise, as it could not be explained with the existing theories describing the three quark types that were known at the time. Kobayashi and Maskawa, building on previous work by Cabibbo [20], succeeded in 1973 to explain the origin of *CP* violation in the Standard Model by introducing the Cabibbo–Kobayashi–Maskawa (CKM) quark mixing matrix [21]. For this matrix to acquire a non-trivial complex phase, and thus introduce differences in the weak transitions of particles and antiparticles, at least three quark families are required. This led them to postulate the existence of three more quark types: the charm, bottom and top. Weak transitions involving bottom quarks, which can be studies in B meson decays, can result in much larger asymmetries than the 10^{-3} effects observed in the kaon system. The B meson systems therefore form an important testing ground for the Standard Model and the CKM mechanism. Although B^0–$\bar{B}^0$ mixing was already observed by the Argus collaboration [22] in 1987, the exploration of the B meson systems really picked up momentum with the start of the *B-factories* BaBar and Belle in 1999 at the PEP-II and KEK-B asymmetric e^+e^- accelerators, respectively. These e^+e^- accelerators primarily operated at the $\Upsilon(4S)$ resonance, which, being slightly above the $B^0\bar{B}^0$ threshold in energy, predominantly decays into entangled pairs of either B^+B^- or $B^0\bar{B}^0$ mesons. The most notable achievement of the B-factories is the discovery of *CP* violation outside the kaon system. This was first established with the measurement of time-dependent *CP*-violation in the decay $B^0 \to J/\psi K^0_S$. The measured *CP* asymmetry allows for a high-precision determination of the complex phase ϕ_d associated with the interference between B^0–$\bar{B}^0$ mixing and the decay into the $J/\psi K^0_S$ final state [23, 24], which in the Standard Model is related to the angle β of the Unitarity Triangle. With this and other measurements the B factories had a majority share in establishing a precise and consistent picture of the flavour sector of the Standard Model over the past decade [25, 26].

Due to the rapid B^0_s–$\bar{B}^0_s$ oscillations, which could not be resolved by the B-factories, the study of the B^0_s meson system was left to the CDF and DØ experiments at the Tevatron proton–antiproton accelerator. One of the flagship analyses of their B physics programme was the study of the decay $B^0_s \to J/\psi\,\phi$ [27, 28], which forms the B^0_s meson equivalent of the $B^0 \to J/\psi K^0_S$ decay as it is the most sensitive probe to measure the complex phase ϕ_s associated with the B^0_s–$\bar{B}^0_s$ mixing process. The results obtained by CDF and DØ for ϕ_s suggested a large deviation from the Standard Model prediction. Given this exciting situation, it was up to the LHCb experiment at the LHC to sharpen the emerging picture and either confirm or reject the hints seen by the Tevatron experiments. After three years of operation, LHCb has significantly reduced the uncertainty on ϕ_s [29, 30], and turned it into yet another parameter that is consistent with its Standard Model prediction. But although not confirming the promising hints seen by the Tevatron experiments,

LHCb has also provided new hope for finding signs of new physics. Particularly exciting at the time of writing are the results on the angular parameters describing the $B^0 \to K^{*0}\mu^+\mu^-$ decay [31], and the so-called R_K ratio of the $B^+ \to K^+\mu^+\mu^-$ to $B^+ \to K^+e^+e^-$ branching fractions [32], which both show tension with respect to the Standard Model calculations. Global fits including these results, which use the operator product expansion framework introduced in Section 3.2 below, suggest that a solution with new physics modifying the Wilson coefficient C_9 is preferred over the Standard Model with 3.7σ [33]. It will be interesting to see whether these deviations survive the coming years, or if they can be explained by not-yet-understood Standard Model effects.

The above discussion leads to the main conclusion that the deviations from the Standard Model will be small or hard to find. Further improvements, both from the experimental and from the theoretical side, are thus necessary to successfully claim future new physics observations. This, in turn, means that we need to have a careful look at the theoretical assumptions linking the experiment measurements with the Standard Model parameters, because the currently used approximations will no longer remain sufficient. This observation is particularly relevant for the determination of the phases ϕ_d and ϕ_s from the mixing-induced *CP* asymmetries in the $B^0 \to J/\psi K^0_S$ and $B^0_s \to J/\psi\,\phi$ channel, respectively. In order to achieve a precision on the B–$\bar{B}$ *mixing phases*[b] ϕ_d and ϕ_s of below the degree level, as is the goal of the LHCb upgrade [34] and Belle II [35] programmes, controlling higher-order hadronic corrections to the *CP* observables becomes mandatory [36, 37, 38]. The decay amplitudes of both decay modes consist of a leading-order contribution from the *tree* topology, but in addition also get corrections from suppressed *penguin* topologies. The presence of these loop diagrams affects the relation between the measured *CP* asymmetries and the complex phases ϕ_d and ϕ_s by introducing an additional shift [39] $\Delta\phi_d$ and $\Delta\phi_s$, respectively, which has so far been ignored. These shifts can potentially be as large as one degree, thus exceeding the foreseen experimental precision. Controlling them is therefore mandatory in order to differentiate possible new physics effects from higher order Standard Model corrections.

Although theoretical estimates for these shifts are available [40, 41], it is, in view of the non-perturbative long-distance QCD contributions to these corrections, difficult to calculate them directly within the quantum field theory framework. In this thesis, we therefore follow an alternative approach, and rely on the $SU(3)_F$ flavour symmetry of QCD to relate the penguin contributions in the decay amplitudes of $B^0 \to J/\psi K^0_S$ and $B^0_s \to J/\psi\,\phi$ to those of similar decay modes in which they are no longer suppressed [36, 37]. This symmetry argument allows us to constrain the shifts directly from experimentally accessible observables like branching

[b] This is colloquial terminology and implicitly assumes the standard parametrisation of the CKM matrix, introduced in Section 2.2. It will nonetheless be used throughout this thesis.

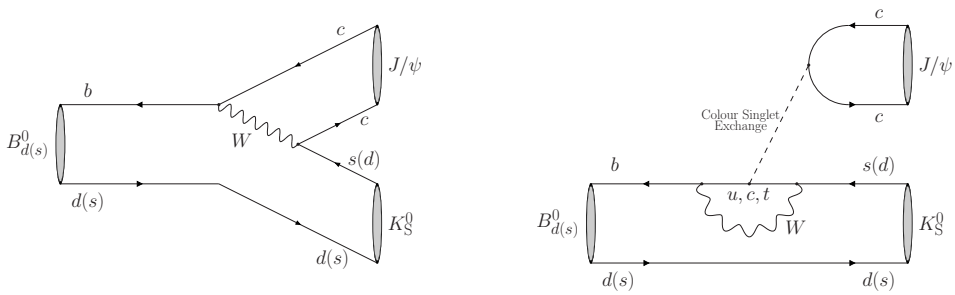

Figure 1.1: Illustration of the relation between the tree [Left] and penguin [Right] topologies of the $B^0 \to J/\psi K^0_S$ and $B^0_s \to J/\psi K^0_S$ decays. Further details are provided in Chapter 5.

ratios and *CP* asymmetries, where the latter quantities play the dominant role in constraining the penguin effects.

The research reported in this thesis is a shared project between theoretical and experimental particle physics. On the theoretical side, we explore the potential of the $SU(3)_F$ symmetry based method, while the experimental half of the research focuses on the measurement of the decay channel $B^0_s \to J/\psi K^0_S$, using data collected by the LHCb experiment.

In the phenomenological study, we analyse the currently available information on the penguin shifts $\Delta\phi_d$ and $\Delta\phi_s$, provide a roadmap for future measurements, and illustrate the potential of this method for the LHCb upgrade and Belle II era. Current constraints on $\Delta\phi_d$ can be obtained by performing a global analysis of the decay modes $B^0 \to J/\psi K^0_S$, $B^0_s \to J/\psi K^0_S$, $B^+ \to J/\psi K^+$, $B^+ \to J/\psi \pi^+$ and $B^0 \to J/\psi \pi^0$, while information on $\Delta\phi_s$ is available from measurements of the $B^0 \to J/\psi \rho^0$ and $B^0_s \to J/\psi \overline{K}^{*0}$ decays. Further details on the method, its underlying assumptions and the obtained results can be found in Chapter 5, which is based on work published in Ref. [42].

For the $B^0 \to J/\psi K^0_S$ channel, the most promising candidate in the long run is the $B^0_s \to J/\psi K^0_S$ decay [36]. It is related to the $B^0 \to J/\psi K^0_S$ decay by interchanging all s and d quarks with one another, i.e. via the U-spin subgroup of $SU(3)_F$, and leads to a one-to-one relation between all decay topologies of both modes, as illustrated in Fig. 1.1. Because of this feature, the use of the $B^0_s \to J/\psi K^0_S$ mode will ultimately lead to the most precise determination of the penguin shift $\Delta\phi_d$, as U-spin-breaking corrections associated with this method can easily be taken into account. Experimentally, however, the situation is more challenging. Although the contributions from the penguin topologies are enhanced compared to those originating from the tree topology, the tree amplitude itself is suppressed. As a result,

experimental information on the $B_s^0 \to J/\psi K_S^0$ mode was at the start of this four-year research project limited to a first measurement of the branching ratio by the CDF collaboration [43]. The experimental half of this thesis therefore focuses on the experimental study of the $B_s^0 \to J/\psi K_S^0$ decay, performed by the author for the LHCb collaboration using the data collected between 2010 and 2012 [44, 45, 46]. This culminated in a first measurement of the $B_s^0 \to J/\psi K_S^0$ *CP* asymmetry parameters [46], with the details on the selection, modelling and study of the systematic effects reported in Chapter 7. The uncertainties associated with this measurement are, however, still too large to successfully execute the $SU(3)_F$ symmetry based procedure outline above. But the results nonetheless demonstrate LHCb's capabilities for exploring the B_s^0 meson system and for further sharpening the picture of the Standard Model flavour sector in the years to come.

Brief Outline of this Thesis

The outline of this thesis is as follows. Chapter 2 introduces the Standard Model framework and the CKM matrix. Chapter 3 discusses non-leptonic B-meson decays and the challenges we face to control the hadronic uncertainties affecting their decay amplitudes. Chapter 4 then focuses on B–$\overline{B}$ mixing, its associated observables, and the consequences for the branching ratio, the decay time distributions, and the *CP* asymmetry parameters. Chapter 5 describes the above introduced method to control the penguin contributions affecting the determination of the B–$\overline{B}$ mixing phases ϕ_d and ϕ_s from the mixing-induced *CP* asymmetries in $B^0 \to J/\psi K_S^0$ and $B_s^0 \to J/\psi \phi$, respectively. Chapter 6 makes the transition towards the experimental part of the thesis by discussing the detector requirements for a successful analysis of the $B_s^0 \to J/\psi K_S^0$ mode, and illustrates how these are met by the LHCb detector. Chapter 7 then provides all the details on the experimental analyses of the $B_s^0 \to J/\psi K_S^0$ decay, focusing on the first measurement of the *CP* asymmetry parameters.

The numerical results presented in thesis are based on the latest theory calculations, experimental measurements, averages and compilations that were available on April 1st, 2015.

2 The Standard Model Framework

The Standard Model of elementary particle physics [1, 2, 3] provides a successful description of the strong, weak, and electromagnetic interaction between the fundamental particles making up our Universe. This Chapter offers a compact, but basic introduction to the Standard Model, where the focus lies on its flavour sector and the origin of *CP* violation. Further reading on these topics can be found in many textbooks and lecture notes; notably Ref. [47] for a general introduction to particle physics, and Refs. [48, 49, 50] and [51, 52, 53] for dedicated discussions on *CP* violation and strategies for measuring it through the decays of weak mesons.

2.1 Quark Flavour Mixing

The Standard Model

The quantum mechanical framework in which the Standard Model is formulated is that of a relativistic quantum field theory, where the particles are represented as fundamental fields. Two types of fields are identified: fermionic fields and bosonic fields. The building blocks of matter originate from fermionic fields, whereas the fields mediating the interactions between the particles are bosonic in nature. The fields are further characterised by the charges they carry. The charge associated with the strong interaction is referred to as *colour*, and can be either red, green or blue. Elementary fermionic fields that carry a non-trivial colour charge are called *quarks*, those without are referred to as *leptons*. The electric charge, related to the electromagnetic interaction, can be used to further separate the quarks into *up-type* quarks with charge $+2/3\,e$, and *down-type* quarks with charge $-1/3\,e$, as well as divide the leptons into electrically neutral *neutrinos* and charged leptons with charge $-1\,e$. The elementary fermions group together into *families*, each consisting of an up-type quark, a down-type quark, a neutrino and a charged lepton. The Standard Model has three families, which, as discussed below, is a necessary requirement for having *CP* violation. Thus a total of six quark *flavours* can be identified. They are, in order of increasing mass, the *up* (u), *down* (d), *strange* (s), *charm* (c), *bottom* (b) and *top* (t) quark. Similarly, the leptons consist of the *electron* (e), *muon* (μ) and *tau* (τ) and their associated neutrinos. In addition, each particle also has a

corresponding *antiparticle* with the same mass, but opposite quantum numbers.

The dynamics of the fundamental fermionic fields are described by a Lagrangian $\mathcal{L}$. Requiring that this Lagrangian is invariant under a continuous group of local symmetry, or *gauge*, transformations naturally leads to the introduction of additional bosonic fields. Known as *gauge fields*, these new quantities describe the interactions between the fermions and thus form the representations of the fundamental forces. To describe the strong, weak and electromagnetic interactions, the Standard Model uses the symmetry group

$$SU(3)_C \times SU(2)_L \times U(1)_Y \,. \tag{2.1}$$

The $SU(3)_C$ gauge group describes conservation of colour charge. It arranges the quarks into colour triplets, whereas the colour neutral leptons form a singlet under $SU(3)_C$ transformations. $SU(3)_C$ has eight generators, called *gluons*, which act as force carriers of the strong interaction. The resulting theory of quarks and gluons is known as *Quantum Chromodynamics* (QCD). A special property of QCD is *colour confinement*. It postulates that quarks and antiquarks must form colourless bound states, referred to as *hadrons*, through the process of *hadronisation*. The combination of three quarks forms a *baryon*, whereas a quark–antiquark pair is called a *meson*. Of special interest for this thesis are the pseudo-scalar B mesons, which are composed of a light quark $q \in \{u, d, s\}$ and a b antiquark.

The remaining gauge group $SU(2)_L \times U(1)_Y$, where L stands for *left* and Y refers to *hypercharge*, describes the electroweak interactions. Its four generators mix to form the $W^{\pm}$ and Z bosons, associated with the weak interaction, as well as the photon (γ), mediating electromagnetism.

Experimentally it has been well established [54, 55] that the weak interaction breaks parity symmetry, and does so maximally. This property is incorporated in the field theory description of the Standard Model by letting the weak gauge bosons couple only to the left-handed component of a fermion field. Consequently, the left-handed fields form doublets, whereas the right-handed fields remain singlets. For the quark fields, these doublets are generically referred as $Q_{L,i}$, where the index i is used to distinguish between the three fermion families, and are given by

$$\begin{pmatrix} u_L \\ d_L \end{pmatrix}, \qquad \begin{pmatrix} c_L \\ s_L \end{pmatrix}, \qquad \begin{pmatrix} t_L \\ b_L \end{pmatrix}. \tag{2.2}$$

The corresponding singlet quark fields are labelled as $u_{R,i}$ and $d_{R,i}$. Similar quantities can be defined for the lepton sector. The left- and right-handed components of the fermion fields can be obtained using the projection operators

$$\mathcal{P}_L = \frac{1}{2}(1 - \gamma_5)\,, \qquad \mathcal{P}_R = \frac{1}{2}(1 + \gamma_5)\,, \tag{2.3}$$

where γ_5 is the special product of Dirac matrices.

Spontaneous Symmetry Breaking

The formulation of the Standard Model as a gauge invariant theory prevents the inclusion of explicit mass terms in its Lagrangian. An additional mechanism is thus required to generate the masses of the Standard Model particles, and in particular explain the heavy mass of the $W^{\pm}$ and Z bosons. One elegant way to accomplish this, first proposed by Brout and Englert [56] and Higgs [57], is through spontaneous symmetry breaking by means of a new complex scalar field. This *Higgs* field is charged under the $SU(2)_L \times U(1)_Y$ gauge group, has four degrees of freedom, and takes the form

$$H \equiv \begin{pmatrix} H^+ \\ H^0 \end{pmatrix}. \tag{2.4}$$

By construction, the kinetic and potential terms describing the dynamics of this new field H are invariant under the symmetry group (2.1) and can thus be added to the Standard Model Lagrangian without jeopardising its gauge properties. The Higgs potential is, however, chosen in such a way that its minimum, representing the lowest energy state, i.e. the vacuum, breaks the electroweak symmetry. In the standard parametrisation, the non-zero vacuum expectation value of the Higgs field is given by

$$\langle H \rangle = \begin{pmatrix} 0 \\ \frac{v}{\sqrt{2}} \end{pmatrix}. \tag{2.5}$$

Upon expansion around this minimum, three massless excitations, one for each broken symmetry (direction), appear [58, 59]. When identifying these three *Nambu-Goldstone bosons* with the longitudinal degrees of freedom of the $W^{\pm}$ and Z bosons, the latter particles effectively acquire a mass term, proportional to the Higgs vacuum expectation value. The fourth symmetry direction, corresponding to the subgroup $U(1)_Q$ associated with electromagnetism, remains unbroken. The photon therefore stays massless.

The lowest energy excitation of the Higgs field above its ground state (2.5) is known as the *Higgs boson*, and essentially captures the fourth remaining degree of freedom of the original H field. The observation of a Higgs-like particle by the Atlas [11] and CMS [12] collaborations in July 2012, 48 years after its original invention, experimentally proved the existence of this Higgs field, and thus confirms the above described *Higgs mechanism*. But it remains an ongoing experimental challenge to determine whether or not this new particle is *the* Standard Model Higgs boson.

Yukawa Couplings

The inclusion of a Higgs sector to the Standard Model Lagrangian does not yet introduce masses for the quarks and leptons. The required interactions with the

Higgs field, known as the *Yukawa couplings*, thus need to be added *by hand* to the theory. For the quark sector, which is most relevant to the discussion here, these take the form

$$\mathcal{L}_{\text{Yukawa}} \equiv \sum_{i,j} Y_u^{ij} \left(\overline{Q_{L,i}} \cdot i\sigma_2 H^*\right) u_{R,j} + \sum_{i,j} Y_d^{ij} \left(\overline{Q_{L,i}} \cdot H\right) d_{R,j} + \text{h.c.}\,, \tag{2.6}$$

where σ_2 is one of the Pauli matrices. The coupling constants Y_u^{ij} and Y_d^{ij} are arbitrary complex numbers, making these terms in general not invariant under *CP* transformations.

Upon expanding around the electroweak vacuum (2.5), the Lagrangian (2.6) reduces to the form

$$\mathcal{L}_{\text{mass}} = \sum_{i,j} m_u^{ij} \overline{u_{L,i}} u_{R,j} + \sum_{i,j} m_d^{ij} \overline{d_{L,i}} d_{R,j} + \text{h.c.}\,, \tag{2.7}$$

where $\mathbf{m} \equiv v\mathbf{Y}/\sqrt{2}$.

In view of this result it is convenient to introduce a mass eigenbasis, which arises upon diagonalising the matrices $\mathbf{m}_u$ and $\mathbf{m}_d$[a]. In Eq. (2.7) one then recognises the familiar expressions for a mass term, which were previously not permitted as they break gauge invariance, but now appear as a consequence of spontaneous symmetry breaking through the Higgs mechanism. The new mass basis is related to the flavour or interaction eigenbasis used in the Lagrangian (2.6) by the unitary transformations

$$\begin{aligned} u_{L,i}^m &= \sum_j U_{L,ij}^u u_{L,j}\,, & d_{L,i}^m &= \sum_j U_{L,ij}^d d_{L,j}\,, \\ u_{R,i}^m &= \sum_j U_{R,ij}^u u_{R,j}\,, & d_{R,i}^m &= \sum_j U_{R,ij}^d d_{R,j}\,, \end{aligned} \tag{2.8}$$

$$\text{diag}(m_u, m_c, m_t) = \mathbf{U}_L^{u\dagger} \mathbf{m}_u \mathbf{U}_R^u\,, \qquad \text{diag}(m_d, m_s, m_b) = \mathbf{U}_L^{d\dagger} \mathbf{m}_d \mathbf{U}_R^d\,.$$

Due to the structure of the $SU(2)_L$ generators, this change of basis does not affect neutral current interactions like

$$\overline{\mathbf{u}}_L \gamma^\mu \mathbf{u}_L \quad \rightarrow \quad \overline{\mathbf{u}}_L^m \gamma^\mu \mathbf{u}_L^m\,. \tag{2.9}$$

As such, the Standard Model does not allow for flavour changing neutral currents (FCNC) at tree level, a feature known as the GIM-mechanism [60]. This mechanism is named after Glashow, Iliopoulos and Maiani who predicted the existence of the

[a] To ensure that the obtained diagonal elements, which represent the quark masses, are real and positive definite, we actually diagonalise the combination $\mathbf{m}\,\mathbf{m}^+ = \mathbf{U}_L \text{diag}^2(m) \mathbf{U}_L^\dagger$, where $\mathbf{U}_L$ is a unitary matrix . Upon inserting $\mathbf{U}_R^\dagger \mathbf{U}_R = \mathbf{1}$, using a second unitary matrix $\mathbf{U}_R$, we then get $\text{diag}(m) = \mathbf{U}_L^\dagger \mathbf{m}\, \mathbf{U}_R$.

charm quark in order to explain the absence of $s \leftrightarrow d$ transitions at tree level. At loop level, FCNCs are permitted, and are, for example, responsible for neutral mesons mixing, discussed in Chapter 4.

The change of basis (2.8), however, does modify the charged current interaction of the weak force

$$i\frac{g_{\text{EW}}}{\sqrt{2}} W_\mu^+ \overline{\mathbf{u}}_L \gamma^\mu \mathbf{d}_L + \text{h.c.} \quad \rightarrow \quad i\frac{g_{\text{EW}}}{\sqrt{2}} W_\mu^+ \overline{\mathbf{u}}_L^m \left(\mathbf{U}_L^u \mathbf{U}_L^{d\dagger}\right) \gamma^\mu \mathbf{d}_L^m + \text{h.c.} \tag{2.10}$$

The Cabibbo–Kobayashi–Maskawa (CKM) quark mixing matrix [20, 21]

$$\mathbf{V}_{\text{CKM}} \equiv \mathbf{U}_L^u \mathbf{U}_L^{d\dagger} = \begin{pmatrix} V_{ud} & V_{us} & V_{ub} \\ V_{cd} & V_{cs} & V_{cb} \\ V_{td} & V_{ts} & V_{tb} \end{pmatrix}, \tag{2.11}$$

introduced by Eq. (2.10), is non-diagonal and therefore gives rise to tree level flavour changing charged currents between the different quark generations. It contains information from the original Yukawa couplings in Eq. (2.6) and is the source of *CP* violation in the quark sector of the Standard Model.

Although the discussion regarding the Yukawa couplings has been focused on the quark sector, the same arguments also apply to the lepton sector. The equivalent lepton mixing matrix is known as the Pontecorvo–Maki–Nakagawa–Sakata (PMNS) matrix [61, 62, 63], and describes the mixing between the different neutrino flavours.

2.2 The CKM Matrix

Let us have a more detailed look at the CKM matrix, starting with its general structure.

The CKM matrix is an $n \times n$ complex matrix, where n counts the number of families and equals three in the Standard Model. Being the product of two unitary matrices, i.e. Eq. (2.11), it is itself unitary and thus described by n^2 free parameters. Allowing for general redefinitions of the $2n$ quark fields as

$$q_j \rightarrow \exp(i\phi_j)\, q_j\,, \qquad V_{jk} \rightarrow \exp(i\phi_j)\, V_{jk} \exp(-i\phi_k)\,, \tag{2.12}$$

eliminates up to $2n-1$ of these parameters, leaving only an overall quark phase that has no physical meaning. The CKM matrix is thus described by

$$\underbrace{(n-1)^2}_{\text{Free parameters}} = \underbrace{\frac{1}{2}n(n-1)}_{\text{Euler angles}} + \underbrace{\frac{1}{2}(n-1)(n-2)}_{\text{Complex phases}} \tag{2.13}$$

free parameters, of which $\binom{n}{2}$ are Euler angles and the remaining ones are complex phases.

In the Standard Model the CKM matrix can thus be described by three angles $(\theta_{12}, \theta_{23}, \theta_{13})$ and one complex phase (δ_{13}), with the *standard parametrisation* [64] given by

$$\mathbf{V}_{\text{CKM}} = \begin{pmatrix} 1 & 0 & 0 \\ 0 & c_{23} & s_{23} \\ 0 & -s_{23} & c_{23} \end{pmatrix} \begin{pmatrix} c_{13} & 0 & s_{13}e^{-i\delta_{13}} \\ 0 & 1 & 0 \\ -s_{13}e^{i\delta_{13}} & 0 & c_{13} \end{pmatrix} \begin{pmatrix} c_{12} & s_{12} & 0 \\ -s_{12} & c_{12} & 0 \\ 0 & 0 & 1 \end{pmatrix}, \tag{2.14}$$

where c_{ij} and s_{ij} are short-hand notations for $\cos\theta_{ij}$ and $\sin\theta_{ij}$, respectively.

Experimentally, a strong hierarchy in the sizes of the different CKM elements has been observed, resulting in the relation $s_{13} \ll s_{23} \ll s_{12} \ll 1$. It is therefore more convenient to adopt the *Wolfenstein parametrisation* [65, 66] in terms of the four parameters λ, A, ρ and η, which are related to the four standard angles as

$$s_{12} \equiv \lambda\,, \qquad s_{23} \equiv A\lambda^2\,, \qquad s_{13}e^{-i\delta_{13}} \equiv A\lambda^3(\rho - i\eta)\,. \tag{2.15}$$

One can then make an expansion in powers of $\lambda = 0.22548^{+0.00068}_{-0.00034}$ [25], resulting, to leading order, in

$$\mathbf{V}_{\text{CKM}} = \begin{pmatrix} 1-\frac{1}{2}\lambda^2 & \lambda & A\lambda^3(\rho - i\eta) \\ -\lambda & 1-\frac{1}{2}\lambda^2 & A\lambda^2 \\ A\lambda^3(1-\rho-i\eta) & -A\lambda^2 & 1 \end{pmatrix} + \mathcal{O}(\lambda^4)\,. \tag{2.16}$$

This shows that transitions within the same quark family proceed at order unity, while mixing between the generations is always suppressed.

For some of the expressions below also next-to-leading order terms in λ are required. Up to $\mathcal{O}(\lambda^6)$, these additional terms are

$$\begin{pmatrix} -\frac{1}{8}\lambda^4 & 0 & 0 \\ A^2\lambda^5(\frac{1}{2} - \rho - i\eta) & -\frac{1}{8}\lambda^4(1+4A^2) & 0 \\ \frac{1}{2}A\lambda^5(\rho + i\eta) & A^2\lambda^4(\frac{1}{2} - \rho - i\eta) & -\frac{1}{2}A^2\lambda^4 \end{pmatrix}. \tag{2.17}$$

Having a complex phase in the CKM matrix, i.e. $\delta_{13} \neq 0$ or $\eta \neq 0$, is a necessary condition to obtain observable *CP*-violating effects. But it is, however, not sufficient. In case any two quarks with the same charge also had the same mass, the quark phase rotations (2.12) could be used to eliminate the *CP*-violating phase. One must therefore also have that

$$(m_t^2 - m_c^2)(m_t^2 - m_u^2)(m_c^2 - m_u^2)(m_b^2 - m_s^2)(m_b^2 - m_d^2)(m_s^2 - m_d^2) \times J_{\text{CP}} \neq 0\,. \tag{2.18}$$

Here

$$J_{\text{CP}} \equiv \left| \mathcal{I}\text{m}(V_{i\alpha} V_{j\beta} V_{i\beta}^* V_{j\alpha}^*) \right| \qquad (i \neq j,\ \alpha \neq \beta) \tag{2.19}$$

is the Jarlskog parameter [67], which quantifies the amount of *CP* violation in the Standard Model. It is invariant under rotations (2.12) of the quark phases and takes the form

$$J_{\rm CP} = s_{12}s_{13}s_{23}c_{12}c_{23}c_{13}^2 \sin\delta_{13} = \lambda^6 A^2 \eta\,. \tag{2.20}$$

The condition (2.18) thus intertwines (the origin of) *CP* violation in the Standard Model with the hierarchy of the quark masses, neither of which can presently be explained.

2.3 The Unitarity Triangle

The unitarity of the CKM matrix leads to six orthogonality conditions that can be visualised as triangles in the complex plane. All six triangles have the same area, given by

$$\mathcal{S} = \frac{1}{2}\lambda^6 A^2 \eta = \frac{1}{2}\, J_{\rm CP} \tag{2.21}$$

to lowest order in λ. But of special interest is the unitarity condition

$$V_{ud}V_{ub}^* + V_{cd}V_{cb}^* + V_{td}V_{tb}^* = 0\,, \tag{2.22}$$

which leads to a triangle with sides of equal power in λ, of which one side, at least up to $\mathcal{O}(\lambda^6)$, coincides with the real axis. The condition (2.22) is therefore divided by $V_{cd}V_{cb}^*$ such that one side has unit size. The resulting triangle, shown in Fig. 2.1, is known in the literature as *the* Unitarity Triangle (UT). The sides and angles of this triangle are physical observables that can be probed directly by experiments. The non-unit sides are given by

$$R_b \equiv \left|\frac{V_{ud}V_{ub}^*}{V_{cd}V_{cb}^*}\right| = \sqrt{\bar\rho^2+\bar\eta^2}\,, \qquad R_t \equiv \left|\frac{V_{td}V_{tb}^*}{V_{cd}V_{cb}^*}\right| = \sqrt{(1-\bar\rho)^2+\bar\eta^2}\,, \tag{2.23}$$

where [66]

$$\bar\rho \equiv \rho\left(1-\frac{1}{2}\lambda^2\right), \qquad \bar\eta \equiv \eta\left(1-\frac{1}{2}\lambda^2\right), \tag{2.24}$$

are, up to $\mathcal{O}(\lambda^6)$, the coordinates of the apex of this triangle. The angles of the Unitarity Triangle are defined as

$$\alpha \equiv \arg\left(-\frac{V_{td}V_{tb}^*}{V_{ud}V_{ub}^*}\right), \qquad \beta \equiv \arg\left(-\frac{V_{cd}V_{cb}^*}{V_{td}V_{tb}^*}\right), \qquad \gamma \equiv \arg\left(-\frac{V_{ud}V_{ub}^*}{V_{cd}V_{cb}^*}\right) \tag{2.25}$$

and satisfy the relation $\alpha+\beta+\gamma=\pi$. To leading order, the angles β and γ are directly associated with the complex phase of the CKM elements V_{td} and V_{ub}, respectively.

Measurements of the sides and angles of the Unitarity Triangle can be used to over-constrain the position of its apex $(\bar\rho,\bar\eta)$, and thus test the consistency of the

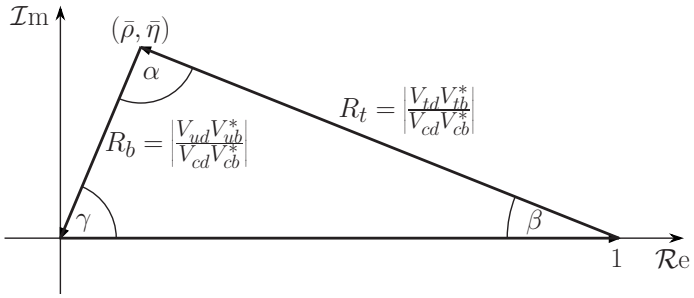

Figure 2.1: *The* Unitarity Triangle of CKM matrix, corresponding to the orthogonality relation (2.22).

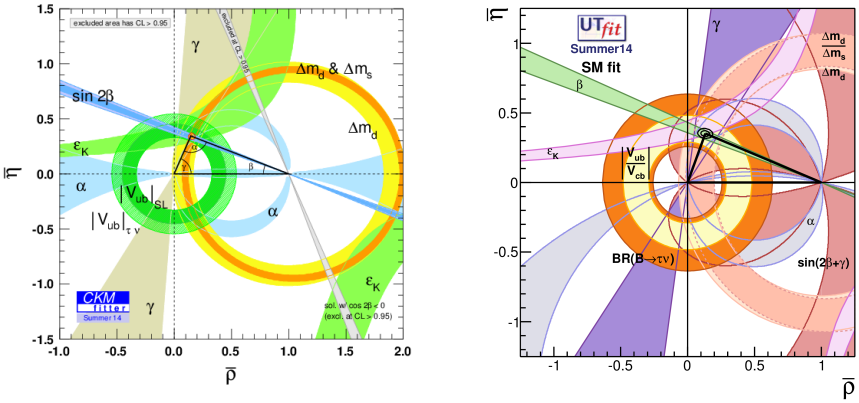

Figure 2.2: Global fits of the Unitarity Triangle performed by the CKMfitter [25] [Left] and UTfit [26] [Right] groups.

CKM paradigm with the experimental data. Global fits of the Unitarity Triangle and its parameters are performed by the CKMfitter [25] and UTfit [26] groups, whose latest fits are given in Fig. 2.2. These global fits seek to establish whether the Standard Model CKM matrix provides a complete picture of *CP* violation in the quark sector, or if there are also other sources present. Such sources would reveal themselves as inconsistencies between the different input measurements, and could ultimately prevent the global fits from finding a unique solution for the UT apex. The current fits show an overall consistent picture, although slight tensions between different input quantities certainly exist.

Two important examples should be mentioned. The first one is a long-standing

discrepancy between the inclusive and exclusive determinations of the CKM elements $|V_{ub}|$ and $|V_{cb}|$ from semileptonic B meson decays. Together these quantities have a large impact on the value of the parameter R_b, which forms one of the sides of the UT triangle. For $|V_{ub}|$ the individual averages are [64]

$$|V_{ub}| = \begin{cases} (4.41 \pm 0.21) \times 10^{-3} & \text{Inclusive} \\ (3.28 \pm 0.29) \times 10^{-3} & \text{Exclusive}\,, \end{cases} \tag{2.26}$$

which differ from each other by $3.2\,\sigma$, while for $|V_{cb}|$ they are [64]

$$|V_{cb}| = \begin{cases} (42.2 \pm 0.7) \times 10^{-3} & \text{Inclusive} \\ (39.5 \pm 0.8) \times 10^{-3} & \text{Exclusive}\,, \end{cases} \tag{2.27}$$

and differ from each other by $2.5\,\sigma$. Combined with the parameter λ, these results lead to

$$R_b = \begin{cases} 0.452 \pm 0.023 & \text{Inclusive} \\ 0.359 \pm 0.033 & \text{Exclusive}\,. \end{cases} \tag{2.28}$$

The inclusive determinations of $|V_{ub}|$ and $|V_{cb}|$ exploit the properties of the total semileptonic decay rate. The theoretical input needed to determine the CKM factors from the experimental measurements is calculated in the *Heavy Quark Expansion* [68, 69], in which the decay amplitude $\Gamma(B \to X_{(c,u)} l^+ \nu_l)$ is expanded in powers of $1/m_b$ [70, 71, 72]. The exclusive determinations of $|V_{ub}|$ and $|V_{cb}|$, on the other hand, are based on measurements of the differential decay rates of $B \to \pi l^+ \nu_l$ and $B \to D^{(*)} l^+ \nu_l$ transitions, respectively. In the analysis of these modes, input from lattice calculations is required to disentangle the CKM elements from the hadronic physics involved in the decays. From a theoretical point of view, the inclusive calculations are better under control than their exclusive counterparts, while from the experimental point of view the roles are reversed. Improved understanding of the lattice calculations can hopefully settle this issue in the near future. A recent update on the $B \to \pi$ form factors by the MILC collaboration [73] at least points in the right direction. For a more detailed discussion on the discrepancy between the inclusive and exclusive determinations of $|V_{ub}|$ and $|V_{cb}|$ the reader is referred to the Particle Data Group's review on this topic [64].

Secondly, the latest UT fits show a $1.6\,\sigma$ tension [25] between the direct measurement of $\sin(2\beta)$ from $B^0 \to J/\psi\, K_S^0$ and the Standard Model prediction of this quantity, which follows from the relation [51]

$$\sin 2\beta = \frac{2R_b \sin\gamma (1 - R_b \cos\gamma)}{(R_b \sin\gamma)^2 + (1 - R_b \cos\gamma)^2}\,. \tag{2.29}$$

Given the relatively large value of the UT angle γ, the Standard Model value for β is mainly determined by the side R_b. Experimental input on R_b is provided by the

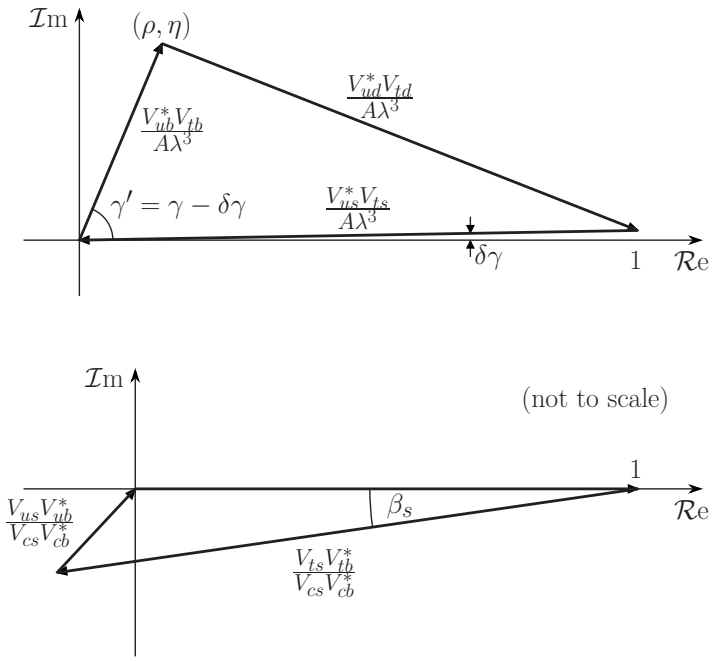

Figure 2.3: The CKM triangles introducing the complex phase associated with V_{ts}. Top: Corresponding to the orthogonality relation (2.31), and explaining the notation $\delta\gamma$; Bottom: Corresponding to the orthogonality relation (2.32), and explaining the notation β_s.

above discussed in- and exclusive semileptonic B meson decays, and the branching ratio measurement of $B^+ \to \tau^+ \nu_\tau$, which provides complementary information on $|V_{ub}|$. The tension between the measurement of $\sin(2\beta)$ and the $B^+ \to \tau^+ \nu_\tau$ branching ratio is softened when including the latest $\sin(2\beta)$ measurement from the LHCb collaboration [74]

$$\sin(2\beta) = 0.731 \pm 0.035\,(\text{stat.}) \pm 0.020\,(\text{syst.}) \tag{2.30}$$

in the UT fits, and by the inclusion of higher order corrections to the measurement of $\sin(2\beta)$. Controlling these corrections forms the main topic of this thesis.

At higher orders in λ also the CKM element V_{ts} obtains a complex phase. This phase appears either as a slight rotation of the basis of the second non-squashed triangle, which arises from the condition

$$V_{ud}^* V_{td} + V_{us}^* V_{ts} + V_{ub}^* V_{tb} = 0\,, \tag{2.31}$$

or as the equivalent "β" angle in the squashed triangle arising from the condition

$$V_{us}V_{ub}^{*} + V_{cs}V_{cb}^{*} + V_{ts}V_{tb}^{*} = 0\,. \tag{2.32}$$

Both options are illustrated in Fig. 2.3. When derived from the first condition, this phase is referred to as $\delta\gamma$ because of its connection, explained by Fig. 2.3, with the UT angle γ. The second option leads to the more common notation β_s. The phase is formally defined as

$$\delta\gamma = \beta_s \equiv \arg\left(-\frac{V_{ts}V_{tb}^{*}}{V_{cs}V_{cb}^{*}}\right) = -\lambda^2\eta\,, \tag{2.33}$$

and can be measured with processes involving B_s^0–$\bar{B}_s^0$ mixing.

3 The Theory of Non-Leptonic Decays

The $B \to J/\psi X$ decays, where X is a light pseudo-scalar or vector meson, play a dominant role in this thesis. The decay amplitude of these weak transitions can be split into two parts: the time-independent transition amplitude, and the decay time evolution of the initial state. The latter is described in detail in Chapter 4, while methods to deal with the time-independent amplitudes are discussed here. The focus in this Chapter lies on the non-leptonic B meson decays, of which the $B \to J/\psi X$ modes are an example.

Calculations of non-leptonic transition amplitudes are limited by our understanding of the hadronisation dynamics and other low-energy QCD physics involved in these processes. This Chapter therefore introduces some basic concepts that are commonly used to simplify the phenomenological description of these decays. Specifically, it discusses the use of low-energy effective Hamiltonians, the framework of the operator product expansion (OPE), the concept of factorisation, and the (approximate) flavour symmetry of QCD[a]. Combined, these tools allow us to related the hadronic effects in different decay modes to one another. In some cases the (nuisance) parameters describing the hadronisation dynamics can therefore be factored out completely, while in others they may be constrained directly using experimentally available data.

3.1 Classification of Non-Leptonic B Decays

Before providing further technical details regarding the above listed theoretical tools, it is useful to introduce a classification for the non-leptonic B meson decays [52, 53]. Ignoring interactions between the b antiquark and the light spectator quark, which together make up the B meson, these decays proceed via a $\bar{b} \to \bar{q}_1 q_2 \bar{q}_3$ quark-level transition, with $q_1 \in \{d, s\}$. This transition can proceed via two main types of decay topologies: the *tree* diagram, and the *penguin* diagram, which are both illustrated in Fig. 3.1. Depending on the flavour of the quarks q_2 and q_3, three classes of non-leptonic B meson decays can now be identified. If q_2 and q_3 differ in

[a] For a more detailed discussion on these topics, the readers is referred to Refs. [75, 76], among others.

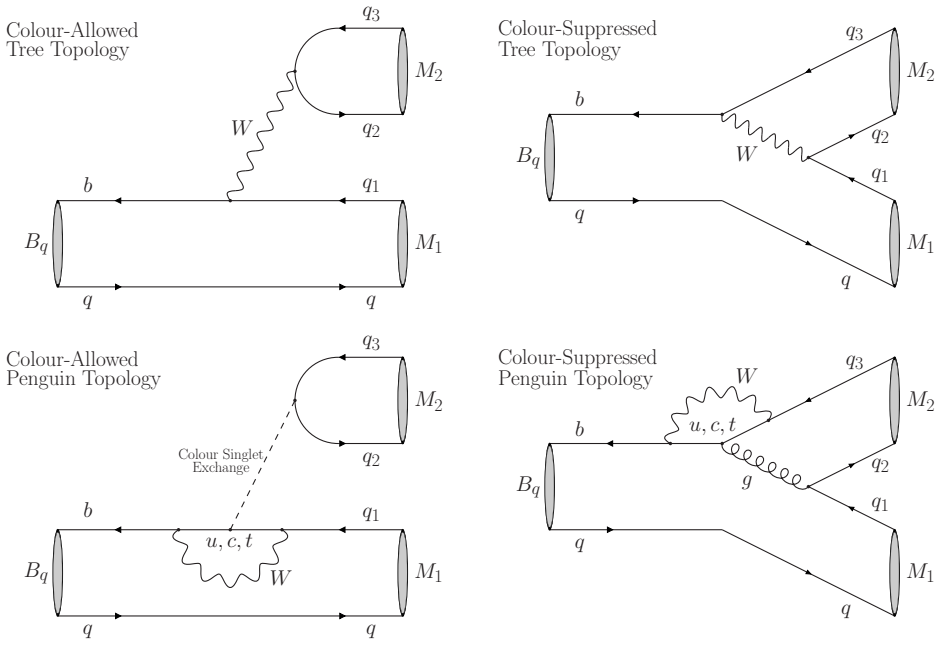

Figure 3.1: Illustration of colour-allowed [Left] and colour-suppressed [Right] tree [Top] and penguin [Bottom] topologies affecting the non-leptonic B meson decays.

quark flavour, like for the decays $B^0 \to D^- K^+$ and $B_s^0 \to D_s^- \pi^+$, only tree topologies can contribute to the amplitude. If $q_2 = q_3 \in \{d, s\}$, like for the decay $B_s^0 \to \phi\phi$, only penguin topologies can contribute to the amplitude. And finally, if $q_2 = q_3 \in \{u, c\}$, like for the $B \to J/\psi\, X$ decays, both tree and penguin topologies contribute to the amplitude. The structure of the low-energy effective Hamiltonian depends on the topologies that contribute, and thus differs for the three decay classes.

The tree and penguin topologies can be split further into two subclasses: the colour-allowed and colour-suppressed topologies, also illustrated in Fig. 3.1. In the amplitudes associated with colour-allowed topologies, the colour can be summed over individually for the two final state mesons, while for colour-suppressed amplitudes the colour flow between the final state mesons is correlated, leading to a single colour sum in the transition amplitude. Because of this restriction on the colour flow, the amplitudes associated with the colour-suppressed topologies are proportional to $1/N_C$, with N_C the number of colours, while the colour-allowed amplitudes do not have such a suppression factor. Examples of decays with only colour-allowed tree topologies are $B^0 \to D^- K^+$ and $B^0 \to D^- \pi^+$, while decays like $B^0 \to \overline{K}^0 J/\psi$ and $B^0 \to \pi^0 \overline{D}^0$ have only colour-suppressed tree topologies, and

decays like $B^+ \to \overline{D}^0 K^+$ and $B^+ \to \overline{D}^0 \pi^+$ have both colour-allowed and colour-suppressed tree topologies.

Lastly, the penguin topologies can also be split depending on whether the radiated vector boson is a gluon or a photon/Z, leading to yet another division in the topologies: the gluonic and the electroweak penguins.

3.2 Operator Product Expansion

The OPE Framework

In B meson decays, two vastly different energy scales are encountered: On the one hand, the typical energy scale E of the decay is well approximated by the mass of the b quark $m_b = 4.18 \pm 0.03\,\mathrm{GeV}/c^2$ [64]. On the other hand, weak decays are mediated by the heavy W boson, which has a mass $m_W = 80.385 \pm 0.015\,\mathrm{GeV}/c^2$ [64]. As E is much smaller than m_W, the exchanged W boson must be highly virtual. Consequently, to a decaying meson, this intermediate particle is not resolvable. Weak transitions through tree topologies therefore effectively proceed via a point interaction, similar to the explanation for nuclear β decay provided by Fermi in 1933 [77]. This description of B meson decays using a four-point contact interaction is an example of a low-energy effective theory. The formal framework in which we formulate the low-energy effective transitions of B meson decays, including those proceeding via different decay topologies, is the operator product expansion [78].

In the OPE framework, all degrees of freedom associated with energy scales larger than $E \approx m_b$, i.e. the W and Z bosons as well as the top quark, are removed from the full (Standard Model) theory to form a low-energy effective Hamiltonian $\mathcal{H}_{\mathrm{eff}}$. This Hamiltonian is expanded in a basis of local, mass dimension six operators $\mathcal{O}_j$ [79]. Higher dimensional operators are suppressed by additional powers of $1/m_W$, and therefore neglected in the above expansion. The operators differ in their flavour and colour structures, and can be loosely associated with the tree, gluonic penguin and electroweak penguin topologies, as made explicit below. In terms of these operators, the low-energy effective Hamiltonian is decomposed as

$$\mathcal{H}_{\mathrm{eff}} = \frac{G_{\mathrm{F}}}{\sqrt{2}} V_{pq}^* V_{p'q'} \sum_j C_j \mathcal{O}_j \,, \tag{3.1}$$

where V_{pq} are the relevant CKM matrix elements and

$$G_{\mathrm{F}} \equiv \frac{\sqrt{2} g_{\mathrm{EW}}^2}{8 m_W^2} \tag{3.2}$$

is the Fermi constant, which can be expressed in terms of W mass and the electroweak coupling constant. The factors C_j are referred to as the *Wilson coefficients*, and represent the coupling constants of the effective theory.

The OPE is a powerful tool for computing weak decay processes. Using the effective Hamiltonian (3.1), the amplitude for the transition of a B meson into some final state f takes the form

$$\langle f|\mathcal{H}_{\text{eff}}|B\rangle = \frac{G_{\text{F}}}{\sqrt{2}} V_{pq}^* V_{p'q'} \sum_j C_j(\mu)\langle f|\mathcal{O}_j(\mu)|B\rangle\,, \tag{3.3}$$

where both C_j and $\mathcal{O}_j$ depend on the QCD renormalisation scale μ. This expansion separates the amplitude calculation into two distinct parts, describing different energy regimes. The Wilson coefficients describe the short-distance physics, associated with energies above the scale μ, while the *hadronic matrix elements* $\langle f|\mathcal{O}_j(\mu)|B\rangle$ describe the long-distance QCD effects associated with energies below the scale μ. In this sense, the scale μ, which for B meson decays is typically chosen to be m_b, doubles as a factorisation scale. As the physical process itself cannot depend on μ, it must drop out of the final result, implying that the dependencies inside C_j and $\mathcal{O}_j$ must cancel each other. It is therefore a matter of choice what physics are exactly accounted for by C_j and what by $\langle f|\mathcal{O}_j(\mu)|B\rangle$.

The Wilson coefficients capture the contributions from the high energy physics, including the high-energy QCD effects. Due to asymptotic freedom of QCD, the Wilson coefficients can be calculated using a perturbative expansion in the strong coupling constant $\alpha_s(\mu)$ for energies μ down to hadronic scales $\mathcal{O}(1\,\text{GeV})$, and can thus be determined to any desired level of precision.

The formal procedure for calculating the Wilson coefficients [80] is referred to as *matching* of the full theory onto the effective theory. It is rather technical and the exact details, see Ref. [75] for a more in-depth introduction, go beyond the scope of this thesis. Let us nonetheless sketch the different steps involved. First, a perturbative calculation of the weak transition is performed with the full theory, including all dynamical degrees of freedom. The resulting transition amplitude is expressed in terms of the tree-level currents, i.e. without explicitly evaluating the long-distance dynamics that are to be represented by the hadronic matrix elements. As a second step, the same calculation is repeated for the effective theory. The treatment of the obtained results is more involved compared to the calculation in the full theory as it requires additional corrections and manipulations, which go under the names of *operator renormalisation* and *operator mixing*. The outcome is again expressed in terms of the tree-level currents. By comparing the expressions for the transition amplitude in the full and effective theory, the Wilson coefficients can now straightforwardly be extracted.

The obtained expressions contain logarithms of the form $\log m_W^2/\mu^2$, which become large when $\mu \ll m_W^2$. In such a situation, which is the case for the default working point of the OPE approach, the perturbative expansion no longer converges. To avoid this problem, the Wilson coefficients are therefore calculated at

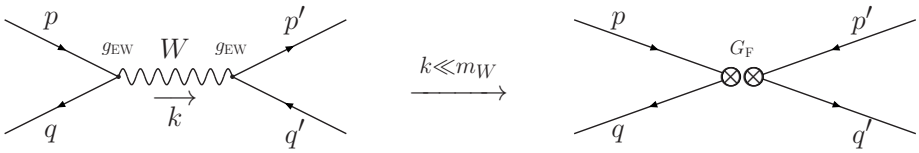

Figure 3.2: Illustration for the weak transition $pq \to p'q'$ in the full [Left] and low-energy effective [Right] theory, in which the W propagator is replaced by a four-point contact interaction.

the energy scale $\mu = m_W$ and run down to the desired working point, in our case $\mu = m_b$, using the renormalisation group equations. This has the effect of summing the log terms to all orders in the perturbative expansion, and leads to so-called *renormalisation group improved* perturbation theory.

The hadronic matrix elements describe the energy regime below the renormalisation scale μ, in which the strong coupling constant cannot be treated perturbatively. Consequently, they contain the non-perturbative physics of the decay process, whose determination poses a major challenge for the study of weak decays. Insights can be obtained with approaches like factorisation, as is discussed in Section 3.3 below, but the emerging picture is still far from satisfactory. The hadronic matrix elements therefore constitute the most important source of uncertainty[b] on the theoretical calculation of observables associated with weak decays.

A Basic Example

Let us illustrate the features of the operator product expansion using the very basic example of a $pq \to p'q'$ transition process. Consider therefore the weak decay process shown on the left-hand side of Fig. 3.2. Using Greek letters[c] to explicitly show the $SU(3)_C$ colour indices, the Hamiltonian associated with this interaction is given by

$$\mathcal{H} = \frac{g_{\text{EW}}^2}{8} V_{pq}^* V_{p'q'} \Delta^{\mu\nu} (\bar{q}_\alpha p_\alpha)_{\text{V-A}} (\bar{q}'_\beta p'_\beta)_{\text{V-A}} \,, \tag{3.4}$$

where

$$(\bar{q}p)_{\text{V}\pm\text{A}} \equiv \bar{q}\gamma_\mu(1 \pm \gamma_5)p \tag{3.5}$$

[b] Certain exceptions apply: For a small list of (semi)leptonic decays, like $B_s^0 \to \mu^+\mu^-$, the hadronic matrix elements can be related to perturbative quantities and/or decay constants. In these decays, the problem of long-distance QCD can therefore (almost) completely be avoided.

[c] The *Einstein summation convention* is implied.

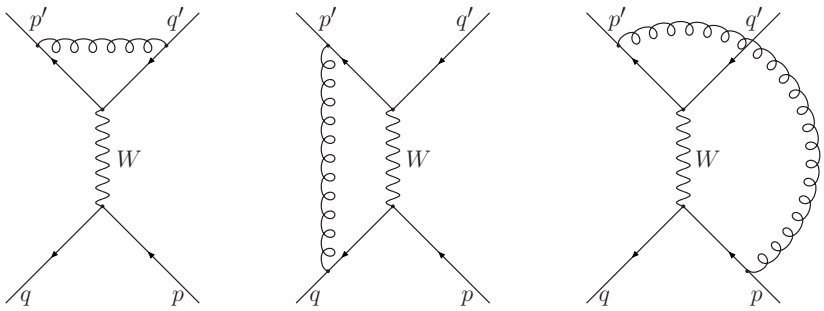

Figure 3.3: Leading order QCD corrections to the weak transition $pq \to p'q'$.

gives the vector–axial-vector structure of the weak interaction in terms of the projection operators introduced in Eq. (2.3), and is a consequence of the fact that the W boson only couples to the left-handed component of the quark fields. In terms of the momentum transfer $k \sim E$, the W propagator takes the form

$$\Delta^{\mu\nu}(k) \equiv \frac{1}{k^2 - m_W^2}\left(g^{\mu\nu} - \frac{k^\mu k^\nu}{m_W^2}\right) \qquad \xrightarrow{k \ll m_W} \qquad \frac{g^{\mu\nu}}{m_W^2} + \mathcal{O}\left(\frac{k^2}{M_W^2}\right). \tag{3.6}$$

Upon expanding in powers of k^2/m_W^2, the Hamiltonian becomes

$$\mathcal{H} = \frac{G_F}{\sqrt{2}} V_{pq}^* V_{p'q'} (\bar{q}_\alpha p_\alpha)_{V-A} (\bar{q}'_\beta p'_\beta)_{V-A} + \mathcal{O}\left(\frac{k^2}{M_W^2}\right). \tag{3.7}$$

The first term in this expansion is independent of the momentum transfer k, and therefore insensitive to the presence of the intermediate W boson. It represents a four-point contact interaction, as illustrated on the right-hand side of Fig. 3.2. When considered to all orders in k^2/m_W^2, the expansion (3.7) is completely equivalent to the formulation in Eq. (3.4). The truncation of the series after the leading term yields a low-energy effective Hamiltonian, valid for $E \ll m_W$. In this limit, the W boson is said to have been *integrated out*, which refers to the formal procedure for removing it from the generating functional by integrating over its field in the absence of source terms [76]. Comparing the truncated Hamiltonian in Eq. (3.7) with the low-energy effective Hamiltonian in Eq. (3.1), allows us to identify the product of quark currents with the operator

$$\mathcal{O}_2 \equiv (\bar{q}_\alpha p_\alpha)_{V-A} (\bar{q}'_\beta p'_\beta)_{V-A}\,, \tag{3.8}$$

which in this example has an effective coupling coefficient $C_2 = 1$.

When also including the leading order QCD corrections illustrated in Fig. 3.3, the above Hamiltonian becomes insufficient to describe the low-energy dynamics

of the weak transition $pq \to p'q'$. The virtual QCD corrections do not all have the same colour structure as the operator $\mathcal{O}_2$. In particular, the amplitudes associated with the middle and right-most diagram are proportional to the product of colour charges $T^a_{\alpha\beta} T^a_{\gamma\delta}$. They can be related to the leading order amplitude using the $SU(N_C)$ colour-algebra relation

$$T^a_{\alpha\beta} T^a_{\gamma\delta} = \frac{1}{2}\left[\delta_{\alpha\delta}\delta_{\beta\gamma} - \frac{\delta_{\alpha\beta}\delta_{\gamma\delta}}{N_C}\right], \tag{3.9}$$

where N_C is the number of colours, i.e. three in the Standard Model. The second term on the right-hand side has the colour structure of the operator $\mathcal{O}_2$, and thus leads to $1/N_C$ corrections to the coefficient C_2. The first term, on the other hand, gives rise to a new operator

$$\mathcal{O}_1 \equiv (\bar{q}_\alpha p_\beta)_{\mathrm{V-A}} (\bar{q}'_\beta p'_\alpha)_{\mathrm{V-A}}\,, \tag{3.10}$$

which has the same flavour structure as $\mathcal{O}_2$, but a different colour structure. To also describe QCD corrections to the tree-level $pq \to p'q'$ transition, the original Hamiltonian (3.7) thus needs to be extended to

$$\mathcal{H}_{\mathrm{eff}} = \frac{G_{\mathrm{F}}}{\sqrt{2}} V^*_{pq} V_{p'q'} \left(C_1 \mathcal{O}_1 + C_2 \mathcal{O}_2\right). \tag{3.11}$$

As the QCD effects are higher order corrections, $C_1 \ll C_2$, while C_2 remains of $\mathcal{O}(1)$.

The $\Delta B = 1$ Effective Hamiltonian

QCD corrections to the leading-order diagrams result in operator pairs, which are related in flavour structure but differ in colour structure. A combination of operators is thus required to successfully describe the individual decay topologies identified above. Let us therefore provide a short overview of the operators relevant for the non-leptonic B meson decays. The effective Hamiltonian describing these hadronic decays via Standard Model transitions with $|\Delta B| = 1$[d] is given by [76]

$$\mathcal{H}_{\mathrm{eff}} = \frac{G_{\mathrm{F}}}{\sqrt{2}} \sum_{j=u,c} V^*_{jr} V_{jb} \left(\sum_{k=1}^{2} C_k(\mu) \mathcal{O}^j_k(\mu) + \sum_{k=3}^{10} C_k(\mu) \mathcal{O}_k(\mu) \right) + \mathrm{h.c.}\,, \tag{3.12}$$

where $r \in \{d, s\}$. In this expression the unitarity of the CKM matrix has been used to rewrite the term

$$V^*_{tr} V_{tb} = -V^*_{ur} V_{ub} - V^*_{cr} V_{cb}\,. \tag{3.13}$$

[d] The parameter $\Delta B = \#b - \#\bar{b}$ counts the difference in number of b and $\bar{b}$ quarks between the initial and final state.

The current–current operators are given by

$$\mathcal{O}_1^j = (\bar{r}_\alpha j_\beta)_{\mathrm{V-A}}(\bar{j}_\beta b_\alpha)_{\mathrm{V-A}}\,, \qquad \mathcal{O}_2^j = (\bar{r}_\alpha j_\alpha)_{\mathrm{V-A}}(\bar{j}_\beta b_\beta)_{\mathrm{V-A}}\,; \tag{3.14}$$

the operators associated with QCD penguin topologies with internal top quark are

$$\mathcal{O}_3 = (\bar{r}_\alpha b_\alpha)_{\mathrm{V-A}} \sum_q (\bar{q}_\beta q_\beta)_{\mathrm{V-A}}\,, \qquad \mathcal{O}_4 = (\bar{r}_\alpha b_\beta)_{\mathrm{V-A}} \sum_q (\bar{q}_\beta q_\alpha)_{\mathrm{V-A}}\,, \tag{3.15}$$

$$\mathcal{O}_5 = (\bar{r}_\alpha b_\alpha)_{\mathrm{V-A}} \sum_q (\bar{q}_\beta q_\beta)_{\mathrm{V+A}}\,, \qquad \mathcal{O}_6 = (\bar{r}_\alpha b_\beta)_{\mathrm{V-A}} \sum_q (\bar{q}_\beta q_\alpha)_{\mathrm{V+A}}\,, \tag{3.16}$$

where $q \in \{u, d, s, c\}$; and the equivalent electroweak penguin operators are

$$\mathcal{O}_7 = \frac{3}{2}(\bar{r}_\alpha b_\alpha)_{\mathrm{V-A}} \sum_q e_q (\bar{q}_\beta q_\beta)_{\mathrm{V+A}}\,, \qquad \mathcal{O}_8 = \frac{3}{2}(\bar{r}_\alpha b_\beta)_{\mathrm{V-A}} \sum_q e_q (\bar{q}_\beta q_\alpha)_{\mathrm{V+A}}\,, \tag{3.17}$$

$$\mathcal{O}_9 = \frac{3}{2}(\bar{r}_\alpha b_\alpha)_{\mathrm{V-A}} \sum_q e_q (\bar{q}_\beta q_\beta)_{\mathrm{V-A}}\,, \qquad \mathcal{O}_{10} = \frac{3}{2}(\bar{r}_\alpha b_\beta)_{\mathrm{V-A}} \sum_q e_q (\bar{q}_\beta q_\alpha)_{\mathrm{V-A}}\,, \tag{3.18}$$

where e_q represents the electric charge of the quark q. In addition, the neutral B meson systems also have a $|\Delta B| = 2$ operator, which is given in Eq. (4.22) and further discussed in the accompanying paragraph.

At the renormalisation scale $\mu = m_b$, the sizes of the Wilson coefficients associated with the two current–current operators are $C_1 = \mathcal{O}(10^{-1})$ and $C_2 = \mathcal{O}(1)$. C_1 is suppressed compared to C_2 because the operator $\mathcal{O}_1$ requires additional gluon exchange to alter the colour flow of the transition. Compared to C_1 and C_2, the QCD penguin coefficients are suppressed by an additional factor $\alpha_s(m_b)/4\pi$, and thus one typically has $C_{3,\ldots,6} = \mathcal{O}(10^{-2})$. Likewise, the electroweak penguin coefficients are suppressed by an additional factor $\alpha_{\mathrm{QED}}(m_b)/4\pi$, and therefore even smaller than $C_{3,\ldots,6}$.

In view of the discussion in Chapter 5 on the presence of penguin topologies, it is useful to stress that in the above OPE only the W, Z and top quark degrees of freedom have been integrated out. That means that penguin diagrams with internal top quark propagators are represented explicitly by local operators, i.e. $Q_{3,\ldots,10}$, but diagrams with internal up and charm quark propagators are implicitly still present in the effective theory. These diagrams appear as next-to-leading order corrections to the matrix elements calculated from the current–current operators [81, 82, 83].

3.3 Factorisation

Introduction

The OPE factorises a weak decay amplitude into Wilson coefficients and matrix elements, where the former quantities describe the high energy physics and are

therefore perturbatively calculable. The direct determination of the latter quantities, which capture the non-perturbative long-distance physics, is, however, extremely difficult, if not impossible [84]. But the calculation would simplify if the matrix elements can be decomposed into more elementary building blocks. The *factorisation* approach [85, 86, 87, 88] assumes such a decomposition is indeed possible for non-leptonic decays. It postulates that the transition amplitude of a decay $B \to M_1 M_2$, where $M_1 = |\bar{q}_1 p\rangle$ and $M_2 = |\bar{q}_3 q_2\rangle$, can be written as the product of a $B \to M_1$ *form factor* $f_{B_q^0 \to M_1}$ and a *decay constant* f_{M_2}. That is

$$\langle M_1 M_2 | \mathcal{O}_i | B \rangle \sim \langle M_2 | (\bar{q_3} q_2)_{\mathrm{V-A}} | 0 \rangle \langle M_1 | (\bar{q}_1 b)_{\mathrm{V-A}} | B \rangle \sim f_{B_q^0 \to M_1} f_{M_2} \,. \tag{3.19}$$

The decay constant f_P parametrises the transition between the vacuum and a meson P, and is consequently a property of the meson, independent of the decay mode. For a pseudo-scalar meson P with momentum p_μ and quark content $|\bar{q}q'\rangle$ it is formally defined as [89]

$$\langle 0 | (\bar{q} q')_{\mathrm{V-A}} | P(p) \rangle = -\langle 0 | \bar{q} \gamma_\mu \gamma_5 q' | P(p) \rangle \equiv -i f_P p_\mu \,. \tag{3.20}$$

The equivalent expression for a vector meson V with polarisation vector ϵ_μ and quark content $|\bar{q}q'\rangle$ is given by [89]

$$\langle 0 | (\bar{q} q')_{\mathrm{V-A}} | V(p, \epsilon) \rangle = \langle 0 | \bar{q} \gamma_\mu q' | V(p, \epsilon) \rangle \equiv f_V m_V \epsilon_\mu \,. \tag{3.21}$$

The form factors $f^+_{P \to P'}$ and $f^0_{P \to P'}$, on the other hand, parametrise the transition $P \to P'$ of a pseudo-scalar P with momentum p_μ into a second pseudo-scalar P' with momentum p'_μ. They are defined through the matrix element

$$\begin{aligned} \langle P'(p') | \bar{q} \gamma_\mu q' | P(p) \rangle = &\left[(p + p')_\mu - \frac{m_P^2 - m_{P'}^2}{q^2} q_\mu \right] f^+_{P \to P'}(q^2) \\ &+ \left[\frac{m_P^2 - m_{P'}^2}{q^2} q_\mu \right] f^0_{P \to P'}(q^2) \,, \end{aligned} \tag{3.22}$$

where $q_\mu \equiv p_\mu - p'_\mu$. As for the decay constants, a similar expression also exists for pseudo-scalar to vector transitions [89].

Both the decay constants and the form factors differ depending on the mesons involved, but are otherwise assumed to be independent of the complete decay chain. This means that once they have been calculated or measured individually, they can be used together to make predictions for related decay channels. To this end, the relevant quantities have been calculated using many different approaches, including heavy quark expansion [90], QCD factorisation [91], soft collinear effective theory (SCET) [92], perturbative QCD [93], etc.

It can be explicitly shown [89] that the matrix element $\langle M_1 M_2|\mathcal{O}_i|B\rangle$ factorises in the $1/N_C$ expansion of the decay amplitude. But beyond this limiting case it should be stressed that the factorisation approach is an assumption, and only under certain conditions leads to a good approximation for the non-perturbative hadronic matrix element. The intuitive picture supporting the factorisation assumption is the following: The B meson consist of a heavy $\bar{b}$ quark and a light(er) spectator quark. As described by the relevant operator of the effective low-energy Hamiltonian, the $\bar{b}$ quark decays into three lighter quarks $\bar{q}_1 q_2 \bar{q}_3$[e]. The difference in invariant mass between the $\bar{b}$ quark and the three decay products is carried away by the quarks in the form of kinetic energy. Assume now that the two lightest quarks q_2 and $\bar{q}_3$, which acquire the highest velocity, pair up to form a colour-singlet object M_2, and the slower third quark $\bar{q}_1$ combines with the spectator quark to form the second meson M_1. In this scenario, the difference in velocity between both systems allows them to spatially separate themselves from each other before hadronisation occurs. As a consequence, long-distance QCD effects are expected to be negligible in this scenario, i.e. soft and hard QCD interactions between the two final-state mesons can be ignored.

Regardless of whether the conditions to realise the above sketched situation are met, the factorisation is never perfect and non-factorisable contributions must also appear. The most straightforward argument for the presence of non-factorisable contributions is related to the renormalisation scale μ. As discussed in Section 3.2, physical processes cannot depend on this scale. The renormalisation scale dependence in the Wilson coefficients must therefore be cancelled by the matrix elements. The decay constants and form factors are, however, by construction independent of μ and thus cannot perform this task. Non-factorisable effects must therefore also contribute to the transition amplitude to accomplish the cancellation. These enter, for example, through the presence of additional gluon exchanges like those in the middle and right-most diagram of Fig. 3.3.

Applicability of the Factorisation Approach

To identify the non-leptonic decay modes for which factorisation works well, a closer look at the properties of the mesons M_1 and M_2 is necessary. Based on the strong hierarchy between the six quark masses, the top, bottom and charm quark are considered *heavy*, while the strange, down and up quark are *light*. Likewise the mesons can be split into two categories: *heavy mesons* and *light mesons*. Heavy mesons consist of one bottom or charm (anti)quark and one light quark, while light mesons consist of only up, down or strange valence quarks. The reader is

[e] As far as the discussion here is concerned, the spectator quark is only involved in the hadronisation of the final state, but does not participate in the interaction itself.

referred to Ref. [91] for more rigorous definitions of these concepts. In the literature, quarkonia, like the J/ψ, are not included in this classification. Decay modes containing quarkonia in the final state are therefore not covered by the following discussion. With this in mind, the non-leptonic B meson decays can now be split into three categories.

The case where M_1 is heavy and M_2 light, like in the decay $B_q^0 \to D_q^- \pi^+$, most closely fits the intuitive picture for factorisation sketched above. The large velocity of the light quarks making up the M_2 meson allows them to separate from the heavy, slow moving c quark before the onset of the hadronisation process, and the small amount of kinetic energy carried by the c quark ensures that it can easily pair up with the spectator quark into a colour-singlet final state. It is therefore expected that factorisation forms a good approximation to describe this type of decays, or, said differently, that the non-factorisable corrections to the hadronic matrix elements are small [94]. This statement has also been put on a more rigorous footing within the QCD factorisation [95, 91] and SCET [96] approaches.

If M_1 and M_2 are both light mesons, like in the decay $B^0 \to \pi^+\pi^-$, the two quarks forming the M_2 meson will still be separated from the remaining two quarks before hadronisation takes place, but the third quark is now also fast moving. This complicates the hadronisation process of the M_1 meson, and usually requires additional gluon exchanges to dissipate the third quark's excess in kinetic energy. Consequently, the non-factorisable corrections to the hadronic matrix elements are larger compared to the previous case. Attempts have nonetheless been made to describe this class of decays within the factorisation approach [97, 98].

Finally, if M_2 is a heavy meson, like in the decay $B_s^0 \to K^+ D^+$, M_2 is neither fast nor small, and the above made arguments do not apply. The factorisation approach therefore offers a poor description of the hadronic matrix element, and large non-factorisable corrections are necessary to match the resulting theory calculation with the experimental data. It turns out that this statement also applies to decays containing quarkonia in the final state, like $B^0 \to J/\psi K_S^0$. The hadronic matrix elements for this class of decay channels thus need to be estimated using different methods. Alternatively, the phenomenological analysis of the experimental data needs to be set up in such a way that information on the absolute amplitude of the decay, and thus an explicit calculation of the hadronic matrix elements, is not needed. A crucial ingredient in this last approach is the flavour symmetry of QCD, which is discussed below. A further illustration of this method is provided in Chapter 5.

3.4 Flavour Symmetries

For decay channels that cannot be described satisfactorily within the factorisation approximation, like the $B \to J/\psi X$ decays that play a central role in this thesis, alternative methods need to be explored to obtain insights into the hadronic long-distance physics contributing to their decay amplitudes. The method adopted in this thesis takes advantage of the approximate flavour symmetries of QCD to relate hadronic quantities of different decay channels to one another. These symmetries are a consequence of the light masses of the u, d and s quarks compared to the typical hadronisation scale Λ_{QCD}.

To illustrate the origin of these symmetries, consider the QCD Lagrangian for N flavours of massless quarks

$$\mathcal{L} = i \sum_j \bar{q}_{L,j} \gamma^\mu D_\mu q_{L,j} + i \sum_j \bar{q}_{R,j} \gamma^\mu D_\mu q_{R,j} - \frac{1}{4} F^a_{\mu\nu} F^{a\mu\nu} \,, \tag{3.23}$$

where D_μ is the standard covariant derivative of $SU(3)_C$, and $F^a_{\mu\nu}$ is the gluon field strength tensor. This Lagrangian is invariant under a global $SU(N)_L \times SU(N)_R$ transformation, referred to as *chiral symmetry*[f], in which the left- and right-handed quarks are allowed to transform independently as

$$q_L \to L\, q_L \,, \qquad q_R \to R\, q_R \,, \tag{3.24}$$

and where L and R are unitary matrices.

This chiral symmetry is spontaneously broken by the quark condensate, whose formation is analogous to Cooper pairing of electrons [100] in a superconducting magnet. It is energetically favourable for quarks and antiquarks to pair up into bound states. The vacuum therefore gets filled with a sea of such pairs, and thus acquires a non-zero expectation value

$$\langle 0|\bar{q} q|0\rangle = \langle 0|\bar{q}_L q_R + \bar{q}_R q_L|0\rangle \neq 0 \,. \tag{3.25}$$

This leads to the relation

$$\langle 0|\bar{q}^j_R q^k_L|0\rangle = v\, \delta^{kj} \,, \tag{3.26}$$

where the indices j and k are flavour indices, labelling the different quark types. The chiral symmetry (3.24) transforms the vacuum expectation value as

$$v\, \delta^{kj} = \langle 0|\bar{q}^j_R q^k_L|0\rangle \qquad \to \qquad \langle 0|(\bar{q}_R R^\dagger)^j (L q_L)^k|0\rangle = v\, (L R^\dagger)^{kj} \,. \tag{3.27}$$

But because the expectation value cannot depend on the chosen representation of the quarks, the only allowed solution is $L = R$, and the chiral symmetry is broken

[f] See, for example, Ref. [99] for an introduction to the topic.

to a single $SU(N)$ symmetry: the diagonal subgroup $SU(N)_V$. When discussed in the context of the three light quarks, this unbroken symmetry is referred to as the $SU(3)_\text{F}$ *flavour symmetry of QCD* [101, 102].

Besides the $SU(3)_\text{F}$ symmetry relation $m_u = m_d = m_s \to 0$ between the three lightest quarks, also the relations $m_u = m_d$, $m_d = m_s$ and $m_u = m_s$ can be considered on an individual basis. This leads to the $SU(2)$ flavour symmetries known as *isospin*, U-spin and V-spin, respectively, which are subgroups of the $SU(3)_\text{F}$ flavour symmetry.

In the Standard Model, the chiral symmetry is broken by the non-zero masses of the quarks, and in particular the large mass difference between the s quark on the one hand, and the u and d quarks on the other. The size of typical $SU(3)$-breaking corrections is estimated by the ratio $(m_s - m_d)/\Lambda_\text{QCD} \approx 42\%$ [64] or the quantity $f_K/f_\pi - 1 \approx 19\%$ [25], with other dedicated studies also putting estimates in the order of 20–30% [103, 104]. Consequently, quantifying the impact of $SU(3)$-symmetry-breaking effects forms a crucial aspect of the symmetry-based method that is explored in Chapter 5. As an example, a discussion on the U-spin-breaking effects in $B \to J/\psi X$ decays is given in Ref. [105].

The $SU(3)_\text{F}$ flavour symmetry provides a powerful tool to relate the hadronic matrix elements of certain B meson decays to one another, and thereby avoid the need for an explicit theoretical calculation of these quantities. To further elaborate on this statement, consider the diagrammatic approach introduced in Ref. [106], which allows us to decompose any transition amplitude into contributions from at most six different decay topologies. These are: the colour-allowed tree (T), colour-suppressed tree (C), penguin (P), annihilation (A), exchange (E) and penguin-annihilation (PA) diagrams. Illustrations of the tree and penguin diagrams are given in Fig. 3.1, while examples of annihilation, exchange and penguin-annihilation topologies are given later on in Fig. 5.2. The $SU(3)_\text{F}$ symmetry then allows us to relate the individual topologies, or specifically the hadronic matrix elements they represent, between different decay modes.

The wide range of applications of the $SU(3)_\text{F}$ symmetry can be divided into two main groups, depending on whether or not the decay channels being compared proceed via the same weak transition and thus share the same CKM matrix elements. If the decay modes have all CKM matrix elements in common, the $SU(3)_\text{F}$ symmetry can be used to derive interesting amplitude relations. For example, the transition amplitudes of the decays $B^0 \to D^- \pi^+$, $B^0 \to \pi^0 \overline{D}^0$ and $B^+ \to \overline{D}^0 \pi^+$ can be decomposed as [94]

$$A(B^0 \to D^- \pi^+) = T + E\,, \qquad \sqrt{2} A(B^0 \to \pi^0 \overline{D}^0) = C - E\,, \qquad A(B^+ \to \overline{D}^0 \pi^+) = T + C\,, \tag{3.28}$$

leading to the isospin relation

$$A(B^0 \to D^- \pi^+) + \sqrt{2} A(B^0 \to \overline{D}^0 \pi^0) = A(B^+ \to \overline{D}^0 \pi^+) \,. \tag{3.29}$$

A similar decomposition of the $B^0 \to \pi^+\pi^-$, $B^0 \to \pi^0\pi^0$ and $B^+ \to \pi^+\pi^0$ decays leads to the isospin relation [107]

$$A(B^0 \to \pi^+ \pi^-) + \sqrt{2} A(B^0 \to \pi^0 \pi^0) = \sqrt{2} A(B^+ \to \pi^+ \pi^0) \,. \tag{3.30}$$

This relation allow us to control the penguin contributions in these modes and thereby determine the UT angle α from a time-dependent analysis of the $B^0 \to \pi^+\pi^-$ decay [107, 108].

The second class of $SU(3)_{\rm F}$ symmetry applications aims to related the hadronic matrix elements of decays proceeding via different weak transitions, which hence do not share all CKM matrix elements involved. Consider, for example, two decay modes $B \to f$ and $B \to f'$, which can be decomposed in terms of the contributing topologies as

$$A(B \to f) = V_{\rm CKM}(C + P) \,, \qquad A(B \to f') = V'_{\rm CKM}(C' + P') \,, \tag{3.31}$$

where $V_{\rm CKM}$ represents the relevant CKM matrix elements. In the $SU(3)_{\rm F}$ symmetry limit we identify

$$C = C' \,, \qquad P = P' \,, \tag{3.32}$$

and can thus use information on $B \to f$ to say something about the hadronic physics involved in the decay $B \to f'$, or, alternatively, compare information from both modes to say something on $SU(3)$-symmetry breaking. In case there exists a one-to-one relation between all the decay topologies of the decay channels being compared, the theoretical uncertainty associated with this method is minimal and only arises from possible $SU(3)$-breaking effects due to the non-zero masses of the light quarks. If, on the other hand, one of the decay channels has additional decay topologies which do not have a counterpart in the other modes, additional assumptions still need to be made. In case these additional contributions come from annihilation, exchange or penguin-annihilation topologies, which are dynamically suppressed, they can at leading order be ignored. Examples where the $SU(3)_{\rm F}$ flavour symmetry method needs to be extended with further dynamical assumptions include the relations between $B^0 \to J/\psi K^0_{\rm S}$ and $B^0 \to J/\psi \pi^0$, and between $B^0_s \to J/\psi \phi$ and $B^0_s \to J/\psi \overline{K}^{*0}$, discussed in Chapter 5.

In the second class of $SU(3)_{\rm F}$ symmetry applications, the U-spin subgroup plays an important role. It can relate the hadronic matrix elements of a large number of B^0 and B^0_s meson decays, and therefore provides a powerful tool to control higher order corrections to key observables accessible through some of these B^0 and B^0_s meson decays [36, 109, 37, 110]. An important example are the $B^0 \to J/\psi K^0_{\rm S}$

and $B_s^0 \to J/\psi K_S^0$ decay channels, whose decay topologies are related by interchanging all down and strange quarks. In addition, there exists a one-to-one correspondence between these diagrams. As a consequence, no further assumptions besides the U-spin symmetry are thus needed to identify the hadronic matrix elements of both modes, and the relation is therefore theoretically well under control. General estimates put the U-spin-breaking corrections at the 20% level, but the actual size of these corrections strongly depends on the parameter in question and can in fact be much smaller. In the factorisation approach, the matrix elements of these two decays can be written in terms of decay constants and $B_{d,s} \to K$ form factors. Comparing the numerical results on these quantities, discussed in Section 5.3.1, indeed gives results that are compatible with the general estimates. However, when considering certain ratios of matrix elements, the relevant form factors and decay constants can cancel. In such cases the leading order U-spin-breaking effects vanish, leaving only higher-order corrections from non-factorisable effects, which are expected to be much smaller. An example of such a quantity is the ratio between the penguin and tree amplitudes, studied in Chapter 5.

4 Observables of the B Meson System

4.1 The Neutral B Meson System

4.1.1 The Flavour and Mass Eigenbases

Chapter 2 introduced the B_q^0 meson as the strongly bound ground state composed of a light quark $q \in \{d, s\}$ and an b antiquark. Together with its antiparticle $\bar{B}_q^0$ it forms the *flavour* eigenbasis in which its strong and electromagnetic interactions are described. The decay of these unstable particles is governed by the weak interaction, which, as discussed in Chapter 2, has a different eigenbasis. As a consequence of the non-trivial relation between both eigenbases, the neutral B and $\bar{B}$ flavour eigenstates can oscillate into one another. The process of neutral meson mixing is not unique to the B_q^0 systems. The discussion that will follow, although focused towards B^0 and B_s^0 mesons, applies equally well to the K^0 and D^0 systems. However, due to the different characteristics governing these systems, not all observables are as relevant for the latter two systems as they are for the B^0 and B_s^0 mesons.

The most general quantum mechanical state $|\psi(t)\rangle$ describing this system at time t is therefore given by

$$|\psi(t)\rangle = a(t)|B\rangle + b(t)|\bar{B}\rangle + \sum_i c_i(t)|f_i\rangle \tag{4.1}$$

where the sum includes all possible final states $|f_i\rangle$ of the B and $\bar{B}$ mesons, and $\langle i|j\rangle \equiv \delta_{ij}$. The time evolution of this state is governed by the Schrödinger equation

$$i\frac{\partial}{\partial t}|\psi(t)\rangle = \mathcal{H}_{\mathrm{SM}}|\psi(t)\rangle\,, \tag{4.2}$$

where $\mathcal{H}_{\mathrm{SM}}$ is the Standard Model Hamiltonian. The hermiticity of $\mathcal{H}_{\mathrm{SM}}$ implies that the transition probabilities between the $|B\rangle$, $|\bar{B}\rangle$ and $|f_i\rangle$ states are conserved and that $|\psi(t)\rangle$ forms a closed system, i.e.

$$|a(t)|^2 + |b(t)|^2 + \sum_i |c_i(t)|^2 = 1\,. \tag{4.3}$$

Direct transitions between the decay products $|f_i\rangle$ are thus also possible and make Eq. (4.2) difficult to solve in its most general form. Further simplifications therefore need to be made.

When starting from the initial condition

$$|a(0)|^2 + |b(0)|^2 = 1\,, \quad \forall i : c_i(0) = 0\,, \tag{4.4}$$

and aiming for an effective description of the B–$\bar{B}$ mixing process, the interactions between the final states $|f_i\rangle$ can be ignored [111, 112]. This strategy is known as the Wigner–Weisskopf approximation and leads to a time evolution of the B meson system that is described by the effective Schrödinger equation

$$i\frac{\partial}{\partial t}|\hat{\psi}(t)\rangle = \mathcal{H}_{\text{eff}}|\hat{\psi}(t)\rangle \equiv \left(\mathbf{M} - \frac{i}{2}\mathbf{\Gamma}\right)|\hat{\psi}(t)\rangle\,, \qquad |\hat{\psi}(t)\rangle \equiv \begin{pmatrix} a(t) \\ b(t) \end{pmatrix}, \tag{4.5}$$

where $\mathbf{M}$ and $\mathbf{\Gamma}$ are the mass and decay matrices into which the interactions with the final states $|f_i\rangle$ have been absorbed. These 2×2 matrices are Hermitian, thus constraining $M_{12} = M_{21}^*$ and $\Gamma_{12} = \Gamma_{21}^*$. Their combination, however, is not, and $|\hat{\psi}(t)\rangle$ therefore no longer forms a closed system; particles leak out as the B mesons decay. CPT invariance, i.e. $[\mathcal{H}_{\text{SM}}, \mathcal{CPT}] = 0$, ensures that the masses and lifetimes of the B and $\bar{B}$ flavour eigenstates are equal. Therefore, $M_{11} = M_{22} \equiv M_0$ and $\Gamma_{11} = \Gamma_{22} \equiv \Gamma_0$. The effective Hamiltonian

$$\mathcal{H}_{\text{eff}} = \begin{pmatrix} H_0 & H_{12} \\ H_{21} & H_0 \end{pmatrix} = \begin{pmatrix} M_0 - \frac{i}{2}\Gamma_0 & M_{12} - \frac{i}{2}\Gamma_{12} \\ M_{12}^* - \frac{i}{2}\Gamma_{12}^* & M_0 - \frac{i}{2}\Gamma_0 \end{pmatrix} \tag{4.6}$$

thus has six remaining degrees of freedom, which are discussed in depth below. The off-diagonal elements M_{12} and Γ_{12} are responsible for the mixing between B and $\bar{B}$ mesons.

To solve the time evolution of the B and $\bar{B}$ flavour eigenstates, the matrix (4.6) needs to be diagonalised. Its eigenvalues are

$$\lambda_\pm = H_0 \pm H_{12}\,\alpha\,, \qquad \alpha \equiv \sqrt{\frac{H_{21}}{H_{12}}} = \sqrt{\frac{M_{12}^* - \frac{i}{2}\Gamma_{12}^*}{M_{12} - \frac{i}{2}\Gamma_{12}}}\,, \tag{4.7}$$

where it should be noted that with the above definition the unphysical sign of α[a] remains ambiguous. The corresponding *mass* eigenstates of the B meson system, expressed in terms of the flavour eigenstates, are then given as

$$|B_\pm\rangle = \frac{1}{\sqrt{1+\alpha^2}}\left(|B\rangle \pm \alpha|\bar{B}\rangle\right), \tag{4.8}$$

[a] In the literature the notation $\alpha = q/p$ is also commonly used.

and the mass and decay width of these physical particles are

$$m_\pm \equiv \quad \mathcal{R}\mathrm{e}[\lambda_\pm] = M_0 \pm \mathcal{R}\mathrm{e}\left[\left(M_{12} - \frac{i}{2}\Gamma_{12}\right)\alpha\right], \tag{4.9}$$

$$\Gamma_\pm \equiv -2\,\mathcal{I}\mathrm{m}[\lambda_\pm] = \Gamma_0 \mp \mathcal{I}\mathrm{m}\left[\left(M_{12} - \frac{i}{2}\Gamma_{12}\right)\alpha\right]. \tag{4.10}$$

The latter two expressions are used to construct the experimentally measurable representations of the degrees of freedom in $\mathcal{H}_{\text{eff}}$. Let us now define these six mixing parameters one by one. The mean mass of the two mass eigenstates is given by

$$m_B \equiv \frac{m_+ + m_-}{2} = M_0\,, \tag{4.11}$$

and corresponds to the mass of both flavour eigenstates. The mass difference between $|B_+\rangle$ and $|B_-\rangle$ is defined as the positive-definite quantity

$$\Delta m \equiv |m_+ - m_-| = 2\left|\mathcal{R}\mathrm{e}\left[\left(M_{12} - \frac{i}{2}\Gamma_{12}\right)\alpha\right]\right| > 0\,. \tag{4.12}$$

Due to the sign ambiguity in α, this definition does not specify which of the two eigenstates is to be identified as the heavier one; that mapping remains a convention-dependent choice. The observable Δm itself is, however, independent of the sign of α. To trace the mapping's arbitrariness in the time-dependent decay equations that follow, we introduce the index $k \in \{0,1\}$ and identify $\Delta m = e^{i\pi k}(m_+ - m_-)$.

Similarly, the mean decay width of the two mass eigenstates is given by

$$\Gamma \equiv \frac{\Gamma_+ + \Gamma_-}{2} = \Gamma_0\,, \tag{4.13}$$

and corresponds to the decay width of both flavour eigenstates. The decay width difference between $|B_+\rangle$ and $|B_-\rangle$ is represented by the signed quantity

$$\Delta\Gamma = e^{i\pi l}(\Gamma_+ - \Gamma_-) = -e^{i\pi l}4\,\mathcal{I}\mathrm{m}\left[\left(M_{12} - \frac{i}{2}\Gamma_{12}\right)\alpha\right], \tag{4.14}$$

where we have introduced a second index $l \in \{0,1\}$ to trace the two possible definitions of $\Delta\Gamma$. The sign of $\Delta\Gamma$ needs to be determined experimentally. Often it is convenient to replace the above two decay width parameters with

$$y \equiv \frac{\Delta\Gamma}{2\Gamma}\,, \qquad \tau \equiv \frac{1}{\Gamma}\,, \tag{4.15}$$

where the latter is referred to as the mean B lifetime. Finally, the two complex phases in $\mathcal{H}_{\text{eff}}$ are parametrised as

$$\phi_q \equiv \arg(M_{12}) - \pi + \xi_{B_q^0} + \xi_q - \xi_b\,, \tag{4.16}$$

$$\tilde{\phi} \equiv \arg(-M_{12}/\Gamma_{12})\,, \tag{4.17}$$

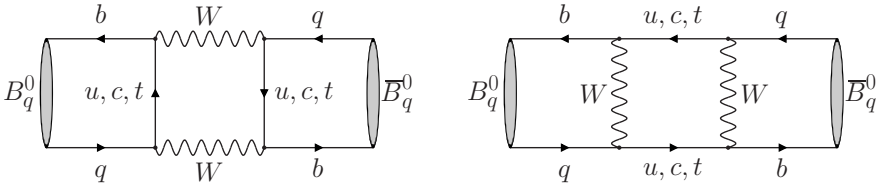

Figure 4.1: The Standard Model *box* diagrams representing the leading real and virtual contributions to the B_q^0–$\bar{B}_q^0$ mixing process.

where the ξ_j are convention-dependent phases associated with the *CP* transformation of the state j, i.e.

$$\mathcal{CP}|B\rangle = e^{i\xi_B}|\bar{B}\rangle\,, \tag{4.18}$$

and added to cancel similar phases hidden inside M_{12}.

For completeness, it is convenient to already highlight the two convention-dependent choices we will make for the remainder of this thesis: Firstly, we identify

$$|B_+\rangle = |B_{\rm H}\rangle\,, \qquad |B_-\rangle = |B_{\rm L}\rangle\,, \tag{4.19}$$

which in combination with Eq. (4.12) fully specifies the sign of α. Secondly we define

$$\Delta\Gamma \equiv \Gamma_{\rm L} - \Gamma_{\rm H}\,. \tag{4.20}$$

This fixes our two free indices: $k = 0$ and $l = 1$.

4.1.2 The Standard Model Mixing Parameters

Standard Model predictions for the mixing parameters characterising the neutral B meson systems are available from the literature. They are based on detailed calculations of the individual matrix elements M_{12} and Γ_{12}, which represent respectively the virtual and real part the FCNC transitions between B and $\bar{B}$ mesons. In the Standard Model these transitions are GIM-suppressed and can only proceed via loop processes, with the dominant contribution originating from the *box* diagrams shown in Fig. 4.1.

The Dispersive Part M_{12}

The matrix element M_{12} is responsible for the virtual, or dispersive, transitions between B_q^0 and $\bar{B}_q^0$ mesons, which proceed through off-shell W-boson and up-type quark exchanges. The contribution originating from a transition with internal

quarks i and j is proportional to $x_i x_j$, where $x_i \equiv m_i^2/m_W^2$[b]. Due to the strong hierarchy in quark masses, this implies that M_{12} is dominated by the pure top quark diagrams, and contributions involving up or charm quarks can be neglected.

In the OPE framework, the effective Hamiltonian describing the transitions between B_q^0 and $\bar{B}_q^0$ mesons can be parametrised as [113]

$$\mathcal{H}_{\text{eff}}^{\Delta B=2} = \frac{G_F^2 m_W^2}{16\pi^2}(V_{tb}^* V_{tq})^2 C^{\Delta B=2}(\mu_b)\mathcal{O}^{\Delta B=2}(\mu_b) + \text{h.c.}\,, \tag{4.21}$$

where $\mathcal{O}^{\Delta B=2}(\mu_b)$ is the four-quark operator

$$\mathcal{O}^{\Delta B=2}(\mu_b) = (\bar{b}_\alpha q_\alpha)_{V-A}(\bar{b}_\beta q_\beta)_{V-A}\,, \tag{4.22}$$

$C^{\Delta B=2}(\mu_b)$ the associated Wilson coefficient, and μ_b is the factorisation scale, taken to be m_b.

The non-perturbative long-distance physics is contained in the hadronic matrix element

$$\langle \bar{B}_q^0|\mathcal{O}^{\Delta B=2}|B_q^0\rangle \equiv \frac{8}{3} m_{B_q^0}^2 \hat{B}_{B_q^0}(\mu_b) f_{B_q^0}^2 \times e^{i(\xi_{B_q^0}+\xi_q-\xi_b-\pi)}\,. \tag{4.23}$$

where ξ are the convention-dependent CP phases already introduced in Eq. (4.18), and $f_{B_q^0}$ is the B_q^0 meson decay constant defined in Eq. (3.20). The parameter [114]

$$\hat{B}_{B_q^0}(\mu_b) \equiv \frac{\langle \bar{B}_q^0|\mathcal{O}^{\Delta B=2}|B_q^0\rangle}{\frac{8}{3} m_{B_q^0}^2 f_{B_q^0}^2} \tag{4.24}$$

is historically referred to as the *bag parameter* and represents the deviation from the factorisation limit. Within the factorisation approach

$$\langle \bar{B}_q^0|\mathcal{O}^{\Delta B=2}|B_q^0\rangle\big|_{\text{fact}} = \frac{8}{3} m_{B_q^0}^2 f_{B_q^0}^2\,, \tag{4.25}$$

and $\hat{B}_{B_q^0}(\mu_b)$ would thus be one. Like the decay constant, it is obtained from lattice gauge theory calculations, which model the relevant hadronic matrix elements directly on the lattice. The latest lattice averages compiled by the CKMfitter group[c] are [25]

$$f_{B^0} = 187.2 \pm 4.7\ \text{MeV} \qquad \hat{B}_{B^0} = 1.290 \pm 0.041\,, \tag{4.26}$$

$$f_{B_s^0} = 225.6 \pm 5.5\ \text{MeV} \qquad \hat{B}_{B_s^0} = 1.320 \pm 0.034\,, \tag{4.27}$$

$$f_{B_s^0}/f_{B^0} = 1.205 \pm 0.008 \qquad \hat{B}_{B_s^0}/\hat{B}_{B^0} = 1.023 \pm 0.019\,, \tag{4.28}$$

[b] The matrix element calculations of M_{12} and Γ_{12} are performed in the $\overline{\text{MS}}$ scheme. The quantity m_i thus corresponds to the $\overline{\text{MS}}$ mass $\overline{m}_i$.

[c] To be consistent with other results presented in this thesis, which rely more heavily on the inputs and results provided by the CKMfitter group, their averages are preferred over those from the FLAG group.

while a more detailed comparison between the different lattice results is offered by the Flavour Lattice Averaging Group (FLAG) [114].

The perturbative, short-distance physics is contained in the Wilson coefficient

$$C^{\Delta B=2}(\mu_b) = \hat{\eta}_B(\mu_b) S_0(x_t)\,, \tag{4.29}$$

where

$$S_0(x_t) = \frac{4x_t - 11x_t^2 + x_t^3}{4(1-x_t)^2} - \frac{3x_t^3 \log x_t}{2(1-x_t)^3} \tag{4.30}$$

is the *Inami-Lim* function [115]. The leading and next-to-leading QCD corrections to $S_0(x_t)$ are encapsulated in the factor $\hat{\eta}_B(\mu_b)$ [113]. It is possible to transfer the renormalisation dependence of the QCD correction factor to the bag parameter, $\hat{\eta}_B(\mu_b)\hat{B}_{B_q^0}(\mu_b) = \eta_B B_{B_q^0}$, making both parameters independent of the scale μ_b. This leads to $\eta_B = 0.55 \pm 0.01$ [113].

From the relation

$$\langle \bar{B}_q^0 | \mathcal{H}_{\text{eff}}^{\Delta B=2} | B_q^0 \rangle = 2 m_{B_q^0} M_{12}^{*q}\,, \tag{4.31}$$

where the factor $2m_{B_q^0}$ is related to the normalisation of states, it then follows that

$$M_{12}^{*q} = \frac{G_{\text{F}}^2 m_W^2}{12\pi^2} m_{B_q^0} (V_{tb}^* V_{tq})^2 \eta_B S_0(x_t) B_{B_q^0} f_{B_q^0}^2 \times e^{i(\xi_{B_q^0} + \xi_q - \xi_b - \pi)}\,, \tag{4.32}$$

and thus that

$$\phi_d^{\text{SM}} \equiv 2\arg\left(V_{td}^* V_{tb}\right) = 2\beta\,, \qquad \phi_s^{\text{SM}} \equiv 2\arg\left(V_{ts}^* V_{tb}\right) = -2\beta_s\,, \tag{4.33}$$

where the latter equalities only hold for the *standard parametrisation* of the CKM matrix. These phases are colloquially referred to as the B^0–$\bar{B}^0$ and B_s^0–$\bar{B}_s^0$ *mixing phases*, respectively; a notation that is also adopted in this thesis.

The Absorptive Part Γ_{12}

The matrix element Γ_{12} is responsible for the real, or absorptive, transitions between B_q^0 and $\bar{B}_q^0$ mesons, which proceed through on-shell, intermediate states. As the top quark is far too heavy to be on-shell, Γ_{12} only receives contributions from transitions associated with the charm or up quark diagrams in Fig. 4.1. It can thus schematically be decomposed as

$$\Gamma_{12}^{*q} = -\left[(V_{cb}^* V_{cq})^2 \Gamma_{12}^{cc} + 2\, V_{cb}^* V_{cs} V_{ub}^* V_{uq} \Gamma_{12}^{uc} + (V_{ub}^* V_{uq})^2 \Gamma_{12}^{uu}\right]. \tag{4.34}$$

As there are many hadronic final states accessible from both B_q^0 and $\bar{B}_q^0$, the calculation of the individual terms Γ_{12}^{ab} is potentially cumbersome. But instead of explicitly summing over all these exclusive states[d], one typically relies on the

[d] An example of such a calculation is given in Ref. [116]

quark–hadron duality [117, 118] to obtain Γ_{12}^{ab} from an inclusive approach that only considers the intermediate on-shell quark configurations. The most commonly used inclusive approach is known as the *Heavy Quark Expansion* [68, 69].

The presence of long-lived intermediate states normally prevents a direct, perturbative calculation of Γ_{12}^{ab}. In B mesons, however, the heavy mass of the b quark introduces an additional short-distance — compared to the hadronic scales involved — scale $1/m_b$, and leads to large — compared to Λ_{QCD} — energy transfers into the intermediate states. Because it is thus required that the two quarks inside the meson with characteristic size $1/\Lambda_{\text{QCD}}$ find each other within a distance $1/m_b$, B–$\bar{B}$ mixing through real intermediate states effectively also is a local $\Delta B = 2$ process. For the calculation of Γ_{12}^{ab}, the OPE introduced in Section 3.2 to provide an effective description of all B meson decays is therefore expanded in powers of $1/m_b$ and used to construct a new set of local $\Delta B = 2$ operators.

For one specific choice of operator basis[e], the individual terms Γ_{12}^{ab} can at leading order be parametrised in terms of two effective operators [119]:

$$\Gamma_{12}^{ab} \equiv \frac{G_{\text{F}}^2 m_b^2}{24\pi\, m_{B_q^0}} \left[G^{ab} \langle \bar{B}_q^0 | \mathcal{O}^{\Delta B=2} | B_q^0 \rangle - G_S^{ab} \langle \bar{B}_q^0 | \mathcal{O}_S^{\Delta B=2} | B_q^0 \rangle \right] + \mathcal{O}\left(\frac{1}{m_b} \right). \tag{4.35}$$

The first operator is also present in the standard OPE framework, and its hadronic matrix element was already defined in Eq. (4.23). The second effective four-quark operator

$$\mathcal{O}_S^{\Delta B=2} = (\bar{b}_\alpha (1+\gamma_5) q_\alpha)(\bar{b}_\beta (1+\gamma_5) q_\beta)\,, \tag{4.36}$$

represents scalar-type interactions and its hadronic matrix element is defined as

$$\langle \bar{B}_q^0 | \mathcal{O}_S^{\Delta B=2} | B_q^0 \rangle \equiv -\frac{5}{3} \frac{m_{B_q^0}^4 f_{B_q^0}^2 B_S^q}{(m_b + m_q)^2} \times e^{i(\xi_{B_q^0} + \xi_q - \xi_b - \pi)}\,, \tag{4.37}$$

where B_S^q is its corresponding bag parameter.

The prefactors G^{ab} and G_S^{ab} are functions of the original OPE parameters. Their description can be found in Ref. [119], but is not required for the remainder of the discussion here.

Standard Model Predictions

The relative magnitudes of the off-diagonal matrix elements M_{12}^{*q} and Γ_{12}^{*q} can be estimated from their parametric expressions in Eqs. (4.32) and (4.35), respectively.

[e] The operator basis for the heavy quark expansion is not unique. As was pointed out in Ref. [119], the choice of parametrisation can have a large impact on the theoretical precision that can be reached with the calculation. The choice made here was not used to obtain the most precise answer on Γ_{12} that is available in the literature, but it is more transparent for the current discussion.

Based on the mass dependence only, one readily obtains

$$\frac{\Gamma_{12}^{*q}}{M_{12}^{*q}} \propto \frac{m_b^2}{m_W^2 S_0(x_t)} = \mathcal{O}\left(\frac{m_b^2}{m_t^2}\right) \ll 1\,, \tag{4.38}$$

and more precise calculations yield [119]

$$\frac{\Gamma_{12}^{d}}{M_{12}^{d}} = (52.7^{+11.5}_{-12.8}) \times 10^{-4}\,, \qquad \frac{\Gamma_{12}^{s}}{M_{12}^{s}} = (51.9 \pm 9.8) \times 10^{-4}\,. \tag{4.39}$$

Thus $|\Gamma_{12}/M_{12}|$ is a valid expansion parameter in the Standard Model.

Expanding the mixing parameter α gives

$$\alpha = e^{-i\phi_q} e^{i(\xi_{B_q^0} + \xi_q - \xi_b - \pi)} \left[1 - \frac{1}{2}\left|\frac{\Gamma_{12}}{M_{12}}\right| \sin\tilde{\phi} + \mathcal{O}\left(\left|\frac{\Gamma_{12}}{M_{12}}\right|^2\right)\right], \tag{4.40}$$

and shows that to leading order α only depends on the phase of M_{12}^q. In addition, a deviation of $|\alpha|$ from unity would imply $\tilde{\phi} \neq 0$ and thus a difference between the $B_q^0 \to \bar{B}_q^0$ and $\bar{B}_q^0 \to B_q^0$ mixing processes, referred to as *CP violation in mixing*. It can be experimentally probed using *flavour specific* decays. These are decay modes for which $f \neq \bar{f}$ and only the transitions $B_q^0 \to f$ and $\bar{B}_q^0 \to \bar{f}$ are allowed, i.e. the complementary channels $B_q^0 \to \bar{f}$ and $\bar{B}_q^0 \to f$ are forbidden, as illustrated by Fig. 4.2 A typical example of such a decay are the semileptonic modes $B_q^0(t) \to X l^+ \nu$. Through the *semileptonic asymmetry*

$$a_{\mathrm{sl}}^q \equiv \frac{\Gamma(\bar{B}_q^0(t) \to X l^- \bar{\nu}) - \Gamma(B_q^0(t) \to X l^+ \nu)}{\Gamma(\bar{B}_q^0(t) \to X l^- \bar{\nu}) + \Gamma(B_q^0(t) \to X l^+ \nu)} = \frac{1 - |\alpha|^4}{1 + |\alpha|^4}\,, \tag{4.41}$$

defined in terms of the decay rates $\Gamma(B_q^0(t) \to X l^+ \nu)$ introduced in Eq. (4.46) below, these modes provide experimental access to $|\alpha|$, and thus probe *CP* violation in B_q^0–$\bar{B}_q^0$ mixing. For the direct application of Eq. (4.41), it is necessary to differentiate between initially produced B_q^0 and $\bar{B}_q^0$ mesons, which is an experimental disadvantage. At the B-factories, the entanglement between the B^0 and $\bar{B}^0$ mesons is therefore exploited to express a_{sl}^q as a *wrong charge asymmetry*

$$a_{\mathrm{sl}}^q = \frac{N^{++} - N^{--}}{N^{++} + N^{--}}\,. \tag{4.42}$$

This asymmetry compares the number of positive and negative same-sign lepton pairs in a data sample where both B^0 mesons decayed semileptonically. These dilepton events can only occur when one of the two B^0 mesons first oscillated before decaying. At hadron colliders, where the produced B^0 and B_s^0 mesons are not entangled, a_{sl}^q can be related to the difference in event yield between the $X l^+ \nu$ and $X l^- \bar{\nu}$ final states [120], up to higher order corrections.

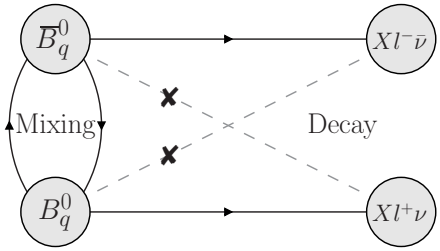

Figure 4.2: Illustration of the allowed and forbidden transitions for the flavour specific decay $B^0_q(t) \to Xl^+\nu$.

Inserting Eq. (4.40) gives

$$a^q_{\mathrm{sl}} = \left|\frac{\Gamma_{12}}{M_{12}}\right| \sin\tilde{\phi} + \mathcal{O}\left(\left|\frac{\Gamma_{12}}{M_{12}}\right|^2\right), \tag{4.43}$$

and shows that a^q_{sl} is expected to be tiny in the Standard Model. Its Standard Model prediction as well as the latest experimental measurements are listed in Table 4.1. Current data is consistent with the assumption $|\alpha| = 1$, which will be used throughout this thesis.

The expansion in Eq. (4.40) also leads to

$$\Delta m = 2\,|M_{12}| \qquad + \mathcal{O}\left(\left|\frac{\Gamma_{12}}{M_{12}}\right|^2\right), \tag{4.44}$$

$$\Delta\Gamma = 2\,|\Gamma_{12}|\cos\tilde{\phi} + \mathcal{O}\left(\left|\frac{\Gamma_{12}}{M_{12}}\right|^2\right). \tag{4.45}$$

The latest Standard Model predictions and experimental averages for the six free parameters describing the B^0 and B^0_s meson system are summarised in Table 4.1. In addition, the S-wave contribution to the decay $B^0_s \to J/\psi K^+K^-$ has been used to unambiguously determine the sign of $\Delta\Gamma_s$ and rule out the discrete ambiguity $\phi_s \to \phi_s + \pi$ and $y_s \to -y_s$ [124]. Finally, it can be noted that current data is consistent with the assumption $\Delta\Gamma_d = 0$, which will be used throughout this thesis.

[f] Our calculation based on Eq. (4.32) and uses inputs from [25, 64].

[g] Although analytic expressions for the B^0_q lifetimes are — amongst others — available in Ref. [123], they depend heavily on the adopted parametrisations. Typically only the ratios, where these effects cancel, are therefore evaluated numerically.

Table 4.1: Standard Model predictions and current experimental averages for the six free parameters describing the B^0 and B_s^0 meson system.

Par.	SM Prediction	Ref.	Experimental Average	Ref.
m_{B^0}	—		5279.58 ± 0.17 MeV/c^2	[64]
Δm_d	0.557 ± 0.069 ps^{-1}	[f]	0.510 ± 0.003 ps^{-1}	[121]
Γ_d	—	[g]	0.6579 ± 0.0017 ps^{-1}	[121]
$\Delta\Gamma_d/\Gamma_d$	$(4.2 \pm 0.8) \times 10^{-3}$	[122]	0.001 ± 0.010	[121]
ϕ_d	$(50.4 \pm {}^{1.6}_{3.6})^\circ$	[25]	$(43.0 \pm 1.5)^\circ$	[121]
$\tilde{\phi}_d$	$-(4.3 \pm 1.4)^\circ$	[122]	—	
a_{sl}^d	$-(4.1 \pm 0.6) \times 10^{-4}$	[122]	$-(1.5 \pm 1.7) \times 10^{-3}$	[121]
$m_{B_s^0}$	—		5366.77 ± 0.24 MeV/c^2	[64]
Δm_s	16.9 ± 1.2 ps^{-1}	[f]	17.757 ± 0.021 ps^{-1}	[121]
Γ_s	—	[g]	0.6628 ± 0.0019 ps^{-1}	[121]
$\Delta\Gamma_s$	0.087 ± 0.021 ps^{-1}	[122]	0.0806 ± 0.0060 ps^{-1}	[121]
ϕ_s	$-(2.092 \pm {}^{0.069}_{0.075})^\circ$	[25]	$-(0.9 \pm 2.1)^\circ$	[121]
$\tilde{\phi}_s$	$(0.22 \pm 0.06)^\circ$	[122]	—	
a_{sl}^s	$(1.9 \pm 0.3) \times 10^{-5}$	[122]	$-(7.5 \pm 4.1) \times 10^{-3}$	[121]
Γ_d/Γ_s	1.001 ± 0.002	[123]	0.9926 ± 0.0039	

4.2 Time-Dependent Decay Rate

4.2.1 Time Evolution

The time-dependent decay rate of a given mode $B \to f$ is defined as

$$\Gamma(B(t) \to f) \equiv \frac{1}{2\, m_B} \int \mathrm{d}\Phi_f \, |\langle f|\mathcal{H}|B(t)\rangle|^2 \,, \tag{4.46}$$

where $\int \mathrm{d}\Phi_f$ is the phase-space integral associated with the final state f. Because the flavour eigenstates of neutral B mesons are coupled through mixing, the decay time distribution of the $B \to f$ transitions does not necessarily follow a single exponential function. Instead, the mixing processes introduce oscillating terms in the time-dependent squared matrix element [125]. The time dependence of this element can be derived as follows:

The time evolution of the mass eigenstates is given by

$$|B_\pm(t)\rangle = e^{-i\lambda_\pm t}|B_\pm(0)\rangle \,. \tag{4.47}$$

In the flavour eigenbasis, obtained through the inverse of Eq. (4.8), these equations

take the form

$$|B(t)\rangle = \quad g_+(t)\,|B\rangle + \alpha\, g_-(t)\,|\bar{B}\rangle\,, \tag{4.48}$$

$$|\bar{B}(t)\rangle = \frac{1}{\alpha}\, g_-(t)\,|B\rangle + \quad g_+(t)\,|\bar{B}\rangle\,, \tag{4.49}$$

where the functions $g_\pm(t)$ are defined as

$$g_\pm(t) = \frac{1}{2}\left(e^{-i\lambda_+ t} \pm e^{-i\lambda_- t}\right). \tag{4.50}$$

The time evolution of the decay amplitude $|\langle f|\mathcal{H}|B(t)\rangle|^2$ is therefore given by

$$\begin{aligned}|\langle f|\mathcal{H}|B(t)\rangle|^2 = |\langle f|\mathcal{H}|B\rangle|^2 \times \Big(&|g_+(t)|^2 + |\lambda_f|^2 |g_-(t)|^2 \\ &+ 2\,\mathcal{R}\mathrm{e}\Big[\lambda_f\, g_+^*(t)\, g_-(t)\Big]\Big),\end{aligned} \tag{4.51}$$

where the convention-independent[h] quantity λ_f is defined as

$$\lambda_f \equiv \alpha\, \frac{\langle f|\mathcal{H}|\bar{B}\rangle}{\langle f|\mathcal{H}|B\rangle}\,. \tag{4.52}$$

A similar expression exists for $|\langle f|\mathcal{H}|\bar{B}(t)\rangle|^2$. Inserting the products

$$|g_\pm(t)|^2 = \frac{e^{-\Gamma t}}{2}\left(\cosh\left(\frac{\Delta\Gamma}{2}t\right) \pm \cos\left(\Delta m t\right)\right), \tag{4.53}$$

$$g_+^*(t)\, g_-(t) = -\frac{e^{-\Gamma t}}{2}\left(\underbrace{\qquad}_{e^{i\pi l}} \sinh\left(\frac{\Delta\Gamma}{2}t\right) + \underbrace{\qquad}_{e^{i\pi k}}\, i \sin\left(\Delta m t\right)\right), \tag{4.54}$$

where the convention-dependent indices $k = 0$ and $l = 1$ are explicitly kept, into

[h] The convention-dependent phases affecting α, $\langle f|\mathcal{H}|B\rangle$ and $\langle f|\mathcal{H}|\bar{B}\rangle$ explicitly cancel in this ratio. In addition, this parameter is invariant under redefinitions of the quark fields, which potentially shift complex phases between α and the decay amplitudes $\langle f|\mathcal{H}|B\rangle$ and $\langle f|\mathcal{H}|\bar{B}\rangle$.

Eq. (4.51) then yields

$$|\langle f|\mathcal{H}|B(t)\rangle|^2 = \frac{1+|\lambda_f|^2}{2}|\langle f|\mathcal{H}|B\rangle|^2\, e^{-\Gamma t}\Bigg[\cosh\left(\frac{\Delta\Gamma}{2}t\right) + \underbrace{\qquad}_{-e^{i\pi l}}\mathcal{A}_{\Delta\Gamma}\sinh\left(\frac{\Delta\Gamma}{2}t\right) + \mathcal{A}_{CP}^{\text{dir}}\cos(\Delta m t) + \underbrace{\qquad}_{e^{i\pi k}}\mathcal{A}_{CP}^{\text{mix}}\sin(\Delta m t)\Bigg], \tag{4.55}$$

$$|\langle f|\mathcal{H}|\bar{B}(t)\rangle|^2 = \frac{1+|\lambda_f|^2}{2}\frac{|\langle f|\mathcal{H}|B\rangle|^2}{|\alpha|^2}\, e^{-\Gamma t}\Bigg[\cosh\left(\frac{\Delta\Gamma}{2}t\right) + \underbrace{\qquad}_{-e^{i\pi l}}\mathcal{A}_{\Delta\Gamma}\sinh\left(\frac{\Delta\Gamma}{2}t\right) - \mathcal{A}_{CP}^{\text{dir}}\cos(\Delta m t) - \underbrace{\qquad}_{e^{i\pi k}}\mathcal{A}_{CP}^{\text{mix}}\sin(\Delta m t)\Bigg]. \tag{4.56}$$

The above two equations give the time-dependent rates for respectively an initially pure B and pure $\bar{B}$ meson to decay into a final state f. Note that even when the transition $\bar{B} \to f$ is not allowed, $\Gamma(\bar{B}(t) \to f)$ can be non-zero because oscillated $\bar{B}$ mesons can decay via the allowed path $B \to f$. Eqs. (4.55) and (4.56) introduce the three decay specific *CP observables*[i]

$$\mathcal{A}_{\Delta\Gamma} \equiv \frac{2\mathcal{R}\text{e}[\lambda_f]}{1+|\lambda_f|^2}, \qquad \mathcal{A}_{CP}^{\text{dir}} \equiv \frac{1-|\lambda_f|^2}{1+|\lambda_f|^2}, \qquad \mathcal{A}_{CP}^{\text{mix}} \equiv \frac{2\mathcal{I}\text{m}[\lambda_f]}{1+|\lambda_f|^2}, \tag{4.57}$$

which are discussed below.

4.2.2 *CP* Asymmetry Parameters

The time-dependent decay rates Eqs. (4.55) and (4.56) provide experimental access to the B meson mixing parameters and the decay specific *CP* asymmetry parameters. Their measurements proceed along two main strategies, depending on whether or not an attempt is made to identify the initial flavour of the B mesons.

When it is not possible, or desirable, to *tag* the B meson's flavour, Eqs. (4.55) and (4.56) can be combined, under the assumption $|\alpha| = 1$, to form the *untagged decay rate*[j] [126, 127]

$$\langle\Gamma(B(t) \to f)\rangle \equiv \Gamma(B(t) \to f) + \Gamma(\bar{B}(t) \to f), \tag{4.58}$$

$$\propto e^{-\Gamma t}\left[\cosh\left(\frac{\Delta\Gamma}{2}t\right) + \mathcal{A}_{\Delta\Gamma}\sinh\left(\frac{\Delta\Gamma}{2}t\right)\right] \tag{4.59}$$

[i] These three observables parametrise the (time-dependent) *CP* asymmetry of the $B \to f$ decay. We will refer to them as the *CP* asymmetry parameters, *CP* asymmetries or *CP* observables interchangeably.

[j] For the discussion here, experimental effects like the production asymmetry are ignored and it is assumed that B and $\bar{B}$ mesons are produced in equal numbers.

in which the oscillation terms, proportional to $\cos(\Delta m t)$ and $\sin(\Delta m t)$, cancel. This quantity is sensitive to the B meson mixing parameters Γ and $\Delta\Gamma$, and in case the latter is non-zero, to the CP observable $\mathcal{A}_{\Delta\Gamma}$. Eq. (4.58) can also be expressed in terms of the heavy and light mass eigenstates

$$\langle \Gamma(B(t) \to f) \rangle = \Gamma(B_{\mathrm{H}}(t) \to f) + \Gamma(B_{\mathrm{L}}(t) \to f)\,, \tag{4.60}$$

which allows us to identify $\mathcal{A}_{\Delta\Gamma}$ with the *mass eigenstate rate asymmetry*

$$\mathcal{A}_{\Delta\Gamma} = \frac{\Gamma(B_{\mathrm{H}} \to f) - \Gamma(B_{\mathrm{L}} \to f)}{\Gamma(B_{\mathrm{H}} \to f) + \Gamma(B_{\mathrm{L}} \to f)}\,. \tag{4.61}$$

When flavour tagging information is available, Eqs. (4.55) and (4.56) can be used to construct the time-dependent CP asymmetry

$$a_{CP}(t) \equiv \frac{\Gamma(B(t) \to f) - \Gamma(\overline{B}(t) \to f)}{\Gamma(B(t) \to f) + \Gamma(\overline{B}(t) \to f)}\,, \tag{4.62}$$

which in our conventions yields

$$a_{CP}(t) = \frac{\mathcal{A}_{CP}^{\mathrm{dir}} \cos(\Delta m t) + \mathcal{A}_{CP}^{\mathrm{mix}} \sin(\Delta m t)}{\cosh\left(\frac{\Delta\Gamma}{2} t\right) + \mathcal{A}_{\Delta\Gamma} \sinh\left(\frac{\Delta\Gamma}{2} t\right)}\,. \tag{4.63}$$

For CP eigenstates f with eigenvalue η_f such that

$$\mathcal{CP}|f\rangle \equiv \eta_f |f\rangle\,, \tag{4.64}$$

the parameter $\mathcal{A}_{CP}^{\mathrm{dir}}$[k] quantifies the difference in decay probabilities between the transition $B \to f$ and its CP conjugate process $\overline{B} \to f$. The parameter can therefore be identified with the time-integrated *direct CP asymmetry*

$$\mathcal{A}_{CP}^{\mathrm{dir}} = \frac{\Gamma(B \to f) - \Gamma(\overline{B} \to f)}{\Gamma(B \to f) + \Gamma(\overline{B} \to f)}\,. \tag{4.65}$$

Let us now quantify the conditions for measurable direct CP violation in a decay $B \to f$. Assuming unitarity of the CKM matrix, i.e. using relations like Eq. (3.13), the most general expression for the $B \to f$ and $\overline{B} \to f$ transition amplitudes can be written as

$$\langle f|\mathcal{H}|B\rangle = \left(|A_1| e^{i\delta_1} e^{+i\phi_1} + |A_2| e^{i\delta_2} e^{+i\phi_2}\right), \tag{4.66}$$

$$\langle f|\mathcal{H}|\overline{B}\rangle = \eta_f e^{-i\xi_B} \left(|A_1| e^{i\delta_1} e^{-i\phi_1} + |A_2| e^{i\delta_2} e^{-i\phi_2}\right). \tag{4.67}$$

[k] In the literature the notations $\mathcal{A}_{CP}^{\mathrm{dir}} = C_f$ and $\mathcal{A}_{CP}^{\mathrm{mix}} = -S_f$ are also commonly used.

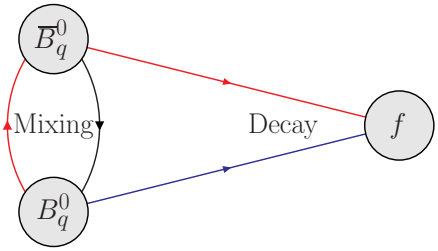

Figure 4.3: Illustration of the possible transitions in the decay of a B_q^0 meson into a *CP* eigenstate f. The interference between the red and blue decay paths leads to mixing-induced *CP* violation.

Here δ_i is the *CP* invariant strong phase associated with the amplitude A_i, while ϕ_i is the associated weak phase, which contrary to δ_i does flip sign under a *CP* transformation. The amplitudes A_1 and A_2 can be related to the operator product expansion (3.1). As an example, A_1 could represent the contributions from the tree topologies, and A_2 those from the penguin topologies. Using Eqs. (4.66) and (4.67), the time-integrated *CP* asymmetry takes the form

$$\mathcal{A}_{CP}^{\text{dir}} = \frac{2|A_1||A_2|\sin(\delta_1-\delta_2)\sin(\phi_1-\phi_2)}{|A_1|^2+2|A_1||A_2|\cos(\delta_1-\delta_2)\cos(\phi_1-\phi_2)+|A_2|^2}\,. \tag{4.68}$$

From this expression it becomes clear that $\mathcal{A}_{CP}^{\text{dir}}$ is non-zero only when three conditions are met: the transition $B \to f$ gets contributions from at least two decay amplitudes A_1 and A_2, and these amplitudes have a non-zero relative weak and strong phase difference, i.e. $\phi_1 \neq \phi_2$ and $\delta_1 \neq \delta_2$.

For final states f that are accessible to both the B and $\bar{B}$ meson, $\mathcal{A}_{CP}^{\text{mix}}$ arises from interference between the decay and mixing processes, referred to as *mixing-induced CP violation*, and illustrated in Fig. 4.3. For the gold-plated modes $B^0 \to J/\psi\, K_S^0$ and $B_s^0 \to J/\psi\,\phi$, which give access to the UT angles β and ϕ_s, respectively, this is the dominant source of *CP* violation.

Finally, from the definitions in Eq. (4.57) it follows that the three *CP* observables are not independent, but instead must satisfy the relation

$$|\mathcal{A}_{\Delta\Gamma}|^2 + |\mathcal{A}_{CP}^{\text{dir}}|^2 + |\mathcal{A}_{CP}^{\text{mix}}|^2 = 1\,. \tag{4.69}$$

The theoretical calculation of the *CP* observables, which by default requires information on the full amplitudes $\langle f|\mathcal{H}|B\rangle$ and $\langle f|\mathcal{H}|\bar{B}\rangle$, simplifies significantly when there is only a single amplitude contributing to the $B \to f$ decay. From the above discussion it immediately follows that the direct *CP* violation must vanish. But

in addition, also the *CP* conserving hadronic contributions to $\langle f|\mathcal{H}|B\rangle$ and $\langle f|\mathcal{H}|\bar{B}\rangle$ cancel in their ratio. Consequently, the parameter λ in Eq. (4.52) reduces to

$$\lambda = -\eta e^{-i(\phi_M + 2\phi_D)}\,, \tag{4.70}$$

where ϕ_M represents the phase associated with the mixing process, i.e. ϕ_q in Eq. (4.40), and ϕ_D the phase associated with the decay process, i.e. ϕ_1 in Eqs. (4.66) and (4.67). The mixing-induced *CP* violation is then given by

$$\mathcal{A}_{CP}^{\text{mix}} = \eta_f \sin(\phi_M + 2\phi_D)\,, \tag{4.71}$$

from which the phase $(\phi_M + 2\phi_D)$ can be determined. It should be stressed that this phase is independent of the chosen parametrisation for the CKM matrix, and any convention-dependent phases, like, for example, the *CP* phases ξ, drop out in the combination $(\phi_M + 2\phi_D)$. In the standard parametrisation, also adopted in this thesis, $\phi_D = 0$ and the the phase determined from the mixing-induced *CP* asymmetry is therefore associated with the mixing phase $\phi_M = \phi_q$, with $q \in \{d, s\}$.

In the decays $B^0 \to J/\psi\, K_S^0$ and $B_s^0 \to J/\psi\,\phi$ the contributions from penguin topologies are strongly suppressed, and this approximation is therefore applied to determine the B_q^0–$\bar{B}_q^0$ mixing phases ϕ_d and ϕ_s from the mixing-induced *CP* asymmetry. But in view of the future experimental precisions that can be obtained in these decays, this approximation is no longer sufficient, as is discussed in Chapter 5.

4.2.3 Effective Lifetimes

The non-zero value of the decay width difference $\Delta\Gamma_s$ in the B_s^0 system allows us to obtain information on the mass eigenstate rate asymmetry $\mathcal{A}_{\Delta\Gamma}$. When the yields of the studied event sample do not yet allow for a detailed *CP* analysis of a decay mode $B_s^0 \to f$, its *effective lifetime* can provide early access to $\mathcal{A}_{\Delta\Gamma}$. This tool is theoretically defined as the time expectation value of the untagged[1] decay rate Eq. (4.58) [128]:

$$\tau_f^{\text{eff}} \equiv \frac{\int_0^\infty t\,\langle\Gamma(B_s(t) \to f)\rangle\,\mathrm{d}t}{\int_0^\infty \langle\Gamma(B_s(t) \to f)\rangle\,\mathrm{d}t}\,. \tag{4.72}$$

In terms of the physics observables, τ_f^{eff} is parametrised as

$$\tau_f^{\text{eff}} = \frac{\tau_{B_s^0}}{1 - y_s^2}\left[\frac{1 + 2\,\mathcal{A}_{\Delta\Gamma}\,y_s + y_s^2}{1 + \mathcal{A}_{\Delta\Gamma}\,y_s}\right], \tag{4.73}$$

[1] Whenever information from both the $B_q^0 \to f$ and the $\bar{B}_q^0 \to f$ decay paths is needed to determine an observable, as is the case for *CP* asymmetries or untagged branching ratios, the notations B_d and B_s are used instead of B^0 and B_s^0.

where y_s is the normalised decay width difference defined in Eq. (4.15). Its current experimental value, based on the averages listed in Table 4.1, is

$$y_s = 0.0608 \pm 0.0045\,. \tag{4.74}$$

Due to its dependence on $\mathcal{A}_{\Delta\Gamma}$, τ_f^{eff} is potentially sensitive to the mixing phase ϕ_s. Effective lifetimes can therefore be used as a tool to constrain $\Delta\Gamma_s$ and ϕ_s [128] that is complementary to the standard *CP* analyses. In addition, a mode's effective lifetime can also be used to translate between the time-integrated and instantaneous branching ratio definitions, as is discussed in the Section 4.3.

Single Exponential Fit

The effective $B_s^0 \to f$ lifetime is in practice obtained by fitting a single exponential function to the decay channel's untagged decay rate. As its time evolution is in general described by two exponential functions, corresponding to the two mass eigenstates with different lifetimes, the single exponential fit is an approximation. For the experimentally allowed range of y_s, given in Eq. (4.74), the difference with the formal definition turns out to be small, i.e. of the order of 0.1%. Let us nonetheless provide further details regarding this subtle difference. This summarises the work originally presented in the appendix of Ref. [16].

Let the true Probability Density Function (PDF) describing the untagged decay rate in the presence of an experimental acceptance function $\text{Acc}(t)$ be defined as

$$f_{\text{true}}(t) \equiv \frac{\text{Acc}(t)\,\langle\Gamma(B_s(t) \to f)\rangle}{\int_0^\infty \text{Acc}(t)\,\langle\Gamma(B_s(t) \to f)\rangle\,\mathrm{d}t}\,. \tag{4.75}$$

The equivalent PDF for the single exponential is

$$f_{\text{fit}}(t;\tau_{\text{fit}}) \equiv \frac{\text{Acc}(t)\,e^{-t/\tau_{\text{fit}}}}{\int_0^\infty \text{Acc}(t)\,e^{-t/\tau_{\text{fit}}}\,\mathrm{d}t}\,, \tag{4.76}$$

where τ_{fit} is the fitted lifetime. Its fit value is obtained by extremising a likelihood function, for which there are three common methods: the log-likelihood, the least squares and the modified least squares. Assuming that the above PDFs represent the number of experimentally measured events in an infinitesimal decay time bin $\mathrm{d}t$, the likelihood functions for the above three methods are then given by

$$\log\mathcal{L}(\tau_{\text{fit}}) = \int_0^\infty f_{\text{true}}(t)\log\left[f_{\text{fit}}(t;\tau_{\text{fit}})\right]\mathrm{d}t\,, \tag{4.77}$$

$$\chi^2(\tau_{\text{fit}}) = \int_0^\infty \left[\frac{f_{\text{true}}(t) - f_{\text{fit}}(t;\tau_{\text{fit}})}{\sqrt{f_{\text{fit}}(t;\tau_{\text{fit}})}}\right]^2 \mathrm{d}t\,. \tag{4.78}$$

For the log-likelihood fit, this setup corresponds to performing an unbinned fit. To perform a modified least squares fit, which uses the data instead of the fit function as a weight, $f_{\text{fit}}(t)$ in the denominator of the χ^2 integrand should be replaced by $f_{\text{true}}(t)$.

The fitted lifetime τ_{fit} resulting from respectively maximising the log-likelihood or minimising the χ^2 functions is then given implicitly by the formula

$$\frac{\int_0^\infty t\, e^{-t/\tau_{\text{fit}}} \text{Acc}(t)\,\mathrm{d}t}{\int_0^\infty e^{-t/\tau_{\text{fit}}} \text{Acc}(t)\,\mathrm{d}t} = \frac{\int_0^\infty t\, g(t;\tau_{\text{fit}}) \text{Acc}(t)\,\mathrm{d}t}{\int_0^\infty g(t;\tau_{\text{fit}}) \text{Acc}(t)\,\mathrm{d}t}\,, \tag{4.79}$$

where

$$g(t;\tau_{\text{fit}}) \equiv \begin{cases} \langle \Gamma(B_s(t) \to f) \rangle & : \text{Maximum Likelihood}\,, \\ \langle \Gamma(B_s(t) \to f) \rangle^2\, e^{\,t/\tau_{\text{fit}}} & : \text{Least Squares}\,, \\ \langle \Gamma(B_s(t) \to f) \rangle^{-1}\, e^{-2t/\tau_{\text{fit}}} & : \text{Modified Least Squares}\,. \end{cases} \tag{4.80}$$

If, for the sake of argument, $\langle \Gamma(B_s(t) \to f) \rangle$ is taken to be a single exponential function, then the solution for τ_{fit} will match the definition of τ_f^{eff} in Eq. (4.72), regardless of the chosen fit method. If, instead, $\langle \Gamma(B_s(t) \to f) \rangle$ has contributions from two exponential functions, this will in general no longer be true. Only in the absence of acceptance effects, i.e. $\text{Acc}(t) = 1$, will the maximum likelihood fit for τ_{fit} correspond to the effective lifetime, as was originally presented in Ref. [129]. For neither of the two least square fit methods could such a limit be found.

The origin of difference between τ_{fit} and τ_f^{eff} can be understood as follows: An acceptance function affecting the small decay times will remove a larger fraction of the short-lived component compared to its long-lived counterpart. This favours the latter component, and drives τ_{fit} to be larger than τ_f^{eff}. For an acceptance function affecting the large decay times the situation is reversed. In general, the result from the single exponential fit thus needs to be corrected to obtain an unbiased estimate of τ_f^{eff}. The required correction factor depends on the shape of the acceptance function and is thus analysis specific. It can be obtained from toy studies. Note that for the currently allowed range of y_s this bias is a sub-leading effect.

4.3 Branching Ratios

The sizeable decay width difference of the B_s^0 system introduces an important subtlety in relating an experimental branching ratio measurement with its theoretical prediction. Let us address this effect below, following the work presented in Ref. [16].

The branching ratio of the $B \to f$ channel represents the relative fraction of B mesons that decays into the final state f. But what this statement does not specify

is how the B meson decay time evolution should be handled. In experiments, the branching ratio is commonly determined from a measurement of the $B \to f$ event yield in a selected data sample, thereby ignoring information about the decay times of these particles. When identifying the time-dependent decay rate Eq. (4.46) with the number of $B \to f$ decays in the time window $[t, t + \mathrm{d}t]$ as [130]

$$\Gamma(B(t) \to f) = \frac{1}{N_B} \frac{\mathrm{d}N(B(t) \to f)}{\mathrm{d}t}\,, \tag{4.81}$$

it becomes transparent that the experimentally measured branching fraction corresponds to the time-integrated quantity [130]

$$\mathcal{B}(B_q \to f)_{\mathrm{exp}} \equiv \frac{1}{2} \int_0^\infty \langle \Gamma(B_q(t) \to f) \rangle \, \mathrm{d}t\,, \tag{4.82}$$

$$= \frac{\tau_{B_q^0}}{2} \left[\frac{1 + \mathcal{A}_{\Delta\Gamma}\, y_q}{1 - y_q^2} \right] \left(\Gamma(B_q^0 \to f) + \Gamma(\bar{B}_q^0 \to f) \right), \tag{4.83}$$

where Eq. (4.58) was used to obtain the second formula. This definition gives the average of the heavy and light mass eigenstate branching ratios.

From a theoretical perspective, however, decay rates are customarily computed in the flavour eigenbasis as CP-averaged quantities. This leads to the following branching ratio definition:

$$\mathcal{B}(B_q \to f)_{\mathrm{theo}} \equiv \frac{\tau_{B_q^0}}{2} \left\langle \Gamma(B_q(t) \to f) \right\rangle \Big|_{t=0}\,, \tag{4.84}$$

$$= \frac{\tau_{B_q^0}}{2} \left(\Gamma(B_q^0 \to f) + \Gamma(\bar{B}_q^0 \to f) \right), \tag{4.85}$$

which is unaffected by B_q^0–$\bar{B}_q^0$ mixing. The advantage of this definition over the time-integrated version is that it allows a straightforward comparison [36, 131] between the B^+, B^0 and B_s^0 branching ratios by means of the $SU(3)_{\mathrm{F}}$ flavour symmetry of QCD, as is discussed in Section 3.4.

The dictionary[m] to convert between the two branching ratio definitions is given by

$$\frac{\mathcal{B}(B_q \to f)_{\mathrm{theo}}}{\mathcal{B}(B_q \to f)_{\mathrm{exp}}} = \left[\frac{1 - y_q^2}{1 + \mathcal{A}_{\Delta\Gamma}\, y_q} \right]. \tag{4.86}$$

This shows that if $\Gamma_{\mathrm{H}} = \Gamma_{\mathrm{L}}$ and thus $\Delta\Gamma = y = 0$, as is the case in the B^0 system to good approximation, then the two definitions Eqs. (4.82) and (4.84) are equivalent. For the B_s^0 system this is, however, not the case and care must thus be taken when comparing experimental results of B_s^0 branching ratios with their theoretical predictions.

[m] Eqs. (4.82), (4.84) and (4.86) can be generalised to apply to B_s^0 transitions into two vector mesons, such as $B_s^0 \to J/\psi\,\phi$. These polarisation-dependent equations are given in Ref. [16].

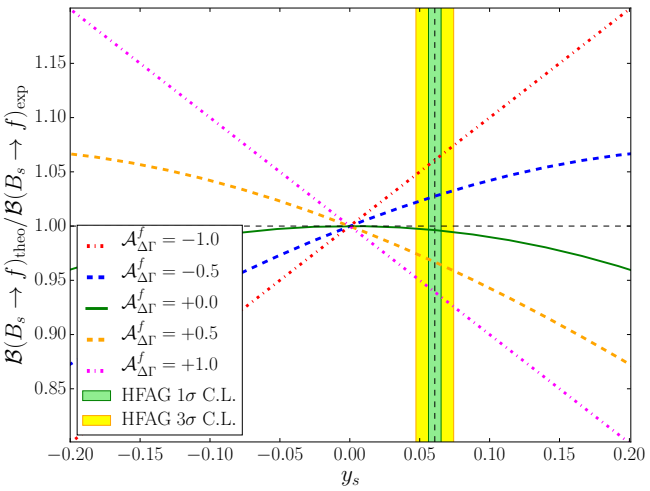

Figure 4.4: Illustration of the conversion factor in Eq. (4.86) as a function of y_s for various values of the *CP* observable $\mathcal{A}_{\Delta\Gamma}$. As reference, the latest experimental average of y_s is also shown.

For the B^0_s branching ratios, the size of the conversion factor in Eq. (4.86) depends on the value of y_s and on the decay specific *CP* parameter $\mathcal{A}_{\Delta\Gamma}$, as illustrated in Fig. 4.4. For the current experimental value of y_s, given in Eq. (4.74), differences between the two branching ratio definitions can be as large as 6.5%. Calculating the exact value of this conversion factor for each decay mode requires additional information on the parameter $\mathcal{A}_{\Delta\Gamma}$. Where possible, this information can be provided from theoretical considerations. For example, in flavour-specific decay modes, like $B^0_s \to D^-_s \pi^+$, $\mathcal{A}_{\Delta\Gamma}$ is necessarily zero and the conversion factor thus reduces to $(1 - y_s^2)$. For a general $B^0_s \to f$ decay, however, the theoretical value of $\mathcal{A}_{\Delta\Gamma}$ is often not (precisely) known as it depends on non-perturbative hadronic parameters which are difficult to calculate theoretically or constrain experimentally. Examples of decay modes where the Standard Model value of $\mathcal{A}_{\Delta\Gamma}$ is available are listed in Table 4.2. In these cases the hadronic parameters have been obtained or eliminated by relying on the $SU(3)_{\text{F}}$ flavour symmetry of QCD.

The conversion factor (4.86) plays a crucial role in the search for signs of beyond the Standard Model physics with the decay channel $B^0_s \to \mu^+\mu^-$ [17], as many models of weak supersymmetry predict deviations from its Standard Model branching fraction [15]. In the Standard Model, the difference between the time-integrated branching fraction and its theoretical equivalent is maximal for this decay, and it

can thus fake a new physics signal when not properly taken into account. Because the observables of the $B_s^0 \to \mu^+\mu^-$ decay in general depend on the helicity of the final state muons, this statement about the value of the conversion factor is a non-trivial result. The decay amplitude of the $B_s^0 \to \mu^+\mu^-$ decay gets contributions from the $\mu_L^+\mu_L^-$ and $\mu_R^+\mu_R^-$ helicity states, which are related to each other via a CP transformation. Therefore, also the quantity λ_f, defined in Eq. (4.52), differs for the left- and right-handed helicity states. In the $B_s^0 \to \mu^+\mu^-$ decay it is, however, observed that these quantities obey the relation [17]

$$\lambda_L \lambda_R^* = \lambda_R \lambda_L^* = 1\,. \tag{4.87}$$

As a consequence, the CP observables $\mathcal{A}_{\Delta\Gamma}$ and $\mathcal{A}_{CP}^{\text{mix}}$ turn out to be helicity independent. For the Standard Model it then follows that $\mathcal{A}_{\Delta\Gamma} = 1$, meaning that the $B_s^0 \to \mu^+\mu^-$ decay only receives contributions from the heavy mass eigenstate. This leads to the maximal value $(1 - y_s)$ for the conversion factor.

As a side remark to the above discussion, it is interesting to note that for new physics searches in $B_s^0 \to \mu^+\mu^-$ the branching fraction measurement can be complemented with information from the CP parameter $\mathcal{A}_{\Delta\Gamma}$. Because even if the $B_s^0 \to \mu^+\mu^-$ branching fraction is compatible with its Standard Model prediction, $\mathcal{A}_{\Delta\Gamma}$ can still reveal signs of new physics [17, 137]. Experimentally, the parameter $\mathcal{A}_{\Delta\Gamma}$ can be determined from a measurement of the $B_s^0 \to \mu^+\mu^-$ effective lifetime. Such a measurement, although challenging, should be possible at the end of the LHCb upgrade programme.

The main downside of using explicit estimates for $\mathcal{A}_{\Delta\Gamma}$ to determine the conversion factor (4.86) is that the result relies heavily on external theoretical input and its assumptions. Therefore, ideally the conversion factor should be obtained directly from experiment. This can be done using a measurement of the effective lifetime. The underlying reason for this, is that τ_f^{eff} provides access to the product of $\mathcal{A}_{\Delta\Gamma}$ and y_s that is also appearing in Eq. (4.86). Substituting the effective lifetime into the dictionary Eq. (4.86) gives

$$\frac{\mathcal{B}(B_q \to f)_{\text{theo}}}{\mathcal{B}(B_q \to f)_{\text{exp}}} = \left[2 - \left(1 - y_s^2\right)\frac{\tau_f^{\text{eff}}}{\tau_{B_s^0}}\right]. \tag{4.88}$$

Table 4.2 also lists the conversion factors derived using the available measurements of τ_f^{eff}. These results are in good agreement with the ones obtained using Eq. (4.86). Although less precise, they do not rely on any theoretical assumptions, which are necessary to estimate $\mathcal{A}_{\Delta\Gamma}$.

4.4 Experimental Considerations

The order in which the experimental observables of the B meson systems have been presented in this chapter is driven by their theoretical derivation and its prerequisites. Central in the theoretical discussion are the results on the time evolution of the neutral B mesons, given in Eqs. (4.55) and (4.56). It is from these master formulae that afterwards the *CP* parameters, effective lifetime and branching ratio can be defined.

The order in which they can be experimentally measured is, however, quite different. As more and more data is collected by an experiment, its analysis of a decay channel $B \to f$ classically goes as follows: When the collected yields in the $B \to f$ decays is still very limited, the analysis focuses on a (first) observation of this mode. Such an analysis rarely includes the B meson decay time as one of its observables. As the collected data sample increases, the analysis shifts to a measurement of the $B \to f$ time-integrated branching ratio. Only once this measurement is firmly established, does the analysis continue with the time-dependent studies of the $B \to f$ mode. Such studies require more data than is strictly necessary to observe the decay because of experimental complications like more complicated fit models, acceptance effects or dilution due to decay time resolution. At this stage the (effective) lifetime associated with the $B \to f$ mode can be measured. Finally, for a full *CP* analysis, also information on flavour tagging is required. Due to the intrinsic inefficiencies of these algorithms and the resulting dilution of the oscillation amplitudes, these analyses require even more data to be collected and are therefore considered to be the final stage in the study of the $B \to f$ decay.

Table 4.2: Conversion factors between the time-integrated branching ratio definition Eq. (4.82) and the theoretical branching ratio definition Eq. (4.84) for selected decay modes. The mass eigenstate rate asymmetry $\mathcal{A}_{\Delta\Gamma}$ has been calculated using the methods and inputs described in the listed references. They are in most cases not stated explicitly.

Mode	$\mathcal{B}(B \to f)$		$\mathcal{A}_{\Delta\Gamma}$		Eq. (4.86)	τ_f^{eff}		Eq. (4.88)
$B_s^0 \to \mu^+\mu^-$	$(2.8 \pm 0.7)\times 10^{-4}$	[14]	1 (SM, exact)	[17]	0.9392 ± 0.0045	—		—
$B_s^0 \to J/\psi\, f_0$	$(1.39 \pm 0.14)\times 10^{-4}$	[64]	0.9975 ± 0.0025	[128]	0.9393 ± 0.0045	1.700 ± 0.048	[132]	0.877 ± 0.032
$B_s^0 \to J/\psi\, K_S^0$	$(1.87 \pm 0.17)\times 10^{-5}$	[64]	0.957 ± 0.061	[42]	0.9415 ± 0.0055	1.75 ± 0.14	[45]	0.844 ± 0.092
$B_s^0 \to D_s^- \pi^+$	$(3.04 \pm 0.23)\times 10^{-3}$	[64]	0 (exact)		0.9963 ± 0.0005	1.535 ± 0.021	[133]	0.986 ± 0.014
$B_s^0 \to K^+ K^-$	$(2.49 \pm 0.17)\times 10^{-5}$	[64]	-0.972 ± 0.013	[128]	1.0589 ± 0.0044	1.407 ± 0.017	[134]	1.071 ± 0.012
$B_s^0 \to D_s^- D_s^+$	$(4.4 \pm 0.5)\times 10^{-3}$	[64]	-0.9967 ± 0.0038	[135]	1.0606 ± 0.0045	1.379 ± 0.031	[136]	1.089 ± 0.021

5 A Roadmap to Controlling Penguin Effects in $B^0 \to J/\psi K_S^0$ and $B_s^0 \to J/\psi \phi$

5.1 Introduction

Although the first run of the Large Hadron Collider (LHC) has been a great success, we have yet to see a clear signal from physics beyond the Standard Model. The picture emerging from three years of data taking is, within the current level of precision, globally consistent with the Standard Model. In the flavour sector large deviations have now been ruled out, and we thus need to prepare ourselves to deal with smallish new physics (NP) effects. As the forthcoming physics runs at the LHC and KEK e^+e^- super B factory promise to reduce the experimental uncertainties even further, this implies that we need to have a critical look at the theoretical assumptions underlying the experimental analyses. Only by doing so can we match the (future) experimental measurements with equally accurate theoretical predictions.

For the determination of the B_q^0–$\bar{B}_q^0$ mixing phases ϕ_d and ϕ_s from *CP* violation measurements in $B^0 \to J/\psi K_S^0$ and $B_s^0 \to J/\psi \phi$, respectively, this implies that controlling higher order hadronic corrections to the *CP* observables, originating from so-called penguin topologies, becomes mandatory [36, 37, 38]. The presence of these loop diagrams affects the relation between the measured *CP* asymmetries and the complex phases ϕ_d and ϕ_s by introducing an additional shift [39] $\Delta\phi_d$ and $\Delta\phi_s$, respectively. These shifts have so far been ignored, but can potentially be as large as one degree. The LHCb upgrade [34] and Belle II [35] programmes, on the other hand, foresee to achieve a precision of below the degree level. Controlling the size of these penguin shifts is therefore necessary in order to differentiate possible NP effects from higher order Standard Model corrections. Although theoretical estimates for these shifts are available [40, 41], it is, in view of the non-perturbative long-distance QCD contributions to these corrections, difficult to calculate them directly within the quantum field theory framework. We therefore follow an alternative approach, and rely on the $SU(3)_F$ flavour symmetry of QCD, introduced in Section 3.4, to relate the doubly Cabibbo-suppressed penguin contributions in the decay amplitudes of $B^0 \to J/\psi K_S^0$ and $B_s^0 \to J/\psi \phi$ to those of similar decay modes in which they are no longer suppressed [36, 37]. In this way, the sizes of the penguin shifts can be estimated directly from the experimental data

[36, 37, 38, 138, 39, 131, 139, 140, 141, 42].

Comparing all $SU(3)_F$ symmetry based strategies, the most promising method to obtain high precision estimates of the shift $\Delta\phi_d$ relies on the use of the $B_s^0 \to J/\psi K_S^0$ decay. It is related to the $B^0 \to J/\psi K_S^0$ mode by interchanging all down and strange quarks, leading to a one-to-one correspondence between the decay topologies of both modes. The two channels are therefore connected through the U-spin symmetry of strong interactions. This allows us to relate the hadronic parameters of both modes with minimal additional theoretical assumptions, and thereby control the penguin corrections affecting the determination of ϕ_d from *CP* violation measurements in $B^0 \to J/\psi K_S^0$ with minimal theoretical uncertainty. As the penguin contributions are, contrary to $B^0 \to J/\psi K_S^0$, not suppressed in $B_s^0 \to J/\psi K_S^0$, they can be determined from the *CP* asymmetries in this channel. First measurements of the *CP* asymmetries in $B_s^0 \to J/\psi K_S^0$ have been performed by the author for the LHCb collaboration [46], and are reported in Chapter 7. However, the precision on these observables is still very limited and does not provide meaningful constraints on the penguin parameters. The results should therefore only be seen as a demonstration of LHCb's potential.

In order to already obtain an estimate on the size of the penguin contributions in $B^0 \to J/\psi K_S^0$, general $SU(3)_F$ flavour symmetry arguments and plausible assumptions for various modes of similar decay dynamics are therefore used to set up a global fit in Section 5.3. This fit includes CP and/or branching ratio information from the modes: $B^0 \to J/\psi K_S^0$, $B_s^0 \to J/\psi K_S^0$, $B^+ \to J/\psi K^+$, $B^+ \to J/\psi \pi^+$ and $B^0 \to J/\psi \pi^0$. Its results are used to explore a benchmark scenario for $B_s^0 \to J/\psi K_S^0$ in the LHCb upgrade era in Section 5.4.

Concerning the $B_s^0 \to J/\psi \phi$ channel, an analysis of *CP* violation is more involved as the final state consists of two vector mesons, and thus is an admixture of different *CP* eigenstates which have to be disentangled through an angular analysis of their decay products [142, 143]. This implies that also the penguin contributions, in general, are dependent on the final state configuration. Controlling the penguin effects in $B_s^0 \to J/\psi \phi$ therefore requires similar decay modes, which also have two vector mesons in the final state. Finding suitable $SU(3)_F$ related partners for the $B_s^0 \to J/\psi \phi$ decay is more challenging than for the $B^0 \to J/\psi K_S^0$ decay, as performing a *CP* asymmetry measurement in the partner mode needs to be experimentally feasible. This strongly disfavours the theoretically interesting U-spin partner $B^0 \to J/\psi \omega(782)$. The two decay modes that are experimentally pursued at the moment are the $B^0 \to J/\psi \rho^0$ and $B_s^0 \to J/\psi \overline{K}^{*0}$ decays, further discussed in Section 5.5. Regarding the former mode, the LHCb collaboration has recently announced the first results of a pioneering study of its *CP* asymmetries [144], whereas for the latter mode only branching ratio and angular amplitude information is currently avail-

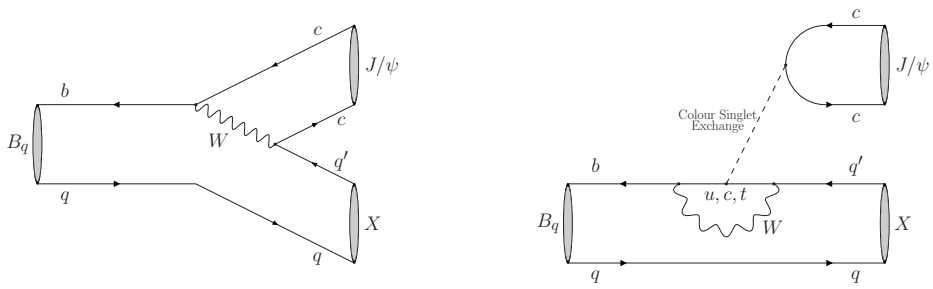

Figure 5.1: Illustration of the colour-suppressed tree [Left] and penguin [Right] topologies contributing to the $B_q \to J/\psi X$ channels, where $q \in \{u,d,s\}$, $q' \in \{d,s\}$ and X represents any of the π^0, π^+, K^+, K^0_S, ρ^0, ϕ^0 or $\overline{K}^{*0}$ mesons.

able [145]. But an updated analysis of $B^0_s \to J/\psi\,\overline{K}^{*0}$, including first measurements of the *CP* asymmetries, is expected soon. From the theoretical side, the $B^0 \to J/\psi\,\rho^0$ mode is favoured over the $B^0_s \to J/\psi\,\overline{K}^{*0}$ decay, as it leads to smaller theoretical uncertainties associated with the penguin analysis and relies on fewer assumptions.

This Chapter closely follows the work published in Ref. [42], but the numerical results have been updated to include the latest theory calculations, experimental measurements, averages and compilations that were available on April 1st, 2015. This in particular refers to the updated input on the UT angle γ from the CKMfitter group [25], the updated measurements of the $B^0_s \to J/\psi\,K^0_S$ branching ratio [46] and $B^0 \to J/\psi\,K^0_S$ *CP* asymmetries [74] from LHCb, and the new calculation of the $B \to$ Vector form factors from Ref. [146]. The first results on the $B^0_s \to J/\psi\,K^0_S$ *CP* asymmetries [46] are not included in the analysis. Because of the large statistical uncertainties on these observables, their impact on the fit results is negligible.

5.2 General Formalism

5.2.1 Formal Definitions

Following the diagrammatic approach introduced in Ref. [106], any decay amplitude can be decomposed into contributions from at most six different decay topologies. These are: the colour-allowed tree (T), colour-suppressed tree (C), penguin (P), annihilation (A), exchange (E) and penguin-annihilation (PA) diagrams. With exception of the colour-allowed tree, which does not contribute to the decay channel analysed in this Chapter, these topologies are illustrated in Figs. 5.1 and 5.2.

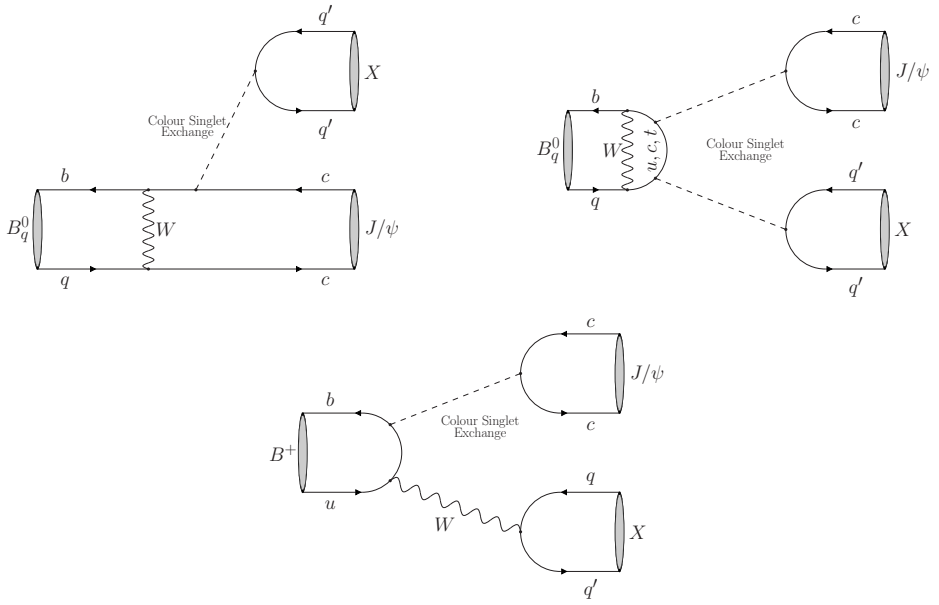

Figure 5.2: Illustration of the exchange [Left], penguin-annihilation [Right] and annihilation [Bottom] topologies contributing to some of the $B_q \to J/\psi X$ channels.

In terms of the decay topologies only, i.e. the CKM factors are omitted to shorten the notation, the different $B_q \to J/\psi P$[a] modes are decomposed as:

$$B^0 \to J/\psi K^0_S = C' + \sum_{u,c,t} P' , \qquad B^0_s \to J/\psi K^0_S = C + \sum_{u,c,t} P , \tag{5.1}$$

$$B^+ \to J/\psi K^+ = C' + \sum_{u,c,t} P' + A' , \qquad B^+ \to J/\psi \pi^+ = C + \sum_{u,c,t} P + A , \tag{5.2}$$

$$B^0 \to J/\psi \pi^0 = C + \sum_{u,c,t} P + E + \sum_{u,c,t} PA , \tag{5.3}$$

where the primes are introduced to distinguish between the $\bar{b} \to \bar{c}c\bar{s}$ quark-level processes (primed) and the $\bar{b} \to \bar{c}cd$ quark-level processes (unprimed). For the

[a]Here P stands for pseudo-scalar and represents the π^+, π^0, K^+ and K^0_S mesons, while V stands for vector and represents the ρ^0, ϕ^0 and $\bar{K}^{*0}$ mesons.

$B_q \to J/\psi\, V$ modes the decomposition is

$$B_s^0 \to J/\psi\,\phi = C' + \sum_{u,c,t} P' + E' + \sum_{u,c,t} PA' \,, \tag{5.4}$$

$$B^0 \to J/\psi\,\rho^0 = C + \sum_{u,c,t} P + E + \sum_{u,c,t} PA \,, \tag{5.5}$$

$$B_s^0 \to J/\psi\,\overline{K}^{*0} = C + \sum_{u,c,t} P \,. \tag{5.6}$$

Because the contributions from the annihilation, exchange and penguin-annihilation topologies are expected to be small[b], they are ignored in this analysis. Their size can be probed through the $B_s^0 \to J/\psi\,\pi^0$ and $B_s^0 \to J/\psi\,\rho^0$ decay channels, which have not yet been seen experimentally [147, 148].

Thus assuming only contributions from tree and penguin topologies, the transition amplitudes for the neutral $B_q^0 \to J/\psi\, X$ modes, where X represent any of the π^0, K_S^0, ρ^0, ϕ^0 or $\overline{K}^{*0}$ mesons, can be written in the general form [36]

$$A(B_q^0 \to f) \equiv |\langle f|\mathcal{H}|B\rangle|^2 = \quad \mathcal{N}_f \left[1 - b_f e^{\rho_f} e^{+i\gamma}\right], \tag{5.7}$$

$$A(\overline{B}_q^0 \to f) \equiv |\langle f|\mathcal{H}|\overline{B}\rangle|^2 = \eta_f \mathcal{N}_f \left[1 - b_f e^{\rho_f} e^{-i\gamma}\right], \tag{5.8}$$

where η_f is the *CP* eigenvalue of the final state f. In these expressions $\mathcal{N}_f$ is a *CP*-conserving normalisation factor that represents the tree topology of the $B_q^0 \to J/\psi\, X$ decay, and b_f then parametrises the relative contribution from the penguin topologies. The *CP*-conserving strong phase difference between both terms is parametrised as ρ_f, whereas their relative weak phase difference is given by the UT angle γ. The parameters $\mathcal{N}_f$ and b_f depend both on CKM factors and on hadronic matrix elements of four-quark operators entering the corresponding low-energy effective Hamiltonian, as illustrated below for the $B^0 \to J/\psi\, K_S^0$ and $B_s^0 \to J/\psi\, K_S^0$ modes.

The three *CP* observables (4.57) then depend on the penguin parameters b_f and

[b] Section 5.3.3 gives a more detailed discussion of the annihilation contributions in $B^+ \to J/\psi\, K^+$ and $B^+ \to J/\psi\,\pi^+$, and their importance based on constraints from current data. This does not indicate any enhancement.

ρ_f as [36][c]

$$\mathcal{A}_{CP}^{\rm dir}(B_q \to f) = \frac{2\, b_f \sin\rho_f \sin\gamma}{1 - 2\, b_f \cos\rho_f \cos\gamma + b_f^2}\,, \tag{5.9}$$

$$\mathcal{A}_{CP}^{\rm mix}(B_q \to f) = \eta_f \left[\frac{\sin\phi_q - 2\, b_f \cos\rho_f \sin(\phi_q+\gamma) + b_f^2 \sin(\phi_q+2\gamma)}{1 - 2\, b_f \cos\rho_f \cos\gamma + b_f^2}\right], \tag{5.10}$$

$$\mathcal{A}_{\Delta\Gamma}(B_q \to f) = -\eta_f \left[\frac{\cos\phi_q - 2\, b_f \cos\rho_f \cos(\phi_q+\gamma) + b_f^2 \cos(\phi_q+2\gamma)}{1 - 2\, b_f \cos\rho_f \cos\gamma + b_f^2}\right]. \tag{5.11}$$

In the absence of penguin contributions, i.e. $b_f = 0$, the expressions for the direct and mixing-induced *CP* asymmetries simplify to

$$\mathcal{A}_{CP}^{\rm dir}(B_q \to f)|_{b_f=0} = 0\,, \qquad \eta_f \mathcal{A}_{CP}^{\rm mix}(B_q \to f)|_{b_f=0} = \sin\phi_q\,, \tag{5.12}$$

allowing ϕ_q to be determined directly from $\mathcal{A}_{CP}^{\rm mix}$. Eq. (5.12) is approximately valid in the decays $B^0 \to J/\psi K_S^0$ and $B_s^0 \to J/\psi\phi$, as the parameters corresponding to b_f, given respectively in Eqs. (5.27) and (5.111) below, are doubly Cabibbo-suppressed in these modes. However, given the expected precision at the LHCb upgrade [34] and Belle II [35] experiments, we need to go beyond the approximation (5.12) and control the effects arising from $b_f \neq 0$.

Experimentally, the quantity

$$\sin\left(\phi_{q,f}^{\rm eff}\right) \equiv \frac{\eta_f \mathcal{A}_{CP}^{\rm mix}(B_q \to f)}{\sqrt{1 - \left(\mathcal{A}_{CP}^{\rm dir}(B_q \to f)\right)^2}} = \sin\left(\phi_q + \Delta\phi_q^f\right) \tag{5.13}$$

determines the effective mixing phase

$$\phi_{q,f}^{\rm eff} = \phi_q + \Delta\phi_q^f\,, \tag{5.14}$$

which differs from the B_q^0–$\bar{B}_q^0$ mixing phase ϕ_q by a phase shift $\Delta\phi_q^f = \Delta\phi_q^f(b_f, \rho_f, \gamma)$. This shift is caused by the presence of the penguin topologies and cannot be calculated reliably within QCD. Nonetheless, a high precision estimate of its size is required to compare

$$\phi_q = \phi_q^{\rm SM} + \phi_q^{\rm NP}\,. \tag{5.15}$$

with its Standard Model prediction and translate the measurement of $\phi_q^{\rm eff}$ into a limit on the NP phase $\phi_q^{\rm NP}$. The dependence of $\Delta\phi_q^f$ on the penguin parameters

[c] Whenever information from both the $B_q^0 \to f$ and the $\bar{B}_q^0 \to f$ decay paths is needed to determine an observable, as is the case for *CP* asymmetries or untagged branching ratios, the notations B_d and B_s are used instead of B^0 and B_s^0.

can be deduced by comparing Eq. (5.13) with Eqs. (5.9) and (5.10), yielding

$$\sin\Delta\phi_q^f = \frac{-2\,b_f\cos\rho_f\sin\gamma + b_f^2\sin 2\gamma}{\left(1-2\,b_f\cos\rho_f\cos\gamma+b_f^2\right)\sqrt{1-\left(\mathcal{A}_{CP}^{\rm dir}(B\to f)\right)^2}}\,, \tag{5.16}$$

$$\cos\Delta\phi_q^f = \frac{1-2\,b_f\cos\rho_f\cos\gamma + b_f^2\cos 2\gamma}{\left(1-2\,b_f\cos\rho_f\cos\gamma+b_f^2\right)\sqrt{1-\left(\mathcal{A}_{CP}^{\rm dir}(B\to f)\right)^2}}\,. \tag{5.17}$$

5.2.2 The $B^0 \to J/\psi\, K_S^0$ and $B_s^0 \to J/\psi\, K_S^0$ Systems

Decay Amplitudes

The $B^0 \to J/\psi\, K_S^0$ decay is a transition into a CP eigenstate with eigenvalue $\eta_{J/\psi\, K_S^0} = -1$ and originates from a $\bar{b}\to\bar{c}c\bar{s}$ quark-level process. Its decay amplitude

$$A\left(B^0\to J/\psi\, K_S^0\right) = V_{us}V_{ub}^*\,P'^{(u)} + V_{cs}V_{cb}^*\left[C' + P'^{(c)}\right] + V_{ts}V_{tb}^*\,P'^{(t)} \tag{5.18}$$

is described by CP-conserving strong amplitudes C' and $P'^{(q)}$, with $q\in\{u,c,t\}$ representing the internal quark line, associated respectively with the tree and penguin topologies given in Fig. 5.1. The factors V_{ij} are the relevant elements of the CKM matrix. Using unitarity of the CKM matrix to eliminate the factor $V_{ts}V_{tb}^*$, and applying the Wolfenstein parametrisation (2.16), the decay amplitude (5.18) can be rewritten in the more compact form [36]:

$$A\left(B^0\to J/\psi\, K_S^0\right) = \left(1-\frac{\lambda^2}{2}\right)\mathcal{A}'\left[1+\epsilon a' e^{i\theta'}e^{i\gamma}\right], \tag{5.19}$$

where

$$\mathcal{A}' \equiv \lambda^2 A\left[C' + P'^{(c)} - P'^{(t)}\right] \tag{5.20}$$

and

$$a' e^{i\theta'} \equiv R_b\left[\frac{P'^{(u)} - P'^{(t)}}{C' + P'^{(c)} - P'^{(t)}}\right] \tag{5.21}$$

are CP-conserving hadronic parameters, whereas

$$\epsilon \equiv \frac{\lambda^2}{1-\lambda^2}\,, \qquad A\equiv\frac{|V_{cb}|}{\lambda^2}\,, \qquad R_b = \left(1-\frac{\lambda^2}{2}\right)\frac{1}{\lambda}\left|\frac{V_{ub}}{V_{cb}}\right| \tag{5.22}$$

are combinations of CKM matrix elements. The parameter a' measures the size of the penguin topologies with respect to the tree contribution, and is associated with the CP-conserving strong phase θ'. A key feature of the decay amplitude in Eq. (5.19) is the suppression of the $a'e^{i\theta'}e^{i\gamma}$ term by the tiny factor $\epsilon = 0.0536\pm0.0003$ [25]. Consequently, ϕ_d can be extracted with the help of

Eq. (5.12) up to corrections of $\mathcal{O}(\epsilon a')$.

The $B_s^0 \to J/\psi K_S^0$ decay originates from a $\bar{b} \to \bar{c}c\bar{d}$ quark-level process, and therefore has a CKM structure which is different from $B^0 \to J/\psi K_S^0$. Its decay amplitude is given by

$$A\left(B_s^0 \to J/\psi K_S^0\right) = V_{ud} V_{ub}^* P^{(u)} + V_{cd} V_{cb}^* \left[C + P^{(c)}\right] + V_{td} V_{tb}^* P^{(t)}, \tag{5.23}$$

which in analogy to Eq. (5.19) can be written in the compact form

$$A\left(B_s^0 \to J/\psi K_S^0\right) = -\lambda \mathcal{A}\left[1 - a e^{i\theta} e^{i\gamma}\right]. \tag{5.24}$$

The hadronic parameters $\mathcal{A}$ and $a e^{i\theta}$ are defined in analogy to their $B^0 \to J/\psi K_S^0$ counterparts in Eqs. (5.20) and (5.21). In contrast to Eq. (5.19), there is no ϵ factor present in front of the second term, thereby enhancing the penguin effects. On the other hand, the λ factor in front of the overall amplitude suppresses the branching ratio with respect to $B^0 \to J/\psi K_S^0$ and makes the decay more challenging to study experimentally.

The $B^0 \to J/\psi K_S^0$ and $B_s^0 \to J/\psi K_S^0$ decays are related through the U-spin symmetry of strong interactions, which allows us to relate the hadronic parameters of both modes. That is

$$\mathcal{A}' = \mathcal{A} \tag{5.25}$$

and

$$a' e^{i\theta'} = a e^{i\theta}. \tag{5.26}$$

In the factorisation approximation the hadronic form factors and decay constants cancel in the latter ratio of decay amplitudes [36]. U-spin breaking corrections thus enter $a e^{i\theta}$ through non-factorisable effects only. However, for $\mathcal{A}$ no such cancellation takes place. Eq. (5.25) is thus affected by $SU(3)$-breaking effects at leading order, entering both through hadronic form factors and through the non-factorisable contributions.

Applying the formalism of Section 5.2.1, i.e. making the replacements

$$B^0 \to J/\psi K_S^0 : \; b_f e^{i\rho_f} \to -\epsilon a' e^{i\theta'}, \qquad \mathcal{N}_f \to \left(1 - \frac{\lambda^2}{2}\right)\mathcal{A}', \tag{5.27}$$

$$B_s^0 \to J/\psi K_S^0 : \; b_f e^{i\rho_f} \to \quad a e^{i\theta}, \qquad \mathcal{N}_f \to \quad -\lambda \mathcal{A}, \tag{5.28}$$

yields the following phase shifts

$$\tan\Delta\phi_s^{J/\psi K_S^0} = \frac{-2a\cos\theta\sin\gamma + a^2\sin 2\gamma}{1-2a\cos\theta\cos\gamma + a^2\cos 2\gamma}\,, \tag{5.29}$$

$$= -2a\cos\theta\sin\gamma - a^2\cos 2\theta\sin 2\gamma + \mathcal{O}(a^3)\,, \tag{5.30}$$

$$\tan\Delta\phi_d^{J/\psi K_S^0} = \frac{2\epsilon a'\cos\theta'\sin\gamma + \epsilon^2 a'^2\sin 2\gamma}{1+2\epsilon a'\cos\theta'\cos\gamma + \epsilon^2 a'^2\cos 2\gamma}\,, \tag{5.31}$$

$$= 2\epsilon a'\cos\theta'\sin\gamma + \mathcal{O}(\epsilon^2 a'^2)\,. \tag{5.32}$$

The expansions in terms of the penguin parameters show an interesting feature: the phase shift $\Delta\phi_q$ is maximal for a strong phase difference $\theta^{(\prime)}$ around 0° or 180°. Conversely, the penguin shifts will be tiny for strong phase differences around 90° or 270°, regardless of the value of a.

Branching Ratio Information

Besides the three *CP* observables $\mathcal{A}_{CP}^{\rm dir}$, $\mathcal{A}_{CP}^{\rm mix}$ and $\mathcal{A}_{\Delta\Gamma}$, also the branching fraction $\mathcal{B}$ contains information on the penguin parameters a and θ. But in order to utilise this information, the overall normalisation factor $\mathcal{N}_f$ in Eqs. (5.7) and (5.8) needs to be cancelled. This can be accomplished by making ratios of branching fractions. We therefore construct the observable [36]

$$H \equiv \frac{1}{\epsilon}\left|\frac{\mathcal{A}'}{\mathcal{A}}\right|^2 \frac{\mathrm{PhSp}\left(B_d\to J/\psi K_S^0\right)}{\mathrm{PhSp}\left(B_s\to J/\psi K_S^0\right)}\frac{\tau_{B^0}}{\tau_{B_s^0}}\frac{\mathcal{B}\left(B_s\to J/\psi K_S^0\right)_{\rm theo}}{\mathcal{B}\left(B_d\to J/\psi K_S^0\right)_{\rm theo}}\,, \tag{5.33}$$

where

$$\mathrm{PhSp}(B_q\to J/\psi X) \equiv \left[M_{B_q^0}\Phi(M_{J/\psi}/M_{B_q^0}, M_X/M_{B_q^0})\right]^3 \tag{5.34}$$

denotes the phase-space function for these decays and Φ is the standard two-body phase-space function

$$\Phi(x,y) = \sqrt{(1-(x+y)^2)(1-(x-y)^2)}\,. \tag{5.35}$$

Note that Eq. (5.33) uses the theoretical branching ratio concept. In the determination of H from the experimentally measured branching fractions the conversion factor (4.86) is thus implicitly used. This requires knowledge on the mass eigenstate rate asymmetry parameter $\mathcal{A}_{\Delta\Gamma}(B_s\to J/\psi K_S^0)$. In view of the large uncertainties on the available measurements, either through the use of the effective lifetime (Eq. (7.4)) or directly from the *CP* analysis (Eq. (7.42)), we rely directly on Eq. (5.11) in our numerical analyses. Furthermore, the experimental determination of H is affected by U-spin-breaking corrections which enter through the ratio $|\mathcal{A}'/\mathcal{A}|$ as

Eq. (5.25) is only approximately valid. Consequently, H is not a particularly clean observable from a theoretical point of view, and should thus be avoided whenever possible.

In terms of the penguin parameters, the H observable is given by

$$H = \frac{1 - 2\,a\cos\theta\cos\gamma + a^2}{1 + 2\epsilon a'\cos\theta'\cos\gamma + \epsilon^2 a'^2}\,. \tag{5.36}$$

Extremising over a and θ leads to the lower bound [149]

$$H \geq \frac{1 + \epsilon^2 + 2\epsilon\cos^2\gamma - (1+\epsilon)\sqrt{1 - 2\epsilon + \epsilon^2 + 4\epsilon\cos^2\gamma}}{2\epsilon^2(1 - \cos^2\gamma)}\,, \tag{5.37}$$

which, assuming $\gamma = 73.2°$, corresponds to $H \geq 0.908$. Based on Eq. (5.36) and assuming the relation (5.26), the H observable can also be related to the direct CP asymmetries of $B^0 \to J/\psi K_S^0$ and $B_s^0 \to J/\psi K_S^0$ as [39]

$$H = -\frac{1}{\epsilon}\frac{\mathcal{A}_{CP}^{\text{dir}}(B_d \to J/\psi K_S^0)}{\mathcal{A}_{CP}^{\text{dir}}(B_s \to J/\psi K_S^0)}, \tag{5.38}$$

which offers an experimental test of the U-spin symmetry.

5.3 Constraining Penguin Effects in $B^0 \to J/\psi K_S^0$ through Current Data

The impact of penguin contributions to the effective mixing phase $\phi_{d,J/\psi K_S^0}^{\text{eff}}$ can be estimated from the current data using a χ^2 fit based on the CP and/or branching ratio information of the modes $B^0 \to J/\psi K_S^0$, $B_s^0 \to J/\psi K_S^0$, $B^+ \to J/\psi K^+$, $B^+ \to J/\psi \pi^+$ and $B^0 \to J/\psi \pi^0$. The modes $B^+ \to J/\psi \pi^+$ and $B^0 \to J/\psi \pi^0$ are related to $B_s^0 \to J/\psi K_S^0$ by replacing the strange spectator quark with an up or down quark, respectively, and are thus expected to have similar decay dynamics. In particular, the penguin contributions are also Cabibbo-allowed in these channels, while their overall decay amplitude, parametrised similar to Eq. (5.24), is suppressed. The mode $B^+ \to J/\psi K^+$ is related to $B^0 \to J/\psi K_S^0$ by replacing the down spectator quark with an up quark. Its penguin contributions are also doubly Cabibbo-suppressed, and its decay amplitude is parametrised similar to Eq. (5.19). These three modes have additional decay topologies, as listed in Eqs. (5.2) and (5.3), which have no counterpart in $B_s^0 \to J/\psi K_S^0$ or $B^0 \to J/\psi K_S^0$ and are ignored in this analysis.

The χ^2 fit relies on general $SU(3)_F$ flavour symmetry arguments and assumes both vanishing non-factorisable corrections and vanishing exchange and (penguin-) annihilation topologies to extend the relation (5.26) and characterise the penguin effects in all five modes by a universal set of penguin parameters a and θ. This assumption introduces additional theoretical uncertainties, associated with possible

inconsistencies between the different decay modes, which disfavour the method in the long run. In view of performing high precision measurements of ϕ_d using $B^0 \to J/\psi K_S^0$, relying on the theoretically cleaner analysis of $B_s^0 \to J/\psi K_S^0$ will ultimately provide the smallest uncertainty on the penguin shift $\Delta\phi_d^{J/\psi K_S^0}$. But in anticipation of high precision measurements of the $B_s^0 \to J/\psi K_S^0$ *CP* observables, this χ^2 fit can already provide valuable insights on the penguin effects. The resulting picture, presented in Ref. [42], extends and updates the previous analyses of Refs. [138] and [39].

5.3.1 Branching Ratio Information

Ratio Tests

A first consistency check of the data is provided by the ratios

$$\Xi(B_q \to J/\psi X, B_{q'} \to J/\psi Y) \equiv \frac{\mathrm{PhSp}\left(B_{q'} \to J/\psi Y\right)}{\mathrm{PhSp}\left(B_q \to J/\psi X\right)} \frac{\tau_{B_{q'}}}{\tau_{B_q}} \frac{\mathcal{B}\left(B_q \to J/\psi X\right)_{\mathrm{theo}}}{\mathcal{B}\left(B_{q'} \to J/\psi Y\right)_{\mathrm{theo}}}, \quad (5.39)$$

involving decays which originate from the same quark-level processes but differ through their spectator quarks. Neglecting the additional topologies and assuming perfect flavour symmetry of strong interactions, these ratios equal one. Within the uncertainties, this picture is supported by the data, as shown in Fig. 5.3. In this compilation, the *B*-factory branching ratio measurements, listed in Table 5.1, are corrected for the measured pair production asymmetry

$$N_{B^+B^-}/N_{B^0\bar{B}^0} = 1.058 \pm 0.024 \quad (5.40)$$

between the number of produced $B^0\bar{B}^0$ and B^+B^- pairs at the $\Upsilon(4S)$ resonance [121]. The scale factors applied by the Particle Data Group (PDG) [64] to combine slightly inconsistent measurements are ignored. Note that the branching ratios for decays into final states with K_S^0 or π^0 mesons have to be multiplied by a factor of two in Eq. (5.39) to take the K_S^0 and π^0 wave functions into account.

Form Factors

To probe the penguin parameters using the branching ratio information listed in Table 5.1, we define *H observables* in analogy to Eq. (5.33). The construction of these quantities from the experimental data requires knowledge on the amplitude ratios $|\mathcal{A}'/\mathcal{A}|$. In the factorisation approximation these ratios are given as [36]

$$\left|\frac{\mathcal{A}'(B_{q'} \to J/\psi X)}{\mathcal{A}(B_q \to J/\psi Y)}\right|_{\mathrm{fact}} = \frac{f^+_{B_{q'}\to X}(m^2_{J/\psi})}{f^+_{B_q\to Y}(m^2_{J/\psi})}, \quad (5.41)$$

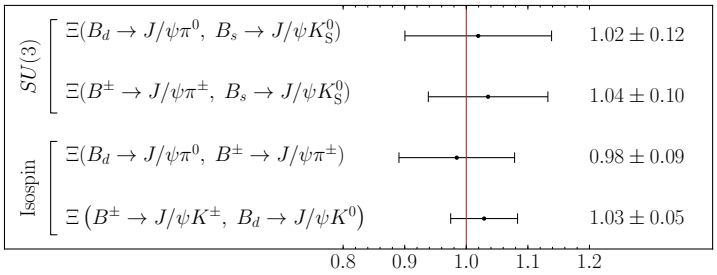

Figure 5.3: Overview of the different ratios defined in Eq. (5.39). In the limit where the contributions from additional decay topologies are neglected and perfect flavour symmetry for the spectator quarks is assumed, these ratios equal unity.

Table 5.1: Time-integrated branching ratio information on the five $B_q \to J/\psi P$ modes, used for the ratio tests (5.39) and for the construction of the H observables in Fig. 5.4.

Parameter	Input	Ref.
$\mathcal{B}(B^\pm \to J/\psi\,\pi^\pm)$	$(3.70 \pm 0.65) \times 10^{-5}$	[150]
$\mathcal{B}(B^\pm \to J/\psi\,K^\pm)$	$(9.96 \pm 0.36) \times 10^{-4}$	[64]
$\mathcal{B}(B_d \to J/\psi\,\pi^0)$	$(1.81 \pm 0.15) \times 10^{-5}$	[64]
$\mathcal{B}(B_d \to J/\psi\,K^0)$	$(8.97 \pm 0.35) \times 10^{-4}$	[64]
$\mathcal{B}(B^\pm \to J/\psi\,\pi^\pm)/\mathcal{B}(B^\pm \to J/\psi\,K^\pm)$	$0.040 \quad \pm 0.001$	[64]
$\mathcal{B}(B_s \to J/\psi\,K^0_S)/\mathcal{B}(B_d \to J/\psi\,K^0_S)$	0.0429 ± 0.0031	[43, 46]

where $f^+_{B\to f}(q^2)$ are hadronic form factors. The form factors relevant for the construction of the H observables are $f^+_{B\to\pi}$, $f^+_{B\to K}$ and $f^+_{B_s\to K}$, where the first two describe transitions for both the B^0_d and the B^+ mesons.

These form factors have been calculated in the literature using a variety of techniques. Some methods, like Lattice QCD, calculate $f^+_{B\to f}$ at large q^2 values and are therefore most accurate in the high q^2 regime $\left(q^2 > 16\ \text{GeV}^2\right)$. Others, like light cone QCD sum rules (LCSR), typically calculate $f^+_{B\to f}$ at $q^2 = 0$ and are thus best suited to describe the low q^2 regime $\left(q^2 < 16\ \text{GeV}^2\right)$. For the situation in Eq. (5.41), with $m^2_{J/\psi} \approx 9\ \text{GeV}^2$, the results from LCSR, listed in Table 5.2, are thus most applicable.

The different form factors are, in view of different research goals, usually calculated on an individual basis and by different research groups, which do not adopt the exact same formalism. For example, the value of $f^+_{B\to\pi}(0)$ is required to de-

Table 5.2: Latest results on the $B \to$ light form factors from LCSR, and the associated multiplication factors, needed to evolve those results to $q^2 = m_{J/\psi}^2$. In the last column, the first uncertainty originates from $f^+(q^2 = 0)$, whereas the second uncertainty is associated with the q^2 dependence.

Form Factor	$f^+(q^2 = 0)$		q^2 Dependence	$f^+(q^2 = m_{J/\psi}^2)$
$f_{B\to\pi}^+$	$0.252^{+0.019}_{-0.028}$	[153]	1.92 ± 0.22	$0.484 \pm 0.045 \pm 0.056$
$f_{B\to K}^+$	$0.34^{+0.05}_{-0.02}$	[152]	1.89 ± 0.22	$0.643 \pm 0.066 \pm 0.076$
$f_{B_s\to K}^+$	$0.30^{+0.04}_{-0.03}$	[151]	1.85 ± 0.22	$0.554 \pm 0.065 \pm 0.067$
$f_{B\to K}^+/f_{B\to\pi}^+$	1.35 ± 0.19		0.9847 ± 0.0067	$1.33 \pm 0.18 \pm 0.0088$
$f_{B\to K}^+/f_{B_s\to K}^+$	1.13 ± 0.18		1.0240 ± 0.0015	$1.16 \pm 0.18 \pm 0.0017$

termine $|V_{ub}|_{\text{excl.}}$ from differential branching ratio measurements of semileptonic B decays, whereas $f_{B\to K}^+$ is needed for the analysis of $B \to K^{(*)} l^+ l^-$. Because common (systematic) uncertainties can hence not be identified, the uncertainties on the form factors must be assumed to be completely uncorrelated. As a consequence of this situation, no additional cancellation can take place in the uncertainties on ratios of form factors, which thus remain sizeable, even though the uncertainties on the individual form factors are already quite small. The form factors are therefore the biggest source of uncertainty in the construction of the H observables. A combined update on all three form factors and their ratios, similar to the results in Ref. [151], which have been partially superseded by Ref. [152], would help to drastically improve the current experimental situation.

The q^2 dependence of the $B \to \pi$ form factor can be fitted to the differential branching ratio measurement of the semileptonic $B^0 \to \pi^- l^+ \nu$ decays. Multiple, equally compatible parametrisations are available in the literature[d]. Here we adopt the BGL method [155, 156] described in Ref. [154]. Although it does not provide the simplest parametrisation of the q^2 dependence, it does allow for a straightforward generalisation to all three form factors, including $f_{B_s\to K}^+$ which is otherwise not covered in the literature. The resulting multiplication factors, needed to evolve the results at $q^2 = 0$ to $q^2 = m_{J/\psi}^2$ are also summarised in Table 5.2.

H Observables

Combining the form factor information in Table 5.2 with the experimental data on the five $B_q \to J/\psi P$ modes, and neglecting non-factorisable $SU(3)$-breaking ef-

[d] See for example Ref. [154] for a detailed comparison, based on the data sample collected by the BaBar collaboration up to 2006.

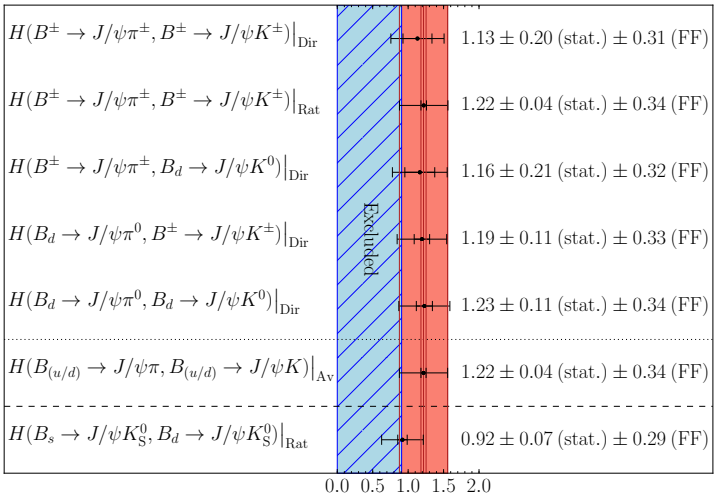

Figure 5.4: H observables which can be constructed from the available branching ratio information of the $B_q \to J/\psi P$ modes. The label "Dir" indicates that H is determined from direct branching fraction measurements in Table 5.1, whereas the label "Rat" is used for H observables calculated from a ratio of branching fractions. The inner error bars indicate the statistical uncertainty (stat.) whereas the outer ones give the total uncertainty, including the common uncertainty due to the form factors (FF). The red band indicates the average H observable of the $B_{(u/d)} \to J/\psi\,(\pi/K)$ modes. The hatched blue region is excluded by Eq. (5.37).

fects, leads to the various H observables compiled in Fig. 5.4. With exception of the last entry, all H observables share the same ratio of form factors $f_{B\to K}^+/f_{B\to\pi}^+$. Consequently, their central values and uncertainties are highly correlated. But restricting the comparison to the statistical uncertainties shows an excellent compatibility between the various H results. The agreement between the isospin related $B_{(u/d)} \to J/\psi\,(\pi/K)$ modes and the last entry, which involved $B_s^0 \to J/\psi K_S^0$ instead of $B \to J/\psi\,\pi$ modes, suggests that non-factorisable $SU(3)$-breaking effects[e] and the impact of additional decay topologies are small, thereby complementing the picture of Fig. 5.3. The uncertainties are, however, still too large to draw definite conclusions.

As different individual H observables imply different solutions for the penguin parameter a, and not all H observables are independent, the best strategy to in-

[e] Note that the LCSR result on the ratio of form factors, which forms the dominant source of uncertainty on H, provides information on the factorisable $SU(3)$-breaking effects (which can still be large), but not on the non-factorisable $SU(3)$-breaking effects.

Table 5.3: Input quantities for the χ^2 fit to the penguin parameters a, θ and ϕ_d.

Observable	Input	Ref.
$\mathcal{A}_{CP}^{\text{dir}}(B^\pm \to J/\psi \pi^\pm)$	-0.001 ± 0.023	[64]
$\mathcal{A}_{CP}^{\text{dir}}(B_d \to J/\psi \pi^0)$	-0.13 ± 0.13	[64]
$\mathcal{A}_{CP}^{\text{mix}}(B_d \to J/\psi \pi^0)$	0.94 ± 0.15	[64]
$\mathcal{A}_{CP}^{\text{dir}}(B^\pm \to J/\psi K^\pm)$	-0.0030 ± 0.0033	[64]
$\mathcal{A}_{CP}^{\text{dir}}(B_d \to J/\psi K^0)$	-0.007 ± 0.018	[121, 74]
$\mathcal{A}_{CP}^{\text{mix}}(B_d \to J/\psi K^0)$	-0.680 ± 0.019	[121, 74]
$H(B_{(u/d)} \to J/\psi (\pi/K))$	1.22 ± 0.34	Fig. 5.4
$H(B_{(s/d)} \to J/\psi K_S^0)$	0.92 ± 0.29	Fig. 5.4

clude branching ratio information into the χ^2 fit is to combine all $B_{(u/d)} \to J/\psi (\pi/K)$ modes into a single, averaged H observable. This average is constructed by first combining all phase-space corrected branching ratio information on the Cabibbo-favoured and Cabibbo-suppressed modes, i.e. the numerator and denominator, individually, before taking their ratio. The result is then multiplied by the form factor ratio $f_{B\to K}^+/f_{B\to\pi}^+$. For simplicity, the $B_s^0 \to J/\psi K_S^0$ H observable is treated independently, even though it shares the information on the $f_{B\to K}^+$ form factor with the above average. Possible correlations induced by this are ignored.

5.3.2 Grand Fit

Input

Besides the branching ratio information discussed above, the global χ^2 fit also includes *CP* asymmetry information from $B^0 \to J/\psi K^0$, $B^+ \to J/\psi K^+$, $B^+ \to J/\psi \pi^+$ and $B^0 \to J/\psi \pi^0$, as summarised in Table 5.3. Following the same strategy as the Heavy Flavour Averaging Group (HFAG) [121], we have refrained from inflating the uncertainties in case of slightly incompatible data. This choice on how to treat the experimental inputs results in a more optimistic picture regarding the current constraints on the penguin parameters. In view of the limited precision that can be obtained with the currently available data, it also improves the fit stability. For the charged decays $B^+ \to J/\psi K^+$ and $B^+ \to J/\psi \pi^+$, which do not exhibit mixing-induced *CP* violation, the included quantities are the direct *CP* asymmetries (4.65). For the $B^0 \to J/\psi \pi^0$ mode, first measurements of the time-dependent *CP* asymmetry were

reported by the BaBar and Belle collaborations, quoting

$$\mathcal{A}_{CP}^{\rm dir}(B_d \to J/\psi \pi^0) = \begin{cases} -0.08 \pm 0.16\,({\rm stat.}) \pm 0.05\,({\rm syst.}) & ({\rm Belle}\ [157]) \\ -0.20 \pm 0.19\,({\rm stat.}) \pm 0.03\,({\rm syst.}) & ({\rm BaBar}\ [158])\,, \end{cases} \tag{5.42}$$

$$\mathcal{A}_{CP}^{\rm mix}(B_d \to J/\psi \pi^0) = \begin{cases} 0.65 \pm 0.21\,({\rm stat.}) \pm 0.05\,({\rm syst.}) & ({\rm Belle}\ [157]) \\ 1.23 \pm 0.21\,({\rm stat.}) \pm 0.04\,({\rm syst.}) & ({\rm BaBar}\ [158])\,. \end{cases} \tag{5.43}$$

The two results for the mixing-induced *CP* asymmetry are not in good agreement with each other. The central value of the BaBar result even lies outside the physical region. It is not obvious how to correctly deal with this unsatisfactory situation, especially because $\mathcal{A}_{CP}^{\rm mix}(B_d \to J/\psi \pi^0)$ is the most important parameter in constraining the size of the penguin parameter a using the current data. We choose to follow the Heavy Flavour Averaging Group [121], and simply average the two results without inflating the thus obtained uncertainty. Hopefully, the Belle II experiment will be able to quickly clarify this situation.

In order to add the mixing-induced *CP* asymmetry of the $B^0 \to J/\psi \pi^0$ channel to the fit, the B^0–$\bar{B}^0$ mixing phase ϕ_d is needed as an input. However, the measured *CP*-violating asymmetries of the $B^0 \to J/\psi K_S^0$ decay only allow us to determine the effective mixing phase[f]

$$\phi_{d,J/\psi K_S^0}^{\rm eff} = \phi_d + \Delta\phi_d^{J/\psi K_S^0} = (42.2 \pm 1.5)^\circ \tag{5.44}$$

from Eq. (5.13). By explicitly expressing the phase shift $\Delta\phi_d^{J/\psi K_S^0}$ in terms of the penguin parameters, through the use of Eq. (5.31), this observable can nonetheless be added to the analysis in a mathematically clean way.

Although the global χ^2 fit contains sufficient observables to determine the UT angle γ in combination with the penguin parameters a and θ, the sensitivity to this parameter is very limited [139][g]. It is therefore advantageous to employ γ as an input. Using data from pure tree decays of the kind $B \to D^{(*)}K^{(*)}$, the following averages are obtained by the CKMfitter and UTfit collaborations:

$$\gamma = \left(73.2^{+6.3}_{-7.0}\right)^\circ \quad ({\rm CKMfitter}\ [25])\,, \qquad \gamma = (68.3 \pm 7.5)^\circ \quad ({\rm UTfit}\ [26])\,. \tag{5.45}$$

For the global χ^2 fit, we have chosen to include the CKMfitter result, and added it as an asymmetric Gaussian constraint.

[f] The numerical value in Eq. (5.44) corresponds to the mixing-induced *CP* asymmetry $\mathcal{A}_{CP}^{\rm mix}(B_d \to J/\psi K^0)$, which is an average of $B^0 \to J/\psi K_S^0$ and $B^0 \to J/\psi K_L^0$ data [121].

[g] An illustration is given for the $B_s^0 \to J/\psi K_S^0$ benchmark scenario in Section 5.4

Contour Methods

Following Ref. [39], each of the observables in Table 5.3 can be represented as a contour in the θ–a plane when assuming fixed values for the angles ϕ and γ. These contours are parametrised by the two functions [36]

$$a(\theta|\phi,\gamma) = f \times \left(U_{\mathcal{O}} \pm \sqrt{U_{\mathcal{O}}^2 - V_{\mathcal{O}}} \right), \tag{5.46}$$

where $f = 1$ for the modes with Cabibbo-allowed penguin contributions, while $f = -1/\epsilon$ for the two modes with Cabibbo-suppressed penguin contributions. The parameters $U_{\mathcal{O}}$ and $V_{\mathcal{O}}$ represent the expressions

$$U_{\text{dir}} \equiv \cos\theta\cos\gamma + \frac{\sin\theta\sin\gamma}{\mathcal{A}_{CP}^{\text{dir}}}, \qquad V_{\text{dir}} \equiv 1 \tag{5.47}$$

for the direct *CP* asymmetries,

$$U_{\text{mix}} \equiv \left[\frac{\sin(\phi+\gamma) - \eta\mathcal{A}_{CP}^{\text{mix}}\cos\gamma}{\sin(\phi+2\gamma) - \eta\mathcal{A}_{CP}^{\text{mix}}} \right] \cos\theta\,, \qquad V_{\text{mix}} \equiv \frac{\sin\phi - \eta\mathcal{A}_{CP}^{\text{mix}}}{\sin(\phi+2\gamma) - \eta\mathcal{A}_{CP}^{\text{mix}}} \tag{5.48}$$

for the mixing-induced *CP* violation and

$$U_H \equiv \left(\frac{1+\epsilon H}{1-\epsilon^2 H} \right) \cos\theta\cos\gamma\,, \qquad V_H \equiv \left(\frac{1-H}{1-\epsilon^2 H} \right) \tag{5.49}$$

for the H observables.

In the absence of large $SU(3)$-breaking effects or contributions from additional topologies, these contours all overlap in a single region of the θ–a plane. In analogy to the global fits of the Unitarity Triangle, they can thus be used to over-constrain the penguin parameters. Like the UT fits, inconsistencies between the input data show up as tensions between the different contours. The fit by itself thus provides yet another cross-check, complementing the picture emerging from the branching ratio tests in Figs. 5.3 and 5.4. But contrary to the UT fits such tensions should not immediately be interpreted as signs of New Physics. Instead, they would point to the breakdown of the $SU(3)_{\text{F}}$ symmetry and/or differences between the hadronisation dynamics of the involved decay modes.

From a technical point of view it is more convenient to parametrise the penguin contributions in terms of their real and imaginary part:

$$a e^{i\theta} = \mathcal{R}\text{e}[a] + i\,\mathcal{I}\text{m}[a]\,. \tag{5.50}$$

This improves fit stability and avoids numerical problems when a gets close to its physical boundary $a = 0$. In addition, it also simplifies plotting. The complicated

parametrisation of the contours in Eq. 5.46 reduces to simple circles in the complex plane of the form

$$(\mathcal{R}\mathrm{e}[a] - f \times x_0)^2 + (\mathcal{I}\mathrm{m}[a] - f \times y_0)^2 = (f \times R)^2 \,. \tag{5.51}$$

The circular contours for the direct *CP* violation parameters are defined by

$$x_0 = \cos\gamma \,, \qquad y_0 = \frac{\sin\gamma}{\mathcal{A}_{CP}^{\mathrm{dir}}} \,, \qquad r = \frac{\sin\gamma}{\mathcal{A}_{CP}^{\mathrm{dir}}} \sqrt{1 - \left(\mathcal{A}_{CP}^{\mathrm{dir}}\right)^2} \,, \tag{5.52}$$

those for the mixing-induced *CP* violation by

$$x_0 = \frac{\eta \mathcal{A}_{CP}^{\mathrm{mix}} \cos\gamma - \sin(\phi+\gamma)}{\eta \mathcal{A}_{CP}^{\mathrm{mix}} - \sin(\phi+2\gamma)} \,, \qquad y_0 = 0 \,, \qquad r = \sqrt{\frac{\sin\phi - \eta \mathcal{A}_{CP}^{\mathrm{mix}}}{\eta \mathcal{A}_{CP}^{\mathrm{mix}} - \sin(\phi+2\gamma)} + x_0^2} \,, \tag{5.53}$$

and, finally, those for the H observables by

$$x_0 = -\frac{(\epsilon H + 1)\cos\gamma}{\epsilon^2 H - 1} \,, \qquad y_0 = 0 \,, \qquad r = \sqrt{\frac{1-H}{\epsilon^2 H - 1} + x_0^2} \,. \tag{5.54}$$

Fit Result

A modified least squares fit using the parametrisation in Eq. (5.50) is performed to the input listed in Table 5.3. It has four degrees of freedom: $\mathcal{R}\mathrm{e}[a]$, $\mathcal{I}\mathrm{m}[a]$, ϕ_d and γ, with the latter parameter being Gaussian constrained. The χ^2 function reaches its minimum value at

$$\mathcal{R}\mathrm{e}[a] = -0.17^{+0.12}_{-0.14} \,, \qquad \mathcal{I}\mathrm{m}[a] = 0.002 \pm 0.013 \,, \tag{5.55}$$

$$\phi_d = (43.9 \pm 1.7)^\circ \,, \qquad \gamma = \left(73.9^{+6.2}_{-6.8}\right)^\circ \,, \tag{5.56}$$

which translates to

$$a = 0.17^{+0.14}_{-0.12} \,, \qquad \theta = (179.3 \pm 4.2)^\circ \,. \tag{5.57}$$

Comparing the fit value for γ with its input in Eq. (5.45), demonstrates that the input observables indeed do have some constraining power on γ, and that they prefer a slightly larger value compared to the one obtained from $B \to D^{(*)}K^{(*)}$ decays. The minimum value $\chi^2_{\mathrm{min}} = 3.0$ can be used as a goodness of fit, indicating good agreement between the different input quantities.

The constraints on the penguin parameters derived from the individual observables entering the χ^2 fit are illustrated as different light-coloured bands in Figs. 5.5 and 5.6 for the parametrisations in terms of (θ, a) and $(\mathcal{R}\mathrm{e}[a], \mathcal{I}\mathrm{m}[a])$, respectively. Similar to the UT fit analyses, the single overlap region of all contours

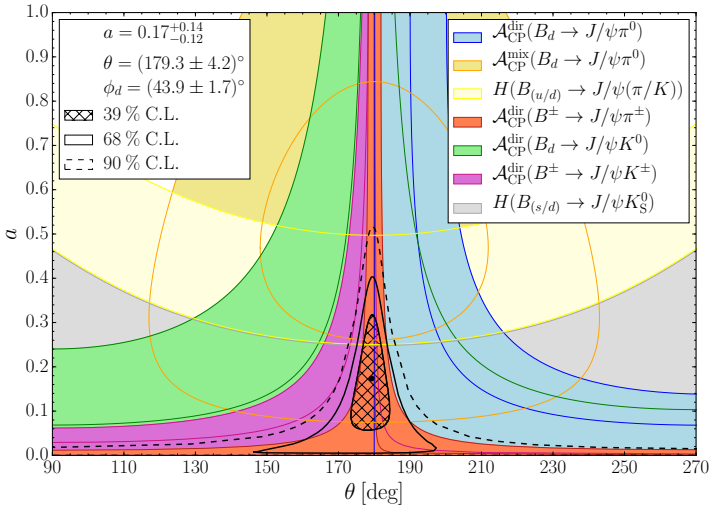

Figure 5.5: Determination of the penguin parameters a and θ through intersecting contours derived from *CP* and branching ratio information of the $B_q \to J/\psi P$ decays. Superimposed are the confidence level contours obtained from a χ^2 fit to the current data. To improve the visualisation of the individual contours, the allowed range for a is extended to 1.

pins down the solution for the penguin parameters. As many of the contour bands (partially) overlap, Eqs. (5.46) and (5.51) for the central value and the $\pm 1\sigma$ variations of the specific observable are highlighted by dark lines of the same colour as the band in order to show the full range of the constraint. The contour associated with $\mathcal{A}_{CP}^{\text{mix}}(B_d \to J/\psi\,\pi^0)$ is plotted for the value of ϕ_d in Eq. (5.56). Note that in the $(\mathcal{R}\text{e}[a], \mathcal{I}\text{m}[a])$ parametrisation, the constraints derived from the individual observables are represented by circles. Given the small radii for the circles associated with the $\mathcal{A}_{CP}^{\text{mix}}$ and H observables, their contours therefore form disks and annuli in the $(\mathcal{R}\text{e}[a], \mathcal{I}\text{m}[a])$ plane. The shapes of the different bands in the (θ, a) plane can be understood as mappings of these circles into polar coordinates. Figs. 5.5 and 5.6 also show the confidence level contours for (θ, a) and $(\mathcal{R}\text{e}[a], \mathcal{I}\text{m}[a])$ obtained from the χ^2 fit by marginalising over ϕ_d and γ. These are represented by the superimposed black (hatched) regions. The correlation between ϕ_d and a is shown in Fig. 5.7.

The solution for θ preferred by the fit, i.e. $\theta \approx 180°$, is in good agreement with the expectation from factorisation. But given the current experimental situation, this might very well be an accident. Because in the absence of (large) penguin contributions the direct *CP* asymmetry in all input modes would be (compatible

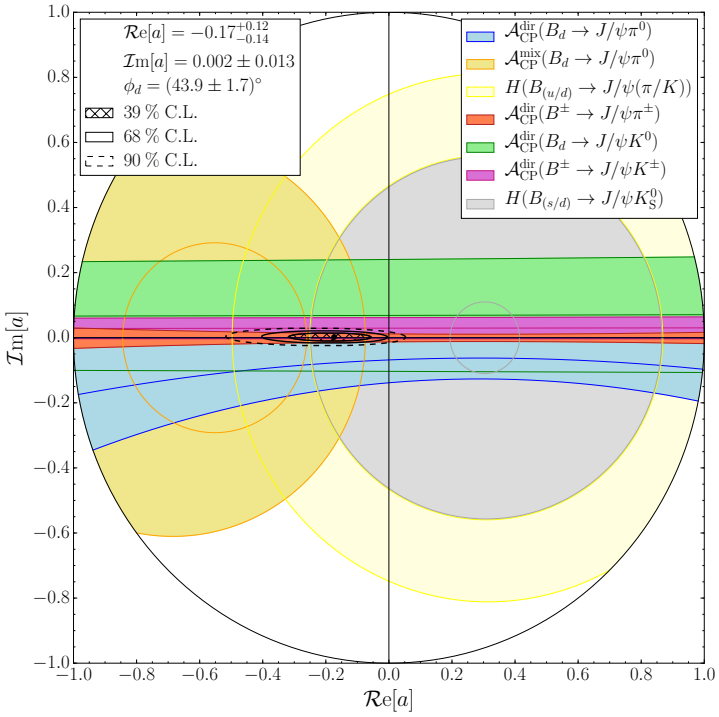

Figure 5.6: Determination of the penguin parameters $\mathcal{R}\mathrm{e}[a]$ and $\mathcal{I}\mathrm{m}[a]$ through intersecting contours derived from *CP* and branching ratio information of the $B_q \to J/\psi P$ decays. Superimposed are the confidence level contours obtained from a χ^2 fit to the current data. To improve the visualisation of the individual contours, the allowed range for a is extended to 1.

with) zero, and the resulting contours would thus constrain $ae^{i\theta}$ to the real axis. In addition, slight tensions can be observed between the direct *CP* asymmetries in $B^+ \to J/\psi K^+$ and $B^0 \to J/\psi \pi^0$, and between the mixing-induced *CP* asymmetry in $B^0 \to J/\psi \pi^0$ and H observables associated with $B_s^0 \to J/\psi K_S^0$. These tensions all force the solution for $ae^{i\theta}$ towards the real axis, which then naturally leads to the solution $\theta \approx 180°$.

The penguin parameters in Eq. (5.57) result in a penguin phase shift

$$\Delta\phi_d^{J/\psi K_S^0} = -\left(1.03^{+0.69}_{-0.85}\right)^\circ , \tag{5.58}$$

which is implicitly taken into account in the fit results (5.56). The associated confidence level contours for $\Delta\phi_d^{J/\psi K_S^0}$ are shown in Fig. 5.8, and the individual con-

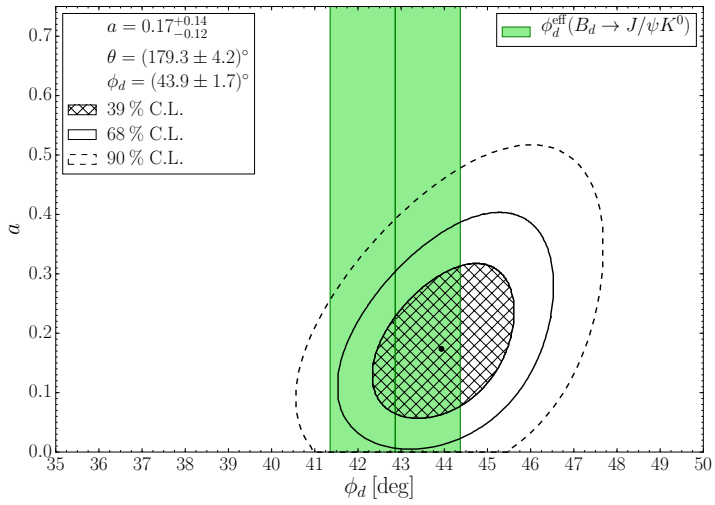

Figure 5.7: Correlation between the B^0–$\bar{B}^0$ mixing phase ϕ_d and the penguin parameter a arising from the χ^2 fit to current data.

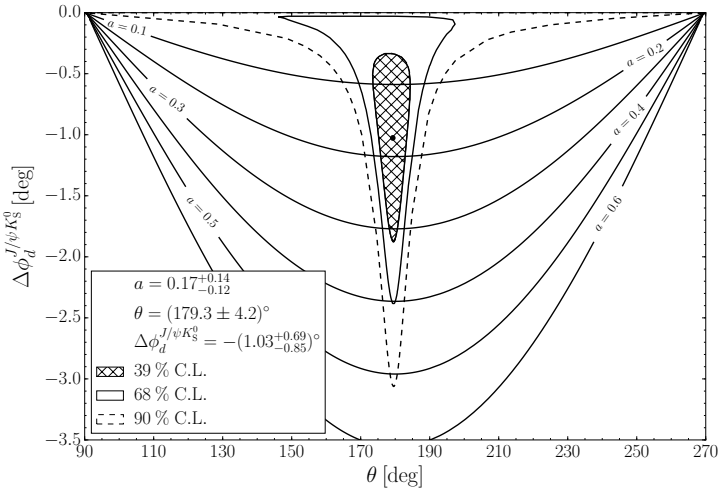

Figure 5.8: Confidence level contours for the penguin shift $\Delta\phi_d^{J/\psi K_S^0}$ as a function of the strong phase θ obtained from the χ^2 fit to the current data. Superimposed are the contour levels for the penguin parameter a.

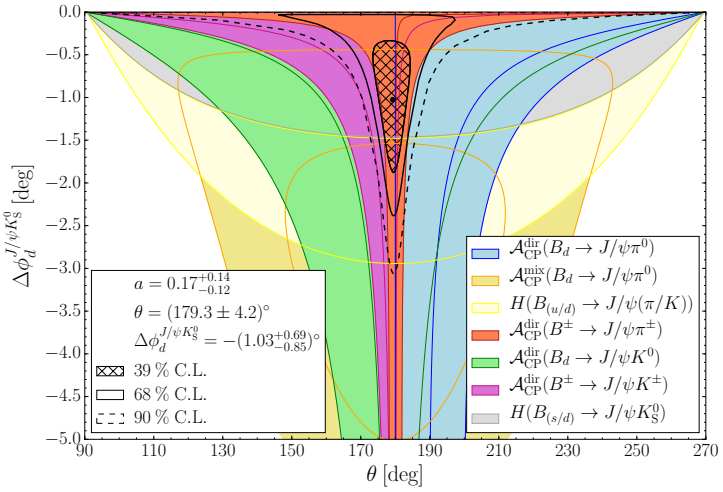

Figure 5.9: Determination of the penguin shift $\Delta\phi_d^{J/\psi K_S^0}$ through intersecting contours derived from *CP* and branching ratio information of the $B_q \to J/\psi P$ decays. Superimposed are the confidence level contours derived from those for the penguin parameters in Figs. 5.6 and 5.5.

straints on $\Delta\phi_d^{J/\psi K_S^0}$ originating from the various observables entering the χ^2 fit in Fig. 5.9.

5.3.3 Contributions from Annihilation Topologies

The framework introduced in Section 5.2.1 can be extended to also allow non-zero contributions A_c originating from the annihilation topologies. The amplitude of the decay $B^+ \to J/\psi\pi^+$ can then be written as

$$A(B^+ \to J/\psi\pi^+) = -\lambda\mathcal{A}_c\left[1 - a_c e^{i\theta_c} e^{i\gamma}\right], \tag{5.59}$$

where

$$\mathcal{A}_c \equiv \lambda^2 A\left[C_c + P_c^{(c)} - P_c^{(t)}\right] \tag{5.60}$$

is defined as in Eq. (5.20), whereas

$$a_c e^{i\theta_c} = \tilde{a}_c e^{i\tilde{\theta}_c} + x e^{i\sigma} \tag{5.61}$$

with

$$\tilde{a}_c e^{i\tilde{\theta}_c} \equiv R_b\left[\frac{P_c^{(u)} - P_c^{(t)}}{C_c + P_c^{(c)} - P_c^{(t)}}\right] \tag{5.62}$$

and

$$x e^{i\sigma} \equiv R_b \left[\frac{A_c}{C_c + P_c^{(c)} - P_c^{(t)}} \right]. \tag{5.63}$$

The penguin parameter $\tilde{a}_c e^{i\tilde{\theta}_c}$ is defined in analogy to Eq. (5.21), while the relative contribution from the annihilation topology is probed by $x e^{i\sigma}$. The direct *CP* asymmetry in $B^+ \to J/\psi \pi^+$ takes the form

$$\mathcal{A}_{CP}^{\text{dir}} = \frac{2(\tilde{a}_c \sin\tilde{\theta}_c + x \sin\sigma)\sin\gamma}{1 - 2(\tilde{a}_c \cos\tilde{\theta}_c + x\cos\sigma)\cos\gamma + 2\tilde{a}_c x \cos(\tilde{\theta}_c - \sigma) + \tilde{a}_c^2 + x^2}\,, \tag{5.64}$$

whereas the ratio $\Xi\left(B^\pm \to J/\psi \pi^\pm, B_s \to J/\psi K_S^0\right)$ depends on x and σ as

$$\Xi = \frac{1 - 2(\tilde{a}_c \cos\tilde{\theta}_c + x\cos\sigma)\cos\gamma + 2\tilde{a}_c x \cos(\tilde{\theta}_c - \sigma) + \tilde{a}_c^2 + x^2}{1 - 2\tilde{a}_c \cos\tilde{\theta}_c \cos\gamma + \tilde{a}_c^2}\,. \tag{5.65}$$

Similar expressions can be obtained for the direct *CP* asymmetry in $B^+ \to J/\psi K^+$ and the ratio $\Xi\left(B^\pm \to J/\psi K^\pm, B_d \to J/\psi K_S^0\right)$ by making the substitution

$$\tilde{a}_c \to \epsilon \tilde{a}_c'\,, \qquad \tilde{\theta}_c \to \tilde{\theta}_c' + \pi\,, \qquad x \to \epsilon x'\,, \qquad \sigma \to \sigma' + \pi\,. \tag{5.66}$$

Assuming

$$x' e^{i\sigma'} = x e^{i\sigma} \tag{5.67}$$

and universal penguin parameters, i.e.

$$\tilde{a}_c e^{i\tilde{\theta}_c} = \tilde{a}_c' e^{i\tilde{\theta}_c'} = a e^{i\theta}, \tag{5.68}$$

the annihilation parameters x and σ can be obtained from a χ^2 fit to the two direct *CP* asymmetries and the two Ξ ratios listed above. Including the observables γ (from Eq. (5.45)), a and θ (from Eq. (5.57)) as Gaussian constraints results in the solution

$$x = 0.04^{+0.10}_{-0.04}\,, \qquad \sigma = (177 \pm 0.28)^\circ\,, \tag{5.69}$$

with the corresponding confidence level contours shown in Fig. 5.10. The result is compatible with $x = 0$, which is consistent with our assumption to neglect contributions from annihilation topologies in the main χ^2 fit.

The results in Eq. (5.69) assume external input for the penguin parameters a and θ, and therefore do not take into account the back reaction of a non-zero value of $x e^{i\sigma}$ on $a e^{i\theta}$. To include this back reaction, a simultaneous fit of $a e^{i\theta}$ and $x e^{i\sigma}$ to all *CP* and branching ratio information is necessary. However, including only the annihilation topologies in such an extended fit is misleading as the contributions from exchange and penguin annihilation topologies can potentially be of similar size as those from the annihilation topologies. Hence all additional topologies need

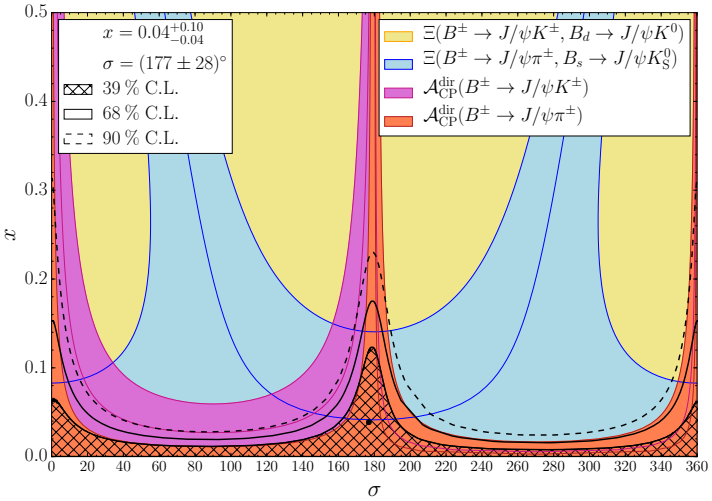

Figure 5.10: Determination of the parameters x and σ, which probe the contribution from annihilation topologies in the decays $B^+ \to J/\psi\pi^+$ and $B^+ \to J/\psi K^+$, through intersecting contours derived from *CP* and branching ratio information. Superimposed are the confidence level contours obtained from a χ^2 fit to the current data.

to be put on the same footing, i.e. either all included, or all neglected in the fit. Including the contributions from all additional topologies is possible in the future, when stringent constraints on the branching ratio of the $B_s^0 \to J/\psi\pi^0$ decay are available. But by that time also high-precision measurements of the *CP* asymmetries in $B_s^0 \to J/\psi K_S^0$ should be available, allowing us to implement the theoretically superior U-spin strategy discussed in detail below. The extended fit would nevertheless offer an interesting cross-check to complement the picture of the penguin parameters.

5.4 A Benchmark Scenario for $B_s^0 \to J/\psi K_S^0$

The $SU(3)_F$ symmetry arguments and the assumptions regarding additional decay topologies, which lie at the basis of the grand fit described in the previous section, introduce additional theoretical uncertainties that are difficult to quantify. Given the precision on the penguin parameters a and θ in Eq. (5.57), they can currently still be ignored, but that will no longer be the case in the Belle II and LHCb upgraded era. High precision constraints on the shift $\Delta\phi_d^{J/\psi K_S^0}$ can thus only come from the theoretically cleaner analysis of $B_s^0 \to J/\psi K_S^0$. Let us therefore explore the

potential of the $B_s^0 \to J/\psi K_S^0$ mode using a future benchmark scenario pointing to the LHCb upgrade era.

Penguin Parameters

Based on the results in Eq. (5.57) and assuming the Standard Model value for ϕ_s, the predictions for the $B_s^0 \to J/\psi K_S^0$ *CP* observables are

$$\mathcal{A}_{\Delta\Gamma}(B_s \to J/\psi K_S^0) = \quad 0.962 \pm 0.060\,, \tag{5.70}$$

$$\mathcal{A}_{CP}^{\text{dir}}(B_s \to J/\psi K_S^0) = \quad 0.004 \pm 0.021\,, \tag{5.71}$$

$$\mathcal{A}_{CP}^{\text{mix}}(B_s \to J/\psi K_S^0) = -0.27 \quad \pm 0.21 \quad . \tag{5.72}$$

The confidence level contours for $\mathcal{A}_{CP}^{\text{dir}}(B_s \to J/\psi K_S^0)$ and $\mathcal{A}_{CP}^{\text{mix}}(B_s \to J/\psi K_S^0)$ associated with these predictions are shown in Fig. 5.11. The current experimental results on the $B_s^0 \to J/\psi K_S^0$ *CP* observables, discussed in Chapter 7 and given in Eqs. (7.42)–(7.44), do not yet allow for a meaningful comparison. The penguin parameters in Eq. (5.57) in addition also yield

$$\tau_{J/\psi K_S^0}^{\text{eff}} = (1.603 \pm 0.010)\,\text{ps}\,, \tag{5.73}$$

in agreement with the experimental result given in Eq. (7.4), and

$$H(B_{(s/d)} \to J/\psi K_S^0) = 1.13 \pm 0.13\,, \tag{5.74}$$

which can directly be compared with the input in Table 5.3. This shows a slight tension with the experimental value, as can also be seen when comparing the best fit with the grey contour in Fig. 5.6, although it is insignificant given the large uncertainties on the B to light form factors.

To illustrate the potential of the $B_s^0 \to J/\psi K_S^0$ mode with a benchmark scenario, let us assume that by the end of the LHCb upgrade programme the $B_s^0 \to J/\psi K_S^0$ *CP* asymmetry parameters have been measured with high precision, and that these hypothetical results are given by

$$\mathcal{A}_{CP}^{\text{dir}}(B_s \to J/\psi K_S^0) = 0.004 \pm 0.065\,, \quad \mathcal{A}_{CP}^{\text{mix}}(B_s \to J/\psi K_S^0) = -0.274 \pm 0.065\,, \tag{5.75}$$

i.e. with the central values of Eqs. (5.71) and (5.72). The associated uncertainties are extrapolated from the statistical uncertainties obtained with LHCb's $3\,\text{fb}^{-1}$ data sample and quoted in Eqs. (7.42)–(7.44), and assume $6\,\text{fb}^{-1}$ collected during Run II and another $50\,\text{fb}^{-1}$ collected after the LHCb upgrade, both at a centre-of-mass energy of 14 TeV. Note that these are not official LHCb prospects, but only naive extrapolations performed by the author. These hypothetical measurements are complemented with external inputs for the CKM angle γ and the mixing phase

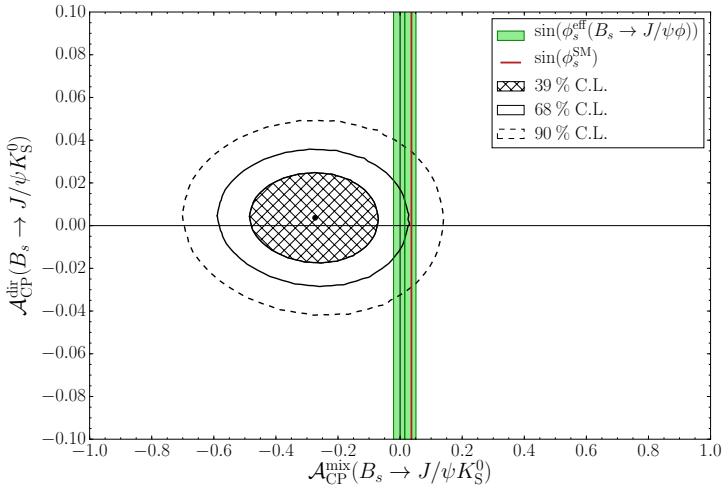

Figure 5.11: Prediction of *CP* violation in $B_s^0 \to J/\psi K_S^0$, following from the χ^2 fit to the present data discussed in Section 5.3.2.

ϕ_s. It is assumed that the angle γ has been determined in a clean way from pure tree decays of the form $B \to D^{(*)}K^{(*)}$, yielding a precision of

$$\gamma = (73.2 \pm 1.0)^\circ \tag{5.76}$$

when using the total data sample collected during the LHCb upgrade programme [34]. For the B_s^0–$\bar{B}_s^0$ mixing phase ϕ_s we assume as input a value

$$\phi_s = -\left(2.1 \pm 0.5|_{\rm exp} \pm 0.3|_{\rm theo}\right)^\circ = -(2.1 \pm 0.6)^\circ\,, \tag{5.77}$$

where the first uncertainty originates from the effective phase measured in the $B_s^0 \to J/\psi\,\phi$ channel [34] and the second one is associated with the penguin shift $\Delta\phi_s^{J/\psi\,\phi}$, further discussed below. We consider the assessment of the theoretical uncertainty affecting ϕ_s in Eq. (5.77) as conservative.

A modified least squares fit using the parametrisation in Eq. (5.50) is performed to these inputs, yielding

$$a = 0.174^{+0.041}_{-0.039}\,, \qquad \theta = (179.3 \pm 12.7)^\circ\,. \tag{5.78}$$

The corresponding confidence level contours are shown in Fig. 5.12. In contrast to the fit in Section 5.3.2, this "future" determination of a and θ is theoretically clean. The precision on the penguin parameters is only limited by the experimental uncertainties on the input quantities.

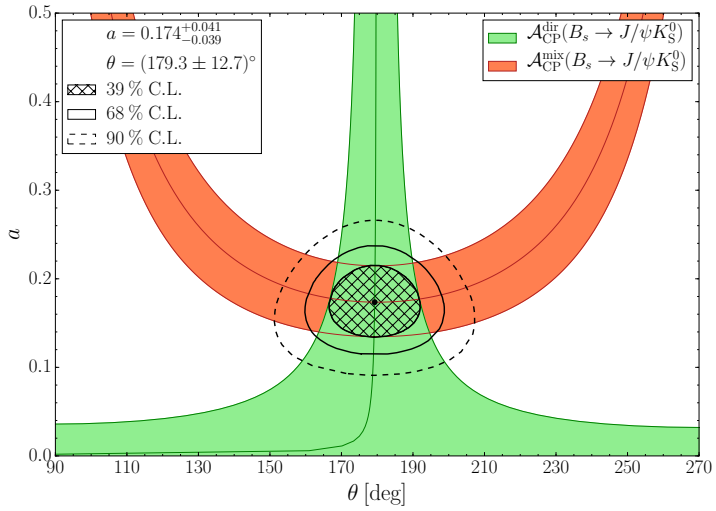

Figure 5.12: Benchmark scenario illustrating the determination of the penguin parameters a and θ from the *CP* asymmetries of the $B_s^0 \to J/\psi K_S^0$ decay.

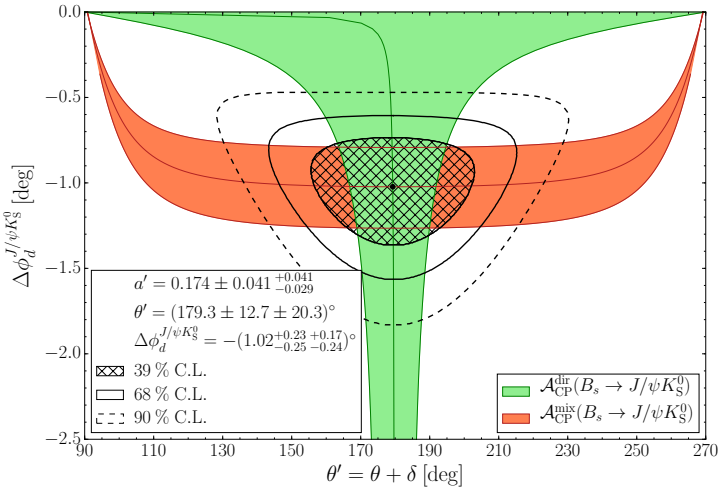

Figure 5.13: Benchmark scenario illustrating the determination of $\Delta\phi_d^{J/\psi K_S^0}$ from the *CP* asymmetries of the $B_s^0 \to J/\psi K_S^0$ decay. The confidence level contours assume a 20% uncertainty for *U*-spin breaking effects, parametrised through Eq. (5.79).

Using the U-spin relation (5.26) and the functional dependence in Eq. (5.31), these parameters can be converted into the penguin phase shift $\Delta\phi_d^{J/\psi K_S^0}$. Only at this point do potential U-spin breaking effects enter. They can be included by introducing the parameters ξ and δ to generalise the relation (5.26) to

$$a' = \xi \cdot a\,, \qquad \theta' = \theta + \delta\,. \tag{5.79}$$

Assuming 20% U-spin-breaking, i.e. $\xi = 1.00 \pm 0.20$ and $\delta = (0 \pm 20)^\circ$, the results for a and θ in Eq. (5.78) yield

$$\Delta\phi_d^{J/\psi K_S^0} = -\left(1.02^{+0.23}_{-0.25}\,(\text{stat.})^{+0.17}_{-0.24}\,(U-spin)\right)^\circ, \tag{5.80}$$

where the first uncertainty is statistical, i.e. due to the uncertainties on a and θ in Eq. (5.78), and the second quantifies the uncertainty on possible U-spin breaking effects. The confidence level contours for $\Delta\phi_d^{J/\psi K_S^0}$ are shown in Fig. 5.13. In this benchmark scenario, the experimental and theoretical uncertainties are of the same size, with a total uncertainty of 0.3° when added in quadrature.

Hadronic Parameters

It is important to emphasise that for the determination of the penguin parameters in $B_s^0 \to J/\psi K_S^0$ the H observable is not required. Information on the direct and mixing-induced CP violation is sufficient to pin down a and θ. In theory, the H observable can be added to the χ^2 fit to further reduce the uncertainties, but in practice the impact is very limited due to the large uncertainties associated with the ratio of form factors. Instead it is more interesting to combine the results from the χ^2 fit with the branching ratio information in $B_s^0 \to J/\psi K_S^0$ and $B^0 \to J/\psi K_S^0$ to provide experimental constraints on the ratio of hadronic amplitudes.

Assuming the relation (5.79) to relate the penguin parameters in $B_s^0 \to J/\psi K_S^0$ and $B^0 \to J/\psi K_S^0$, the fit results in Eq. (5.78) lead to

$$H_{(a,\theta)} = 1.136 \pm 0.039\,(a,\theta) \pm 0.0012\,(\xi,\delta)\,. \tag{5.81}$$

Because a' enters Eq. (5.36) in combination with the tiny ϵ factor, the U-spin breaking corrections have a negligible impact on H, as the above numerical results illustrate. By comparing this quantity with Eq. (5.33), the ratio of hadronic amplitudes can then be calculated as

$$\left|\frac{\mathcal{A}'}{\mathcal{A}}\right| = \sqrt{\epsilon\, H_{(a,\theta)}\, \frac{\text{PhSp}\left(B_s \to J/\psi K_S^0\right)}{\text{PhSp}\left(B_d \to J/\psi K_S^0\right)}\, \frac{\tau_{B_s}}{\tau_{B_d}}\, \frac{\mathcal{B}\left(B_d \to J/\psi K_S^0\right)_{\text{theo}}}{\mathcal{B}\left(B_s \to J/\psi K_S^0\right)_{\text{theo}}}}\,. \tag{5.82}$$

To illustrate this strategy for our benchmark scenario, requires further assumptions regarding the future measurement of the ratio of branching fractions. Its systematic uncertainty will be limited by the ratio $f_s/f_d = 0.259 \pm 0.015$ [159, 160] of

the B_s^0 to B^0 production fractions, which enters in the normalisation of the event yields. This measurement is currently limited by its systematic uncertainties. Assuming therefore no further improvements in the determination of this parameter, which is conservative, and assuming all other source of systematic uncertainties, as well as the statistical uncertainty, to be negligible, results in the experimental constraint

$$\left|\frac{\mathcal{A}'}{\mathcal{A}}\right|_{\text{exp}} = 1.160 \pm 0.034\,. \tag{5.83}$$

The experimental uncertainty is about five times smaller than the current theoretical uncertainty associated with the factorisation result

$$\left|\frac{\mathcal{A}'}{\mathcal{A}}\right|_{\text{fact}} = 1.16 \pm 0.18 \tag{5.84}$$

using LCSR form factors, as already reported in Table 5.2. Consequently, the experimental determination of $|\mathcal{A}'/\mathcal{A}|$ at the LHCb upgrade can provide valuable insights into possible non-factorisable U-spin breaking effects and the hadronisation dynamics of the $B^0 \to J/\psi K_S^0$ and $B_s^0 \to J/\psi K_S^0$ systems.

Illustration for γ

Besides the above described strategy to obtain experimental insights on the ratio of hadronic amplitudes, information on the H observable can also be used to extend the χ^2 fit. When complementing the direct and mixing-induced *CP* violation observables of the $B_s^0 \to J/\psi K_S^0$ channel with the ratio H, sufficient information is available to determine, in addition to the penguin parameters a and θ, the UT angle γ [36]. This determination is possible due to the U-spin relation in Eq. (5.26), and provides an alternative measurement of γ that, when compared to the results obtained from pure tree decays of the form $B \to D^{(*)}K^{(*)}$, can help to constrain new physics contributions present in loop diagrams. In practice, however, the precision on γ that can thus be obtained is not competitive with other strategies, and would not lead to new insights. Let us quantify this statement by using the benchmark scenario as an illustration.

When assuming a fixed value for the angles θ and ϕ_s, each of the three input observables can be represented as a contour in the γ–a plane. These contours are also parametrised by Eq. (5.46), when simply interchanging the roles of γ and θ. Alternatively, the information from the direct and mixing-induced *CP* asymmetries, and from the H observable and the mixing-induced *CP* asymmetry, can be combined to eliminate the dependence on θ [36]. Both parametrisation are illustrated in Figs. 5.14 and 5.15, and show that the sensitivity to γ is primarily driven by the H observable. The impact of the direct *CP* asymmetry, on the other hand, is negligible, as its contour band covers the whole visible range for both a and γ.

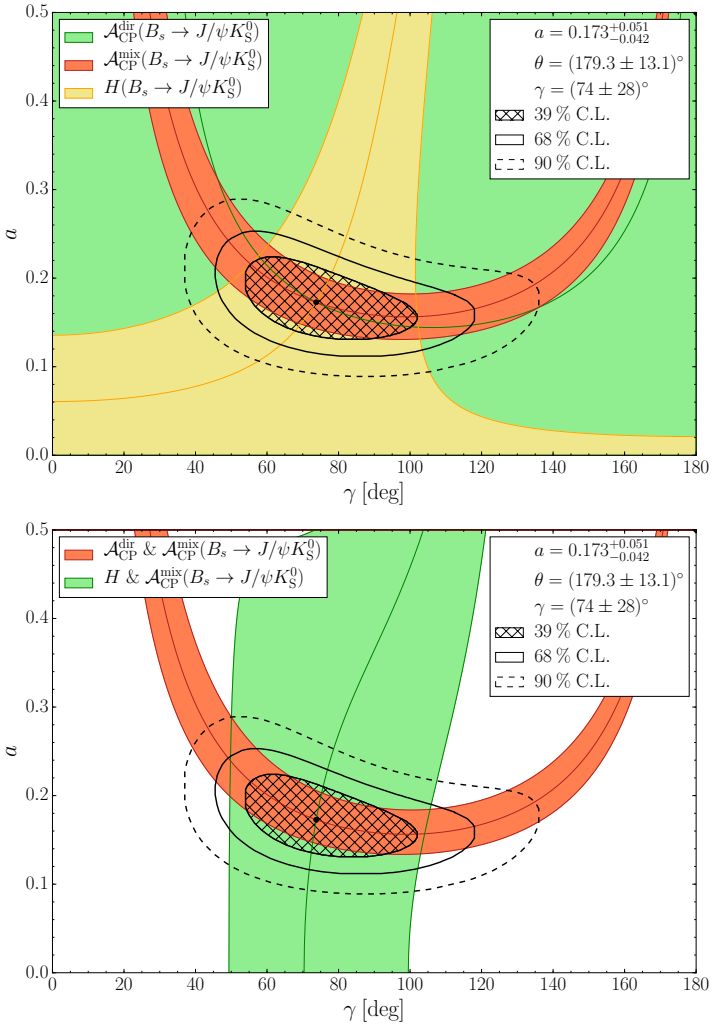

Figure 5.14: Benchmark scenario I, illustrating the determination of the UT angle γ from the *CP* asymmetries of the $B_s^0 \to J/\psi K_S^0$ decay and the ratio of $B_s^0 \to J/\psi K_S^0$ to $B^0 \to J/\psi K_S^0$ branching fractions. The scenario assumes a 50% improvement in the determination of the hadronic amplitudes, leading to an input value $H = 1.17 \pm 0.18$. Top: Illustration showing the three individual constraints $\mathcal{A}_{CP}^{dir}$, $\mathcal{A}_{CP}^{mix}$ and H, plotted for the best fit value of the strong phase θ. Bottom: Illustration showing the combined constraints from $\mathcal{A}_{CP}^{dir}\&\mathcal{A}_{CP}^{mix}$ and $H\&\mathcal{A}_{CP}^{mix}$, independent of the value of θ.

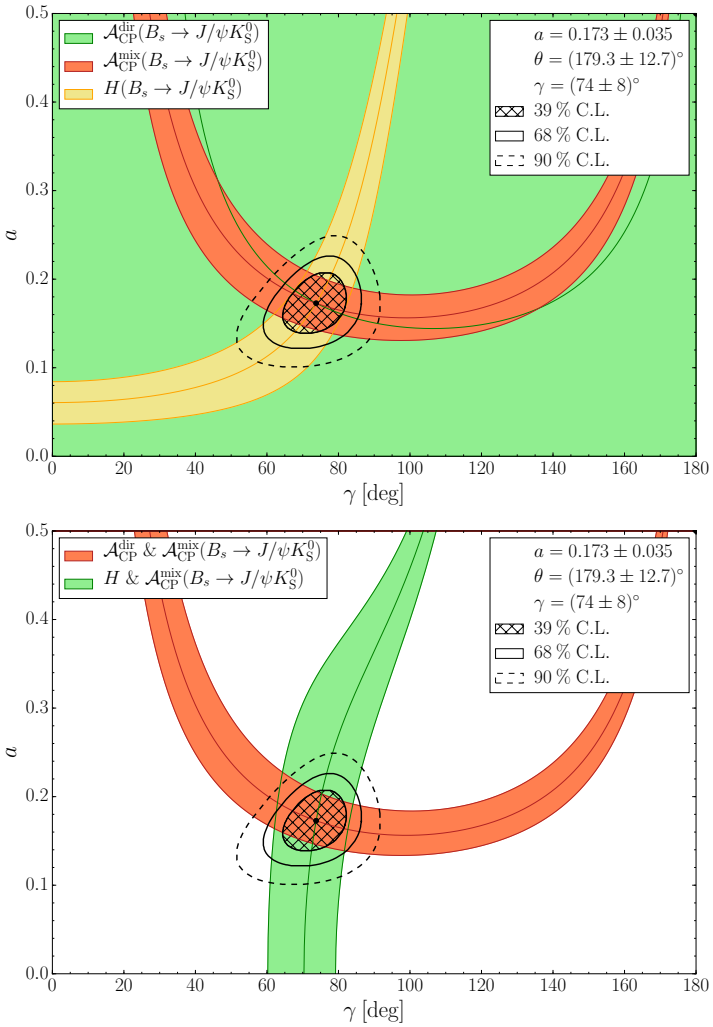

Figure 5.15: Benchmark scenario II, illustrating the determination of the UT angle γ from the *CP* asymmetries of the $B_s^0 \to J/\psi K_S^0$ decay and the ratio of $B_s^0 \to J/\psi K_S^0$ to $B^0 \to J/\psi K_S^0$ branching fractions. The scenario assumes perfect knowledge on the hadronic amplitudes, leading to an input value $H = 1.17 \pm 0.05$. Top: Illustration showing the three individual constraints $\mathcal{A}_{CP}^{dir}$, $\mathcal{A}_{CP}^{mix}$ and H, plotted for the best fit value of the strong phase θ. Bottom: Illustration showing the combined constraints from $\mathcal{A}_{CP}^{dir}\&\mathcal{A}_{CP}^{mix}$ and $H\&\mathcal{A}_{CP}^{mix}$, independent of the value of θ.

The uncertainty on γ is therefore directly related to the precision on the ratio of hadronic amplitudes that can be achieved with LCSR or lattice calculations. For the benchmark scenario it is thus crucial to know how these calculations of the form factors will improve between now and the end of the LHCb upgrade programme. However, when looking back at the results from the past ten years, such an extrapolation is far from straightforward. With each new iteration, LCSR calculations are better understood and controlled, and take into account more sub-leading effects. But the numerical precision on the final results has not changed noticeably between the different updates. It is hence unclear how the uncertainties will reduce over the coming years. Instead of providing a clear benchmark for the LHCb upgrade, we therefore only illustrate the different possibilities using two scenarios. In the first scenario, a 50% improvement in the determination of the hadronic amplitudes is considered, leading to the input

$$H_{\text{Scen. I}} = 1.13 \pm 0.18\,. \tag{5.85}$$

Such a precision could potentially be achieved by performing a simultaneous calculation of the $B_s \to K$ and $B_d \to K$ form factors in such a way that common systematic effects cancel in the ratio. The second scenario illustrates the most ideal case. It assumes perfect knowledge on the hadronic amplitudes and vanishing statistical and systematic uncertainties on the ratio of branching fractions such that the only source of uncertainty on H originates from the ratio f_s/f_d of hadronisation fractions. The input for the ratio H is then

$$H_{\text{Scen. II}} = 1.13 \pm 0.05\,. \tag{5.86}$$

A modified least squares fit using the parametrisation in Eq. (5.50) is performed to the three input observables. In this fit, the value of ϕ_s is again Gaussian constrained to the input in Eq. (5.77). But contrary to the benchmark scenario above, no further information on γ is added. This χ^2 fit yields

$$\gamma = (73 \pm 28)^\circ\,, \qquad a = 0.173^{+0.051}_{-0.042}\,, \qquad \theta = (179 \pm 13)^\circ \tag{5.87}$$

for scenario I and

$$\gamma = (73.8^{+8.4}_{-9.3})^\circ\,, \qquad a = 0.173^{+0.035}_{-0.034}\,, \qquad \theta = (179 \pm 13)^\circ \tag{5.88}$$

for scenario II. The latter result is in essence equivalent to the benchmark fit for a and θ in Eq. (5.78), albeit obtained with slightly different input observables. The corresponding confidence level contours for these two scenarios are shown in Figs. 5.14 and 5.15, respectively. The results in Eqs. (5.87) and (5.88) confirm the initial statement that this strategy is not competitive with other methods. It is therefore more advantageous to take γ from external inputs, and use the branching ratio information instead to experimentally measure $|\mathcal{A}'/\mathcal{A}|$.

5.5 B Decays into Two Vector Mesons

5.5.1 Polarisation Amplitudes

Compared to the $B \to J/\psi\,(\pi/K)$ decays, the analyses of the $B_s^0 \to J/\psi\,\phi$, $B^0 \to J/\psi\,\rho^0$ and $B_s^0 \to J/\psi\,\overline{K}^{*0}$ decay channels are complicated by having two vector mesons in the final state. The zero angular momentum final state configurations can be formed with three possible values for the orbital angular momentum: $L \in \{0,1,2\}$. For the CP eigenstates $J/\psi\,\phi$ and $J/\psi\,\rho^0$, these three states have different CP eigenvalues: the $L = 1$ mode is CP odd while the other two are CP even. In a CP analysis of these decays, the mixture of CP-even and CP-odd eigenstates therefore needs to be disentangled. This can be done with the help of an angular analysis of the $J/\psi \to \ell^+\ell^-$ and $\phi \to K^+K^-$ or $\rho^0 \to \pi^+\pi^-$ decay products [142, 143]. A detailed discussion of the general structure of the various observables provided by the angular distribution in the presence of the penguin contributions is given in Ref. [37].

For the experimental analysis of the $B_s^0 \to J/\psi\,\phi$ and $B^0 \to J/\psi\,\rho^0$ modes, it is convenient to introduce linear polarisation states $A_0(t)$, $A_\parallel(t)$ and $A_\perp(t)$ [161], which are either longitudinal (0) or transverse to the direction of motion of the two vector mesons. In the latter case, they can be parallel ($\parallel$) or perpendicular ($\perp$) to one another. The relative contributions from each of these three polarisation states are experimentally accessible through the polarisation fractions

$$f_i \equiv \frac{|A_i|^2}{|A_0|^2 + |A_\parallel|^2 + |A_\perp|^2} = \frac{\mathcal{B}(B \to (f)_i)_{\rm exp}}{\sum_j \mathcal{B}(B \to (f)_j)_{\rm exp}}\,. \tag{5.89}$$

These three observables are not all independent, but satisfy the relation

$$f_0 + f_\parallel + f_\perp = 1\,. \tag{5.90}$$

The 0 and $\parallel$ final state configurations are parity even, while $\perp$ describes a parity-odd state. Since J/ψ, ϕ and ρ^0 are all C-odd eigenstates, the properties under parity are the same as those under the combined CP transformation. Even though the $B_s^0 \to J/\psi\,\overline{K}^{*0}$ decay has a flavour-specific final state, the same three linear polarisation amplitudes can be employed to describe the decay, both experimentally and theoretically [131].

Consider the vector–vector decay $B \to V_1 V_2$. In terms of the polarisation three-vectors $\boldsymbol{\epsilon}_{V_1}$ and $\boldsymbol{\epsilon}_{V_2}$, the two parity even decay amplitudes are proportional to the combinations $\boldsymbol{\epsilon}^*_{V_1} \cdot \boldsymbol{\epsilon}^*_{V_2}$ and $(\boldsymbol{\epsilon}^*_{V_1} \cdot \hat{\mathbf{p}})(\boldsymbol{\epsilon}^*_{V_1} \cdot \hat{\mathbf{p}}) \equiv \epsilon^{*L}_{V_1}\epsilon^{*L}_{V_2}$, where $\hat{\mathbf{p}}$ is the unit vector along the direction of motion of V_2 in the rest frame of V_1. The parity odd decay amplitude is proportional to $\boldsymbol{\epsilon}^*_{V_1} \times \boldsymbol{\epsilon}^*_{V_2} \cdot \hat{\mathbf{p}}$. The decay amplitude for the $B \to V_1 V_2$

decay can then be decomposed as [142]

$$A(B \to V_1 V_2) = \frac{A_0}{x} \boldsymbol{\epsilon}_{V_1}^{*L} \boldsymbol{\epsilon}_{V_2}^{*L} - \frac{A_\parallel}{\sqrt{2}} \boldsymbol{\epsilon}_{V_1}^{*T} \cdot \boldsymbol{\epsilon}_{V_2}^{*T} - i \frac{A_\perp}{\sqrt{2}} \boldsymbol{\epsilon}_{V_1}^{*} \times \boldsymbol{\epsilon}_{V_2}^{*} \cdot \hat{\mathbf{p}}_{V_2}\,, \tag{5.91}$$

where

$$x \equiv \frac{p_{V_1} \cdot p_{V_2}}{m_{V_1} m_{V_2}} = \frac{m_B^2 - m_{V_1}^2 - m_{V_2}^2}{2 m_{V_1} m_{V_2}}\,. \tag{5.92}$$

The superscript T refers to the transverse component of the polarisation vector, which is obtained by subtracting its longitudinal component.

From the theoretical point of view, it is, however, more convenient to perform calculations in a Lorentz-invariant framework, where the time-independent decay amplitude is decomposed as [162, 163, 164]

$$A(B \to V_1 V_2) = \epsilon_{V_1,\mu}^* \epsilon_{V_2,\nu}^* \times \left[a g^{\mu\nu} + \frac{b}{m_{V_1} m_{V_2}} p_{V_2}^\mu p_{V_1}^\nu + i \frac{c}{m_{V_1} m_{V_2}} \epsilon^{\mu\nu\alpha\beta} p_{V_1,\alpha} p_{V_2,\beta} \right]. \tag{5.93}$$

The two parametrisations in Eqs. (5.91) and (5.93) are related to each other as [142]

$$A_0 = -xa - (x^2 - 1)\, b\,, \tag{5.94}$$

$$A_\parallel = \sqrt{2}\, a\,, \tag{5.95}$$

$$A_\perp = \sqrt{2(x^2 - 1)}\, c\,. \tag{5.96}$$

Using the OPE framework, the parameters a, b and c can be expressed as combinations of Wilson coefficients and low-energy effective operators. The factorisable part of these operators is related to the $B \to$ vector form factors.

In the limit where non-factorisable contributions are ignored, the expressions for the parameters a, b and c describing the $B_s^0 \to J/\psi\,\phi$, $B^0 \to J/\psi\,\rho^0$ and $B_s^0 \to J/\psi\,\overline{K}^{*0}$ decays are given by [143]

$$a_{\text{fact}} = -\frac{G_F}{\sqrt{2}} V_{cq} V_{cb}^* \mathcal{C}_{\text{eff}}(\mu) \times f_{J/\psi}\, m_{J/\psi} (m_{B_q} + m_X) A_1^{B_q \to X}(m_{J/\psi}^2)\,, \tag{5.97}$$

$$b_{\text{fact}} = \frac{G_F}{\sqrt{2}} V_{cq} V_{cb}^* \mathcal{C}_{\text{eff}}(\mu) \times 2 \frac{f_{J/\psi}\, m_{J/\psi}^2\, m_X}{m_{B_q} + m_X} A_2^{B_q \to X}(m_{J/\psi}^2)\,, \tag{5.98}$$

$$c_{\text{fact}} = \frac{G_F}{\sqrt{2}} V_{cq} V_{cb}^* \mathcal{C}_{\text{eff}}(\mu) \times 2 \frac{f_{J/\psi}\, m_{J/\psi}^2\, m_X}{m_{B_q} + m_X} V^{B_q \to X}(m_{J/\psi}^2)\,, \tag{5.99}$$

where $(q, X) \in \{(d, \rho^0), (s, \phi), (s, \overline{K}^{*0})\}$, $f_{J/\psi}$ is the J/ψ decay constant and $\mathcal{C}_{\text{eff}}(\mu)$ is a combination of Wilson coefficients. The quantities $A_{1,2}^{B_q \to X}(q^2)$ and $V^{B_q \to X}(q^2)$ represent the $B_q \to X$ form factors in the parametrisation of Bauer, Stech and Wirbel

[88, 165]. For the calculation of the form factors from LCSR it is convenient to eliminate $A_2^{B_q\to X}(q^2)$ in favour of [146]

$$A_{12}^{B_q\to X}(q^2) \equiv \frac{(m_{B_q^0}+m_X)^2(m_{B_q^0}^2-m_X^2-q^2)A_1^{B_q\to X}(q^2)-\lambda(q^2)A_2^{B_q\to X}(q^2)}{16\,m_{B_q^0}m_X^2\,(m_{B_q^0}+m_X)}\,, \tag{5.100}$$

where

$$\lambda(q^2) \equiv \Big((m_{B_q^0}+m_X)^2-q^2\Big)\Big((m_{B_q^0}-m_X)^2-q^2\Big)\,. \tag{5.101}$$

The dependence of the form factors on the momentum transfer q^2 can be fitted with a function of the form [146]:

$$\frac{1}{1-q^2/m_{\rm Res}^2}\sum_{k=0}^{3}\alpha_k\Big(z(q^2)-z(0)\Big)^k\,, \tag{5.102}$$

where $m_{\rm Res}$ is a resonance mass whose value depends on the type of form factor considered, and

$$z(t) \equiv \frac{\sqrt{t_+-t}-\sqrt{t_+-t_0}}{\sqrt{t_+-t}+\sqrt{t_+-t_0}}\,, \tag{5.103}$$

with

$$t_+ \equiv (m_{B_q^0}+m_X)^2\,, \qquad t_0 \equiv (m_{B_q^0}+m_X)(\sqrt{m_{B_q^0}}-\sqrt{m_X})^2\,. \tag{5.104}$$

The parameters α_i are obtained from a fit, and can be found in Ref. [146], together with the values of the resonance masses $m_{\rm Res}$. The numerical results from LCSR on the $A_{1,12}^{B_q\to X}(m_{J/\psi}^2)$ and $V^{B_q\to X}(m_{J/\psi}^2)$ form factors are summarised in Table 5.4. It should be noted that the form factors do not depend on the renormalisation scale μ. As the overall expression in Eq. (5.93) cannot depend on this scale, this implies that non-factorisable contributions are necessary to cancel the μ dependence in $\mathcal{C}_{\rm eff}$. In the calculations here, they are nonetheless ignored.

Expressions for the polarisation amplitudes in the factorisation limit are ob-

Table 5.4: Latest results on the $B \to$ vector form factors from LCSR [146].

Form Factor	$B_d \to \rho$	$B_s \to K^*$	$B_s \to \phi$
$A_1(q^2=0)$	0.267 ± 0.025	0.246 ± 0.022	0.315 ± 0.027
$A_{12}(q^2=0)$	0.307 ± 0.028	0.246 ± 0.023	0.274 ± 0.022
$V(q^2=0)$	0.333 ± 0.032	0.311 ± 0.029	0.407 ± 0.033
$A_1(q^2=m_{J/\psi}^2)$	0.343 ± 0.031	0.323 ± 0.028	0.406 ± 0.032
$A_{12}(q^2=m_{J/\psi}^2)$	0.365 ± 0.033	0.292 ± 0.027	0.314 ± 0.030
$V(q^2=m_{J/\psi}^2)$	0.620 ± 0.043	0.584 ± 0.045	0.739 ± 0.042

tained by inserting Eqs. (5.97)–(5.99) into Eqs. (5.94)–(5.96), leading to [h]

$$A_0^{\text{fact}}(B_q \to J/\psi X) = \mathcal{C}\text{st} \times \frac{8 m_{B_q} m_X}{m_{J/\psi}} A_{12}^{B_q \to X}(m_{J/\psi}^2), \tag{5.106}$$

$$A_\parallel^{\text{fact}}(B_q \to J/\psi X) = -\mathcal{C}\text{st} \times \sqrt{2}(m_{B_q} + m_X) A_1^{B_q \to X}(m_{J/\psi}^2), \tag{5.107}$$

$$A_\perp^{\text{fact}}(B_q \to J/\psi X) = \mathcal{C}\text{st} \times \sqrt{2(x^2-1)}\, \frac{2 m_{J/\psi} m_X}{m_{B_q} + m_X} V^{B_q \to X}(m_{J/\psi}^2), \tag{5.108}$$

where

$$\mathcal{C}\text{st} = \frac{G_F}{\sqrt{2}} V_{cq} V_{cb}^* \mathcal{C}_{\text{eff}}(\mu) f_{J/\psi}\, m_{J/\psi}\,. \tag{5.109}$$

This common prefactor drops out in the ratio (5.89), which thus only depends on the three form factors themselves and their associated kinematic factors. The theoretical calculations for the polarisation fractions, based on the input listed in Table 5.4, is compared to the equivalent experimental measurements in Figs. 5.16, 5.17 and 5.18 for the $B_s^0 \to J/\psi \phi$, $B^0 \to J/\psi \rho^0$ and $B_s^0 \to J/\psi \bar{K}^{*0}$ mode, respectively. For the latter two modes this shows good agreement within the current uncertainties, but for $B_s^0 \to J/\psi \phi$ 3σ tensions can be observed for the parallel and perpendicular polarisation fractions.

5.5.2 The $B_s^0 \to J/\psi \phi$ Channel

The decay $B_s^0 \to J/\psi \phi$ is the B_s^0-meson equivalent to the decay $B^0 \to J/\psi K_S^0$ as it is the most sensitive probe to measure the complex phase ϕ_s associated with the B_s^0–

[h] In terms of $A_1^{B_q \to X}(q^2)$ and $A_2^{B_q \to X}(q^2)$, the expression for A_0^{fact} is given by

$$A_0^{\text{fact}} = \mathcal{C}\text{st} \times \left(x(m_{B_q} + m_X) A_1^{B_q \to X}(m_{J/\psi}^2) - 2(x^2-1) \frac{m_{J/\psi} m_X}{m_{B_q} + m_X} A_2^{B_q \to X}(m_{J/\psi}^2) \right). \tag{5.105}$$

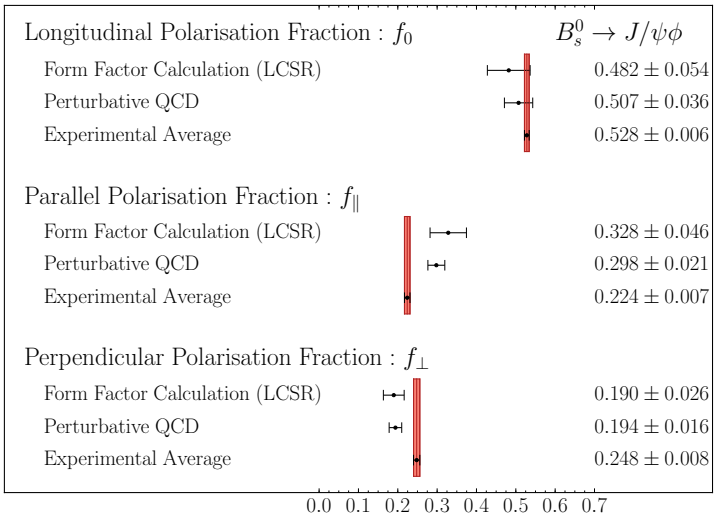

Figure 5.16: Comparison between the theoretically calculated and experimentally measured values of the three polarisation fractions in the $B_s^0 \to J/\psi\,\phi$ decay. LCSR results are based on the input in Table 5.4, perturbative QCD results are taken from Ref. [40] and the experimental averages combine the information from Refs. [64] and [30].

$\overline{B}_s^0$ mixing process. Neglecting contributions from exchange and penguin-annihilation topologies, and assuming that the ϕ meson is a pure $s\bar{s}$ state, i.e. neglecting ω–ϕ mixing[i], both $\bar{b} \to \bar{c}c\bar{s}$ quark-level processes only differ in the flavour of their spectator quark. For $B_s^0 \to J/\psi\,\phi$ this is a strange quark, whereas for $B^0 \to J/\psi\,K_S^0$ it is a down quark. The formalism of Section 5.2.1 can thus readily be applied to $B_s^0 \to J/\psi\,\phi$, with the only additional complication that parameters related to the decay amplitude become polarisation dependent.

In analogy to Eq. (5.19), the $B_s^0 \to J/\psi\,\phi$ decay amplitude can be written as [37, 131]

$$A\left(B_s^0 \to (J/\psi\,\phi)_f\right) = \left(1 - \frac{\lambda^2}{2}\right)\mathcal{A}'_f\left[1 + \epsilon a'_f e^{i\theta'_f} e^{i\gamma}\right], \tag{5.110}$$

where the label $f \in \{0, \parallel, \perp\}$ distinguishes between the three possible configurations of the final state vector mesons. Due to differences in the hadronisation dynamics and non-factorisable effects, the penguin parameters a'_f and θ'_f are in general expected to differ for different final-state configurations f, and will in particular be

[i] A detailed discussion on this topic is given in Ref. [131].

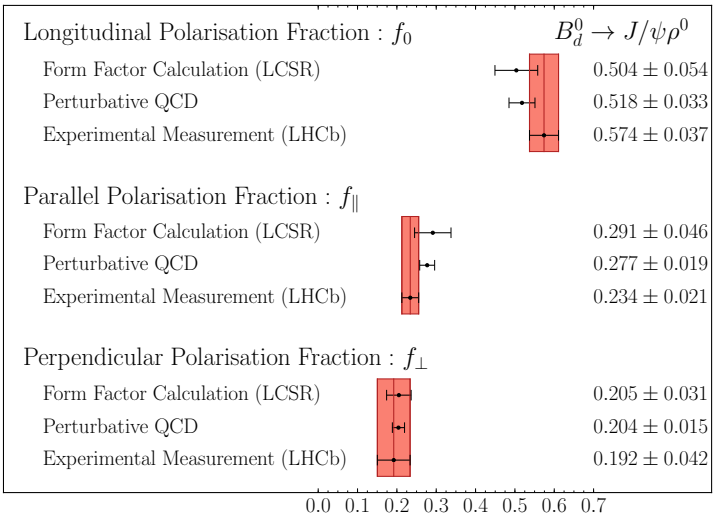

Figure 5.17: Comparison between the theoretically calculated and experimentally measured values of the three polarisation fractions in the $B^0 \to J/\psi \rho^0$ decay. LCSR results are based on the input in Table 5.4, perturbative QCD results are taken from Ref. [40] and the experimental values are taken from Ref. [166].

different from a' and θ' used in the analysis of $B^0 \to J/\psi K_S^0$. The replacement rules

$$B_s^0 \to J/\psi\,\phi:\ b_f e^{i\rho_f} \to -\epsilon a'_f e^{i\theta'_f}\,, \qquad \mathcal{N}_f \to \left(1-\frac{\lambda^2}{2}\right)\mathcal{A}'_f \tag{5.111}$$

associated with the above amplitude are the direct counterparts to Eq. (5.27). Applied to Eqs. (5.16) and (5.17), they define the hadronic phase shifts

$$\phi^{\text{eff}}_{s,(J/\psi\,\phi)_f} = \phi_s + \Delta\phi_s^{(J/\psi\,\phi)_f}\,, \tag{5.112}$$

similar to Eq. (5.14) for the pseudo-scalar–vector systems.

Recently, the LHCb collaboration has presented the first polarisation-dependent measurements of the effective B_s^0–$\bar{B}_s^0$ mixing phases [30], yielding

$$\phi^{\text{eff}}_{s,(J/\psi\,\phi)_0} = -(2.58 \pm 3.04\,(\text{stat.}) \pm 0.40\,(\text{syst.}))^\circ\,, \tag{5.113}$$

$$\phi^{\text{eff}}_{s,(J/\psi\,\phi)_\parallel} - \phi^{\text{eff}}_{s,(J/\psi\,\phi)_0} = -(1.03 \pm 2.46\,(\text{stat.}) \pm 0.52\,(\text{syst.}))^\circ\,, \tag{5.114}$$

$$\phi^{\text{eff}}_{s,(J/\psi\,\phi)_\perp} - \phi^{\text{eff}}_{s,(J/\psi\,\phi)_0} = -(0.80 \pm 2.01\,(\text{stat.}) \pm 0.34\,(\text{syst.}))^\circ\,. \tag{5.115}$$

Within the uncertainties, no dependence on the final-state configuration is found, and all results are in excellent agreement with the Standard Model value given

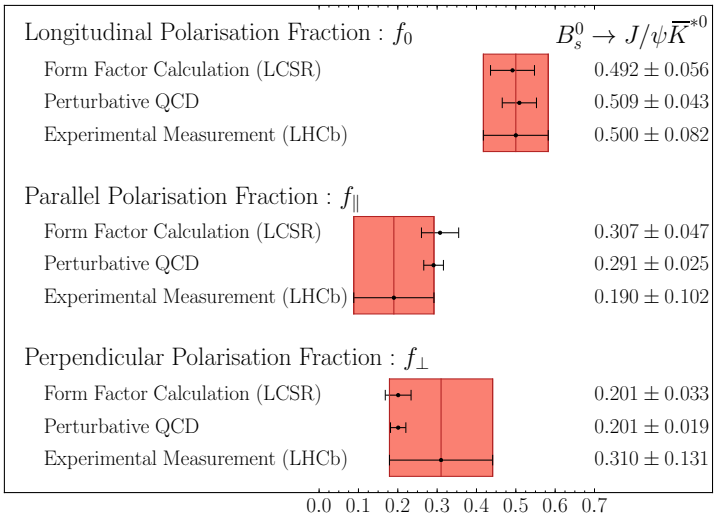

Figure 5.18: Comparison between the theoretically calculated and experimentally measured values of the three polarisation fractions in the $B_s^0 \to J/\psi\, \overline{K}^{*0}$ decay. LCSR results are based on the input in Table 5.4, perturbative QCD results are taken from Ref. [40] and the experimental values are taken from Ref. [145].

in Table 4.1. Using Eq. (5.58) as a first estimate for the size of possible hadronic phase shifts in $B_s^0 \to J/\psi\,\phi$, the current precision is not yet high enough for resolving such effects. This situation is expected to change in the LHCb upgrade era, as the precision on these measurements further increases. Finding significant deviations between the values of the three effective mixing phases $\phi_{s,f}^{\text{eff}}$, would conclusively demonstrate the presence of penguin contributions in the $B_s^0 \to J/\psi\,\phi$ decay.

Together with the effective mixing phases $\phi_{s,(J/\psi\,\phi)_f}^{\text{eff}}$, the LHCb collaboration also reported polarisation-dependent results on the convention-independent parameter λ_f, defined in Eq. (4.52). Its dependence on the penguin parameters is given by

$$|\lambda_{(J/\psi\,\phi)_f}| = \left| \frac{1 + \epsilon a'_f e^{i\theta'_f} e^{-i\gamma}}{1 + \epsilon a'_f e^{i\theta'_f} e^{+i\gamma}} \right|, \tag{5.116}$$

and in essence it contains the same information as the direct CP violation observ-

able $\mathcal{A}_{CP}^{\rm dir}$. The LHCb measurements are

$$|\lambda_{(J/\psi\phi)_0}| = 1.012 \pm 0.058\,(\text{stat.}) \pm 0.013\,(\text{syst.})\,, \tag{5.117}$$

$$|\lambda_{(J/\psi\phi)_\perp}/\lambda_{(J/\psi\phi)_0}| = 1.02 \pm 0.12\,(\text{stat.}) \pm 0.05\,(\text{syst.})\,, \tag{5.118}$$

$$|\lambda_{(J/\psi\phi)_\parallel}/\lambda_{(J/\psi\phi)_0}| = 0.97 \pm 0.16\,(\text{stat.}) \pm 0.01\,(\text{syst.})\,, \tag{5.119}$$

and within the current uncertainties do not show any dependence on the polarisation of the final state. Looking at the structure of Eq. (5.116), where the penguin parameters are doubly Cabibbo-suppressed, and using the fit result in Eq. (5.57) as a guideline, leads to the expectation

$$|\lambda_{(J/\psi\phi)_f}| = 1 + \mathcal{O}(0.01)\,. \tag{5.120}$$

This sets the scale for the precision that is required to resolve possible footprints of the penguin contributions in these measurements, and shows that the dependence of a_f' and θ_f' on the final-state configuration is necessarily small. This can be theoretically understood, because form factors, which are the primary source of polarisation-dependent effects, cancel in the ratios of penguin to tree amplitudes. Applying factorisation arguments therefore leads to the limit [37]

$$a_f' \equiv a_{J/\psi\phi}'\,, \qquad \theta_f' \equiv \theta_{J/\psi\phi}'\,, \qquad \forall f \in \{0, \parallel, \perp\}\,, \tag{5.121}$$

where the subscripts $J/\psi\phi$ where added to differentiate these penguin parameters from the penguin parameters in $B^0 \to J/\psi K_S^0$. As already shown, current experimental data is consistent with the limit (5.121), and it is interesting to continue testing this relation with future measurements.

Assuming the relations in Eq. (5.121), the following results are obtained from the time-dependent and angular analysis of the $B_s^0 \to J/\psi\phi$ decay [30][j]

$$\phi_{s,J/\psi\phi}^{\rm eff} = -(3.32 \pm 2.81\,(\text{stat.}) \pm 0.34\,(\text{syst.}))^\circ\,, \tag{5.122}$$

$$|\lambda_{J/\psi\phi}| = 0.964 \pm 0.019\,(\text{stat.}) \pm 0.007\,(\text{syst.})\,, \tag{5.123}$$

which correspond to

$$\mathcal{A}_{CP}^{\rm dir}(B_s \to J/\psi\phi) = 0.037 \pm 0.021\,, \qquad \mathcal{A}_{CP}^{\rm mix}(B_s \to J/\psi\phi) = 0.058 \pm 0.049 \tag{5.124}$$

when expressed in terms of the direct and mixing-induced *CP* violation parameters. The central value of $|\lambda_{J/\psi\phi}|$, which could well be an experimental fluctuation, especially in view of the results in Eqs (5.117)–(5.119), is surprisingly large compared to the naive estimate (5.120). This becomes even more apparent when using

[j] This result differs from the one quoted in Table 4.1, which is an average that also contains information from $B_s^0 \to J/\psi\pi^+\pi^-$ and $B_s^0 \to D_s^+ D_s^-$ decays. The theoretical interpretation of the results from the latter two modes is slightly different [36, 135, 167], which is why they are not included here.

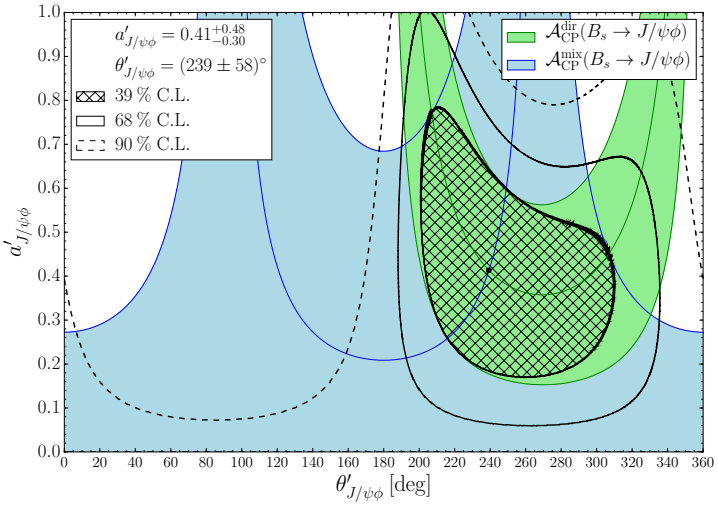

Figure 5.19: Determination of the penguin parameters $a'_{J/\psi\phi}$ and $\theta'_{J/\psi\phi}$ through intersecting contours derived from the CP asymmetry measurements in $B_s^0 \to J/\psi\phi$. Superimposed are the confidence level contours obtained from a χ^2 fit to the current data.

the contour method described in Section 5.3.2 to convert the above results into contour bands in the $\theta'_{J/\psi\phi}$–$a'_{J/\psi\phi}$ plane, as illustrated in Fig. 5.19. To plot the $\mathcal{A}_{CP}^{mix}$ contour derived from $\phi_{s,J/\psi\phi}^{eff}$, the Standard Model value was assumed for ϕ_s.

A modified least squares fit using the parametrisation in Eq. (5.50) and assuming the Standard Model value for ϕ_s is performed to the inputs in Eq. (5.124), yielding

$$a'_{J/\psi\phi} = 0.41^{+0.48}_{-0.30}\,, \qquad \theta'_{J/\psi\phi} = (239 \pm 58)^\circ\,, \qquad \Delta\phi_s^{J/\psi\phi} = -\left(1.2^{+2.9}_{-2.8}\right)^\circ\,. \tag{5.125}$$

Although the uncertainties are too large to draw meaningful conclusions, the fit does illustrate the observation that was made in the context of Eqs. (5.29) and (5.31): in order to have both a small phase shift on ϕ_s and large penguin parameters, strong phases around 90° or 270° are needed. Interestingly, the data for $B^0 \to J/\psi\rho^0$, discussed next, also suggest such a picture for the strong phases.

5.5.3 The $B^0 \to J/\psi\rho^0$ Channel

The decay $B^0 \to J/\psi\rho^0$ can be used to control the penguin shifts affecting the determination of ϕ_s from the effective mixing phases in $B_s^0 \to J/\psi\phi$. In that sense, it plays the same role as $B_s^0 \to J/\psi K_S^0$ and $B^0 \to J/\psi\pi^0$ do for ϕ_d. Neglecting contributions

from exchange and penguin-annihilation topologies, the $B^0 \to J/\psi \rho^0$ decay, which proceeds via a $\bar{b} \to \bar{c}c\bar{d}$ quark-level process, is related to $B_s^0 \to J/\psi K_S^0$ by replacing the strange spectator quark with a down quark. Again following the formalism of Section 5.2.1, the decay amplitude can be written as [37]

$$\sqrt{2}\,A\left(B^0 \to (J/\psi\,\rho^0)_f\right) = -\lambda \mathcal{A}_f \left[1 - a_f e^{i\theta_f} e^{i\gamma}\right], \tag{5.126}$$

where the factor of $\sqrt{2}$ is due to the wave function of the ρ^0, and the replacement rules are given by

$$B^0 \to J/\psi\,\rho^0 : \; b_f e^{i\rho_f} \to a_f e^{i\theta_f}\,, \qquad \mathcal{N}_f \to -\frac{\lambda}{\sqrt{2}}\mathcal{A}_f\,. \tag{5.127}$$

Like $B_s^0 \to J/\psi K_S^0$ and $B^0 \to J/\psi \pi^0$, the penguin contributions thus enter in a Cabibbo-allowed manner. Due to differences in the hadronisation dynamics and non-factorisable effects, they are, however, expected to differ from the penguin parameters a and θ used in the analysis of the $B \to J/\psi P$ modes.

Thanks to new experimental developments [168], the effective mixing phases $\phi^{\text{eff}}_{d,(J/\psi\rho)_f}$, defined through Eq. (5.13), have recently been measured by the LHCb collaboration [144], reporting

$$\phi^{\text{eff}}_{d,(J/\psi\rho)_0} = \left(44.1 \pm 10.2\,(\text{stat.})^{+3.0}_{-6.9}\,(\text{syst.})\right)^\circ\,, \tag{5.128}$$

$$\phi^{\text{eff}}_{d,(J/\psi\rho)_\parallel} - \phi^{\text{eff}}_{d,(J/\psi\rho)_0} = -\left(0.8 \pm 6.5\,(\text{stat.})^{+1.9}_{-1.3}\,(\text{syst.})\right)^\circ\,, \tag{5.129}$$

$$\phi^{\text{eff}}_{d,(J/\psi\rho)_\perp} - \phi^{\text{eff}}_{d,(J/\psi\rho)_0} = -\left(3.6 \pm 7.2\,(\text{stat.})^{+2.0}_{-1.4}\,(\text{syst.})\right)^\circ\,. \tag{5.130}$$

Alternatively, assuming polarisation-independent penguin parameters for the three polarisation states, i.e.

$$a_f \equiv a_{J/\psi\,\rho}\,, \qquad \theta_f \equiv \theta_{J/\psi\,\rho} \qquad \forall f \in \{0, \parallel, \perp\}\,, \tag{5.131}$$

in analogy to the relations in Eq. (5.121), the phase [144]

$$\phi^{\text{eff}}_{d,J/\psi\,\rho} = \left(41.7 \pm 9.6\,(\text{stat.})^{+2.8}_{-6.3}\,(\text{syst.})\right)^\circ \tag{5.132}$$

and the *CP* asymmetries

$$\mathcal{A}_{CP}^{\text{dir}}(B_d \to J/\psi\,\rho^0) = -0.063 \pm 0.059\,, \qquad \mathcal{A}_{CP}^{\text{mix}}(B_d \to J/\psi\,\rho^0) = 0.66 \pm 0.15 \tag{5.133}$$

are extracted from the time-dependent and angular analysis of the $B^0 \to J/\psi\,\pi^+\pi^-$ decay.

In analogy to the analysis in Section 5.3.2, a modified least squares fit using the parametrisation in Eq. (5.50) is performed to the *CP* asymmetries of the

Table 5.5: Input quantities for the χ^2 fit to the penguin parameters a_f and θ_f of the $B^0 \to J/\psi\,\rho^0$ decay [144].

Observable	Input	Observable	Input
$\mathcal{A}_{CP}^{\rm dir}(B_d \to J/\psi\,\rho^0)_0$	-0.094 ± 0.071	$\mathcal{A}_{CP}^{\rm mix}(B_d \to J/\psi\,\rho^0)_0$	0.69 ± 0.15
$\mathcal{A}_{CP}^{\rm dir}(B_d \to J/\psi\,\rho^0)_\parallel$	-0.12 ± 0.12	$\mathcal{A}_{CP}^{\rm mix}(B_d \to J/\psi\,\rho^0)_\parallel$	0.68 ± 0.18
$\mathcal{A}_{CP}^{\rm dir}(B_d \to J/\psi\,\rho^0)_\perp$	0.03 ± 0.22	$\mathcal{A}_{CP}^{\rm mix}(B_d \to J/\psi\,\rho^0)_\perp$	-0.65 ± 0.19

$B^0 \to J/\psi\,\rho^0$ decay. These asymmetries, listed in Table 5.5, are calculated from the measured effective mixing phases (5.128)–(5.130) and the quantities $\alpha_{CP}^f \equiv (1 - |\lambda_{(J/\psi\,\rho)_f}|)/(1 + |\lambda_{(J/\psi\,\rho)_f}|)$ reported in Ref. [144]. Again, the CKMfitter value of γ in Eq. (5.45) is added as an asymmetric Gaussian constraint to the χ^2 fit. Moreover, external input is also required for the B^0–$\bar{B}^0$ mixing phase ϕ_d, which enters the mixing-induced CP observables. The result from the $B \to J/\psi\,P$ fit discussed in Section 5.3.2, i.e. Eq. (5.56), is therefore added as a Gaussian constraint. This last feature differentiates the present analysis from the one done in Ref. [144] itself.

The main results for the polarisation-independent scenario are

$$a_{J/\psi\,\rho} = 0.039^{+0.095}_{-0.039}\,, \qquad \theta_{J/\psi\,\rho} = -\left(58^{+154}_{-121}\right)^\circ\,, \tag{5.134}$$

corresponding to a shift

$$\Delta\phi_d^{J/\psi\,\rho} = -\left(2.2^{+13}_{-11}\right)^\circ \tag{5.135}$$

affecting the effective mixing phase in Eq. (5.132). The associated confidence level contours for $a_{J/\psi\,\rho}$ and $\theta_{J/\psi\,\rho}$ are shown in Fig. 5.20. It is interesting to note that the current experimental measurement of $|\lambda_{J/\psi\,\phi}|$ from $B_s^0 \to J/\psi\,\phi$ is in slight tension with these results from $B^0 \to J/\psi\,\rho^0$. Should this turn out not to be a mere fluctuation of the data, then the effect cannot be explained by the presence of penguin topologies alone.

The main results for the polarisation-dependent scenarios, which form the method of choice in the long run, are

$$a_0 = 0.049^{+0.136}_{-0.037}\,, \qquad \theta_0 = -\left(91^{+118}_{-158}\right)^\circ\,, \tag{5.136}$$

$$a_\parallel = 0.064^{+0.114}_{-0.064}\,, \qquad \theta_\parallel = -\left(84^{+142}_{-102}\right)^\circ\,, \tag{5.137}$$

$$a_\perp = 0.036^{+0.116}_{-0.036}\,, \qquad \theta_\perp = \left(29^{+188}_{-203}\right)^\circ\,, \tag{5.138}$$

with the corresponding confidence level contours shown in Figs. 5.20 and 5.21. They are compatible with the polarisation-independent result in Eq. (5.134), but the current uncertainties are too large to draw further conclusions. The determination of the penguin parameters in Eq. (5.134) and Eqs. (5.136)–(5.138) does not rely on information from decay rates and is therefore theoretically clean.

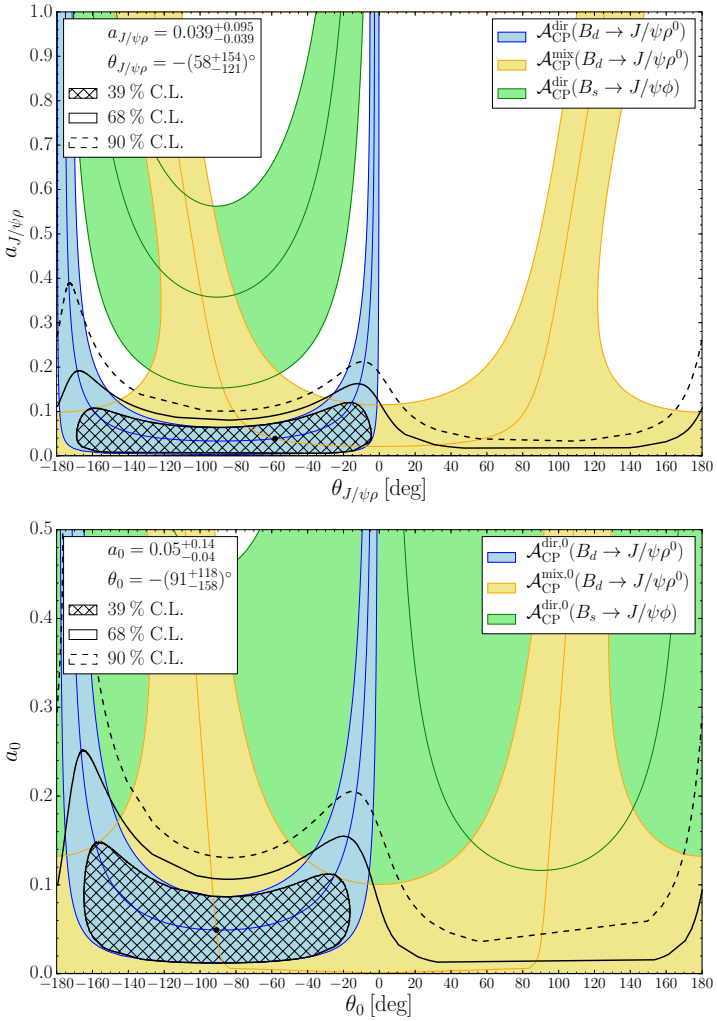

Figure 5.20: Determination of the penguin parameters a_f and θ_f through intersecting contours derived from the *CP* observables in $B^0 \to J/\psi\rho^0$. Superimposed are the confidence level contours obtained from a χ^2 fit to the data. The contour originating from the direct *CP* violation in $B_s^0 \to J/\psi\phi$ has been added for visual comparison, but is not taken into account in the fit.

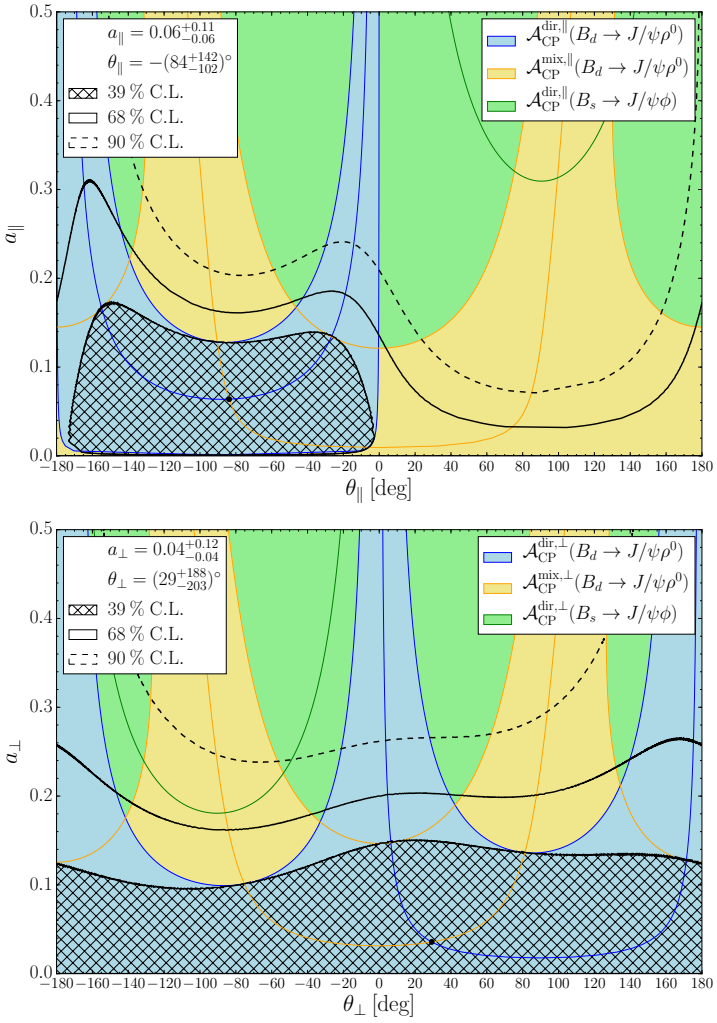

Figure 5.21: Determination of the penguin parameters a_f and θ_f through intersecting contours derived from the *CP* observables in $B^0 \to J/\psi\rho^0$. Superimposed are the confidence level contours obtained from a χ^2 fit to the data. The contour originating from the direct *CP* violation in $B_s^0 \to J/\psi\phi$ has been added for visual comparison, but is not taken into account in the fit.

Neglecting exchange and penguin annihilation topologies, the hadronic parameters of the $B^0 \to J/\psi \rho^0$ decay can be related via the $SU(3)_F$ flavour symmetry to those parametrising the $B_s^0 \to J/\psi \phi$ channel as [37]

$$a'_f e^{i\theta'_f} = a_f e^{i\theta_f} \,. \tag{5.139}$$

This allows us to convert the penguin parameters in Eq. (5.134) and Eqs. (5.136)–(5.138) into the hadronic phase shifts of the $B_s^0 \to J/\psi \phi$ decay. Possible $SU(3)$-breaking effects are parametrised through Eq. (5.79) with $\xi = 1.00 \pm 0.20$ and $\delta = (0 \pm 20)^\circ$, leading to

$$\Delta\phi_s^{J/\psi\phi} = \left(0.12^{+0.56}_{-0.71}\,(\text{stat.})^{+0.16}_{-0.13}\,(SU(3)_F)\right)^\circ \,, \tag{5.140}$$

for the polarisation-independent fit. This result should be compared to the value of ϕ_s^{eff} in Eq. (5.122), which is affected by significantly larger experimental uncertainties. The power of $B^0 \to J/\psi \rho^0$ in constraining penguin effects is thus remarkable. This can be partially explained by the value of the strong phase difference θ, as noted previously in the context of Eqs. (5.29) and (5.31). The corresponding results for the polarisation-dependent fits are

$$\Delta\phi_s^{(J/\psi\phi)_0} = -\left(0.00^{+0.60}_{-0.80}\,(\text{stat.})^{+0.16}_{-0.17}\,(SU(3)_F)\right)^\circ \,, \tag{5.141}$$

$$\Delta\phi_s^{(J/\psi\phi)_\parallel} = \left(0.04^{+0.67}_{-0.93}\,(\text{stat.}) \pm 0.20\,(SU(3)_F)\right)^\circ \,, \tag{5.142}$$

$$\Delta\phi_s^{(J/\psi\phi)_\perp} = \left(0.18^{+0.68}_{-0.93}\,(\text{stat.})^{+0.18}_{-0.14}\,(SU(3)_F)\right)^\circ \,, \tag{5.143}$$

and show a similar behaviour as the polarisation-independent shift.

Similar to the discussion of the $B_s^0 \to J/\psi K_S^0$ benchmark scenario, the information obtained from the $B^0 \to J/\psi \rho^0$ CP asymmetries can be combined with decay rate information from $B^0 \to J/\psi \rho^0$ and $B_s^0 \to J/\psi \phi$ to determine the ratio of CP-conserving strong amplitudes $\mathcal{A}'_f/\mathcal{A}_f$. The only conceptual difference with Eq. (5.82), is that the calculation requires polarisation-dependent information. In particular, the H observables from which the ratios $\mathcal{A}'_f/\mathcal{A}_f$ can be calculated are given by

$$H_i \equiv \frac{1}{\epsilon}\left|\frac{\mathcal{A}'_f}{\mathcal{A}_f}\right|^2 \frac{\text{PhSp}\,(B_s \to J/\psi\,\phi)}{\text{PhSp}(B_d \to J/\psi\,\rho^0)} \frac{\tau_{B_s^0}}{\tau_{B^0}} \frac{\mathcal{B}(B_d \to J/\psi\,\rho^0)_{\text{theo}}}{\mathcal{B}(B_s \to J/\psi\,\phi)_{\text{theo}}} \frac{f_i}{f'_i} \,, \tag{5.144}$$

where f_i is the polarisation fraction defined in Eq. (5.89) and

$$\text{PhSp}(B_q \to J/\psi\,V) \equiv \frac{1}{16\pi m_{B_q^0}} \Phi(M_{J/\psi}/M_{B_q^0}, M_V/M_{B_q^0}) \,. \tag{5.145}$$

Table 5.6: Time-integrated branching ratio information on the three $B_q \to J/\psi V$ modes, used to calculate the ratio of hadronic amplitudes from current experimental data.

Parameter	Input	Ref.
$\mathcal{B}(B_s \to J/\psi\,\phi)$	$(1.10 \pm 0.09) \times 10^{-3}$	[64]
$\mathcal{B}(B_d \to J/\psi\,\rho^0)$	$(2.50 \pm 0.21) \times 10^{-5}$	[166]
$\mathcal{B}(B_s \to J/\psi\,\bar{K}^{*0})$	$(4.88 \pm 0.85) \times 10^{-5}$	[64, 43, 145]

For the $B_q \to J/\psi V$ decays, other mass-dependent terms, which are given explicitly for the $B_q \to J/\psi P$ decays in Eq. (5.34), are absorbed into the hadronic amplitude ratio $|\mathcal{A}'_f/\mathcal{A}_f$. Note that also the conversion factors between the "theoretical" branching ratio concept and the experimentally measured time-integrated branching fraction are polarisation dependent.

Combining the branching ratio information listed in Table 5.6 with the polarisation amplitudes given in Figs. 5.16 and 5.17 and the solutions from the χ^2 fit in Eqs. (5.136)–(5.138) yields the following amplitude ratios

$$\left|\frac{\mathcal{A}'_0(B_s \to J/\psi\,\phi)}{\mathcal{A}_0(B_d \to J/\psi\,\rho^0)}\right|_{\text{exp}} = 1.09 \pm 0.07\,(\text{stat.}) \pm 0.04\,(a_0, \theta_0)\,, \tag{5.146}$$

$$\left|\frac{\mathcal{A}'_\parallel(B_s \to J/\psi\,\phi)}{\mathcal{A}_\parallel(B_d \to J/\psi\,\rho^0)}\right|_{\text{exp}} = 1.11 \pm 0.08\,(\text{stat.}) \pm 0.04\,(a_\parallel, \theta_\parallel)\,, \tag{5.147}$$

$$\left|\frac{\mathcal{A}'_\perp(B_s \to J/\psi\,\phi)}{\mathcal{A}_\perp(B_d \to J/\psi\,\rho^0)}\right|_{\text{exp}} = 1.28 \pm 0.16\,(\text{stat.}) \pm 0.05\,(a_\perp, \theta_\perp)\,, \tag{5.148}$$

which are still consistent with the limit of no $SU(3)$-breaking corrections. These results can be compared with QCD calculations, such as the recent results obtained within the perturbative QCD approach [40], or within naive factorisation with the results derived from LCSR form factors, as discussed in Section 5.5.1. In the latter case, using Eqs. (5.106)–(5.108) yields

$$\left|\frac{\mathcal{A}'_0(B_s \to J/\psi\,\phi)}{\mathcal{A}_0(B_d \to J/\psi\,\rho^0)}\right|_{\text{fact}} = 1.15 \pm 0.15\,, \tag{5.149}$$

$$\left|\frac{\mathcal{A}'_\parallel(B_s \to J/\psi\,\phi)}{\mathcal{A}_\parallel(B_d \to J/\psi\,\rho^0)}\right|_{\text{fact}} = 1.25 \pm 0.15\,, \tag{5.150}$$

$$\left|\frac{\mathcal{A}'_\perp(B_s \to J/\psi\,\phi)}{\mathcal{A}_\perp(B_d \to J/\psi\,\rho^0)}\right|_{\text{fact}} = 1.13 \pm 0.10\,. \tag{5.151}$$

Although the uncertainties are still very large, these numbers are consistent with the results in Eqs. (5.146)–(5.148), and imply

$$\left|\frac{\mathcal{A}'}{\mathcal{A}}\right| = \left|\frac{\mathcal{A}'_{\text{fact}}}{\mathcal{A}_{\text{fact}}}\right| \left|\frac{1+\mathcal{A}'_{\text{non-fact}}/\mathcal{A}'_{\text{fact}}}{1+\mathcal{A}_{\text{non-fact}}/\mathcal{A}_{\text{fact}}}\right| \approx \left|\frac{\mathcal{A}'_{\text{fact}}}{\mathcal{A}_{\text{fact}}}\right| . \tag{5.152}$$

Consequently, either the non-factorisable contributions $\mathcal{A}^{(\prime)}_{\text{non-fact}}$ themselves or the difference (due to $SU(3)$-breaking effects) between the ratio $\mathcal{A}'_{\text{non-fact}}/\mathcal{A}'_{\text{fact}}$ and $\mathcal{A}_{\text{non-fact}}/\mathcal{A}_{\text{fact}}$ is small. Since factorisation is not expected to work for the $B \to J/\psi X$ modes, as discussed in Chapter 3, the latter option is favoured. A similar picture also arises for $SU(3)$-breaking effects in $B^0 \to \pi^+\pi^-$, $B^0 \to \pi^- K^+$ and $B_s^0 \to K^+K^-$ decays, which exhibit different decay dynamics [110]. It is interesting to note that the experimental uncertainties on the ratios in Eqs. (5.146)–(5.148) are already smaller than or of similar size as the uncertainties obtained in the theoretical calculations, which are challenging to improve.

5.5.4 The $B_s^0 \to J/\psi \overline{K}^{*0}$ Channel

Besides $B^0 \to J/\psi \rho^0$, also the decay $B_s^0 \to J/\psi \overline{K}^{*0}$ proceeds via a $\bar{b} \to \bar{c}c\bar{d}$ quark-level process and can thus be used to control the penguin shifts affecting the determination of ϕ_s from the effective mixing phases in $B_s^0 \to J/\psi \phi$. It has the same quark content as the $B_s^0 \to J/\psi K_S^0$ mode, but the $(\bar{d}s)$ quark pair now hadronises into a vector meson. Again following the formalism of Section 5.2.1, the decay amplitude can be written as [131]

$$A\left(B_s^0 \to (J/\psi \overline{K}^{*0})_f\right) = -\lambda \tilde{\mathcal{A}}_f \left[1 - \tilde{a}_f e^{i\tilde{\theta}_f} e^{i\gamma}\right], \tag{5.153}$$

where the tildes are introduced to distinguish the hadronic parameters from their $B^0 \to J/\psi \rho^0$ counterparts. The associated replacement rules are given by

$$B_s^0 \to J/\psi \overline{K}^{*0} : \; b_f e^{i\rho_f} \to \tilde{a}_f e^{i\tilde{\theta}_f} , \qquad \mathcal{N}_f \to -\lambda \tilde{\mathcal{A}}_f , \tag{5.154}$$

showing that the penguin contributions also enter in a Cabibbo-allowed manner.

The analysis of the penguin parameters in $B_s^0 \to J/\psi \overline{K}^{*0}$ channel proceeds in the same way as that of the $B^0 \to J/\psi \rho^0$ mode discussed in detail above. But in contrast to the $B^0 \to J/\psi \rho^0$ channel, the $B_s^0 \to J/\psi \overline{K}^{*0}$ decay does *not* exhibit mixing-induced *CP* violation as the $J/\psi \overline{K}^{*0}$ final state is flavour specific: the pion and kaon charges of the subsequent $\overline{K}^{*0} \to K^-\pi^+$ and $K^{*0} \to \pi^- K^+$ decays[k] distinguish between initially present B_s^0 and $\overline{B}_s^0$ mesons, respectively. Consequently, in order to determine

[k] Other K^{*0} decay modes have significantly smaller branching fractions, and are also experimentally more challenging to analyse. The experimental study of the $B_s^0 \to J/\psi \overline{K}^{*0}$ decay therefore only focuses on the $K^{*0} \to \pi^- K^+$ decay mode. We hence do the same in the phenomenological discussion given here.

the penguin parameters, the polarisation-dependent direct *CP* asymmetries need to be complemented with decay rate information instead [131]. This information can be provided by the H observables, defined in analogy to Eq. (5.144), which take the place of the mixing-induced *CP* observables in the χ^2 fit. For the experimental determination of the H observables theoretical input on the ratio of hadronic amplitudes is required. The results derived from the LCSR form factors discussed in Section 5.5.1, i.e. using Eqs. (5.106)–(5.108), are

$$\left|\frac{\mathcal{A}_0'(B_s \to J/\psi\,\phi)}{\mathcal{A}_0(B_s \to J/\psi\,\overline{K}^{*0})}\right|_{\text{fact}} = 1.23 \pm 0.16\,, \tag{5.155}$$

$$\left|\frac{\mathcal{A}_\parallel'(B_s \to J/\psi\,\phi)}{\mathcal{A}_\parallel(B_s \to J/\psi\,\overline{K}^{*0})}\right|_{\text{fact}} = 1.28 \pm 0.15\,, \tag{5.156}$$

$$\left|\frac{\mathcal{A}_\perp'(B_s \to J/\psi\,\phi)}{\mathcal{A}_\perp(B_s \to J/\psi\,\overline{K}^{*0})}\right|_{\text{fact}} = 1.20 \pm 0.12\,. \tag{5.157}$$

The downside of using the H observables is that they are affected by non-factorisable effects, and have large uncertainties associated with them due to the results in Eqs. (5.155)–(5.157). The determination of the penguin parameters in $B_s^0 \to J/\psi\,\overline{K}^{*0}$ is therefore theoretically less clean than that in the $B^0 \to J/\psi\,\rho^0$ channel.

The CDF [43] and LHCb [145] collaborations have so far only measured the branching ratio and polarisation amplitudes of the $B_s^0 \to J/\psi\,\overline{K}^{*0}$ decay. Measurements of its direct *CP* asymmetries are not yet available, and a determination of the penguin parameters is therefore not yet possible. But the $SU(3)_{\text{F}}$ flavour symmetry relations

$$\tilde{a}_f e^{i\tilde{\theta}_f} = a_f e^{i\theta_f}\,, \qquad \tilde{\mathcal{A}}_f = \mathcal{A}_f\,, \tag{5.158}$$

predict that the direct *CP* asymmetries are equal to those of the $B^0 \to J/\psi\,\rho^0$ mode, given in Table 5.5. It will be interesting to confront these numbers with experimental results.

5.6 Towards the LHCb Upgrade and Belle II Era

High Precision Measurements of ϕ_d

The penguin parameters a' and θ', affecting the determination of ϕ_d from the mixing-induced *CP* asymmetry in $B^0 \to J/\psi\,K_{\text{S}}^0$, can be controlled using multiple $SU(3)_{\text{F}}$ symmetry based strategies:

1. Via a χ^2 fit to all *CP* and branching ratio information of the $B \to J/\psi\,(\pi/K)$ decays, as illustrated in Section 5.3.2.

2. Via the $SU(3)_{\text{F}}$ symmetry relation with $B^0 \to J/\psi\,\pi^0$, explored in Ref. [39].

3. Via the U-spin symmetry relation with $B_s^0 \to J/\psi K_S^0$, as illustrated in Section 5.4.

The first two strategies can already be executed with the currently available data, although the obtained results still have large uncertainties, whereas the third option relies on input from future LHCb upgrade [34] data. As reconstructing the $J/\psi \pi^0$ final state is more challenging at hadron colliders than at e^+e^- colliders, the Belle II experiment [35] will play the most important role in improving the precision that can be obtained with the second strategy. In addition, it is an important task for Belle II to resolve the current discrepancy between the BaBar and Belle measurements of the mixing-induced CP asymmetry in $B^0 \to J/\psi \pi^0$.

Although the first strategy might lead to the smallest statistical uncertainties on a' and θ' towards the end of the LHCb upgrade and Belle II programmes, it is limited by theoretical uncertainties that are challenging to quantify and control at the level that is required to match the foreseen precision on $\phi_d^{\rm eff}$ from $B^0 \to J/\psi K_S^0$. These theoretical uncertainties originate from possible factorisable and non-factorisable $SU(3)$-breaking effects between the different $B \to J/\psi (\pi/K)$ modes and from neglecting the exchange, annihilation and penguin-annihilation topologies. These limitations also apply to the $SU(3)_{\rm F}$ relation between $B^0 \to J/\psi K_S^0$ and $B^0 \to J/\psi \pi^0$, although the impact is smaller than for the global χ^2 fit. The U-spin relation with $B_s^0 \to J/\psi K_S^0$ is therefore the preferred strategy for the LHCb upgrade and Belle II era. The $B_s^0 \to J/\psi K_S^0$ penguin parameters a and θ can be determined in a *theoretically clean* way, only requiring external input on the B_s^0–$\overline{B}_s^0$ mixing phase ϕ_s, and the relation with a' and θ' can be quantified through Eq. (5.26). It therefore has the smallest associated theoretical uncertainty, which will ultimately lead to the smallest overall uncertainty on $\Delta\phi_d^{J/\psi K_S^0}$.

Following either of the above three strategies, the B^0–$\overline{B}^0$ mixing phase ϕ_d can be determined from the effective mixing phase $\phi_d^{\rm eff}$ and compared to the Standard Model value 2β, obtained from global fits of the Unitarity Triangle [25, 26]. For this Standard Model prediction, driven by the relation (2.29), the measurements of the UT angle γ and the UT side R_b play a crucial role. As illustrated by Fig. 5.24 below, especially the knowledge on R_b limits the precision that can be achieved on $\phi_d^{\rm SM} = 2\beta$. In the LHCb upgrade and Belle II era, the angle γ can be determined with high precision from $B \to D^{(*)}K^{(*)}$ decays, as given in Eq. (5.76). Future data collected at Belle II and theoretical progress will hopefully resolve the discrepancy between the determination of R_b from inclusive and exclusive semileptonic B decays. Together, these improvements will lead to a high-precision reference for the Standard Model value of ϕ_d. A possible discrepancy with the experimental measurement of ϕ_d would then reveal the presence of a CP-violating NP phase $\phi_d^{\rm NP}$ in B^0–$\overline{B}^0$ mixing.

High Precision Measurements of ϕ_s

Performing high-precision and polarisation-dependent *CP* violation measurements in $B_s^0 \to J/\psi\,\phi$ will be crucial to find or limit possible NP contributions to the B_s^0–$\bar{B}_s^0$ mixing phase ϕ_s. This requires an equally precise, polarisation-dependent determination of the penguin shifts $\Delta\phi_s^{(J/\psi\,\phi)_f}$ affecting $\phi_{s,f}^{\text{eff}}$. They can be controlled using multiple $SU(3)_{\text{F}}$ symmetry based strategies:

1. Via the $SU(3)_{\text{F}}$ symmetry relation with $B^0 \to J/\psi\,\rho^0$, as illustrated in Section 5.5.3.

2. Via the $SU(3)_{\text{F}}$ symmetry relation with $B_s^0 \to J/\psi\,\overline{K}^{*0}$, as illustrated in Section 5.5.4.

3. Via a combined fit to $B^0 \to J/\psi\,\rho^0$ and $B_s^0 \to J/\psi\,\overline{K}^{*0}$.

In the first strategy, polarisation-dependent measurements of the direct and mixing-induced *CP* violation observables of the $B^0 \to J/\psi\,\rho^0$ channel provide a theoretically clean way to determine the penguin parameters a_f and θ_f, only requiring external input on the B^0–$\bar{B}^0$ mixing phase ϕ_d. The relation with the penguin parameters a_f' and θ_f' of the $B_s^0 \to J/\psi\,\phi$ system can be quantified through Eq. (5.26). This strategy will therefore have the smallest associated theoretical uncertainty.

Alternatively, the penguin effects can also be probed with the $B_s^0 \to J/\psi\,\overline{K}^{*0}$ decay. However, this decay mode does not exhibit mixing-induced *CP* violation, as the $J/\psi(\to \mu^+\mu^-)\overline{K}^{*0}(\to K^-\pi^+)$ final state is flavour specific. Instead the direct *CP* violation observables are complemented with decay rate information. This strategy therefore requires external input on the amplitude ratios $|\mathcal{A}_f'/\tilde{\mathcal{A}}_f|$, and thus introduces additional theoretical uncertainties. These uncertainties are associated with the calculation of the hadronic form factors, and with possible factorisable and non-factorisable effects, and ultimately limit the precision that can be achieved on $\tilde{a}_f$ and $\tilde{\theta}_f$, especially in comparison to a_f and θ_f. Given the large theoretical uncertainties on the form factors, and the remarkable precision that can already be achieved with the $B^0 \to J/\psi\,\rho^0$ mode, an independent determination of the penguin effects in $B_s^0 \to J/\psi\,\phi$ from $B_s^0 \to J/\psi\,\overline{K}^{*0}$ is certainly interesting, but not competitive.

In this respect, the third strategy provides a more optimal way to use the information from the $B_s^0 \to J/\psi\,\overline{K}^{*0}$ decay. This combined analysis extends the relations between the penguin parameters of the $B^0 \to J/\psi\,\rho^0$, $B_s^0 \to J/\psi\,\overline{K}^{*0}$ and $B_s^0 \to J/\psi\,\phi$ modes in Eqs. (5.139) and (5.158) to

$$a_f e^{i\theta_f} = \tilde{a}_f e^{i\tilde{\theta}_f} = a_f' e^{i\theta_f'}\,, \tag{5.159}$$

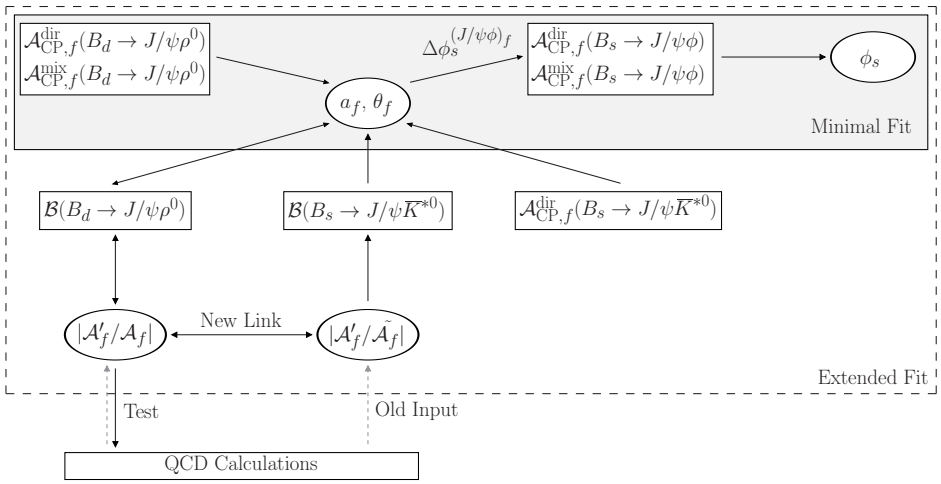

Figure 5.22: Flow chart of the combined analysis of the $B^0 \to J/\psi\rho^0$, $B_s^0 \to J/\psi\overline{K}^{*0}$ and $B_s^0 \to J/\psi\phi$ modes. This analysis would provide a simultaneous determination of the penguin parameters, the ratio of $SU(3)$-breaking strong amplitudes, and the CP-violating B_s^0–$\overline{B}_s^0$ mixing phase ϕ_s.

and identifies the ratios of hadronic amplitudes

$$\left|\frac{\mathcal{A}'_f}{\mathcal{A}_f}\right| = \left|\frac{\mathcal{A}'_f}{\tilde{\mathcal{A}}_f}\right|. \tag{5.160}$$

By combining the CP asymmetry and decay rate information of the $B^0 \to J/\psi\rho^0$, $B_s^0 \to J/\psi\overline{K}^{*0}$ and $B_s^0 \to J/\psi\phi$ modes, these hadronic ratios can then be determined directly from the experimental data in a global χ^2 fit, as illustrated by the flow chart in Fig. 5.22. The underlying mechanism governing this fit would be analogous to the discussion preceding Eqs. (5.146) and (5.148): the CP asymmetries determine the penguin parameters a_f and θ_f, which in turn predict a value for the H_f observables. This prediction can be compared to the decay rate information, thereby providing an experimental determination of the amplitudes $|\mathcal{A}'_f/\mathcal{A}_f|$. By comparing the results on $|\mathcal{A}'_f/\mathcal{A}_f|$ with the predictions from factorisation, such an analysis would offer valuable insights into strong interactions as a by-product.

Even though the direct CP asymmetry measurements in the $B_s^0 \to J/\psi\overline{K}^{*0}$ decay are not yet available, the above strategy can already be implemented by extending the fits in Eqs. (5.136)–(5.138) to include branching ratio information from

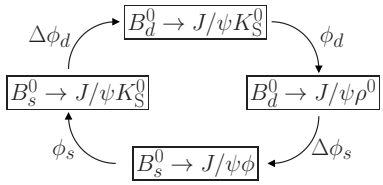

Figure 5.23: Interplay between the decays used to measure the B_q^0–$\bar{B}_q^0$ mixing phases and the channels needed to control the penguin contributions in the former measurements.

$B_s^0 \to J/\psi\,\phi$, $B^0 \to J/\psi\,\rho^0$ and $B_s^0 \to J/\psi\,\bar{K}^{*0}$. The results of this extended analysis are

$$\left|\frac{\mathcal{A}_0'}{\mathcal{A}_0}\right| = 1.099^{+0.089}_{-0.071}\,, \qquad a_0 = 0.05^{+0.14}_{-0.04}\,, \qquad \theta_0 = -\left(91^{+118}_{-158}\right)^\circ\,, \tag{5.161}$$

$$\left|\frac{\mathcal{A}_\parallel'}{\mathcal{A}_\parallel}\right| = 1.116^{+0.108}_{-0.083}\,, \qquad a_\parallel = 0.06^{+0.11}_{-0.06}\,, \qquad \theta_\parallel = -\left(84^{+142}_{-101}\right)^\circ\,, \tag{5.162}$$

$$\left|\frac{\mathcal{A}_\perp'}{\mathcal{A}_\perp}\right| = 1.24^{+0.18}_{-0.13}\,, \qquad a_\perp = 0.04^{+0.12}_{-0.04}\,, \qquad \theta_\perp = \left(29^{+189}_{-204}\right)^\circ\,. \tag{5.163}$$

With the current experimental precision, the additional branching ratio information does not have any impact on the determination of a_f and θ_f with respect to the fits to the $B^0 \to J/\psi\,\rho^0$ system only. The information is fully used to constrain the amplitude ratios $|\mathcal{A}_f'/\mathcal{A}_f|$, which were previously not included in the fit. From a mathematical point of view, the combined experimental precision on the H observables needs to be improved by at least an order of magnitude in order to observe any impact on a_f and θ_f. Numerical differences in $|\mathcal{A}_f'/\mathcal{A}_f|$ compared to Eqs. (5.146) and (5.148) arise due to the added information originating from the $B_s^0 \to J/\psi\,\bar{K}^{*0}$ system. This extended fit may be further refined by adding information from $B_s^0 \to J/\psi\,\rho^0$ to probe exchange and penguin annihilation topologies.

Interplay between ϕ_d and ϕ_s

Although the analyses of the J/ψ–pseudo-scalar and J/ψ–vector final states have so far been discussed separately, there is actually a powerful interplay between the high-precision determinations of ϕ_d and ϕ_s.

First of all, the external input introduces a crucial subtlety in the analyses of the above road map scenarios, and in particular the theoretically clean strategies relying on $B_s^0 \to J/\psi\,K_S^0$ and $B^0 \to J/\psi\,\rho^0$. As illustrated in Fig. 5.23, the value of ϕ_d is needed as an input for the analysis of $B^0 \to J/\psi\,\rho^0$, whereas ϕ_s is required for the analysis of $B^0 \to J/\psi\,K_S^0$. As such, the determinations of ϕ_d and ϕ_s, and

their associated penguin shifts, are related to each other. Consequently, it may be advantageous to perform a simultaneous analysis of the $B^0 \to J/\psi K_S^0$, $B_s^0 \to J/\psi K_S^0$, $B_s^0 \to J/\psi \phi$, $B^0 \to J/\psi \rho^0$ and $B_s^0 \to J/\psi \bar{K}^{*0}$ systems.

Secondly, we have reached a situation where ϕ_d and ϕ_s play equally significant roles in constraining beyond the Standard Model physics, and part of the sensitivity to new physics contributions now originates from the (cor)relation between both mixing phases, as illustrated in Fig. 5.24. It is therefore important to determine both ϕ_d and ϕ_s with the highest possible precision.

One illustration of this feature is provided by extensions of the Standard Model that go beyond *minimal flavour violation* (MFV)[l]. Let us specifically consider a model characterised by flavour-universal *CP*-violating NP phases [170, 171], i.e.

$$\phi_d^{\rm NP} = \phi_s^{\rm NP} \equiv \phi^{\rm NP} \,. \tag{5.164}$$

In this specific class of new physics, referred to as non-$\overline{\rm MFV}$ models, the relation

$$\phi_s = \phi_d + \left(\phi_s^{\rm SM} - \phi_d^{\rm SM}\right) \tag{5.165}$$

is obtained. Fig. 5.24 illustrates this relation for the current situation, as well as for the expected situation after the LHCb upgrade and Belle II programmes. As stated previously, the uncertainty on $\phi_d^{\rm SM} = 2\beta$ is fully governed by R_b. This also affects the band representing the relation in Eq. (5.165). It will be interesting to confront these considerations with experimental data in the next decade.

[l] An overview is given in Ref. [169]

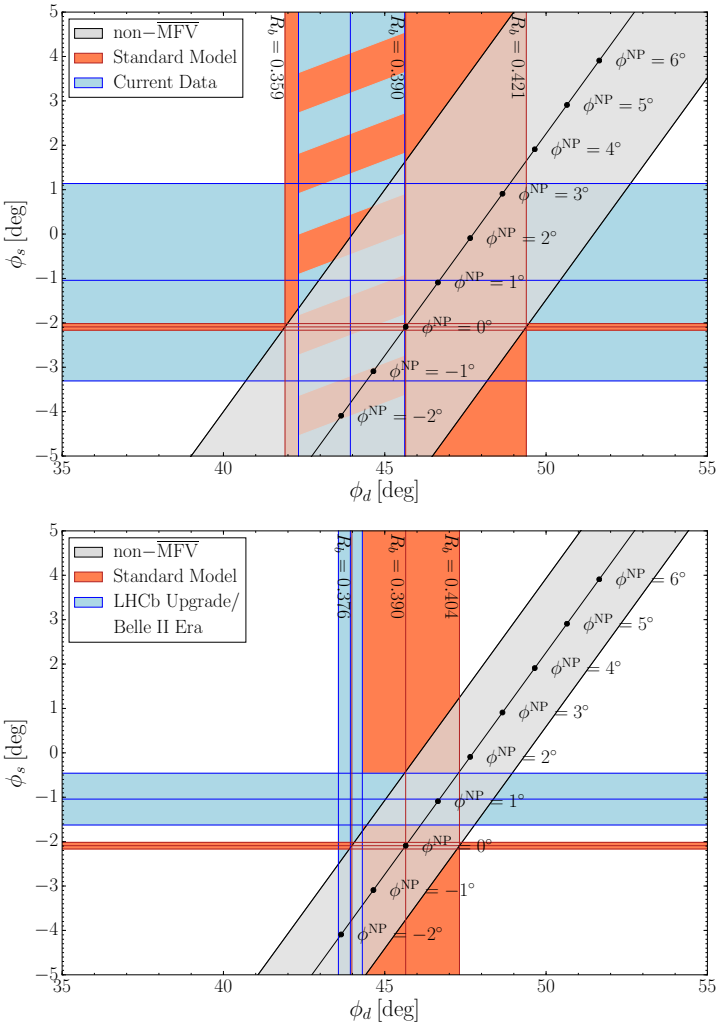

Figure 5.24: Illustration of the correlation between ϕ_d and ϕ_s for non-$\overline{\rm MFV}$ models with flavour-universal *CP*-violating NP phases characterised by Eq. (5.165). Depicted are the current experimental situation [Top] and an extrapolation to the LHCb upgrade and Belle II era [Bottom].

6 The LHCb Experiment

The $B_s^0 \to J/\psi K_S^0$ decay plays an important role in the $SU(3)_F$ symmetry based strategies to control the contributions from doubly Cabibbo-suppressed penguin topologies affecting the determination of the B^0–$\bar{B}^0$ mixing phase ϕ_d from the mixing-induced *CP* asymmetry in $B^0 \to J/\psi K_S^0$. Compared to the other decay modes that can be used for this task, experimental input on the $B_s^0 \to J/\psi K_S^0$ decay is, however, still limited. Besides the phenomenological analysis presented in Chapter 5, the author's research therefore also focused on the experimental study of the $B_s^0 \to J/\psi K_S^0$ mode, culminating in a first measurement of its *CP* asymmetries. This study was performed on behalf of the LHCb collaboration using proton–proton (pp) collision data collected by its detector between 2010 and 2012. Details on the analysis itself are discussed in Chapter 7, but the general requirements for performing *CP* violation measurement of B_s^0 meson decays and their consequences for the detector design are presented here. They specifically focus on the Large Hadron Collider (LHC) and the LHCb detector.

6.1 Analysis Requirements

The precision that can be achieved on *CP* asymmetry measurements in B_s^0 meson decays predominantly depends on the performance of both the accelerator creating the collision events and the detector used to measure them. It is therefore worthwhile to have a closer look at the design specifications that ultimately made the analysis of the $B_s^0 \to J/\psi K_S^0$ mode possible.

Regarding the accelerator performance, the most important quantity is the number of produced B_s^0 mesons. This is determined by two factors: the production cross-section and the integrated *luminosity*. The production cross-section depends, among others, on the type of particle being accelerated, i.e. electrons or protons, and grows with the centre-of-mass energy $\sqrt{s}$. As b quarks are produced in quark–antiquark pairs, $\sqrt{s}$ should at least exceed $2m_{B_s^0} = 10\,733.5\,\text{MeV}/c^2$ for the collision to be sufficiently energetic to produce a B_s^0 meson. This requirement on the centre-of-mass energy has important consequences for the accelerator design at

the B-factories, which operate just above the $B^0\bar{B}^0$ threshold, but no longer influences the design of TeV accelerators such as the Tevatron and the LHC. Beyond the $\sqrt{s} = 2m_{B_s^0}$ threshold, the B_s^0 mesons are no longer created at rest (in the centre-of-mass frame). The momentum they gain, either from excess energy in the collision or from boosting the centre-of-mass frame, increases the distance they travel before decaying, which improves the ability to distinguish the primary production vertex (PV) from the secondary decay vertex; a crucial aspect for time-dependent measurements. For this reason, the B-factories used e^+e^- accelerators with asymmetric beam energies in order to create a large enough boost for the produced B mesons to reach the inner tracking detector[a]. In general, centre-of-mass energies well above the threshold are thus preferred.

The second factor contributing to the B_s^0 yield, the luminosity, is a measure of the accelerator's performance and depends on the characteristics of the particle beams [172]. The accelerator design aims to maximise this quantity within the boundary conditions set by the used accelerator technology and overall project costs. For studying B meson decays, it is, however, also important to take into account the number of interactions per beam crossing event. With more PVs in a single event, assigning the correct PV to the B meson becomes more challenging.

Regarding the detector design, the two most important requirements are the ability to separate the B^0 and B_s^0 meson signals from one another using the invariant B mass, and the ability to resolve the rapid B_s^0-$\bar{B}_s^0$ oscillations in the B decay time distribution. These two points are further discussed in Section 6.3 below, but in essence lead to design specifications for the tracking system, which measures the track momenta, and the sub-detector surrounding the interaction region.

As far as the analysis of the $B_s^0 \to J/\psi K_S^0$ decay is concerned, additional detector components, besides the tracking system, are only required to identify the final state particles. The $B_s^0 \to J/\psi K_S^0$ decay is reconstructed in the $J/\psi \to \mu^+\mu^-$ and $K_S^0 \to \pi^+\pi^-$ final state, so in particular, these sub-detectors need to distinguish muons from other tracks. Due to the multitude of pions produced in the proton–proton collisions at the LHC, the event reconstruction at LHCb by default assumes that all tracks are good pion candidates. The muon identification on the other hand, requires two more detector components downstream of the tracking system. These are a heavy target to absorb all particles except the muons, and an active detector component to trigger on charged tracks that make it through the target.

A last essential ingredient for CP asymmetry measurements is the determination of the initial flavour of the B candidate, i.e. whether it contained a b or a $\bar{b}$ quark at production. Methods that accomplish this task are known as *flavour*

[a] The boost is, however, not large enough to resolve the rapid B_s^0–$\bar{B}_s^0$ oscillations

tagging, and discussed in Section 7.3. To maximise the tagging performance, it is desirable to add further particle identification systems to this minimal detector layout in order to also distinguish electrons and charged kaon tracks from the pions.

The final ingredients for *CP* asymmetry measurements are related to the production of the B mesons. On the one hand, it is essential to determine the initial flavour of the B candidate, i.e. whether it contained a b or a $\bar{b}$ quark at production, on an event-by-event basis. Methods that accomplish this task are known as *flavour tagging*, and discussed in Section 7.3. To maximise the tagging performance, it is desirable to add further particle identification systems to the above described minimal detector layout in order to also distinguish electrons and charged kaon tracks from the pions. On the other hand, also a good understanding of the B meson production asymmetries, i.e. the overall difference between the number of produced B and $\bar{B}$ mesons, is required. In proton–proton collision, such an asymmetry can potentially arise because the excess of up and down valence quarks in the collision remnants favour the hadronisation into B^+ and B^0 mesons over that into B^- and $\bar{B}^0$ mesons. As b quarks are produced in pairs, this production asymmetry must be compensated with an opposite effect in the hadronisation of the other b-hadrons. The production asymmetries are in principle dependent on the conditions under which the collisions are created. They can be determined using flavour specific b-hadron decay modes [173].

6.2 The Large Hadron Collider

6.2.1 Accelerator Complex

The first accelerator matching the above described requirements for the time-dependent study of B_s^0 meson decays was the Tevatron, located at Fermilab, near Chicago, United States. It produced $\sqrt{s} = 1.96\,\text{TeV}$ proton–antiproton collisions for the CDF and DØ experiments. As part of their B physics programme, the CDF and DØ experiments made the first exploration of the B_s^0 meson system, leading to the observation of B_s^0–$\bar{B}_s^0$ mixing by CDF in 2006 [175] and the first measurements of the B_s^0–$\bar{B}_s^0$ mixing phase ϕ_s from mixing-induced *CP* violation in the decay $B_s^0 \to J/\psi\,\phi$ [27, 28].

At present, the task of studying the B_s^0 meson system has been taken over by the Large Hadron Collider [176], located near Geneva, Switzerland. It is the final part of a complex chain of particle accelerators, illustrated in Fig. 6.1, constructed by the European Organisation for Nuclear Research (CERN) to study the properties of atoms and elementary particles. This chain is capable of accelerating protons (and ions) to multi-TeV energies. But before reaching these energies in the 26.7 km long

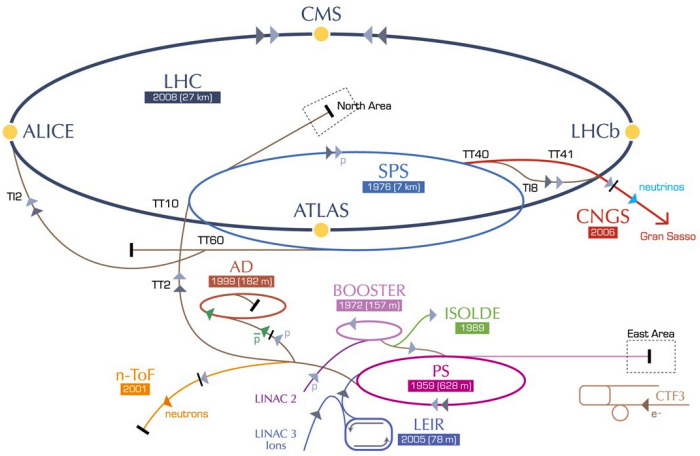

Figure 6.1: Schematic overview of the CERN accelerator complex [174]. Protons are pre-accelerated by the LINAC2, Booster, PS and SPS before being injected into the LHC.

LHC, protons go through an injection sequence involving several pre-accelerator stages.

Low energy protons are obtained by subjecting hydrogen gas to a strong electric field to strip away the electrons. The protons then enter the linear accelerator (LINAC2) where they are grouped together in *bunches*, to ensure optimal acceleration throughout the subsequent stages, and their energy is ramped up to 50 MeV. The bunches continue towards the 157 metre long (Proton Synchrotron) Booster, which accelerates them to 1.4 GeV before transferring them to the 628 metre long Proton Synchrotron (PS). At an energy of 25 GeV the proton bunches leave the PS for the 6.9 km long Super Proton Synchrotron (SPS), in which they reach the 450 GeV injection energy for the LHC. The complete injection sequence is executed twice to end up with two beams circulating the LHC in opposite directions. The two beams are then accelerated simultaneously to the desired energy. In 2010 and 2011 the beams had a maximum energy of 3.5 TeV each, which was further increased to 4 TeV in 2012. Throughout this first run period, the bunches were spaced 50 ns apart. Now that the first *long shutdown* is completed successfully, the LHC is scheduled to ramp up the beam energies to 6.5 TeV in 2015 and reduce the bunch spacing to 25 ns.

The two proton beams intersect each other at four interaction points around the ring, where the major LHC detectors ATLAS, ALICE, CMS and LHCb are located. The purpose of these four experiments is diverse and complementary to one another. ATLAS [177] and CMS [178] are two general purpose detectors. Their main

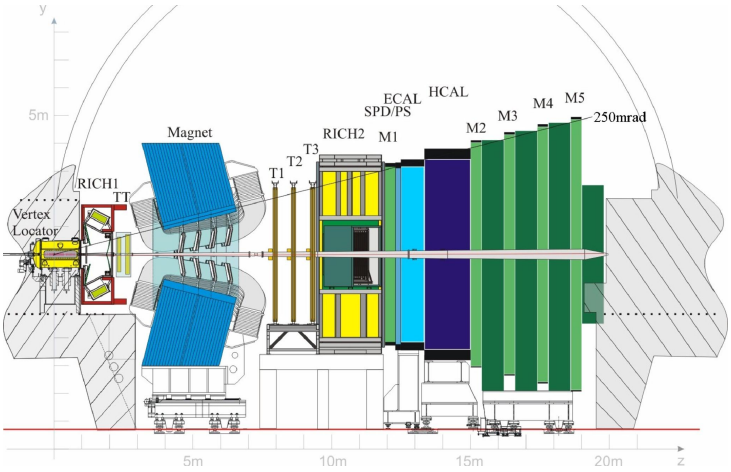

Figure 6.2: Schematic overview of the LHCb detector [181].

objectives are the now successfully completed search for a Higgs boson [11, 12] and the subsequent study of its properties, and the search for new particles associated with beyond the Standard Model physics. The ALICE experiment [179] focuses on measuring the properties of heavy ion collisions and the Quark Gluon Plasma. The LHCb experiment [180] is dedicated to the study of b and c-hadron decays with a focus on finding indirect signs of beyond the Standard Model physics through high precision measurements of rare decays and CP violating processes.

6.2.2 The LHCb Detector

Detector Components

Contrary to the other three main LHC experiments, the LHCb detector is designed as a single-arm spectrometer, and the interaction point is located at the edge of the underground cavern housing the detector. This setup is motivated by the feature that at the LHC b-hadrons are predominantly produced at large absolute pseudo-rapidity $|\eta|$, where $\eta \equiv -\log(\tan(\theta/2))$ is defined in terms of the angle θ between the particle track and the beam axis. Exploiting this effect, the LHCb detector therefore only covers the pseudo-rapidity range $2 < \eta < 5$[b]. Said differently, it has an angular coverage from approximately 15 mrad to 300 (250) mrad in the bending (non-bending) plane. The detector reuses the cavern originally excavated for the Delphi experiment at the Large Electron–Positron Collider (LEP). This limits

[b]Disregarding financial constraints, the LHCb detector would ideally also have a second arm covering the pseudo-rapidity range $-5 < \eta < -2$

the space available for the different sub-detectors, and in particular influences the design of the dipole magnet, as further discussed below.

The detector, whose layout is presented in Fig. 6.2, contains a high precision tracking system and various components for particle identification. The tracking system serves to reconstruct the trajectories of all charged particles, and determine the momenta from these tracks. It consists of a silicon-strip *vertex detector* surrounding the collision point (VELO), an all-silicon tracking station (TT) upstream of a dipole magnet, three further tracking stations (T1, T2, T3) downstream of the magnet, and five muon stations (M1, ..., M5) located at the far end of the cavern. The inner parts of the downstream tracking stations, which have to deal with a significantly higher occupancy than the outer regions, consist of silicon detectors (IT), whereas for the outer region straw tube detectors (OT) are employed. Charged particles require a minimum momentum of 1.5 GeV/c to traverse all four tracking stations [182]. The sub-detectors dedicated to particle identification are: two ring-imaging Cherenkov detectors (RICH), located respectively up- and downstream of the magnet, an electromagnetic (ECAL) and a hadronic (HCAL) calorimeter, and the muon stations of the tracking system. The RICH detectors mainly aim to distinguish kaons from pions by measuring the Cherenkov radiation left by the particles when travelling through these sub-detectors. The upstream RICH detector covers the low momentum range $2 < p < 60\,\text{GeV}/c$, whereas the downstream RICH detector covers the high momentum range $15 < p < 100\,\text{GeV}/c$. Finally, in between RICH2 and the ECAL an additional scintillating pad detector (SPD) and preshower (PS) detector are installed, which improve the performance of the ECAL and in particular the separation power between electrons and photons.

Trigger

In 2011 and 2012, the frequency for inelastic pp collisions at the LHCb interaction point was about 11 MHz [183][c]. The bandwidth and data storage allocated to LHCb, however, limits the output of the detector to 3 kHz. Consequently, real-time data selection is needed to identify the b and c-hadron decays of interest and discard the less interesting "known physics" background.

The *trigger* responsible for this challenging task consists of a hardware level (L0) and a two-stage software level (HLT). The main purpose of the L0 trigger is to reduced the output rate to 1.1 MHz, in order to give the HLT stages sufficient processing time to perform a (partial) event reconstruction. Because of the heavy mass of the b and c-hadrons, the momentum (energy) of their decay products tends to have a large component p_T (E_T) transverse to the proton beams. The L0 trigger therefore searches for muons with high p_T, or hadrons, electrons and photons

[c]Not all possible bunch slots of the LHC are filled with protons, and with an average event multiplicity of 1.4 at the LHCb interaction point, not all bunch crossings result in an actual collision.

with high E_T. These selection criteria are implemented directly on the read-out boards of the muon stations and calorimeters. The HLT trigger, on the other hand, is more flexible and can easily be adjusted based on the conditions provided by the LHC and the analysis demands of the collaboration. Among other things, it performs (partial) track and vertex reconstruction to identify displaced tracks associated with the decay of the b and c-hadrons.

6.3 Simplified Detector Design

6.3.1 Mass Separation

The B^0 and B_s^0 meson resonances are separated by a mass difference $m_{B_s^0} - m_{B^0} = 87.35 \pm 0.23\,\mathrm{MeV}/c^2$ [64]. To clearly distinguish the two mass peaks in the data and thus limit their overlap, which is especially important for an accurate determination of the $B_s^0 \to J/\psi K_S^0$ event yield in the presence of the more prominent $B^0 \to J/\psi K_S^0$ component, the mass resolution should be significantly smaller than this difference. In order to translate this statement into a design specification for the LHCb detector, let us assume that sufficient separation is achieved when the resolution is six times smaller than the mass difference, i.e. $\sigma_m = 15\,\mathrm{MeV}/c^2$.

As is derived below, the two-particle invariant mass is determined by the momenta of the two daughter particles and the opening angle between their tracks. The requirement on the mass resolution can thus be translated into a design specification for the momentum resolution of charged tracks. In turn, the momentum resolution is determined by the strength of the magnetic field and spatial resolution of the tracking system.

Momentum Resolution

Without loss of generality, the coordinate system for the calculation of the two-particle invariant mass can be chosen such that the momentum vector of the first daughter particle defines the positive x-axis and together with the momentum vector of the second daughter particle it spans the x–z plane. The invariant mass m of the two-particle system is then obtained by imposing energy and momentum conservation, and thus solving the system[d]

$$\begin{pmatrix} \sqrt{p_x^2 + p_z^2 + m^2} \\ p_x \\ 0 \\ p_z \end{pmatrix} = \begin{pmatrix} \sqrt{p_a^2 + m_a^2} \\ p_a \\ 0 \\ 0 \end{pmatrix} + \begin{pmatrix} \sqrt{p_b^2 + m_b^2} \\ p_b \cos\theta \\ 0 \\ p_b \sin\theta \end{pmatrix}, \tag{6.1}$$

[d] These equations adopt natural units, in which $c = 1$.

where θ is the opening angle between the two tracks. This leads to the familiar expression

$$m = \sqrt{m_a^2 + m_b^2 - 2p_a p_b \cos\theta + 2\sqrt{m_a^2 + p_a^2}\sqrt{m_b^2 + p_b^2}}\,. \tag{6.2}$$

Starting from the $\mu^+\mu^-\pi^+\pi^-$ final state, Eqs. (6.1) and (6.2) can be used to calculate the momenta and opening angles of the complete $B_s^0 \to J/\psi K_S^0$ decay chain. Let us illustrate this for a scenario in which the momenta of the final state particles are given by $p_{\mu^+} = 25\,\text{GeV}/c$, $p_{\mu^-} = 15\,\text{GeV}/c$, $p_{\pi^+} = 13\,\text{GeV}/c$ and $p_{\pi^-} = 7\,\text{GeV}/c$, which are representative values encountered in the $B_s^0 \to J/\psi K_S^0$ decay. This leads to opening angles $\theta_{\mu^+\mu^-} = 9.15°$ between the two muons, $\theta_{\pi^+\pi^-} = 2.42°$ between the two pions, and $\theta_{J/\psi K_S^0} = 7.51°$ between the reconstructed J/ψ and K_S^0 intermediate states. The reconstructed J/ψ, K_S^0 and B_s^0 momenta are $p_{J/\psi} = 39.881\,\text{GeV}/c$, $p_{K_S^0} = 19.996\,\text{GeV}/c$ and $p_{B_s^0} = 59.762\,\text{GeV}/c$, respectively.

Eq. (6.2) shows that the mass resolution σ_m depends on the momentum resolution and on the precision with which the opening angle θ can be measured. Assuming for simplicity that $\sigma_{p_a}/p_a = \sigma_{p_b}/p_b = \sigma_p/p$, the expression for σ_m leads to a relative momentum uncertainty

$$\left(\frac{\sigma_p}{p}\right) = \sqrt{\frac{\sigma_m^2 - (\sigma_\theta \partial_\theta m)^2}{\left(p_a \partial_{p_a} m\right)^2 + \left(p_b \partial_{p_b} m\right)^2}}\,, \tag{6.3}$$

where

$$\partial_\theta m = \frac{1}{m} p_a p_b \sin\theta\,, \qquad \partial_{p_a} m = \frac{1}{m}\left(p_a \frac{\sqrt{m_b^2 + p_b^2}}{\sqrt{m_a^2 + p_a^2}} - p_b \cos\theta\right), \tag{6.4}$$

and similar for $\partial_{p_b} m$.

As a final input for the design specification on σ_p/p, an estimate of σ_θ is needed. For the majority of charged tracks[e] the opening angle is determined with the track segments reconstructed inside the vertex detector. The VELO is designed to resolve the rapid B_s^0–$\bar{B}_s^0$ oscillations, as discussed below, and achieves a hit resolution of about 20μm [182], much better than what is actually needed here. Given the one metre length of the VELO, this leads to a relative uncertainty on the opening angle of 2×10^{-5}. The impact of the opening angle on the mass resolution, and by extension the momentum resolution, is thus negligible.

For the example $B_s^0 \to J/\psi K_S^0$ decay given above, the relation (6.3) translates the desired mass resolution $\sigma_m = 15\,\text{MeV}/c^2$ into a specification for the relative uncertainty on the momentum of the muon tracks of $\sigma_p/p = 0.7\%$, with similar

[e] An exception are, for example, the pions originating from K_S^0 mesons decaying outside the vertex detector.

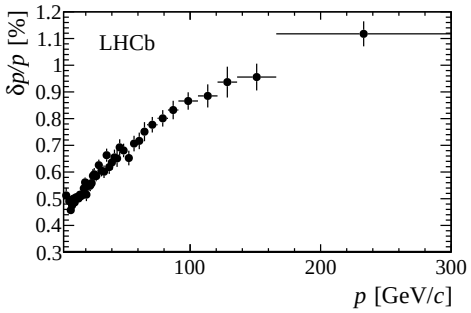

Figure 6.3: Relative momentum resolution σ_p/p for charged tracks as a function of the total momentum p, obtained from $J/\psi \to \mu^+\mu^-$ decays. Figure taken from Ref. [182].

results for the pion momenta. In comparison, the measured momentum resolution for 20 GeV/c tracks at LHCb is 0.5% [182], which rises to 0.8% for 100 GeV/c tracks. At high momenta, the resolution is an approximately linear function of p, where the measured dependence is shown in Fig. 6.3. The resolution at low momenta is dominated by effects due to multiple scattering in the detector material.

Magnetic Field

Charged particles are deflected from their original trajectory when traversing the magnetic field generated by the dipole magnet. The overall change in direction, which is inversely proportional to the momentum of the track, is related to the bending power of the magnet as

$$\Delta\vec{p} = |q| \int \mathrm{d}\vec{l} \times \vec{B}, \tag{6.5}$$

where q is the charge of the particle. Because the LHCb magnet generates a highly non-uniform magnetic field along the particle's trajectory, as illustrated in the left panel of Fig. 6.4, it is convenient to approximate this change in direction with a single momentum kick, as illustrated in the right panel of Fig. 6.4. The quantity $\Delta\vec{p}$ can then be related to the difference $\Delta t_\mathrm{T} \equiv t_{\mathrm{T}_f} - t_{\mathrm{T}_i}$ between the slopes of the track segments reconstructed up- and downstream of the magnet, that is

$$\Delta\vec{p} = p\,\Delta t_\mathrm{T}\,. \tag{6.6}$$

Here $t_\mathrm{T} \equiv l_\mathrm{T}/l_z$, with l_T the displacement perpendicular to the magnetic field between the hits in first and last measurement plane of the tracking detectors, which are separated by a longitudinal distance l_z, as illustrated in the right panel of

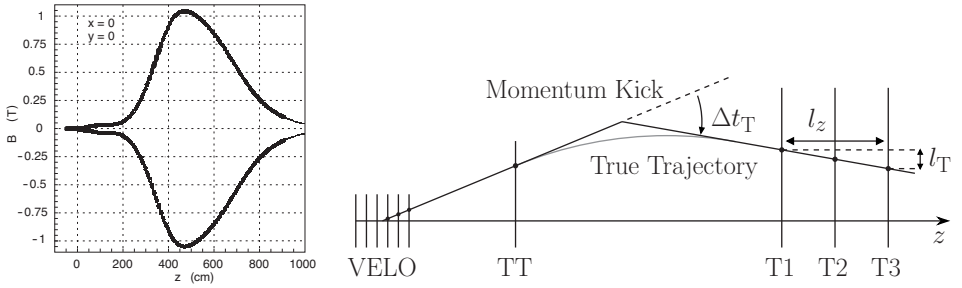

Figure 6.4: Left: Field strength of the LHCb magnet along the beam direction. Figure taken from Ref. [180]. Right: Illustration of the momentum kick method.

Fig. 6.4. For the majority of tracks[e], the slope t_{T_i} is determined from the orientation of the VELO track segment. The impact of its uncertainty on the momentum determination is therefore negligible. The additional information provided by the TT station helps to reduce the effects due to multiple scattering, which is only important for low momentum tracks. The TT station is, of course, indispensable for the reconstruction and momentum determination of charged tracks originating from unstable particles decaying outside the vertex detector, like long-lived or high momentum K^0_{S} mesons.

The three tracking stations downstream of the magnet provide sufficient information to construct a track segment, and thus to obtain an estimate of its slope t_{T_f}. By matching this segment to one of the trajectories extrapolated from the VELO track segments, spurious hits and ghost tracks in the tracking stations can be greatly reduced, thus improving the overall tracking performance. The slope of the track segment is calculated by dividing the measured transverse displacement l_{T} between the hits in the first and third station by the longitudinal separation $l_z \approx 2\,\mathrm{m}$ of the two hit planes, which, for the purpose here, can be assumed to be exactly known.

Summarising the above information, the relative momentum uncertainty can thus be related to the spatial resolution of the tracking stations as

$$\frac{\sigma_p}{p} = \frac{\sigma_{\Delta t_{\mathrm{T}}}}{\Delta t_{\mathrm{T}}} \approx \frac{\sigma_{t_{\mathrm{T}_f}}}{t_{\mathrm{T}_f}} \approx \frac{\sigma_{l_{\mathrm{T}}}}{l_{\mathrm{T}}}\,. \tag{6.7}$$

To obtain a relative momentum uncertainty σ_p/p, a minimal transverse displacement

$$l_{\mathrm{T}} = \frac{\sigma_{l_{\mathrm{T}}}}{\sigma_p/p} \tag{6.8}$$

is thus required, which in turn specifies the needed momentum kick $p\Delta t_{\mathrm{T}}$ and thus also the bending power of the magnet.

The outer tracker achieves a hit resolution of 205μm [182]. To reach the 0.7% relative momentum uncertainty on the 25 GeV/c muon track of our example $B_s^0 \to J/\psi K_S^0$ decay, a displacement $l_T = 29.8$ mm, corresponding to a momentum kick of 372 MeV/c, would be required. The total bending power of the magnet then needs to be at least $\int \mathrm{d}\vec{l} \times \vec{B} = 1.24$ T m. If, on the other hand, we want to reach a 0.8% relative momentum uncertainty on a 100 GeV/c track, i.e. the current LHCb performance, a displacement $l_T = 25.6$ mm, corresponding to a momentum kick of 1.28 GeV/c, would be required. The total bending power of the magnet then needs to be at least $\int \mathrm{d}\vec{l} \times \vec{B} = 4.27$ T m. In comparison, the total bending power of the LHCb dipole magnet is about 4 T m for tracks of 10 metre in length.

The design of the magnet has to accommodate contrasting needs. The field strength inside the VELO and RICH detectors needs to be as low as possible to avoid deteriorating their performance, while it needs to be as high as possible in between the tracking stations to achieve the required momentum resolution. In addition, the magnet needs to fit inside the Delphi cavern, while still being outside the angular acceptance of the downstream detector components. This explains the saddle shape of the magnet coils and the resulting non-uniform magnetic field along the particle's trajectory, shown in Fig. 6.4.

6.3.2 Decay Time Oscillations

Flight Distance

The decay time τ of a long-lived particle is related to the flight distance Δ between its production and decay vertex as

$$c\tau = \frac{m}{p}\Delta\,. \tag{6.9}$$

The uncertainty on the flight distance is determined by the spatial resolution, and in particular its longitudinal component, with which both vertices can be reconstructed by the vertex detector. As illustrated in Fig. 6.5, this in turn depends on the number of tracks making up the vertex. It implies that for B meson decays σ_Δ is dominated by the resolution on the decay vertex, which, contrary to the PV, is made from only a handful of tracks.

To resolve the rapid B_s^0–$\bar{B}_s^0$ oscillations, parametrised by the mass difference $\Delta m_s = 17.757 \pm 0.021\,\mathrm{ps}^{-1}$ [121] between the two B_s^0 eigenstates, a decay time resolution of about $\sigma_\tau \approx 1/\Delta m_s = 56$ fs is needed. Based on Eq. (6.9), this requirement leads to a design specification for the decay vertex resolution σ_Δ, which therefore must be smaller than

$$\sigma_\Delta = p\sqrt{\left(\frac{c\sigma_\tau}{m}\right)^2 - \left(\frac{\Delta\sigma_p}{p^2}\right)^2}\,. \tag{6.10}$$

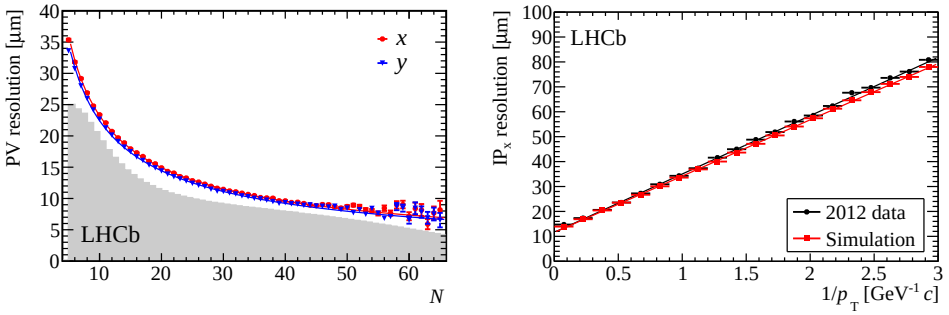

Figure 6.5: Left: The transverse PV resolutions as a function of track multiplicity, for events containing only one reconstructed primary vertex. Right: The impact parameter resolution in the x direction as a function of $1/p_{\mathrm{T}}$. Figures taken from Ref. [180].

Again taking the above introduced example $B_s^0 \to J/\psi K_S^0$ decay as a guideline, and using the specifications for the momentum resolution σ_p from Section 6.3.1, this formula leads to a required decay vertex resolution of 184 μm.

A direct comparison with the actual performance of the VELO is difficult, as no measurements of the decay vertex resolution are available. Our estimate can, however, be put in perspective using the PV resolutions as a guideline for the decay vertex resolution. The VELO has a PV resolution of 13 μm in the transverse direction, and 71 μm in the longitudinal direction, for PVs containing 25 tracks [180]. This rises to 35 μm in the transverse direction for PVs containing only 5 tracks, with a similar behaviour expected for the longitudinal component. The dependence on the track multiplicity is shown in Fig. 6.5.

As an alternative point of comparison between the simplified derivation given above and the actual LHCb performance, also the effective decay time resolutions can be used. The time-dependent analyses of $B_s^0 \to J/\psi K^+K^-$ [184] and $B_s^0 \to J/\psi \pi^+\pi^-$ [29] achieve an effective decay time resolution of 45 fs and 40.3 fs, respectively, thus outperforming the above set target of 56 fs.

Impact Parameter

A final observable that forms an important measure of the performance of the vertex detector is the *impact parameter* (IP). The IP of a track is defined as the smallest distance between the track and the PV. Decay products of long-lived particles tend to have larger IP than those of particles produced in the primary interaction. The IP and its χ^2 therefore form important selection variables to reduce contamination from prompt background in the data. Consequently, the IP resolution is a crucial

variable for the optimisation of the detector design. The vertex detector achieves an IP resolution of $(15+29/p_{\mathrm{T}})\,\mu$m, also illustrated in Fig. 6.5, where p_{T} is the component of the particle's momentum (in GeV/c) transverse to the proton beams. The linear dependence on $1/p_{\mathrm{T}}$ is a consequence of multiple scattering and the VELO's geometry.

6.3.3 Conclusion

For the momentum, mass and decay time resolution, which are crucial ingredients for the analysis of the $B_s^0 \to J/\psi\, K_S^0$ decay, the LHCb detector exceeds the above derived requirements. The reason for this is twofold. First of all, the LHCb physics programme also targets decay modes not in the $B \to J/\psi\, X$ family. The analysis requirements for these modes put different or additional constraints on the detector design. Secondly, during the initial designing stage of the detector the value of the B_s^0–$\bar{B}_s^0$ oscillation frequency Δm_s was still unknown. As time-dependent analyses of B_s^0 meson decays form a main objective of the LHCb experiment, the detector needed to be able to resolve the oscillations for a large range of possible Δm_s values, and thus needed a decay time resolution better than the 56 fs specified above.

The $B \to J/\psi\, X$ analyses exploit the excellent performance of the LHCb detector, resulting from going beyond the minimal design specifications, to improve the event selection and increase the signal purity of their analysed data samples. As a result, LHCb can match the sensitivity of the B-factories in decay modes with charged final states like $B^0 \to J/\psi\, K_S^0$ [74], and outperforms all other detectors at hadron colliders in the study of high profile B meson decays [121].

7 Experimental Analysis of $B_s^0 \to J/\psi K_S^0$

This Chapter summarises the experimental study of the $B_s^0 \to J/\psi K_S^0$ decay, performed by the author on behalf of the LHCb collaboration, and using the data collected by its detector during the first physics run of the LHC. It specifically focuses on the last of three analysis steps, which was done in close collaboration with the LHCb group at the TU Dortmund, and culminated in a first measurement of the *CP* asymmetry parameters. As part of the validation of the likelihood fit used to measure the *CP* observables, two independent implementations of the likelihood were made: one by the author, and one by the group at the TU Dortmund. During the internal review of the analysis by the LHCb collaboration one of the two fitters was chosen to provide the official LHCb results published in Ref. [46]. This happens to be the fitter made by the group at the TU Dortmund. This Chapter, however, presents the likelihood implementation made by the author, which is referred to as *Method I*. Only for the discussion of the final results in Section 7.7 do we jump to the official LHCb results, referred to as *Method II*.

7.1 Analysis Overview

Step-by-Step Approach

This study of the $B_s^0 \to J/\psi K_S^0$ decay at the LHCb experiment closely follows the outline sketched in Section 4.4: it consists of three consecutive steps, performed on increasingly larger data samples, each adding a new layer of complexity to the analysis. As such, these three analyses share a common framework, with each new step superseding the previous. Therefore, only the final step is presented in detail below, while the other two are briefly summarised here.

Comparing the decay amplitudes for the $B^0 \to J/\psi K_S^0$ and $B_s^0 \to J/\psi K_S^0$ channels in Eqs. (5.19) and (5.24), respectively, shows that their ratio of branching fractions is proportional to the factor $\epsilon = 0.0536$ defined in Eq. (5.22). In turn, the ratio R of event yields is related to the ratio of time-integrated branching fractions as

$$\frac{\mathcal{B}(B_s \to J/\psi K_S^0)}{\mathcal{B}(B_d \to J/\psi K_S^0)} \equiv R \times f_{\text{sel}} \times \frac{f_d}{f_s}\,, \tag{7.1}$$

where f_{sel} corrects for differences in selection efficiency between the $B^0 \to J/\psi K_S^0$ and $B_s^0 \to J/\psi K_S^0$ modes, and $f_s/f_d = 0.259 \pm 0.015$ [159, 160] is the ratio of the B_s^0 to B^0 meson production fractions, which depends on the centre-of-mass energy at which the events are produced, and the type of particle being collided. Taking $f_{\text{sel}} = 1$ and using the above estimate for the ratio of branching fractions then leads to an estimate for the ratio of event yields of about 0.014. Thus in view of the expected low yields on the $B_s^0 \to J/\psi K_S^0$ signal, the main challenge in the initial experimental study of the $B_s^0 \to J/\psi K_S^0$ decay is the event selection. The first stage is therefore a time-integrated analysis, and only models the $J/\psi K_S^0$ invariant mass spectrum in order to identify the individual contributions from the combinatoric background, and the $B^0 \to J/\psi K_S^0$ and $B_s^0 \to J/\psi K_S^0$ signal components. The principal objective in this first stage is a measurement of the time-integrated ratio of branching fractions.

Following this strategy, the $B_s^0 \to J/\psi K_S^0$ decay was first observed by the CDF collaboration [43] in early 2011. Based on an event yield of 64 ± 14 $B_s^0 \to J/\psi K_S^0$ decays they found

$$\frac{\mathcal{B}(B_s \to J/\psi K_S^0)}{\mathcal{B}(B_d \to J/\psi K_S^0)} = 0.041 \pm 0.007\,(\text{stat.}) \pm 0.004\,(\text{syst.}) \pm 0.005\,(f_s/f_d)\,, \tag{7.2}$$

where the first uncertainty is statistical, the second due to systematic effects, and the last due to the uncertainty on the ratio f_s/f_d in proton–antiproton collisions at $\sqrt{s} = 1.96$ TeV.

At LHCb, the analysis was performed on a data sample corresponding to an integrated luminosity of $0.41\,\text{fb}^{-1}$ of proton–proton (pp) collisions, recorded at a centre-of-mass energy of $\sqrt{s} = 7$ TeV in 2010 and the first half of 2011. The result, based on an event yield of 116 ± 14 $B_s^0 \to J/\psi K_S^0$ decays, is [44]

$$\frac{\mathcal{B}(B_s \to J/\psi K_S^0)}{\mathcal{B}(B_d \to J/\psi K_S^0)} = 0.0420 \pm 0.0049\,(\text{stat.}) \pm 0.0023\,(\text{syst.}) \pm 0.0033\,(f_s/f_d)\,. \tag{7.3}$$

In the second step, a time-dependent analysis is performed on a data sample corresponding to an integrated luminosity of $1.0\,\text{fb}^{-1}$, recorded at a centre-of-mass energy of 7 TeV in 2011. In addition to the $J/\psi K_S^0$ invariant mass spectrum, also the B decay time distribution of the selected candidates is studied. A full description of the signal and background decay time distributions also requires a parametrisation for the decay time resolution and acceptance effects, caused by the event reconstruction and selection. The principal objective in this second stage is a determination of the $B_s^0 \to J/\psi K_S^0$ effective lifetime, defined in Eq. (4.72). As discussed in Section 4.2.3, it is obtained by fitting a single exponential function to the decay time distribution of the $B_s^0 \to J/\psi K_S^0$ candidates. The result, based on an event yield

of 273 ± 19 $B_s^0 \to J/\psi K_S^0$ decays, is [45]

$$\tau^{\text{eff}}_{J/\psi K_S^0} = 1.75 \pm 0.12\,(\text{stat.}) \pm 0.07\,(\text{syst.})\,\text{ps}\,. \tag{7.4}$$

Given the values for Γ_s and $\Delta\Gamma_s$ in Table 4.1, this corresponds to a value

$$\mathcal{A}_{\Delta\Gamma}(B_s^0 \to J/\psi K_S^0) = 2.1 \pm 1.6 \tag{7.5}$$

for the mass eigenstate rate asymmetry in $B_s^0 \to J/\psi K_S^0$. Simultaneously, the measurement of the ratio of branching fractions is updated to

$$\frac{\mathcal{B}(B_s \to J/\psi K_S^0)}{\mathcal{B}(B_d \to J/\psi K_S^0)} = 0.0439 \pm 0.0032\,(\text{stat.}) \pm 0.0015\,(\text{syst.}) \pm 0.0034\,(f_s/f_d)\,. \tag{7.6}$$

In the final stage, a tagged, time-dependent analysis is performed on a data sample corresponding to an integrated luminosity of $3.0\,\text{fb}^{-1}$, recorded at centre-of-mass energies of 7 and 8 TeV in 2011 and 2012, respectively. The principal objective at this stage is the first determination of the $B_s^0 \to J/\psi K_S^0$ *CP* asymmetry parameters [46]. For such a measurement it is essential to determine the initial flavour of the B candidate, i.e. whether it contained a b or a $\bar{b}$ quark at production. Compared to the previous stage, the event selection is further refined and the analysis is extended with information from various tagging algorithms. As a byproduct of the likelihood fit for the *CP* asymmetry parameters, also the $B_s^0 \to J/\psi K_S^0$ and $B^0 \to J/\psi K_S^0$ event yields are determined, which thus allows us to again measure the ratio of branching fractions. The evolution of the ratio of branching fraction measurements is illustrated in Fig. 7.1.

The Analysis in a Nutshell

The analysis presented in this chapter closely follows Ref. [46]. It consists of two parts. The first part involves the selection of $B \to J/\psi K_S^0$ candidates, where B stands for both the B^0 and B_s^0 mesons, and charge conjugation of the decay descriptor is implied. It is described in Section 7.2 and consists of three steps: the event reconstruction and initial selection, and a two-stage multivariate selection consisting of artificial neural network classifiers [185].

The second part consists of a likelihood fit, performed on the data selected in the first step. The probability density function (PDF) that is used in the construction of the likelihood describes a combinatoric background component, the $B_s^0 \to J/\psi K_S^0$ signal and the more prominent $B^0 \to J/\psi K_S^0$ decay mode. The inclusion of the latter component in the fit model provides experimental advantages that can be used to improve the modelling of the $B_s^0 \to J/\psi K_S^0$ component in the data. Further details on the flavour tagging and the likelihood fit are summarised

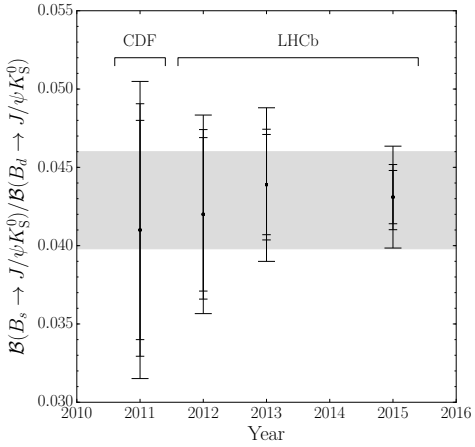

Figure 7.1: Visual comparison between the different measurements of the ratio of $B_s^0 \to J/\psi K_S^0$ to $B^0 \to J/\psi K_S^0$ branching fractions. The inner uncertainty bars represent the statistical uncertainty, the middle ones the sum of the statistical and systematic uncertainties, and the other ones the total uncertainty. The grey band illustrates the world average of the best CDF and LHCb measurements.

in Sections 7.3 and 7.4, respectively. The main parameters of interest for the likelihood fit are the three $B_s^0 \to J/\psi K_S^0$ *CP* asymmetries $\mathcal{A}_{\Delta\Gamma}$, $\mathcal{A}_{CP}^{\text{dir}}$ and $\mathcal{A}_{CP}^{\text{mix}}$, and the $B^0 \to J/\psi K_S^0$ and $B_s^0 \to J/\psi K_S^0$ event yields, whose ratio gives the parameter R used in Eq. (7.1).

As a by-product of fully modelling the $B^0 \to J/\psi K_S^0$ component in the PDF, also the direct and mixing-induced *CP* asymmetries of the $B^0 \to J/\psi K_S^0$ channel are obtained from the likelihood fit. The tight event selection necessary to isolate the $B_s^0 \to J/\psi K_S^0$ candidates, however, limits the precision that can be achieved on these two *CP* observables. Dedicated and more precise measurements of the $B^0 \to J/\psi K_S^0$ *CP* observables are therefore the subject of a separate analysis [74].

7.2 Event Selection

Candidate $B \to J/\psi K_S^0$ decays are reconstructed for the final states $J/\psi \to \mu^+\mu^-$ and $K_S^0 \to \pi^+\pi^-$. With $\mathcal{B}(J/\psi \to \mu^+\mu^-) = (5.961 \pm 0.033)\%$ [64] and $\mathcal{B}(K_S^0 \to \pi^+\pi^-) = (69.20 \pm 0.05)\%$ [64], this implies that only $(4.125 \pm 0.023)\%$ of the produced $B \to J/\psi K_S^0$ events can potentially be selected. But compared to the other J/ψ and K_S^0 decay modes, this specific final state has the highest reconstruction and selection efficiencies, the least amount of background, and leads to the smallest mass and decay time resolution. As such, it is the dominant experimental probe to study

the $B \to J/\psi K_S^0$ decays.

7.2.1 Initial Selection

Trigger

The online event selection is performed by a trigger, which consists of a hardware level, based on information from the calorimeter and muon systems, followed by a two-stage software level, which applies a full event reconstruction. Candidate $B \to J/\psi K_S^0$ decays are triggered on the $J/\psi \to \mu^+\mu^-$ signal. For the events used in this analysis, the hardware trigger therefore only selects 7 (8) TeV pp collisions which have at least one muon with a transverse momentum $p_T > 1.48\,(1.76)\,\text{GeV}/c$ or two muons with $\sqrt{p_T(\mu_1)p_T(\mu_2)} > 1.3\,(1.6)\,\text{GeV}/c$. In the first stage of the software trigger, events are required to have either two oppositely charged muons with combined mass above 2.7 GeV/c^2, or at least one muon or one high-p_T track ($p_T > 1.8$ GeV/c) with an impact parameter larger than 100 μm with respect to all pp interaction vertices (PVs). In the second stage, the tracks of two or more of the final-state particles are required to form a vertex that is significantly displaced from the PVs, and only events containing $J/\psi \to \mu^+\mu^-$ candidates are retained.

Reconstruction

Candidate $B \to J/\psi K_S^0$ decays are obtained by testing all $\mu^+\mu^-\pi^+\pi^-$ track combinations in the pp collision against a set of selection criteria, which include forming the intermediate J/ψ and K_S^0 states. The two muon tracks of the candidate J/ψ decay are required to form a good quality vertex and have an invariant mass in the range $[3030, 3150]\,\text{MeV}/c^2$. This interval corresponds to about eight times the $\mu^+\mu^-$ mass resolution at the J/ψ mass and covers part of the J/ψ radiative tail.

Decays of $K_S^0 \to \pi^+\pi^-$ are reconstructed in two different categories: the first involving K_S^0 mesons that decay early enough for the daughter pions to be reconstructed in the vertex detector; and the second containing K_S^0 that decay later such that track segments of the pions cannot be formed in the vertex detector. These categories are referred to as *long* and *downstream*, respectively. The long category has better mass, momentum and vertex resolution than the downstream category. The larger flight distance of the candidates in the downstream category is mainly caused by a longer K_S^0 lifetime, but can also be due to a larger momentum of the K_S^0 meson. This difference in momentum distribution with the long category will affect the trigger response, and in combination with the above listed resolution effects result in a different signal-to-background composition, with the long K_S^0 being the purest of the two. The long and downstream categories are therefore treated separately throughout the analysis.

The two pion tracks of the long (downstream) K_S^0 candidates are required to form a good quality vertex and their invariant mass must be within 35 (64) MeV/c^2 of the known K_S^0 mass [64]. To remove contamination from $\Lambda \to p\pi^-$ decays, the reconstructed mass of the long (downstream) K_S^0 candidates under the assumption that one of its daughter tracks is a proton instead of a pion is required to be more than 6 (10) MeV/c^2 away from the known Λ mass [64]. Furthermore, the K_S^0 decay vertex is required to be located downstream of the J/ψ decay vertex. This removes approximately 50% of misreconstructed $B^0 \to J/\psi K^{*0}$ background. The remaining $B^0 \to J/\psi K^{*0}$ background is heavily suppressed by the first stage of the multivariate selection described below.

Candidate B mesons are selected from combinations of J/ψ and K_S^0 candidates with mass $m_{J/\psi K_S^0}$ in the range [5180, 5520] MeV/c^2 and a decay time larger than 0.2 ps. The latter selection criterion removes a large contribution of background candidates formed from random combinations of tracks produced directly at the PV. The reconstructed mass and decay time are obtained from a kinematic fit [186] that constrains the masses of the $\mu^+\mu^-$ and $\pi^+\pi^-$ pairs to the known J/ψ and K_S^0 masses [64], respectively, and constrains the B candidate to originate from the PV. A good quality fit is required and the uncertainty on the B mass estimated by the kinematic fit must not exceed 30 MeV/c^2. In the case that the event has multiple PVs, a clear separation of the J/ψ decay vertex from any of the other PVs in the event is required, and all combinations of B candidates and PVs that pass the selection are considered.

The $J/\psi K_S^0$ invariant mass distribution of the $B \to J/\psi K_S^0$ candidates selected following the above described trigger and reconstruction steps is shown as the red data points in Fig. 7.2. The $B^0 \to J/\psi K_S^0$ signal can already be identified, but the $B_s^0 \to J/\psi K_S^0$ events are still hidden by the large background contribution surviving this initial selection. The $B^0 \to J/\psi K^{*0}$ background can be seen as a broad shoulder located left of the $B^0 \to J/\psi K_S^0$ signal peak. To optimise the further background rejection, multivariate selection techniques (MVA) are used.

7.2.2 Multivariate Selection

Artificial Neutral Networks

Classification of events into signal and background categories is a complex task that is difficult to optimise. Classically, selection criteria are applied to individual input observables to improve the signal-to-background ratio in the data sample; the so-called *cut-based selection*. But the performance of this method is limited when the main difference between the signal and background distributions lies in their shape and not in their range, making cuts on the individual observables ineffective. Multivariate selection techniques aim at alleviating the limitations of

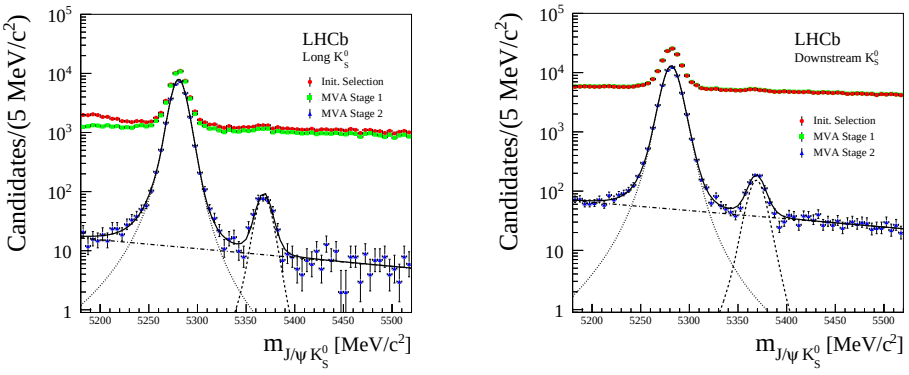

Figure 7.2: Invariant $J/\psi K^0_S$ mass distribution at different stages of the event selection for the long K^0_S [Left] and downstream K^0_S [Right] sample: after the initial selection [Red/Dot], after the first MVA stage [Green/Square] and after the final MVA stage [Blue/Triangle]. Overlaid are projections of the fit described in Section 7.4.

these cut-based selections by exploiting the shapes of the different input distributions and the complex correlations between them.

One particular type of MVA is the artificial neural network (NN), whose design takes inspiration from biological neural networks like the brain. In these NNs the classification task is done collectively and in parallel by a set of individual *neurons* which are linked together into complex structures. Each neuron j receives a set of inputs x_i and combines that information into a single output signal o_j. The input x_i originates either from external sources, or from other neurons in the network. Likewise, the output o_j can again be used as input x_j by other neurons. The processing of the input information inside each neuron is done in two steps. First, the individual inputs are weighted by factors $w_{ij} \in \mathbb{R}$, and the sum $S_j = \sum_i w_{ij} x_i$ is constructed. Next, this sum S is passed through an *activation function*, where the most common choice is the *symmetric sigmoid function*

$$A(S) = \frac{2}{1 + e^{-S}} - 1 \,, \tag{7.7}$$

which maps the range $]-\infty, \infty[$ to the interval $[-1, 1]$. Together with the topological connections between the neurons, the weights w_{ij} fully specify the configuration of the network.

The ability of the NN to accomplishing its requested task depends strongly on the values of the weights w_{ij} used by the different neurons. The optimisation of these weights, referred to as *machine learning* or *training*, therefore forms the most

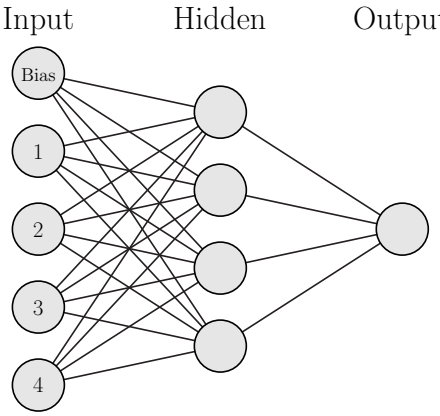

Figure 7.3: Illustration of a feed-forward NN, as used by NeuroBayes [185]: the network consists of an input layer, a hidden layer and an output layer.

important aspect in the setup of a NN classifier. In particle physics applications the standard learning method is *supervised training*: the network is given a set of k example pairs of the form (input observables, output category T), and must find the set of weights that minimises the a priori specified *cost function*. This function penalises the mismatch between the network response and the training data. The cost function used for the MVA selection of the $B_s^0 \to J/\psi K_S^0$ candidates is

$$\text{“Entropy”} = \sum_{\text{nodes j}} \sum_{\text{events k}} -\log\left[\frac{1}{2}(1 + T_{jk} o_{jk})\right], \tag{7.8}$$

which gives zero weight to perfectly categorised example pairs and infinite weight to pairs for which the response is completely opposite to their target.

The most basic class of NNs is the *feed-forward network*, illustrated in Fig. 7.3. In this type of network configuration, the neurons are arranged into one or more layers and information is only passed unidirectional between consecutive layers; there are hence no cycles inside the network. In the NeuroBayes implementation [185], the chosen MVA for the $B_s^0 \to J/\psi K_S^0$ analysis, the network consists of three layers: an input layer, a hidden layer and an output layer. The input layer has $n+1$ neurons; one for each input distribution plus an additional one for a so-called *bias term* that is added to improve the learning performance. The hidden layer can take any number of neurons, but the best performance is achieved with $\mathcal{O}(n)$ neurons, and the output layer has one neuron for each of the initially specified signal categories.

The learning capabilities of a NN can be greatly influenced by the *preprocessing* transformations that are performed on the input distributions prior to the min-

imisation process. In the case of NeuroBayes, this consists of the following steps [185, 187]: each input distribution is split into 100 bins of equal statistics, and the signal purity is determined for each bin. Next, the distributions are normalised, transformed into Gaussian functions and decorrelated. Finally, the importance of each input observable in the training of the NN, i.e. its ability to separate signal from background, is estimated and only the most significant observables (as specified by the user) are kept.

First Stage

The first stage of the multivariate selection focuses on removing the misreconstructed $B^0 \to J/\psi K^{*0}$ background that survives the requirement on the K^0_S flight distance. It only affects the subsample of candidates for which the K^0_S is reconstructed in the long category. The NN is trained using simulated $B^0 \to J/\psi K^0_S$ (signal target) and $B^0 \to J/\psi K^{*0}$ (background target) data and only uses information associated with the K^0_S candidate and its decay products. The input variables are listed in Table 7.1 and include decay time, mass, momentum, impact parameter and particle-identification properties. Where possible, the observables are calculated by the kinematic fit [186] for each (B, PV) pair individually. These observables are labelled with *[Best PV]* in Table 7.1. For events in which multiple pairs survive the initial selection, only the values provided by the fit with the smallest χ^2 are used in the training. For the observables associated with the pion tracks, the information from the π^+ and π^- is combined by taking either the minimal or the maximal value of the two.

To maximise the performance of this MVA, multiple sets of preprocessing options available within NeuroBayes [187] are tested. The NNs obtained with different sets of options are compared using their receiver operating characteristics (ROC curves), i.e. the relation between signal efficiency (true positive) and the background rejection (false positive), as illustrated in Fig. 7.4. The output of the NN with the best learning capabilities, labelled *Prep. 612* in Fig. 7.4, is used as a discriminating variable in the $B^0_s \to J/\psi K^0_S$ event selection. Its distribution is given in Fig. 7.5, and the requirement on this variable is optimised to retain 99% of the original signal candidates in simulation. This is associated with a background rejection on simulated $B^0 \to J/\psi K^{*0}$ candidates of 99.55%, and results in an estimated number of 18 ± 2 $B^0 \to J/\psi K^{*0}$ candidates in the data sample with long K^0_S candidates surviving this stage of the selection. Their yield is further reduced by the second NN classifier, and these candidates are therefore treated as combinatorial background in the remainder of the analysis.

The $J/\psi K^0_S$ invariant mass distribution of the $B \to J/\psi K^0_S$ candidates surviving after the first stage of the MVA is shown as the green data points in Fig. 7.2. Through comparison with the red data points, representing the situation after the

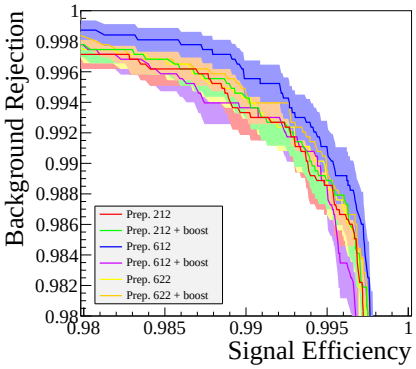

Figure 7.4: Receiver operating characteristics (ROC curves) of the NN configurations studied for the first stage of the MVA selection. The labels ijk identifying the different NN configurations refer to internal NeuroBayes settings for the preprocessing [187]. The bands represent the statistical uncertainty associated with the number of surviving candidates.

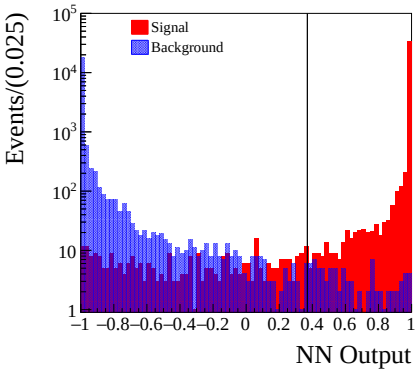

Figure 7.5: Distribution of the network output variable for signal [Red] and background [Blue], with the position of the optimal cut is indicated by the vertical black line. Situation for the optimal network tuning.

Table 7.1: List of input variable for the first stage of the MVA selection, ordered according to their importance in the NN as quantified by their *loss of correlation to the target* and *significance* [187]. The variables below the horizontal line are not used by the best performing NN configuration, although they are available during the preprocessing.

Rank		Variable		Corr.	Sig.
N/A		Bias Node		N/A	N/A
1	K_S^0	Decay Time ($c\tau$)	[Best PV]	92.7 %	217.5 σ
2	$\pi^\pm$	Maximal Kaon Probability		20.7 %	48.5 σ
3	K_S^0	|Mass – 497.614|	[Best PV]	10.7 %	25.1 σ
4	K_S^0	Decay Time Significance	[Best PV]	8.3 %	19.4 σ
5	K_S^0	Total Momentum	[Best PV]	5.1 %	11.9 σ
6	$\pi^\pm$	Minimal Total Momentum	[Best PV]	2.5 %	6.0 σ
7	$\pi^\pm$	Minimal Transverse Momentum	[Best PV]	2.3 %	5.4 σ
8	K_S^0	Minimum IP χ^2	[Best PV]	1.1 %	2.7 σ
9	K_S^0	Mass Error	[Best PV]	0.9 %	2.2 σ
10	$\pi^\pm$	Minimal Minimum IP χ^2	[Best PV]	0.9 %	2.2 σ
11	$\pi^\pm$	Minimal Minimum IP	[Best PV]	0.7 %	1.8 σ
12	K_S^0	Transverse Momentum	[Best PV]	0.3 %	0.8 σ
13	$\pi^\pm$	Maximal Track χ^2_{NDOF}		0.3 %	0.7 σ

initial selection, the original contribution of misreconstructed $B^0 \to J/\psi K^{*0}$ background is revealed as the broad shoulder below $m_{J/\psi K_S^0} < 5250\,\text{MeV}/c^2$. As this first stage of the MVA only affects the long data sample, no effect is observed in the downstream sample.

Second Stage

The second stage of the multivariate selection aims at reducing the combinatorial background to a level that maximises the sensitivity to the small $B_s^0 \to J/\psi K_S^0$ signal. Because the $B^0 \to J/\psi K_S^0$ and $B_s^0 \to J/\psi K_S^0$ modes share the same final state, and the mass difference between the B^0 and B_s^0 meson is small compared to the q^2 value of the decays, both modes have similar properties as far as the event reconstruction and selection is concerned. In contrast to the first NN, this stage of the MVA can therefore be trained entirely on data, using the $B^0 \to J/\psi K_S^0$ signal to represent the distinguishing features of the $B_s^0 \to J/\psi K_S^0$ decay. To avoid introducing biases during the learning phase, candidates for the training sample are only taken from the mass ranges $m_{J/\psi K_S^0} \in [5180, 5340]$ MeV/c^2 and $m_{J/\psi K_S^0} \in [5390, 5520]$ MeV/c^2,

avoiding the intermediate B_s^0 signal region. As the $B^0 \to J/\psi K_S^0$ signal and the combinatoric background are not completely separated in the data, the targets for the NN training are provided by the ${}_s\mathcal{W}$eights, determined using the ${}_s\mathcal{P}$lot technique [188]. These weights are obtained by performing an unbinned maximum likelihood fit to the B mass distribution of the candidates meeting the selection criteria on the first NN classifier's output. The fitted function is defined as the sum of a B^0 signal component and a combinatorial background where the parametrisation of the individual components matches that of the likelihood method used for the full CP analysis and is described in more detail in the Section 7.4.

The NN classifier uses information on the kinematic properties, vertex and track quality, impact parameter and particle-identification information of the candidate and its decay products, as well as global event properties like track and PV multiplicities. The variables that are used in the NN, listed in Tables 7.2 and 7.3 for the long and downstream K_S^0 sample, respectively, are chosen to avoid correlations with the reconstructed B mass. This is tested explicitly on simulated data. Due to differences in the distributions of the input variables, as well as different signal-to-background ratios at the start of the NN training, the multivariate selection is performed separately for the samples containing long and downstream K_S^0 candidates. The long and downstream K_S^0 NNs therefore also use different input observables. Similar to the preprocessing in the first NN stage, the values for the observables are obtained from the kinematic fit where possible, and only the results from the fit with the smallest χ^2 are provided for the training. The information from the observables describing the $\pi^+(\mu^+)$ and $\pi^-(\mu^-)$ final states is combined by taking the minimum or maximum of the two individual input values.

Similar to the strategy adopted for the first stage, multiple sets of preprocessing options are tested in order to maximise the performance of the MVA The NNs obtained with different sets of options are compared using their ROC curves, as illustrated in Fig. 7.6. The output of the NN with the best learning capabilities, labelled respectively *Prep. 212+boost* and *Prep. 612* for the long and downstream sample in Fig. 7.6, is used as the final discriminating variable in the $B_s^0 \to J/\psi K_S^0$ event selection. Their distributions are given in Fig. 7.7.

Final selection requirements on the NN classifier outputs are chosen to optimise the sensitivity to the $B_s^0 \to J/\psi K_S^0$ signal using $N_S/\sqrt{N_S + N_B}$ as figure of merit, where N_S and N_B are respectively the expected number of signal and background events in a 60 MeV/c^2 mass range centred at the B_s^0 peak. These event yields are estimated by appropriately[b] scaling the observed number of $B^0 \to J/\psi K_S^0$ and back-

[a]"DIRA" represents the cosine of the angle between the B momentum vector and the vector pointing to the B decay vertex.

[b]The $B^0 \to J/\psi K_S^0$ yield is multiplied by the ratio 0.0116 ± 0.0008 [45] of $B_s^0 \to J/\psi K_S^0$ to $B^0 \to J/\psi K_S^0$ event yields determined in the 1 fb^{-1} analysis, while the background yield is simply corrected for the difference in mass range.

Table 7.2: List of input variable for the second stage of the MVA selection, ordered according to their importance in the long K_S^0 NN as quantified by their *loss of correlation to the target* and *significance* [187]. The variables below the horizontal line are not used by the best performing NN configuration, although they are available during the preprocessing.

Rank		Variable		Corr.	Sig.
N/A		Bias Node		N/A	N/A
1		χ^2 of Kinematic Fit	[Best PV]	66.9 %	182.2 σ
2	K_S^0	Minimum IP χ^2	[Best PV]	43.5 %	118.5 σ
3	K_S^0	Transverse Momentum	[Best PV]	15.1 %	41.1 σ
4	B^0	Mass Uncertainty Estimate	[Best PV]	14.3 %	38.8 σ
5	B^0	Arccos("DIRA")[a]	[Best PV]	12.3 %	33.6 σ
6	$\mu^\pm$	Minimal Minimum IP χ^2	[Best PV]	7.8 %	21.4 σ
7		Number of PV Tracks	[Best PV]	7.4 %	20.3 σ
8	B^0	Decay Vertex χ^2_{NDOF}		5.7 %	15.6 σ
9	J/ψ	Decay Vertex χ^2		5.8 %	15.8 σ
10	B^0	Transverse Momentum	[Best PV]	5.3 %	14.5 σ
11	$\pi^\pm$	Maximal Track Ghost Probability		4.3 %	11.8 σ
12	K_S^0	Decay Vertex χ^2		4.5 %	12.3 σ
13	K_S^0	Decay Time ($c\tau$)	[Best PV]	4.4 %	11.9 σ
14	J/ψ	Minimum IP χ^2	[Best PV]	3.0 %	8.1 σ
15	J/ψ	Transverse Momentum	[Best PV]	2.3 %	6.2 σ
16	J/ψ	Mass Uncertainty Estimate	[Best PV]	2.3 %	6.2 σ
17	$\pi^\pm$	Maximal Kaon Probability		1.8 %	5.0 σ
18	B^0	Number of PVs		0.9 %	2.5 σ
19		Number of SPD Hits		1.6 %	4.4 σ
20	$\mu^\pm$	Minimal PID(μ)		1.3 %	3.7 σ
21	$\pi^\pm$	Minimal Minimum IP	[Best PV]	1.1 %	3.0 σ
22	J/ψ	|Mass – 3099.0|	[Best PV]	1.1 %	2.9 σ
23	$\mu^\pm$	Minimal Transverse Momentum	[Best PV]	1.0 %	2.7 σ
24	$\pi^\pm$	Maximal Track χ^2_{NDOF}		0.8 %	2.2 σ
25	K_S^0	Decay Time Significance	[Best PV]	0.7 %	2.0 σ
26	$\mu^\pm$	Maximal Track χ^2_{NDOF}		0.7 %	1.9 σ
27	K_S^0	Mass Uncertainty Estimate	[Best PV]	0.5 %	1.3 σ
28	$\mu^\pm$	Minimal Minimum IP	[Best PV]	0.4 %	1.2 σ
29	K_S^0	Decay Vertex z-position		0.4 %	1.1 σ
30		PV χ^2	[Best PV]	0.4 %	1.0 σ
31	$\pi^\pm$	Minimal Transverse Momentum	[Best PV]	0.3 %	0.7 σ

Table 7.3: List of input variable for the second stage of the MVA selection, ordered according to their importance in the downstream K_S^0 NN as quantified by their *loss of correlation to the target* and *significance* [187]. The variables below the horizontal line are not used by the best performing NN configuration, although they are available during the preprocessing.

Rank		Variable		Corr.	Sig.
N/A		Bias Node		N/A	N/A
1		χ^2 of Kinematic Fit	[Best PV]	57.1 %	305.8 σ
2	K_S^0	Transverse Momentum	[Best PV]	36.3 %	194.4 σ
3	J/ψ	Minimum IP χ^2	[Best PV]	29.2 %	156.5 σ
4	B^0	Arccos("DIRA")[a]	[Best PV]	12.2 %	65.4 σ
5	B^0	Mass Uncertainty Estimate	[Best PV]	12.7 %	68.0 σ
6		Number of PV Tracks	[Best PV]	9.0 %	48.0 σ
7	K_S^0	|Mass – 497.614|	[Best PV]	6.9 %	36.9 σ
8	$\mu^\pm$	Minimal Minimum IP χ^2	[Best PV]	5.8 %	31.2 σ
9	B^0	Total Momentum	[Best PV]	5.0 %	26.5 σ
10	B^0	Decay Vertex χ^2_{NDOF}		4.4 %	23.6 σ
11	K_S^0	Decay Vertex χ^2		4.0 %	21.2 σ
12	$\pi^\pm$	Minimal Minimum IP	[Best PV]	2.5 %	13.4 σ
13	K_S^0	Total Momentum	[Best PV]	3.6 %	19.0 σ
14	J/ψ	|Mass – 3099.0|	[Best PV]	3.5 %	18.9 σ
15	J/ψ	Transverse Momentum	[Best PV]	2.7 %	14.5 σ
16		Number of SPD Hits		2.5 %	13.3 σ
17	J/ψ	Decay Vertex χ^2		2.1 %	11.1 σ
18	$\pi^\pm$	Minimal Minimum IP χ^2	[Best PV]	1.1 %	6.0 σ
19	K_S^0	Decay Time Significance	[Best PV]	1.8 %	9.8 σ
20	$\mu^\pm$	Minimal PID(μ)		1.5 %	8.1 σ
21	B^0	Number of PVs		1.4 %	7.4 σ
22	K_S^0	Decay Time ($c\tau$)	[Best PV]	1.4 %	7.3 σ
23	K_S^0	Minimum IP χ^2	[Best PV]	1.3 %	7.0 σ
24	$\pi^\pm$	Maximal Kaon Probability		1.2 %	6.5 σ
25	$\mu^\pm$	Minimal Transverse Momentum	[Best PV]	0.9 %	4.6 σ
26	$\mu^\pm$	Minimal Total Momentum	[Best PV]	1.2 %	6.2 σ
27	J/ψ	Mass Uncertainty Estimate	[Best PV]	1.0 %	5.5 σ
28	$\mu^\pm$	Minimal Minimum IP	[Best PV]	1.0 %	5.3 σ
29	$\mu^\pm$	Maximal Track χ^2_{NDOF}		0.9 %	4.8 σ
30	$\pi^\pm$	Minimal Total Momentum	[Best PV]	0.6 %	3.1 σ
31	$\pi^\pm$	Minimal Transverse Momentum	[Best PV]	0.8 %	4.1 σ
32	$\pi^\pm$	Maximal Track Ghost Probability		0.7 %	3.7 σ
33	B^0	Transverse Momentum	[Best PV]	0.6 %	3.0 σ
34	K_S^0	Decay Vertex z-position		0.2 %	1.2 σ
35	$\pi^\pm$	Maximal Track χ^2_{NDOF}		0.1 %	0.5 σ

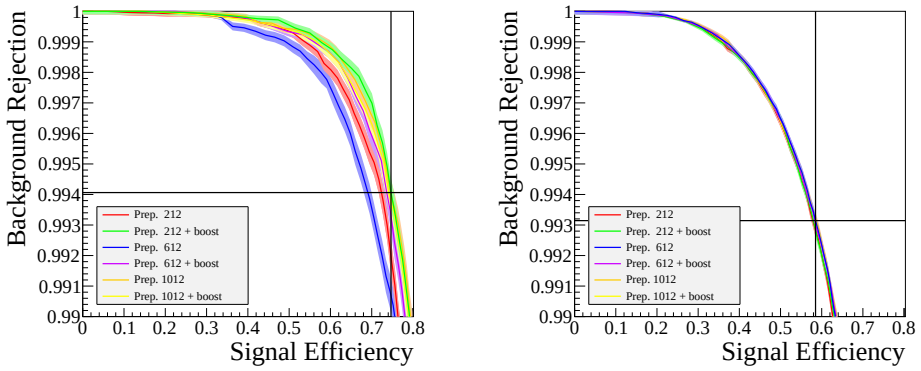

Figure 7.6: Receiver operating characteristics (ROC curves) of the long [Left] and downstream [Right] NN configurations studied for the second stage of the MVA selection. The labels ijk identifying the different NN configurations refer to internal NeuroBayes settings for the preprocessing [187]. The black cross indicates the point on the best ROC curve that maximises the $N_S/\sqrt{N_S + N_B}$ figure of merit for the $B_s^0 \to J/\psi K_S^0$ decay.

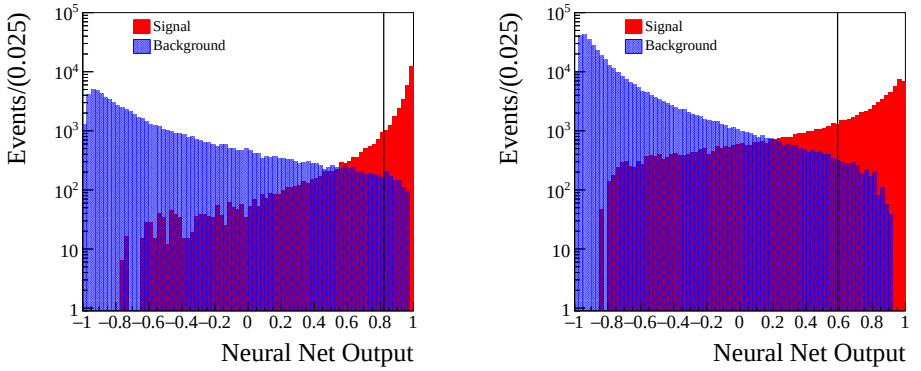

Figure 7.7: Distribution of the network output variable of the long [Left] and downstream [Right] sample for signal [Red] and background [Blue], with the position of the optimal cut is indicated by the vertical black line. Situation for the optimal network tuning.

ground events surviving in the training sample, and thus do not use information from the B_s^0 signal region. After applying the final requirement on the NN classifier output associated with the long (downstream) K_S^0 sample, the multivariate selection rejects, relative to the initial selection, 99.2% of the background in both samples while keeping 72.9% (58.3%) of the $B^0 \to J/\psi K_S^0$ signal. The lower selection efficiency on the downstream K_S^0 sample is due to the worse signal-to-background ratio after the initial selection, which requires a more stringent requirement on the NN classifier output.

The $J/\psi K_S^0$ invariant mass distribution of the $B \to J/\psi K_S^0$ candidates surviving after the second stage of the MVA is shown as the blue data points in Fig. 7.2. The $B_s^0 \to J/\psi K_S^0$ component can now clearly be identified on top of the highly reduced combinatoric background.

Final Corrections: Events with Multiple Candidates

Throughout the whole event selection all B candidates and their associated PVs are treated equally. After the selection requirement on the second NN output has been applied, the long (downstream) B candidate can still be associated with more than one PV in about 1.5% (0.6%) of the events. Likewise, about 0.24% (0.15%) of the selected events have several candidates sharing one or more tracks. Because of the stringent event selection, all these combinations are equally likely[c] to be the true event, even though only one of them can be correct. In these cases, only one of the surviving PVs and one of the candidates is therefore chosen at random.

7.3 Flavour Tagging

Tagging Algorithms

Knowledge on the production flavour of the decaying B meson, i.e. whether it is a B or $\bar{B}$, forms an essential ingredient for performing CP asymmetry measurements. At the LHC, b quarks are predominantly produced in $b\bar{b}$ pairs, which subsequently hadronise and decay independently. The initial flavour of the B meson decay of interest can therefore be inferred by two independent classes of flavour-tagging algorithms, illustrated in Fig. 7.8, depending on which quark out of the pair is used.

The *opposite side* (OS) taggers exploit the entanglement of the $b\bar{b}$ pair to determine the flavour of the signal B meson from the hadronisation and decay of the non-signal b quark [190]. Hence, these algorithms are independent the signal B meson, and can thus be used for B^0 and B_s^0 mesons alike. Four different tagging algorithms are implemented, which aim respectively at identifying the charge of

[c] Any ranking based on the selection variables is no longer well motivated.

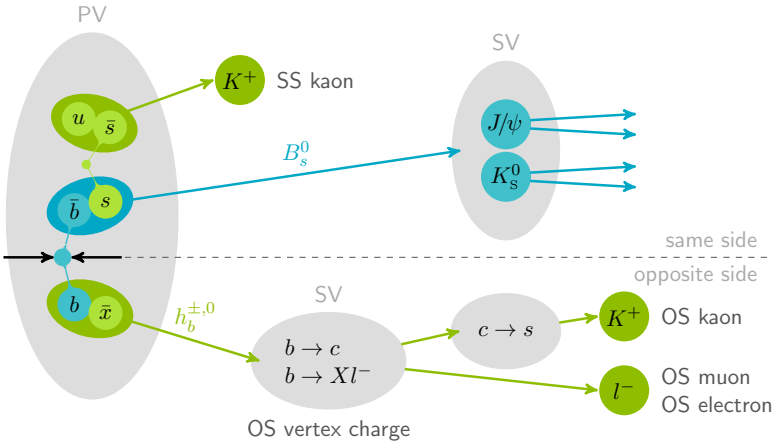

Figure 7.8: Schematic overview of the flavour tagging algorithms [189].

electrons, muons and kaons produced in the decay of the non-signal b-hadron, or at determining the total charge of the tracks originating from the decay vertex of the non-signal b-hadron. Their performance is optimised in data [190] on so-called *self-tagging* modes like $B^+ \to J/\psi K^+$, $B^0 \to J/\psi K^{*0}$ (with $K^{*0} \to K^+\pi^-$) and $B^0 \to D^{*-}\mu^+\nu_\mu$, where the charges of the final state particles determine the original flavour of the B meson[d].

The *same side* taggers [191], on the other hand, rely on the feature that the additional light quark q ($\bar{q}$), which binds together with the $\bar{b}$ (b) quark to form the signal B_q^0 ($\bar{B}_q^0$) meson, is most likely also produced in a quark–antiquark pair. The other quark $\bar{q}$ (q) from this pair often hadronises into a positively (negatively) charged pion (for $q = d$) or kaon (for $q = s$), which thus reveals the flavour of the B meson. These associated charged pions and kaons can be identified in the complete collision event because they remain close in phase-space to the signal B. The algorithms that perform this identification are specifically designed for either the B^0 meson, i.e. the same side pion (SSπ) tagger, or the B_s^0 meson, i.e. the same side kaon (SSK) tagger, but never for both. The performance of the SSK tagger, which is used for this analysis, is optimised using both simulated events and the self-tagging mode $B_s^0 \to D_s^-\pi^+$ [191].

The performance of flavour tagging algorithms is limited, especially in busy hadronic environments like the ones encountered at the LHC. As a result, only a subset of N_R selected signal B mesons is correctly tagged, while N_W events are incorrectly tagged and the remaining N_U events do not have any tagging information;

[d]This assumes that mixing between B^0 and $\bar{B}^0$ mesons can be neglected.

they are untagged. These three numbers together quantify the performance of the algorithms through the *tagging efficiency*

$$\varepsilon_{\text{tag}} \equiv \frac{N_{\text{R}} + N_{\text{W}}}{N_{\text{R}} + N_{\text{W}} + N_{\text{U}}}\,, \tag{7.9}$$

and the *mistag probability*

$$\omega \equiv \frac{N_{\text{W}}}{N_{\text{R}} + N_{\text{W}}}\,. \tag{7.10}$$

The latter quantity dilutes the oscillation amplitudes in the decay time distribution by a factor $\mathcal{D}_{\text{tag}} \equiv (1 - 2\omega)$. The figure of merit for the tagging algorithms, which should be maximised to get the optimal performance, is the *effective tagging efficiency*

$$\varepsilon_{\text{eff}} \equiv \varepsilon_{\text{tag}}(1 - 2\omega)^2 = \varepsilon_{\text{tag}}\mathcal{D}_{\text{tag}}^2\,. \tag{7.11}$$

This effective tagging efficiency represents the statistical power of the tagged sample: A sample consisting of N events with $\varepsilon_{\text{eff}} = x$ has the same statistical power as a sample of xN perfectly tagged events.

The OS and SSK tagging algorithms each provide two observables: the tag decision q and an estimate η for the probability of the tag to be incorrect. The tag decision takes the value $+1$, 0 and -1 when the signal candidate is respectively tagged as a B, untagged or tagged as a $\overline{B}$. The estimate η is determined on an candidate-by-candidate basis using a neural network classifier that combines information on the underlying event with the kinematic and geometrical properties of the flavour-identifying particles, i.e. the OS electrons, muons, kaons and the SS kaons.

The mistag probability η predicted by the tagging algorithms is calibrated in data to determine the true mistag probability ω using the flavour-specific B meson decays listed above. The calibration function is parametrised as

$$\omega(\eta) = p_0 + p_1 \cdot (\eta - \langle\eta\rangle)\,, \tag{7.12}$$

where p_0 and p_1 are calibration parameters, and $\langle\eta\rangle$ is the mean of the η distribution predicted by the taggers. In a perfect scenario, where $\eta = \omega$, the calibration parameters would take the values $p_0 = \langle\eta\rangle$ and $p_1 = 1$. The calibration of the η distributions is done separately for the OS and SSK algorithms.

Combining OS and SSK Tagging Responses

For the fraction of events with both an OS and SSK tag decision, a combined tag decision and mistag probability is derived. For the likelihood fit described in this

Table 7.4: Effective tagging efficiencies ε^{eff} for the different sub-samples used in this analysis. Uncertainties are statistical only.

	B_s^0		B^0	
Sample	Long K_S^0 [%]	Down. K_S^0 [%]	Long K_S^0 [%]	Down. K_S^0 [%]
OS exclusive	2.51 ± 0.15	2.48 ± 0.11	2.28 ± 0.05	2.23 ± 0.05
SSK exclusive	0.27 ± 0.04	1.08 ± 0.11	0.042 ± 0.006	0.064 ± 0.009
OS+SSK overlap	1.02 ± 0.10	0.47 ± 0.04	0.274 ± 0.008	0.327 ± 0.011
Total	3.80 ± 0.18	4.03 ± 0.16	2.60 ± 0.05	2.63 ± 0.05

Chapter[e], the combination of the OS and SSK tagger outputs is based on the delta log-likelihood method. Given a tag decision q and a calibrated mistag estimate $\omega(\eta)$, the probabilities to be either a B or a $\bar{B}$ meson at production are given by

$$\mathcal{P}(B|q,\omega) = \frac{1}{2}(1+q) - q\,\omega\,, \qquad \mathcal{P}(\bar{B}|q,\omega) = \frac{1}{2}(1-q) + q\,\omega\,. \tag{7.13}$$

This information can be condensed into a single delta log-likelihood

$$\Delta\text{LL} \equiv \log\left(\frac{\mathcal{P}(B|q,\omega)}{\mathcal{P}(\bar{B}|q,\omega)}\right). \tag{7.14}$$

Multiple taggers can now be combined by simply adding their log-likelihoods

$$\Delta\text{LL}^{\text{comb}} = \Delta\text{LL}^{\text{OS}} + \Delta\text{LL}^{\text{SSK}}\,, \tag{7.15}$$

from which the combined tag decision and mistag estimate can again be extracted

$$q_{\text{OS+SSK}} = \text{sign}[\Delta\text{LL}^{\text{comb}}]\,, \qquad \omega_{\text{OS+SSK}} = \frac{1}{1+\exp\left|\Delta\text{LL}^{\text{comb}}\right|}\,. \tag{7.16}$$

Tagging Performance for the $B_s^0 \to J/\psi K_S^0$ Analysis

To maximise the sensitivity to the *CP* asymmetry parameters of the $B_s^0 \to J/\psi K_S^0$ decay, the analysis uses information provided by the OS and SSK tagging algorithms; the SSπ tagger is not included. The effective tagging efficiency for the $B_s^0 \to J/\psi K_S^0$ and $B^0 \to J/\psi K_S^0$ modes are summarised in Table 7.4.

In this setup, also the $B^0 \to J/\psi K_S^0$ component uses SSK tagging information, even though the algorithm is not designed to generate a proper response regarding the flavour of the B^0 meson. Nonetheless, a small, but non-vanishing effective

[e] An alternative method is described in Ref. [190].

Table 7.5: List of observables describing the B^0 and B_s^0 meson systems that are included as Gaussian constraints to the likelihood fit.

Parameter	Value	Parameter	Value
Δm_d	0.510 ± 0.003 ps^{-1} [121]	Δm_s	17.757 ± 0.021 ps^{-1} [121]
$\Delta\Gamma_d$	0 ps^{-1}	$\Delta\Gamma_s$	0.081 ± 0.006 ps^{-1} [121]
τ_{B^0}	1.520 ± 0.004 ps [121]	$\tau_{B_s^0}$	1.509 ± 0.004 ps [121]

tagging efficiency is also found for B^0 mesons if separate calibration functions for the η_{SSK} are used. This response originates from same-side protons misidentified as kaons, and kaons from the decay of K^* mesons produced in correlation with the B^0. Both tagged particles have the opposite charge compared to the kaons that are produced in correlation with the B_s^0, and thus require the SSK tag decision to be inverted. The third source generating an SSK tag response for $B^0 \to J/\psi K_S^0$ events consists of misidentified pions carrying the same charge as the kaons correlated with the B_s^0. They are less numerous than the same-side protons and K^* remnants combined, and thus only dilute the effect described above. For the $B^0 \to J/\psi K_S^0$ component, the SSK tag decision is therefore inverted to obtain an overall correct tagging response. The SSK tagging response for the $B^0 \to J/\psi K_S^0$ events in the sample is studied on $B^0 \to J/\psi K^{*0}$ candidates using both data and simulated events.

7.4 Likelihood Fit

The $B_s^0 \to J/\psi K_S^0$ *CP* observables are determined from an unbinned maximum likelihood fit. The PDF with which the likelihood is constructed describes a combinatoric background component, the $B_s^0 \to J/\psi K_S^0$ signal and the more prominent $B^0 \to J/\psi K_S^0$ decay mode. In total, it depends on five observables. The PDF fully models the reconstructed B mass ($m_{J/\psi K_S^0} \in [5180, 5520]$ MeV/c^2), the decay time ($t \in [0.2, 15]$ ps), and the tagging response q, which combines the information from the OS and SSK taggers. Additionally, the PDF also includes information from two conditional observables: the per-candidate decay time uncertainty estimate δ_t, provided by the kinematic fit introduced in Section 7.2.1, and the mistag estimate η, which again combines the information from the OS and SSK taggers. The long and downstream K_S^0 samples are modelled using separate PDFs, but fitted simultaneously. The parameters common to both PDFs are the two $B^0 \to J/\psi K_S^0$ and three $B_s^0 \to J/\psi K_S^0$ *CP* observables, as well as the observables describing the B^0 and B_s^0 meson systems. The inputs used in the experimental analysis are listed in Table 7.5, and match those given previously in Table 4.1.

For this analysis it is assumed that the fitted PDF factorises into two uncor-

related terms: the reconstructed B mass and the decay time distribution. This assumption is tested in simulated data, which does show a correlation between the B mass and the decay time resolution. The effect of this correlation is studied and a systematic uncertainty is assigned accordingly, as discussed in Section 7.5 below. The decay time distributions of the two signal components, $\mathcal{T}(t, q|\eta)$, need to be corrected for experimental effects originating from the detector response and the event selection. This is done by convolving them with a resolution model, $\mathcal{R}(t|\delta_t)$, and combining the result with an acceptance function, $\mathcal{E}(t)$, to give the experimentally observed decay time distribution

$$\left(\int \mathcal{T}(\hat{t}, q|\eta) \times \mathcal{R}(t - \hat{t}|\delta_t) \, \mathrm{d}\hat{t} \right) \times \mathcal{E}(t) \,. \tag{7.17}$$

Let us now describe these individual contributions in more detail.

7.4.1 Invariant $J/\psi K^0_S$ Mass Distribution

The mass lineshapes of the $B \to J/\psi K^0_S$ modes in both data and simulation exhibit non-Gaussian tails on both sides of their signal peaks due to final state radiation, multiple scattering, the detector resolution and its dependence on the decay angles and momenta of the final state particles. The lineshapes are modelled with a (double-sided) *Hypatia* distribution [192]

$$I(m; \mu, \sigma, \lambda, \zeta, \beta, a_{\mathrm{I}}, a_{\mathrm{II}}, n_{\mathrm{I}}, n_{\mathrm{II}}) \propto \begin{cases} \frac{A}{(B+m-\mu)^{n_{\mathrm{I}}}} & \text{if } m - \mu < -a_{\mathrm{I}}\sigma \,, \\ \frac{C}{(D+m-\mu)^{n_{\mathrm{II}}}} & \text{if } m - \mu > a_{\mathrm{II}}\sigma \,, \\ \left((m-\mu)^2 + \delta^2 \right)^{\frac{1}{2}\lambda - \frac{1}{4}} e^{\beta(m-\mu)} K_{\lambda-\frac{1}{2}} \left(\alpha \sqrt{(m-\mu)^2 + \delta^2} \right) & \text{otherwise} \,, \end{cases} \tag{7.18}$$

where $K_\nu(z)$ is the modified Bessel function of the second kind,

$$\delta \equiv \sigma \sqrt{\frac{\zeta \, K_\lambda(\zeta)}{K_{\lambda+1}(\zeta)}} \,, \qquad \alpha \equiv \frac{1}{\sigma} \sqrt{\frac{\zeta \, K_{\lambda+1}(\zeta)}{K_\lambda(\zeta)}} \,, \tag{7.19}$$

and A, B, C, D are obtained by imposing continuity and differentiability. The core of the Hypatia function describes the invariant mass resolution, based on a generalised hyperbolic resolution model, and the tails describe the effect of photon radiation. Because the masses of the intermediate J/ψ and K^0_S resonances are constrained by the kinematic fit, this radiation also causes a tail on the right-hand side in addition to the usual left-hand side [192].

To reduce the number of degrees of freedom that has to be fitted to the data, parameters β and ζ are set to zero. In addition, the tail parameters a_{I}, a_{II}, n_{I} and n_{II}

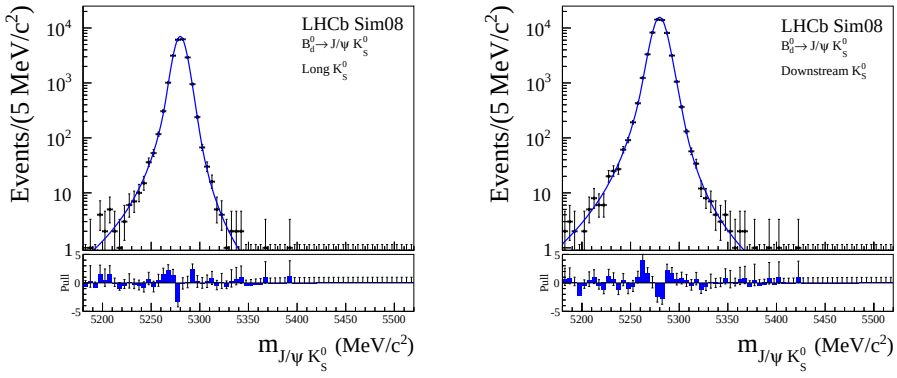

Figure 7.9: Invariant $J/\psi K_S^0$ mass distribution of the simulated $B^0 \to J/\psi K_S^0$ candidates in the Long K_S^0 [Left] and Downstream K_S^0 [Right] sample.

Table 7.6: Fitted values for the parameters of the Hypatia function describing the invariant $J/\psi K_S^0$ mass distribution of the $B^0 \to J/\psi K_S^0$ events in simulated data. The four tail parameters are taken as input for the nominal fit to data.

Par.	Long K_S^0	Down. K_S^0
a_{I}	2.05 ± 0.14	2.22 ± 0.12
a_{II}	2.98 ± 0.46	3.28 ± 0.30
n_{I}	3.40 ± 0.41	3.89 ± 0.39
n_{II}	3.56 ± 0.82	3.42 ± 0.50
λ	−3.69 ± 0.41	−3.27 ± 0.16
σ	6.81 ± 0.11	8.06 ± 0.06

are obtained from a fit to the simulated data, for which the fit projections are shown in Fig. 7.9 and the fitted parameter values are summarised in Table 7.6. The B_s^0 component is constrained to have the same lineshape as the B^0 PDF, but shifted by the B_s^0–B^0 mass difference, which is a free variable in the fit. The mass distribution of the combinatorial background is described by an exponential function.

7.4.2 Resolution Model

The finite decay time resolution of the detector affects the precision on the *CP* parameters as it dilutes the amplitude of the oscillation terms in the decay time distribution by a factor $\mathcal{D} = \exp\left(-\sigma_{\mathrm{eff}}^2 \Delta m^2/2\right)$ [193, 184], where σ_{eff} represents the effective decay time resolution. The impact of the resolution effects depends on

Table 7.7: Values for the parameters describing the resolution model, obtained from a fit to the prompt J/ψ background in data. These five parameters are taken as input for the nominal fit to data.

Par.	Long K^0_S	Down. K^0_S
s_{I}	1.094 ± 0.092	1.039 ± 0.038
r_{II}	1.71 ± 0.70	1.869 ± 0.075
r_{III}	19 ± 13	10.0 ± 1.7
f_{I}	0.608 ± 0.054	0.745 ± 0.060
f_{III}	0.004 ± 0.025	0.00152 ± 0.00078

the oscillation frequency, and therefore affects the $B^0_s \to J/\psi K^0_S$ mode to a much larger extend than the $B^0 \to J/\psi K^0_S$ counterpart. To maximise the sensitivity to the $B^0_s \to J/\psi K^0_S$ *CP* observables in the data, the resolution model $\mathcal{R}$ therefore depends on the per-candidate decay time uncertainty estimate δ_t.

The resolution is modelled as the sum of three Gaussian functions that share a common mean μ, but have different widths $\sigma_i(\delta_t)$, leading to

$$\mathcal{R}(t;\mu,\sigma_i|\delta_t) \propto \sum_{i=1}^{3} f_i \frac{1}{\sqrt{2\pi}\,\sigma_i(\delta_t)} e^{-\frac{1}{2}\left(\frac{t-\mu}{\sigma_i(\delta_t)}\right)^2}, \tag{7.20}$$

where f_i is the fraction of the i^{th} Gaussian component and $f_{\mathrm{I}} + f_{\mathrm{II}} + f_{\mathrm{III}} = 1$. The resolution widths $\sigma_i(\delta_t)$ are parametrised as

$$\sigma_{\mathrm{I}}(\delta_t) = s_{\mathrm{I}} \times \delta_t\,, \qquad \sigma_{\mathrm{II}}(\delta_t) = s_{\mathrm{I}} \times r_{\mathrm{II}} \times \delta_t\,, \qquad \sigma_{\mathrm{III}}(\delta_t) = s_{\mathrm{I}} \times r_{\mathrm{III}} \times \delta_t\,, \tag{7.21}$$

where the use of a relative parametrisation for the second and third Gaussian improves the fit stability.

Calibration

The δ_t estimates are calibrated using a sample of prompt J/ψ decays, which are produced directly at the PV and combined with random K^0_S candidates. This sample is obtained through the same event selection as described in Section 7.2 except for the requirement on the decay time of the B candidates. Its decay time distribution, shown in Fig. 7.10, is projected out of the full data, which also contains the $B^0 \to J/\psi K^0_S$ signal and a negligible contribution from $B^0_s \to J/\psi K^0_S$, using ${}_s\mathcal{W}$eights based on the mass PDF described above.

The convolution of the true decay time distribution of this sample with the decay time resolution causes a fraction of the events to obtain unphysical decay

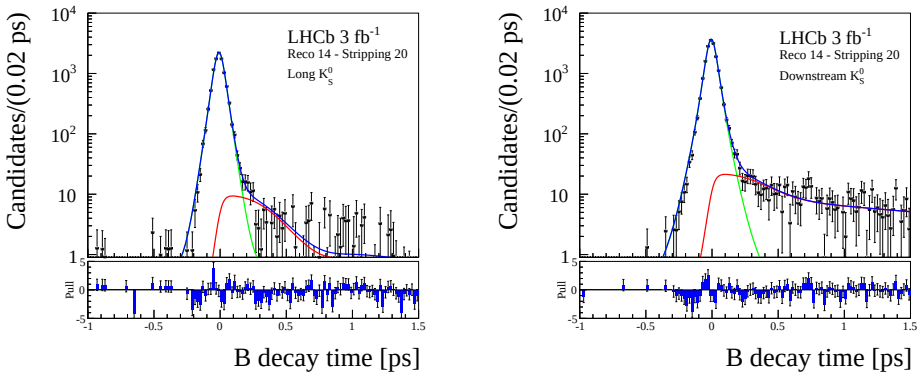

Figure 7.10: ${}_s\mathcal{W}$eighted decay time distribution of the prompt background in the Long K_S^0 [Left] and Downstream K_S^0 [Right] samples, which is used to calibrate the per-candidate decay time uncertainty estimates. Shown are the prompt component [Green], the non-prompt contribution [Red] and the fit projection of the complete model [Blue].

times $t < 0$. As only the presence of a finite decay time resolution can cause such a component in the data, it can be used to extract the parameters of the resolution model directly from this data. The results for the fractions f_i and the calibration parameters s_i and r_i are summarised in Table 7.7.

The model used for the determination of the resolution, whose fit projection is also shown in Fig. 7.10, consists of a prompt component, i.e. the to-be-determined resolution model, and a non-prompt component. The true decay time distribution of the non-prompt events is unknown and depends on the exact composition of the background sample. As such, the region $t \gg 0$ only forms a nuisance for the extraction of the resolution parameters, and it thus suffices to find a good parametric description.

Comparison between the Signal and Background Resolution

It is assumed that the decay time resolution model determined from the prompt background can be directly applied to the signal modes. However, this need not be true as both differences in the per-candidate decay time uncertainty estimate distributions and differences in the required calibration functions between signal and background can cause discrepancies between both resolution models. Because of the stringent background rejection by the second NN, only signal-like background events are retained. Consequently, good agreement is found between the per-candidate decay time uncertainty estimate distributions of the signal and the

remaining background.

Possible discrepancies in the required calibration functions can be studied with simulated data by comparing the *power* of the resolution models. This quantity is independent of the chosen parametrisation; all resolution models that describe the data to the same extent, have the same resolution power. The resolution power is defined as the square of the dilution, and thus given by

$$\mathcal{P}_{\text{res}}(\delta_t) \equiv \mathcal{D}^2_{\text{res}}(\delta_t)\,, \qquad \langle \mathcal{P}_{\text{res}} \rangle \equiv \sum_{\delta_t} \frac{1}{N} \mathcal{P}_{\text{res}}(\delta_t)\,, \tag{7.22}$$

where N is the total number of events in the sample. For the triple Gaussian resolution model used in this analysis, the dilution can be quantified as

$$\mathcal{D}_{\text{res}}(\delta_t) \equiv \sum_{i=1}^{3} f_i \, e^{-\frac{1}{2}\Delta m^2 \, \sigma_i(\delta_t)^2}\,, \qquad \langle \mathcal{D}_{\text{res}} \rangle \equiv \sum_{\delta_t} \frac{1}{N} \mathcal{D}_{\text{res}}(\delta_t)\,. \tag{7.23}$$

Taking $\Delta m = \Delta m_s$ in the above expression, the resolution power in simulated $B^0 \to J/\psi\, K^0_S$, $B^0_s \to J/\psi\, K^0_S$ and inclusive J/ψ data is compared in Fig. 7.11 as a function of the selection requirement on the neural network output. This shows good agreement over a large range of cut values, which include the optimal cut point used in this analysis. The systematic uncertainties, described below, on the parameters of interest also cover the small discrepancies, especially in the downstream K^0_S sample, between the signal and background resolution models. In data, the average dilution factor from the resolution model is $\langle \mathcal{D}_{\text{res}} \rangle = 0.73 \pm 0.13$ and 0.72 ± 0.04 for the long and downstream K^0_S samples, respectively.

7.4.3 Decay Time Acceptance Function

The decay time distribution of the two signal components is affected by acceptance effects due to a decay-time bias induced by the trigger, the initial selection requirements and, most importantly, the NN classifier outputs. The shapes of the acceptance functions for the $B^0 \to J/\psi\, K^0_S$ and $B^0_s \to J/\psi\, K^0_S$ components are assumed to be identical and modelled using spline functions.

Spline Functions

Distributions for which no standard choice of analytic function exists, like the decay time acceptance, can in a finite region be approximated by using a collection of $n+2$ base splines, where n is the number of user-specified interval boundaries, referred to as *knots*, subdividing this region. These splines are continuously differentiable, piece-wise defined polynomial functions. The most commonly used choice of splines are the cubic b-splines, which are constructed from polynomials

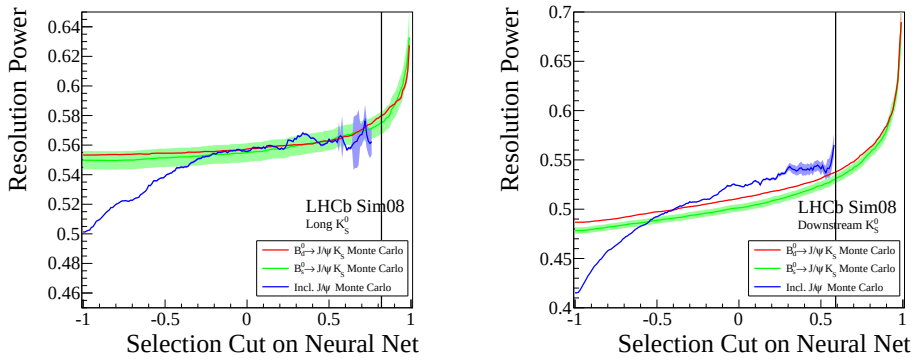

Figure 7.11: Comparison of the resolution power between the $B^0 \to J/\psi K_S^0$, $B_s^0 \to J/\psi K_S^0$ and incl. J/ψ MC samples for the Long K_S^0 [Left] and Downstream K_S^0 [Right] sample, as a function of the cut on the neural network output. The resolution power is calculated for $\Delta M_s = 17.768\ \text{ps}^{-1}$. The black, vertical line indicates the position of the optimised selection cut.

of degree three. They are uniquely defined by the position of the knots, which completely determine the shapes of the individual splines Only the relative normalisation between the different splines can afterwards still be varied. With the exception of the left- and right-most spline, each base spline spans four intervals and likewise each interval has four contributing base splines that together form a partition of unity. Each base spline shares at most three intervals with any other base spline. The to-be-modelled lineshape is now approximated by varying the weights of the individual base splines such that their combined function value matches that of the input data at the knot positions. In this analysis, the cubic b-splines are implemented as an efficiency function that modifies the resolution model [194].

Modelling Acceptance Effects

Assuming $\Delta\Gamma_d = 0$, as is consistent with the current experimental data [121], the untagged $B^0 \to J/\psi K_S^0$ decay time distribution is described by a single exponential. This allows the acceptance parameters to be directly evaluated in the likelihood fit to the data by constraining the lifetime of the B^0 meson using a Gaussian function whose mean is fixed to the known lifetime and whose width accounts for the experimental uncertainty.

The decay time is modelled in the interval $[0.2, 15]$ ps, with the positions of the knots (arbitrarily) chosen at 0.2, 0.5, 1.0, 2.0, 8.0 and 15.0 ps. The spline is

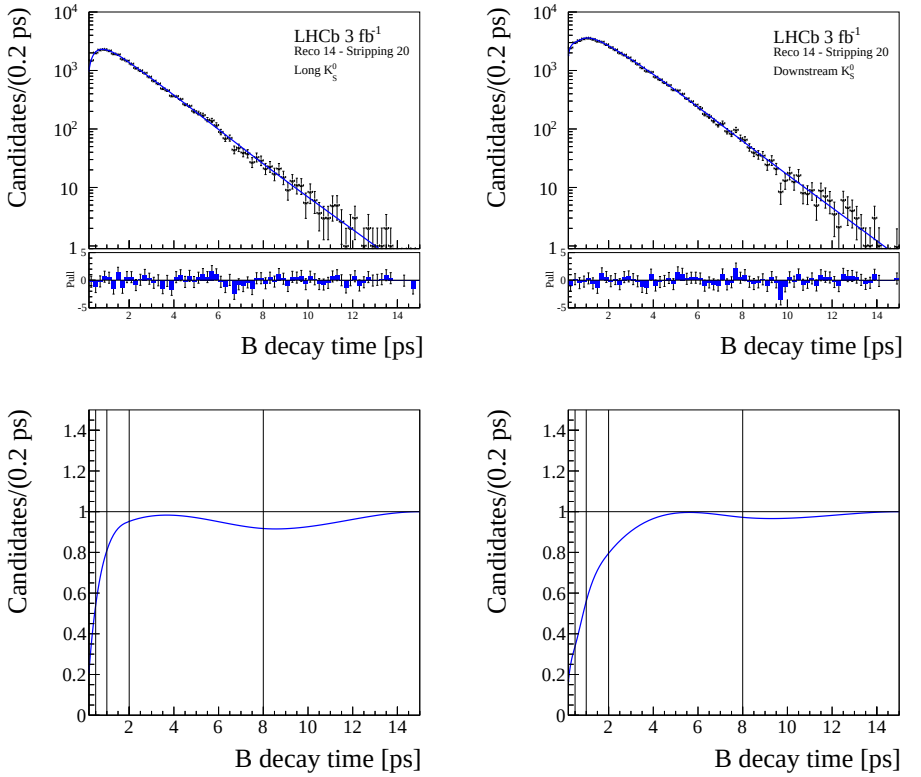

Figure 7.12: ${}_s\mathcal{W}$eighted decay time distribution of the $B^0 \to J/\psi K^0_S$ candidates [Top], and derived acceptance function [Bottom], in the Long K^0_S [Left] and Downstream K^0_S [Right] sample. The vertical black lines indicate the positions of the *knots*.

assumed to continue as a constant, flat function beyond 15 ps, constraining the weights of the two right-most base splines to be equal. To normalise the overall spline function, the weight of the right-most base spline is set to unity. This leaves six free parameters acc_i to describe the shape of the spline function. The decay time distribution of the $B^0 \to J/\psi K^0_S$ events, and the acceptance function derived from it, are shown in Fig. 7.12. This shows a clear *turn-on* curve at small decay times, caused by the selection requirement on the NN. The oscillation at about 8 ps is an artefact of using spline functions to approximate a linear function, and would reduce when increasing the number of knots between 2 and 15 ps.

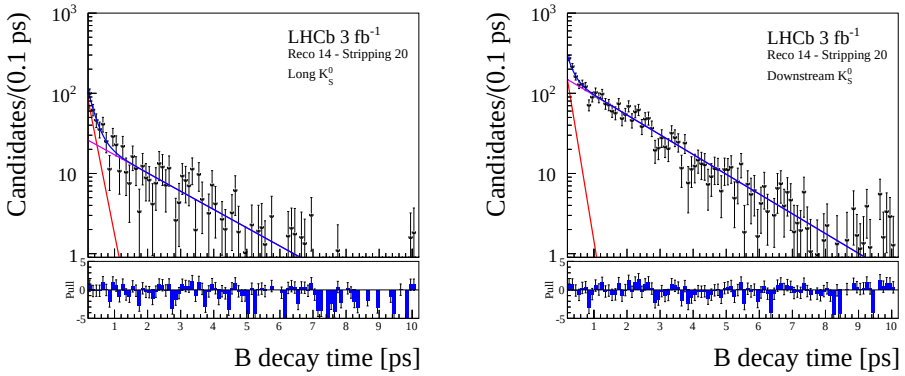

Figure 7.13: ${}_s\mathcal{W}$eighted decay time distribution of the combinatoric background in the Long K_S^0 [Left] and Downstream K_S^0 [Right] sample.

7.4.4 Other Input Distribution

The background decay time distributions, shown in Fig. 7.13, are modelled using two exponential functions

$$f_{\text{bkg}} \times \text{Exponential}(t; \tau_{\text{bkg}}) + (1 - f_{\text{bkg}}) \times \text{Exponential}(t; r_{\text{bkg}} \cdot \tau_{\text{bkg}}), \tag{7.24}$$

empirically describing a short-lived and a long-lived component.

The distributions of the per-candidate decay time uncertainty estimate δ_t and mistag estimate η are shown in Figs. 7.14 and 7.15, respectively. These estimates are included as conditional observables in the PDF; their distributions are therefore not modelled. As no significant deviations are observed in the current data, the input distributions are assumed to be identical for the $B^0 \to J/\psi K_S^0$, $B_s^0 \to J/\psi K_S^0$ and combinatoric background components.

7.4.5 Likelihood Fit Implementation

Setup

The $B_s^0 \to J/\psi K_S^0$ and $B^0 \to J/\psi K_S^0$ *CP* observables are determined from a simultaneous unbinned maximum likelihood fit of the long and downstream K_S^0 samples, using both the OS and SSK tagging information. In addition to the five *CP* observables also the nuisance parameters describing the mass (9 parameters), acceptance (12), background decay time (6) and event yields (6) are floated in the fit. The observables Δm_d, τ_{B^0}, Δm_s, $\tau_{B_s^0}$ and $\Delta\Gamma_s$, parametrising the B^0 and B_s^0 meson systems,

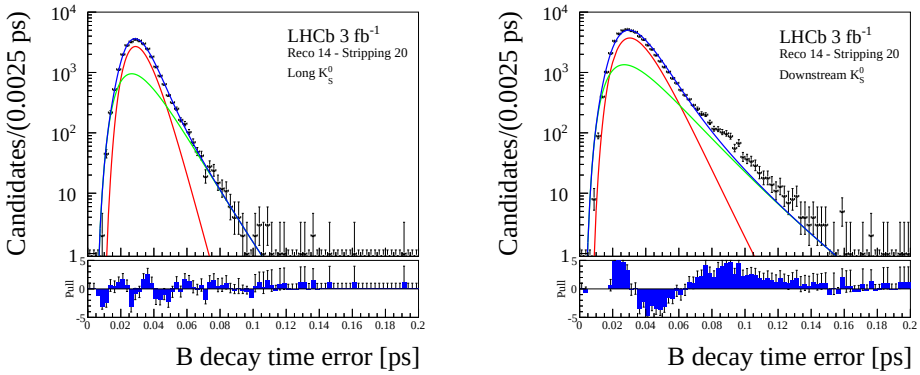

Figure 7.14: Per-candidate decay time uncertainty estimate distribution in the Long K^0_S [Left] and Downstream K^0_S [Right] sample. The overlaid fit projections of a double log-normal function are not used in the likelihood fit.

and the effective B production asymmetries $A^{\text{eff}}_{\text{prod}}(B^0)$ and $A^{\text{eff}}_{\text{prod}}(B^0_s)$ of the long and downstream K^0_S samples are constrained using Gaussian functions. The statistical and systematic uncertainties on the constrained parameters are added in quadrature and treated together. Also the correlation $\rho(\Gamma_s, \Delta\Gamma_s) = -0.271$ [121] between the average decay width and decay width difference of the B^0_s meson is included.

The production asymmetries are defined in terms of the B production cross-section $\sigma(B)$ as

$$A_{\text{prod}}(B) \equiv \frac{\sigma(\bar{B}) - \sigma(B)}{\sigma(\bar{B}) + \sigma(B)}\,. \tag{7.25}$$

The effective B production asymmetries, specific to the data sample used in this analysis, are obtained by reweighting the physical production asymmetries $A_{\text{prod},i}(B)$ measured in bins of B transverse momentum and pseudo-rapidity as

$$A^{\text{eff}}_{\text{prod}}(B) \equiv \sum_{\text{Bins i}} f_i A_{\text{prod},i}(B)\,, \qquad f_i \equiv \frac{\#B^0 \in \text{Bin i}}{N_{B^0}}\,. \tag{7.26}$$

Here f_i is the fraction of B^0 events in bin i, obtained by summing over the ${}_s\mathcal{W}$eights obtained from a fit to the mass distribution of the nominal data sample. Because of the small $B^0_s \to J/\psi K^0_S$ yield and the associated limited precision that can be obtained with is ${}_s\mathcal{W}$eights, the $B^0 \to J/\psi K^0_S$ ${}_s\mathcal{W}$eights are used to calculate both the B^0 and B^0_s asymmetries. The physical production asymmetries that serve as input to Eq. (7.26) are measured for the 2011 run conditions in Ref. [173]. The systematic

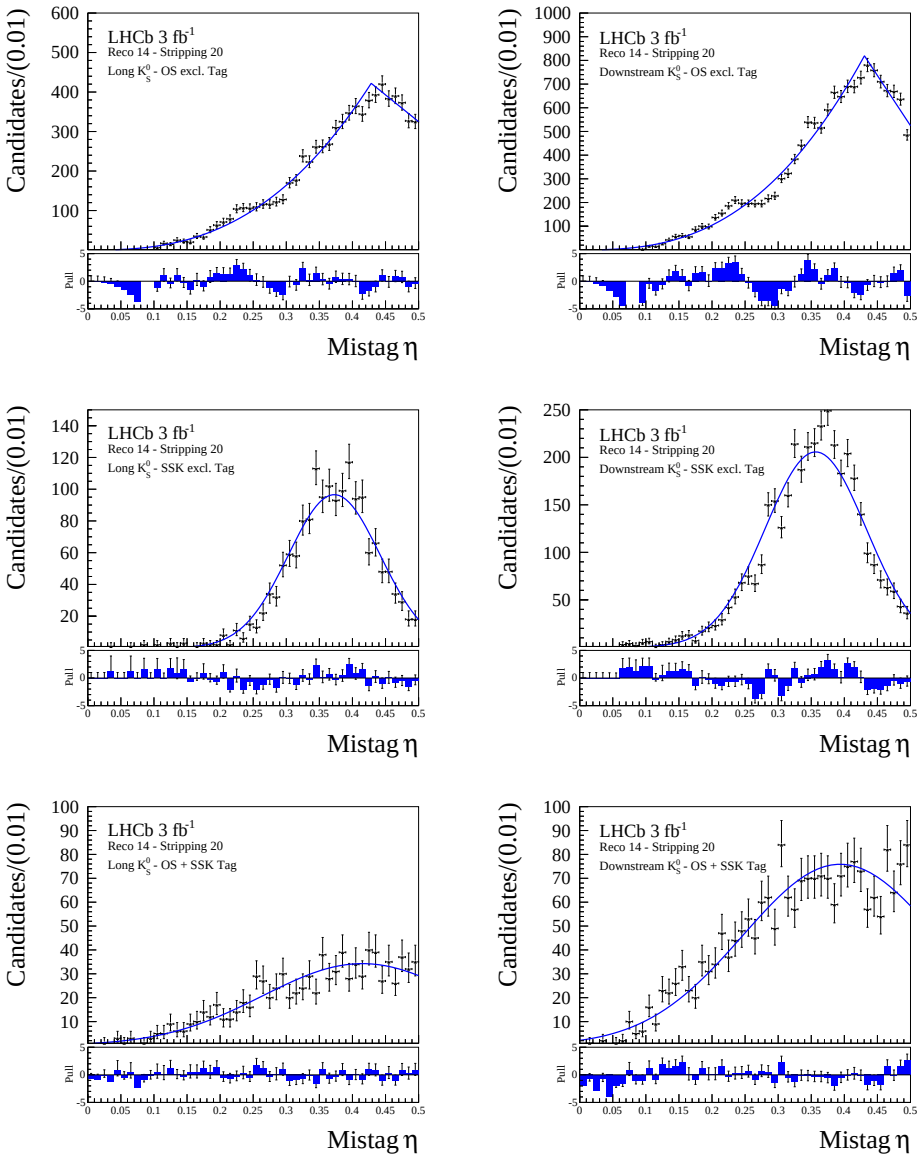

Figure 7.15: Per-candidate mistag estimate distribution in the Long K_S^0 [Left] and Downstream K_S^0 [Right] sample. The histograms are determined separately for the exclusively OS tagged [Top], exclusively SSK tagged [Middle] and OS+SSK tagged [Bottom] events. The overlaid fit projections are not used in the likelihood fit.

Table 7.8: Effective B production asymmetries specific to the data sample used in this analysis.

Sample	Mode	Value
Long K^0_S	B^0	$-0.0117 \pm 0.0057\,(\text{stat}) \pm 0.0013\,(\text{syst})$
Downstream K^0_S	B^0	$-0.0095 \pm 0.0051\,(\text{stat}) \pm 0.0013\,(\text{syst})$
Long K^0_S	B^0_s	$-0.041 \pm 0.032\,(\text{stat}) \pm 0.003\,(\text{syst})$
Downstream K^0_S	B^0_s	$-0.022 \pm 0.024\,(\text{stat}) \pm 0.003\,(\text{syst})$

correlations $\rho_{\text{syst}}(B^0) = 0.0013$ and $\rho_{\text{syst}}(B^0_s) = 0.0030$ between the different $A_{\text{P},i}(B)$ results found in this analysis are taken into account in the reweighting procedure, whose results are listed in Table 7.8. As no significant difference is observed in the total physical production asymmetries for the 2011 and 2012 data taking conditions [195], the results listed in Table 7.8 are used for the 2012 data as well, without applying further corrections.

Fit Validation

Validation of the likelihood implementation has been performed *blinded* to avoid (un)consciously influencing the results of the fit towards certain preferred outcomes. This is done by adding a random and unknown offset to the five *CP* observables determined in the fit, which is only removed after the analysis has been scrutinised by the LHCb collaboration.

The likelihood fit is cross-checked using two independent implementations that both use the individual PDF components described above. These two implementation differ in the way the tagging information is included in the PDF, and in particular on how the OS and SSK tag responses are combined. For the implementation made by the author, the procedure is described in Section 7.3, while for the alternative implementation made by the LHCb group at the TU Dortmund, it is documented in Ref. [190]. Small differences[f] in the nominal fit results obtained with both fitters can be traced back to the treatment of the combined OS and SSK tag decision in the two fitters. Both implementations have been validated with large sets of pseudo-experiments to thoroughly test several aspects of the analysis. These tests also include the use of stand-alone event generators that produce toy data samples independently of the fit implementations.

In addition, the fit model has been tested on simulated data, with signal only and with both signal and background components present. The results from the

[f] These differences are less than 5% of the statistical uncertainty associated with the parameter in question, and can hence be considered negligible.

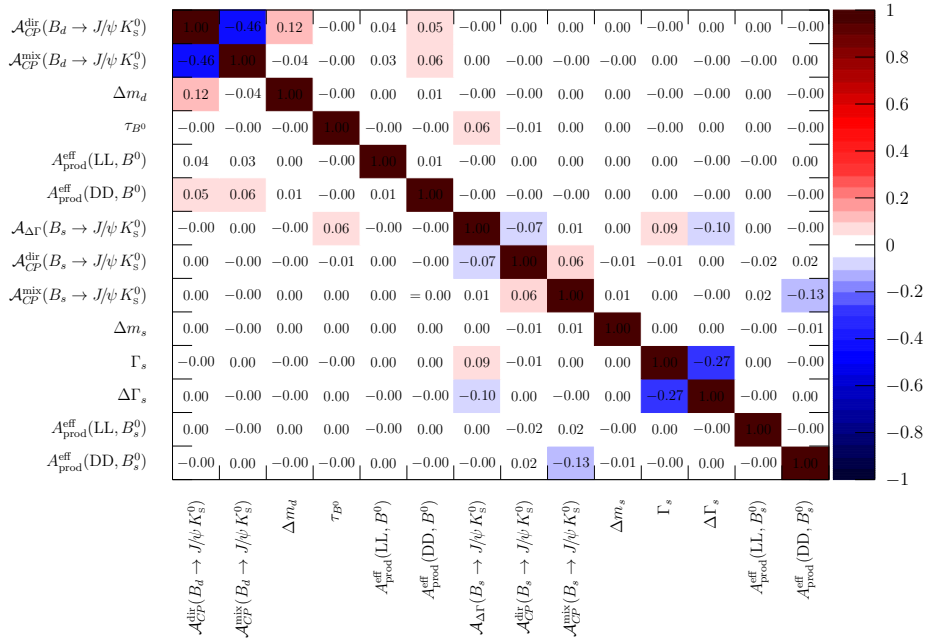

Figure 7.16: Correlation matrix for the likelihood fit to the data.

fit to the full data sample are compared to those from various subsamples, and to those obtained from a weighted fit to the $B_s^0 \to J/\psi K_S^0$ candidates only. All tests agree with the expectations and no biases in the fit are found.

7.4.6 Fit results

The results for the $B^0 \to J/\psi K_S^0$ and $B_s^0 \to J/\psi K_S^0$ *CP* asymmetry parameters are summarised in Table 7.9. This table includes both the results obtained from the likelihood implementation described in this Chapter (Method I), and those obtained from the alternative implementation (Method II). The latter are also published by LHCb in Ref. [46]. Both implementations (necessarily) give compatible results, where the largest relative difference is found in the $\mathcal{A}_{CP}^{\rm dir}(B^0 \to J/\psi K_S^0)$ observable. The results for the two $B^0 \to J/\psi K_S^0$ *CP* asymmetries are compatible with the BaBar [196], Belle [24] and latest LHCb [74] results. The statistical correlations between the $B_s^0 \to J/\psi K_S^0$ *CP* observables are $\rho(\mathcal{A}_{\Delta\Gamma}, \mathcal{A}_{CP}^{\rm dir}) = -0.07$, $\rho(\mathcal{A}_{\Delta\Gamma}, \mathcal{A}_{CP}^{\rm mix}) = 0.01$ and $\rho(\mathcal{A}_{CP}^{\rm dir}, \mathcal{A}_{CP}^{\rm mix}) = 0.06$. The (reduced) correlation matrix, containing all relevant correlations with $\mathcal{A}_{\Delta\Gamma}$, $\mathcal{A}_{CP}^{\rm dir}$ and $\mathcal{A}_{CP}^{\rm mix}$, is given in Fig. 7.16.

Table 7.9: Comparison between the results for the five *CP* asymmetries obtained from the likelihood implementation described in this Chapter (Method I) and those obtained with the alternative implementation [46] (Method II). The uncertainties are statistical only.

Parameter	Method I	Method II
$\mathcal{A}_{CP}^{\text{dir}}\left(B_d \to J/\psi K_S^0\right)$	-0.015 ± 0.036 (stat.)	-0.028 ± 0.034 (stat.)
$\mathcal{A}_{CP}^{\text{mix}}\left(B_d \to J/\psi K_S^0\right)$	-0.718 ± 0.035 (stat.)	-0.719 ± 0.034 (stat.)
$\mathcal{A}_{\Delta\Gamma}\left(B_s \to J/\psi K_S^0\right)$	$0.49 \pm {}^{0.76}_{0.65}$ (stat.)	$0.49 \pm {}^{0.77}_{0.65}$ (stat.)
$\mathcal{A}_{CP}^{\text{dir}}\left(B_s \to J/\psi K_S^0\right)$	-0.28 ± 0.41 (stat.)	-0.28 ± 0.41 (stat.)
$\mathcal{A}_{CP}^{\text{mix}}\left(B_s \to J/\psi K_S^0\right)$	0.10 ± 0.40 (stat.)	0.08 ± 0.40 (stat.)

Table 7.10: Values for the nuisance parameters describing the mass, acceptance and background decay time distributions, obtained from the likelihood fit to data.

Parameter	Long K_S^0	Downstream K_S^0
μ_{B^0}	5280.667 ± 0.046	5281.433 ± 0.039
λ	-3.17 ± 0.19	-2.83 ± 0.12
σ	8.071 ± 0.081	9.402 ± 0.078
Bkg slope	-0.00329 ± 0.00046	-0.00313 ± 0.00021
$m_{B_s^0} - m_{B^0}$	87.12 ± 0.34	
acc_0	0.211 ± 0.044	0.162 ± 0.023
acc_1	0.339 ± 0.069	0.266 ± 0.036
acc_2	0.61 ± 0.12	0.339 ± 0.042
acc_3	0.88 ± 0.17	0.654 ± 0.084
acc_4	1.03 ± 0.18	1.06 ± 0.12
acc_5	0.73 ± 0.22	0.86 ± 0.16
f_{bkg}	0.272 ± 0.060	0.103 ± 0.019
τ_{bkg}	0.203 ± 0.058	0.174 ± 0.035
r_{bkg}	9.2 ± 2.3	10.1 ± 2.0

The nuisance parameters describing the mass, acceptance and background decay time distributions are summarised in Table 7.10. The observed event yields are summarised in Table 7.11, and the fit projections for the mass and decay time distributions are shown in Figs. 7.17 and 7.18, respectively.

Table 7.11: Yields from the unbinned maximum likelihood fit. The uncertainties are statistical only.

Yield	Long K_S^0	Downstream K_S^0
$B_d \to J/\psi K_S^0$	$27\,801 \pm 168$	$51\,351 \pm 231$
$B_s \to J/\psi K_S^0$	307 ± 20	601 ± 30
Combinatorial background	658 ± 37	$2\,852 \pm 74$

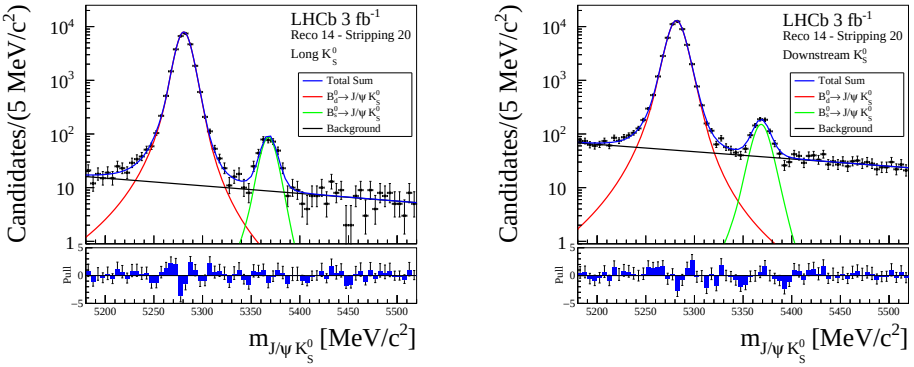

Figure 7.17: Invariant $J/\psi K_S^0$ mass distribution in the long [Left] and downstream [Right] K_S^0 sample. The shown fit projections are: Total [Blue], $B^0 \to J/\psi K_S^0$ [Red], $B_s^0 \to J/\psi K_S^0$ [Green] and combinatoric background [Black].

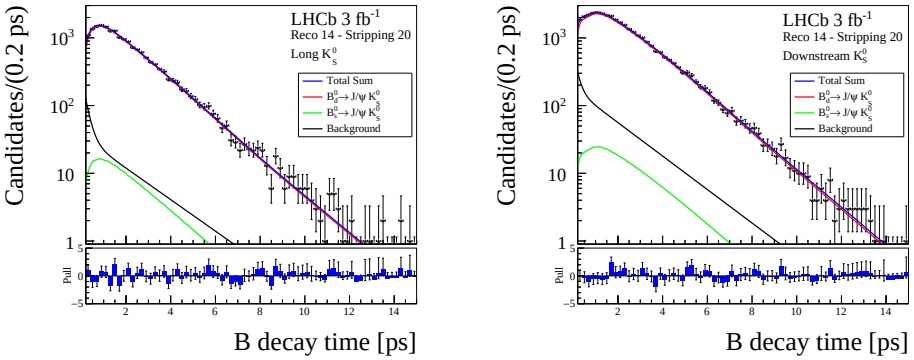

Figure 7.18: Decay time distribution of the B candidates in the long [Left] and downstream [Right] K_S^0 sample. The shown fit projections are: Total [Blue], $B^0 \to J/\psi K_S^0$ [Red], $B_s^0 \to J/\psi K_S^0$ [Green] and combinatoric background [Black].

7.5 Systematic Uncertainties

A number of systematic uncertainties affecting the determination of the $B_s^0 \to J/\psi K_S^0$ *CP* observables and the ratio of event yields R are considered. The main sources of systematic uncertainty are due to assumptions for modelling the different components of the multivariate PDF. These uncertainties are estimated using large sets of simulated pseudo-experiments, in which the shapes and parameters[g] of the individual PDF components are varied.

Method

In the generation of the pseudo-experiments, the values of the parameters are fixed to the ones obtained in the fit to the data, i.e. the nominal setup. For each individual pseudo-experiment, the fitted values of the *CP* observables and event yields are compared between a nominal fit and a second fit in which some of the shapes or nuisance parameters are varied, i.e. the alternative setup. The resulting differences $\mu \equiv x_{\text{nom}} - x_{\text{alt}}$ between both fit values form a Gaussian-like distribution, as illustrated in Fig. 7.19. The uncertainty σ_{syst} due to the preference for the nominal fit setup over the alternative option can then be determined from the mean and width of this distribution as

$$\sigma_{\text{syst}} \equiv \sqrt{\langle \mu \rangle^2 + \sigma_{\text{shift}}^2}\,. \tag{7.27}$$

The average shift $\langle \mu \rangle$ quantifies the bias that using another setup, here represented by the alternative option, would introduce to the measurement of the parameter of interest. The width σ_{shift} of the μ distribution quantifies the ignorance regarding the true accuracy of the uncertainty estimation: a specific choice of fit model might result in an artificially larger or smaller uncertainty compared to other equally valid models.

Modelling

Following the above strategy, the systematic uncertainty due to the chosen mass model is evaluated by varying the Hypatia tail parameters within their uncertainties, replacing the signal model with a double Crystal Ball function [197], and replacing the background model with a second-order Chebychev polynomial. The latter variation has the largest impact on the *CP* observables and yield ratio, and is used to assign a systematic uncertainty.

The systematic uncertainty associated with the decay time resolution is evaluated by varying the dilution of the resolution model, through changes of the resolution parameters, and by comparing the nominal model with one that includes

[g] The impact of a fixed input parameter x with associated total uncertainty σ is studied by varying its value up or down to $x_\pm = \langle x \rangle \pm \sigma$.

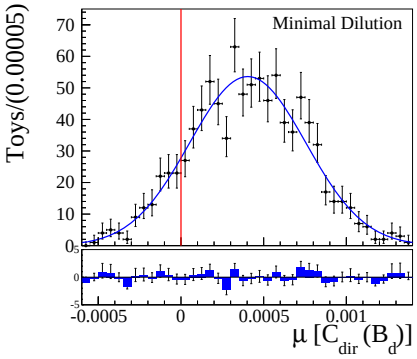

Figure 7.19: Illustration of a μ distribution used to evaluated the systematic uncertainties due to modelling. This specific plot shows the μ distribution for $\mathcal{A}_{CP}^{\text{dir}}(B^0 \to J/\psi K_S^0)$ when changing the decay time resolution model to the one with the smallest dilution still compatible with the data.

a scale offset in the calibration functions for the per-candidate decay time uncertainty estimates. The largest impact on the *CP* observables and yield ratio originates from the limited knowledge on the decay time resolution of the long K_S^0 sample. This forms the dominant systematic uncertainty to the $B_s^0 \to J/\psi K_S^0$ *CP* observables.

Systematic effects due to the modelling of the decay time acceptance mainly affect $\mathcal{A}_{\Delta\Gamma}$, and are evaluated by varying the position and number of knots that define the empirical model for $\mathcal{E}(t)$.

The systematic uncertainty associated with the tagging calibration is obtained by comparing the nominal calibration with the largest and smallest effective tagging efficiency that can be obtained through changes of the calibration parameters within their respective uncertainties.

In the nominal fit, the mass resolution of the $B^0 \to J/\psi K_S^0$ and $B_s^0 \to J/\psi K_S^0$ signal modes is assumed to be identical, but it could depend on the q^2 value of the decay, and thus on the mass of the reconstructed B candidate. This effect is studied by multiplying the width of the $B_s^0 \to J/\psi K_S^0$ mass PDF by different scale factors, obtained by comparing the $B^0 \to J/\psi K_S^0$ and $B_s^0 \to J/\psi K_S^0$ signal shapes in simulation. These variations mainly affect the ratio of event yields.

Finally, a correlation between the reconstructed B mass and decay time resolution is observed in simulated data. The impact of neglecting this correlation in the nominal fit to data is also evaluated with the simulated experiments.

The total systematic uncertainty and its sources are summarised in Table 7.12.

Table 7.12: Summary of the systematic uncertainties on the $B_s^0 \to J/\psi K_S^0$ *CP* observables and the ratio of event yields R.

Source	$\mathcal{A}_{\Delta\Gamma}$	$\mathcal{A}_{CP}^{\text{dir}}$	$\mathcal{A}_{CP}^{\text{mix}}$	Long $R \times 10^5$	Downstream $R \times 10^5$
Mass modelling	0.045	0.009	0.009	15.5	17.2
Decay-time resolution	0.038	0.066	0.070	0.6	0.3
Decay-time acceptance	0.022	0.004	0.004	0.6	0.5
Tagging calibration	0.002	0.021	0.023	0.1	0.2
Mass resolution	0.010	0.005	0.006	12.6	8.0
Mass–time correlation	0.003	0.037	0.036	0.2	0.1
Total	0.064	0.079	0.083	20.0	19.0

7.6 Branching Ratio Measurement

The measured ratio of branching fractions is calculated from the event yields using Eq. (7.1), which thus requires further input on the correction factor f_{sel}.

Selection Efficiencies

Although the event selection is not designed to differentiate between $B^0 \to J/\psi K_S^0$ and $B_s^0 \to J/\psi K_S^0$ decays, this does not guarantee that it treats them in a completely identical way. For the branching ratio update it is therefore necessary to correct the measured event yields for any differences in the overall selection efficiency between both decay channels. These differences can in principle depend on the centre-of-mass energy of the pp collisions, and on the specific run conditions with which the data was taken. They are therefore determined separately for the 2011/7 TeV and 2012/8 TeV data samples. The selection efficiencies are determined from simulation, and corrected for differences between data and simulation.

The contributing factors to the total selection efficiency ϵ_{sel} are: the geometrical acceptance of the LHCb detector $\epsilon_{\text{Geo.}}$ with respect to the final state particles originating from the B decay, the trigger and reconstruction efficiency $\epsilon_{\text{Reco.}}$, and the efficiencies of the initial ϵ_{Init} and multivariate selections ϵ_{MVA1} and ϵ_{MVA2}. It can thus be decomposed as

$$\epsilon_{\text{sel}} = \epsilon_{\text{Geo.}} \times \epsilon_{\text{Reco.}} \times \epsilon_{\text{Init}} \times \epsilon_{\text{MVA1}} \times \epsilon_{\text{MVA2}} \,. \tag{7.28}$$

Comparing the $B^0 \to J/\psi K_S^0$ and $B_s^0 \to J/\psi K_S^0$ selection efficiencies leads to a correction factor

$$f_{\text{MC}} \equiv \epsilon_{\text{Sel}}(B^0)/\epsilon_{\text{Sel}}(B_s^0) \,, \tag{7.29}$$

which for the long (LL) and downstream (DD) K_S^0 samples is given by

$$f_{\mathrm{MC}}^{\mathrm{LL}}(2011) = 0.973 \pm 0.014\,, \qquad f_{\mathrm{MC}}^{\mathrm{DD}}(2011) = 0.986 \pm 0.010\,, \tag{7.30}$$

$$f_{\mathrm{MC}}^{\mathrm{LL}}(2012) = 0.973 \pm 0.015\,, \qquad f_{\mathrm{MC}}^{\mathrm{DD}}(2012) = 0.990 \pm 0.010\,. \tag{7.31}$$

Because the nominal fit does not differentiate between the 2011 and 2012 data samples, these results are combined, using a weighted average to take into account the 1:2 relative abundance of the two samples, into a single efficiency

$$f_{\mathrm{MC}}^{\mathrm{LL}} = 0.973 \pm 0.010\,, \qquad f_{\mathrm{MC}}^{\mathrm{DD}} = 0.9885 \pm 0.0070\,. \tag{7.32}$$

The acceptance effects discussed in Section 7.4.3 do not only affect time-dependent measurements but also the time-integrated event yield, as only the fraction $\epsilon_{\mathcal{B}}$ of the total branching ratio is experimentally measured, i.e.

$$\mathcal{B}(B \to f)_{\mathrm{measured}} \equiv \frac{1}{2}\int_0^\infty \mathcal{E}(t) \times \langle \Gamma(B(t) \to f) \rangle \,\mathrm{d}t\,, \tag{7.33}$$

$$\equiv \epsilon_{\mathcal{B}} \times \mathcal{B}(B \to f)\,. \tag{7.34}$$

This fraction $\epsilon_{\mathcal{B}}$ is included in the overall selection efficiency (7.28) determined in simulation, but depends crucially on the lifetime τ, decay width difference $\Delta\Gamma$, the shape of the acceptance function $\mathcal{E}(t)$, and value of the *CP* asymmetry $\mathcal{A}_{\Delta\Gamma}$, which all differ between data and simulation. A correction factor

$$f_{\mathrm{corr}} \equiv \frac{\epsilon_{\mathcal{B}}^{\mathrm{Data}}(B^0)/\epsilon_{\mathcal{B}}^{\mathrm{Data}}(B_s^0)}{\epsilon_{\mathcal{B}}^{\mathrm{MC}}(B^0)/\epsilon_{\mathcal{B}}^{\mathrm{MC}}(B_s^0)} \tag{7.35}$$

thus needs to be applied to the selection efficiency ratio f_{MC} determined from simulation. The found correction factors are

$$f_{\mathrm{corr}}^{\mathrm{LL}} = 0.999 \pm 0.028\,, \qquad f_{\mathrm{corr}}^{\mathrm{DD}} = 0.998 \pm 0.040\,, \tag{7.36}$$

for the long and downstream K_S^0 samples, respectively.

The overall correction factor $f_{\mathrm{sel}} \equiv f_{\mathrm{corr}} \times f_{\mathrm{MC}}$ for the long and downstream K_S^0 samples is then given by

$$f_{\mathrm{sel}}^{\mathrm{LL}} = 0.972 \pm 0.029\,, \qquad f_{\mathrm{sel}}^{\mathrm{DD}} = 0.987 \pm 0.040\,. \tag{7.37}$$

Results

Combining the results in Table 7.11 with the systematic uncertainties in Table 7.12 yields

$$R^{\mathrm{LL}} = 0.01104 \pm 0.00072\,(\mathrm{stat.}) \pm 0.00020\,(\mathrm{syst.})\,, \tag{7.38}$$

$$R^{\mathrm{DD}} = 0.01170 \pm 0.00059\,(\mathrm{stat.}) \pm 0.00019\,(\mathrm{syst.})\,, \tag{7.39}$$

for the ratio of event yields in the long and downstream K^0_S samples, respectively. The results are multiplied with the selection efficiencies given in Eq. 7.37, and a weighted average of the combinations $R \times f_{\text{sel}}$ for the long and downstream K^0_S samples is performed, assuming that they are uncorrelated measurements. Multiplying this average with the ratio $f_s/f_d = 0.259 \pm 0.015$ [159, 160] of the B^0_s to B^0 meson production fractions, the measured ratio of branching fractions is then given by

$$\frac{\mathcal{B}(B_s \to J/\psi K^0_S)}{\mathcal{B}(B_d \to J/\psi K^0_S)} = 0.0431 \pm 0.0017\,(\text{stat.}) \pm 0.0012\,(\text{syst.}) \pm 0.0025\,(f_s/f_d)\,. \quad (7.40)$$

Combining the ratio of branching fractions with the known $B^0 \to J/\psi K^0$ branching fraction $\mathcal{B}(B_d \to J/\psi K^0) = (8.97 \pm 0.35) \times 10^{-4}$ [64], which accounts for the difference in production rates for the B^+B^- and $B^0\bar{B}^0$ pairs at the $\Upsilon(4S)$ resonance, i.e. $\Gamma(B^+B^-)/\Gamma(B^0\bar{B}^0) = 1.058 \pm 0.024$ [121], the $B^0_s \to J/\psi K^0_S$ branching fraction is

$$\begin{aligned}\mathcal{B}(B_s \to J/\psi K^0_S) = [&1.93 \pm 0.08\,(\text{stat.}) \pm 0.05\,(\text{syst.}) \\ &\pm 0.11\,(f_s/f_d) \pm 0.07\,(\mathcal{B}(B_d \to J/\psi K^0))] \times 10^{-5}\,, \end{aligned} \quad (7.41)$$

where the last uncertainty comes from the $B^0 \to J/\psi K^0$ branching fraction.

7.7 *CP* Asymmetry Measurements

For the final discussion regarding the experimental measurement of the *CP* asymmetry parameters, we now move to the official LHCb results published in Ref. [46], which are obtained by the alternative implementation (Method II) mentioned earlier.

Point Estimates

The $B^0_s \to J/\psi K^0_S$ *CP* asymmetry parameters are given by [46]

$$\mathcal{A}_{\Delta\Gamma}\left(B_s \to J/\psi K^0_S\right) = \quad 0.49 \pm {}^{0.77}_{0.65}\,(\text{stat.}) \pm 0.06\,(\text{syst.})\,, \quad (7.42)$$

$$\mathcal{A}^{\text{dir}}_{CP}\left(B_s \to J/\psi K^0_S\right) = -0.28 \pm 0.41\,(\text{stat.}) \pm 0.08\,(\text{syst.})\,, \quad (7.43)$$

$$\mathcal{A}^{\text{mix}}_{CP}\left(B_s \to J/\psi K^0_S\right) = \quad 0.08 \pm 0.40\,(\text{stat.}) \pm 0.08\,(\text{syst.})\,. \quad (7.44)$$

The large statistical uncertainties on these results do not yet allow for a conclusive comparison with the predictions in Eqs. (5.70)–(5.72), nor do they provide constraints on the shift parameter $\Delta\phi_d$ affecting the *CP* asymmetries in $B^0 \to J/\psi K^0_S$.

Confidence Intervals Obtained with the Feldman–Cousins Method

To study the stability of the likelihood implementation, pseudo-experiments are performed with alternative assumptions for the values of the $B_s^0 \to J/\psi K_S^0$ *CP* asymmetries. In cases where values of the direct and mixing-induced *CP* asymmetries $\mathcal{A}_{CP}^{\text{dir}}$ and $\mathcal{A}_{CP}^{\text{mix}}$ are close to the physical boundaries overcoverage of up to 20% is observed, even though the fit values of the three $B_s^0 \to J/\psi K_S^0$ *CP* asymmetries are not constrained in the likelihood fit.

To obtain confidence intervals not affected by overcoverage, regardless of the central values of $\mathcal{A}_{CP}^{\text{dir}}$ and $\mathcal{A}_{CP}^{\text{mix}}$, the so called Feldman–Cousins method [198, 199] is utilised. The method uses the Neyman construction for confidence bands, and derives intervals $[\mu_1, \mu_2]$ for a parameter of interest μ by applying likelihood ratio ordering. The objective of this method is the construction of a "1 – CL" curve, which gives the probability of finding the observed result or a more extreme value, i.e. the *p*-value, as a function of μ. The interval with the desired confidence level (CL) can then be obtained from the intersection of this curve with the constant function of value 1 – CL.

The strategy to construct the "1 – CL" curve works as follows. For each scan point μ_0 of the parameter μ, the difference

$$\Delta\chi^2 = 2\mathcal{L}_{\text{best}} - 2\mathcal{L}_{\mu=\mu_0} \tag{7.45}$$

between the likelihood $\mathcal{L}_{\text{best}}$ of the nominal fit and the likelihood $\mathcal{L}_{\mu=\mu_0}$ of a fit where $\mu = \mu_0$ is fixed is computed. Next, a large set of N_{toy} pseudo-experiments is generated with $\mu = \mu_0$ as input. Each toy is fitted twice, once with $\mu = \mu_0$ fixed and once with μ left free in the fit, and the equivalent $\Delta\chi^2$ difference is calculated. The "1 – CL" value for the point μ_0 is now given as the fraction of pseudo-experiments whose $\Delta\chi^2$ value exceeds that in data, i.e.

$$1 - \text{CL}(\mu_0) \equiv \frac{N(\Delta\chi^2_{\text{data}}(\mu_0) < \Delta\chi^2_{\text{toy}}(\mu_0))}{N_{\text{toy}}}\,. \tag{7.46}$$

Systematic uncertainties, described in Section 7.5, are added directly to the likelihood by means of Gaussian functions, following the method in Ref. [199]. The resulting 68.3% confidence level intervals for the $B_s^0 \to J/\psi K_S^0$ *CP* asymmetries are

$$\mathcal{A}_{\Delta\Gamma}\left(B_s \to J/\psi K_S^0\right) \in [-0.15, 1.21]\,@\,68\,\%\ \text{C.L.}\,, \tag{7.47}$$

$$\mathcal{A}_{CP}^{\text{dir}}\left(B_s \to J/\psi K_S^0\right) \in [-0.68, 0.14]\,@\,68\,\%\ \text{C.L.}\,, \tag{7.48}$$

$$\mathcal{A}_{CP}^{\text{mix}}\left(B_s \to J/\psi K_S^0\right) \in [-0.31, 0.48]\,@\,68\,\%\ \text{C.L.}\,. \tag{7.49}$$

These values are in very good agreement with the point estimates reported above. Confidence level plots for the three $B_s^0 \to J/\psi K_S^0$ *CP* asymmetries are given in

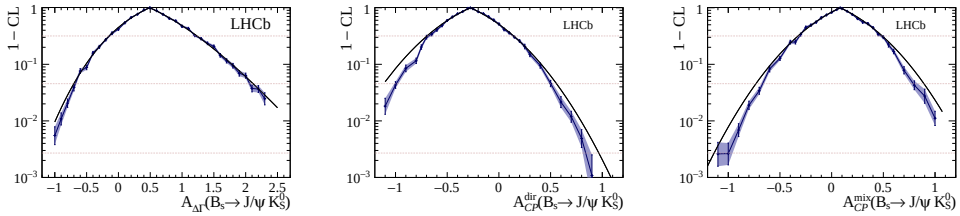

Figure 7.20: Confidence level contours obtained with the Feldman–Cousins method [Blue] [198, 199] for the three $B^0_s \to J/\psi K^0_S$ *CP* asymmetries: $\mathcal{A}_{\Delta\Gamma}$ [Left], $\mathcal{A}^{\text{dir}}_{CP}$ [Middle], $\mathcal{A}^{\text{mix}}_{CP}$ [Right]. The expectation from the likelihood profile [Black] is shown as well.

Fig. 7.20. For the $\mathcal{A}^{\text{dir}}_{CP}$ and $\mathcal{A}^{\text{mix}}_{CP}$ asymmetries, deviations from the likelihood profile expectation become apparent at larger confidence levels.

8 Conclusion

To achieve high precision determinations of the B^0_q–$\bar{B}^0_q$ mixing phases ϕ_d and ϕ_s from the *CP* asymmetry parameters of the $B^0 \to J/\psi K^0_S$ and $B^0_s \to J/\psi\,\phi$ decays, respectively, controlling higher order hadronic corrections, originating from doubly Cabibbo-suppressed penguin topologies, becomes mandatory. In view of the non-perturbative long-distance QCD contributions to these corrections, it is not possible to calculate them directly within the quantum field theory framework. In this thesis, we have therefore outlined and explored an alternative strategy to control the penguin effects. This strategy relies on the $SU(3)_F$ flavour symmetry of QCD to relate the hadronic matrix elements appearing in the $B^0 \to J/\psi K^0_S$ and $B^0_s \to J/\psi\,\phi$ decay amplitudes with those of similar decay modes in which they can be estimated directly from the experimentally available data.

The research reported in this thesis consists of a theoretical and an experimental part, which both aim to advance our understanding of the penguin corrections affecting the $B^0 \to J/\psi K^0_S$ and $B^0_s \to J/\psi\,\phi$ decays. On the theoretical side, we explored the potential of the $SU(3)_F$ symmetry based method, while the experimental half of the research focused on the measurement of the decay channel $B^0_s \to J/\psi K^0_S$, using data collected by the LHCb experiment.

The most promising tool to control the penguin contributions affecting the $B^0 \to J/\psi K^0_S$ decay is the U-spin symmetry relation with the $B^0_s \to J/\psi K^0_S$ mode. This strategy requires precision measurements of the *CP* asymmetry parameters in the latter decay channel, which are currently not yet available. In anticipation of these measurements, which can be expected towards the end of the LHCb upgrade programme, we have performed a global fit to currently available *CP* asymmetry and branching ratio information on the $B^0 \to J/\psi K^0_S$, $B^0_s \to J/\psi K^0_S$, $B^+ \to J/\psi K^+$, $B^+ \to J/\psi \pi^+$ and $B^0 \to J/\psi \pi^0$ modes. These $B \to J/\psi(\pi/K)$ modes have similar decay dynamics as the $B^0 \to J/\psi K^0_S$ decay, and can thus already be used to constrain the hadronic penguin contributions affecting the $B^0 \to J/\psi K^0_S$ channel. The main results of this fit are

$$a = 0.17^{+0.14}_{-0.12}\,, \qquad \theta = (179.3 \pm 4.2)^\circ\,, \qquad \phi_d = (43.9 \pm 1.7)^\circ\,, \tag{8.1}$$

and correspond to a penguin shift

$$\Delta\phi_d^{J/\psi K_S^0} = -\left(1.03^{+0.69}_{-0.85}\right)^\circ . \tag{8.2}$$

affecting the relation between $\phi^{\text{eff}}_{d,J/\psi K_S^0}$ and ϕ_d. In addition to this global fit, we have also illustrated the potential of the $B_s^0 \to J/\psi K_S^0$ mode for the future LHCb upgrade era using a benchmark scenario, and discussed a strategy to probe non-factorisable U-spin-breaking effects between the $B^0 \to J/\psi K_S^0$ and $B_s^0 \to J/\psi K_S^0$ decays.

For the $B_s^0 \to J/\psi\phi$ decay, the penguin contributions can be controlled through the $SU(3)_F$ symmetry relation with the $B^0 \to J/\psi\rho^0$ and $B_s^0 \to J/\psi\overline{K}^{*0}$ modes. We have discussed the potential of these two decays and studied the implications of the first LHCb measurement of the $B^0 \to J/\psi\rho^0$ *CP* asymmetry parameters. Taking into account possible penguin effects in the required input for ϕ_d, i.e. using the value given in Eq. (8.1), we found the following polarisation-independent results

$$a_{J/\psi\rho} = 0.039^{+0.095}_{-0.039}, \qquad \theta_{J/\psi\rho} = -\left(58^{+154}_{-121}\right)^\circ . \tag{8.3}$$

Also the picture emerging from the polarisation-dependent measurements has been explored, and gives results compatible with Eq. (8.3). In view of the excellent precision that can already be obtained with the current data, the $B^0 \to J/\psi\rho^0$ mode is expected to play the key role for the control of the penguin effects in the determination of ϕ_s. To fully benefit from the experimentally available data, we therefore proposed a new strategy for the $B_s^0 \to J/\psi\overline{K}^{*0}$ decay. We suggest to combine the information of the $B^0 \to J/\psi\rho^0$ and $B_s^0 \to J/\psi\overline{K}^{*0}$ modes into a global fit, which would then no longer require knowledge on the form factors for the interpretation of the decay rate information. Instead, the hadronic parameters can be obtained directly from the experimental data, which offers new insights into the non-factorisable $SU(3)$-breaking effects related to these modes. Adding also branching ratio information on the $B_s^0 \to J/\psi\rho^0$ decay, which is currently not yet available, the impact of additional decay topologies, i.e. penguin-annihilation and exchange contributions, which are expected to be small, can be experimentally probed.

To maximise the potential for finding new physics in B_q^0–$\overline{B}_q^0$ mixing, it will be crucial to perform simultaneous high-precision measurements of the phases ϕ_d and ϕ_s at the LHCb and Belle II experiments. We therefore proposed a combined analysis of the $B^0 \to J/\psi K_S^0$, $B_s^0 \to J/\psi K_S^0$, $B_s^0 \to J/\psi\phi$, $B^0 \to J/\psi\rho^0$ and $B_s^0 \to J/\psi\overline{K}^{*0}$ decays, in order to take into account the cross-correlations between these modes.

Regarding the experimental research, this thesis described the study of the $B_s^0 \to J/\psi K_S^0$ decay performed using data samples corresponding to an integrated luminosity of up to 3.0 fb^{-1} of pp collisions recorded by the LHCb detector between 2010 and 2012 at centre-of-mass energies of 7 and 8 TeV. The study consisted of three consecutive steps, using increasingly larger data samples, each adding a new

layer of complexity to the analysis. These steps focus respectively on the event selection, the untagged decay time distribution and the tagged decay time distribution, and resulted in measurements of the $B_s^0 \to J/\psi K_S^0$ branching fraction, effective lifetime and *CP* asymmetry parameters. The event selection uses a two-stage artificial neural network to suppress both the misreconstructed and the combinatoric background. The stage that differentiates between the signal and background candidates is trained entirely on data, using the $B^0 \to J/\psi K_S^0$ signal to represent the distinguishing features of the $B_s^0 \to J/\psi K_S^0$ decay. For the tagged analysis, per-candidate observables for the decay time resolution and wrong-tag probability, and information from both the opposite side and same-side kaon taggers is used to maximise the sensitivity to the *CP* observables. The final result for the ratio of time-integrated branching fractions between the $B_s^0 \to J/\psi K_S^0$ and $B^0 \to J/\psi K_S^0$ mode, measured using the full 3.0 fb^{-1} data sample, is given by

$$\frac{\mathcal{B}(B_s \to J/\psi K_S^0)}{\mathcal{B}(B_d \to J/\psi K_S^0)} = 0.0431 \pm 0.0017\,(\text{stat.}) \pm 0.0012\,(\text{syst.}) \pm 0.0025\,(f_s/f_d)\,. \tag{8.4}$$

The $B_s^0 \to J/\psi K_S^0$ effective lifetime, whose definition is given in Chapter 4, is measured as

$$\tau^{\text{eff}}_{J/\psi K_S^0} = 1.75 \pm 0.12\,(\text{stat.}) \pm 0.07\,(\text{syst.})\,\text{ps}\,, \tag{8.5}$$

using the first 1.0 fb^{-1} of data collected by LHCb. Finally, the *CP* asymmetry parameters are given by

$$\mathcal{A}_{\Delta\Gamma}\left(B_s \to J/\psi K_S^0\right) = \quad 0.49 \pm {}^{0.77}_{0.65}\,(\text{stat.}) \pm 0.06\,(\text{syst.})\,, \tag{8.6}$$

$$\mathcal{A}^{\text{dir}}_{CP}\left(B_s \to J/\psi K_S^0\right) = -0.28 \pm 0.41\,(\text{stat.}) \pm 0.08\,(\text{syst.})\,, \tag{8.7}$$

$$\mathcal{A}^{\text{mix}}_{CP}\left(B_s \to J/\psi K_S^0\right) = \quad 0.08 \pm 0.40\,(\text{stat.}) \pm 0.08\,(\text{syst.})\,. \tag{8.8}$$

The large statistical uncertainties on these results do not yet provide constraints on the penguin parameters a and θ.

The new data that will be collected by the LHCb and Belle II experiments can further improve the measurements of these and other $B \to J/\psi(\pi/K)$ *CP* asymmetry parameters, and ultimately lead to high precision constraints on the penguin contributions affecting the determination of ϕ_d and ϕ_s from $B^0 \to J/\psi K_S^0$ and $B_s^0 \to J/\psi\,\phi$. We therefore eagerly await the first results from the second data taking period of the LHC, and look forward to the possibilities that the LHCb upgrade and Belle II data will offer. Hopefully this will some day lead to the discovery of new physics, either in B_q^0–$\bar{B}_q^0$ mixing, or elsewhere.

Bibliography

[1] S. L. Glashow, *Partial Symmetries of Weak Interactions*, Nucl. Phys. **22** (1961) 579.

[2] S. Weinberg, *A Model of Leptons*, Phys. Rev. Lett. **19** (1967) 1264.

[3] A. Salam, *Weak and Electromagnetic Interactions*, Conf. Proc. **C680519** (1968) 367.

[4] A. Einstein, *Die Grundlage der Allgemeinen Relativitätstheorie*, Annalen Phys. **49** (1916) 769.

[5] S. T. Petcov, *The Nature of Massive Neutrinos*, Adv. High Energy Phys. **2013** (2013) 852987, arXiv:1303.5819.

[6] L. Canetti, M. Drewes, and M. Shaposhnikov, *Matter and Antimatter in the Universe*, New J. Phys. **14** (2012) 095012, arXiv:1204.4186.

[7] G. Bertone, D. Hooper, and J. Silk, *Particle Dark Matter: Evidence, Candidates and Constraints*, Phys. Rept. **405** (2005) 279, arXiv:hep-ph/0404175.

[8] Planck collaboration, R. Adam *et al.*, *Planck 2015 Results. IX. Diffuse Component Separation: CMB Maps*, arXiv:1502.05956.

[9] S. Weinberg, *Implications of Dynamical Symmetry Breaking*, Phys. Rev. **D13** (1976) 974.

[10] R. D. Peccei, *The Strong CP Problem and Axions*, Lect. Notes Phys. **741** (2008) 3, arXiv:hep-ph/0607268.

[11] ATLAS collaboration, G. Aad *et al.*, *Observation of a New Particle in the Search for the Standard Model Higgs Boson with the ATLAS Detector at the LHC*, Phys. Lett. **B716** (2012) 1, arXiv:1207.7214.

[12] CMS collaboration, S. Chatrchyan *et al.*, *Observation of a New Boson at a Mass of 125* GeV *with the CMS Experiment at the LHC*, Phys. Lett. **B716** (2012) 30, arXiv:1207.7235.

[13] E. Halkiadakis, G. Redlinger, and D. Shih, *Status and Implications of Beyond-the-Standard-Model Searches at the LHC*, Ann. Rev. Nucl. Part. Sci. **64** (2014) 319, arXiv:1411.1427.

[14] CMS collaboration, LHCb collaboration, V. Khachatryan *et al.*, *Observation of the Rare $B_s^0 \to \mu^+\mu^-$ Decay from the Combined Analysis of CMS and LHCb Data*, Nature (2015) , arXiv:1411.4413.

[15] D. M. Straub, *New Physics Correlations in Rare Decays*, Proceedings of the 6th International Workshop on the CKM Unitarity Triangle (2010) arXiv:1012.3893.

[16] K. De Bruyn *et al.*, *Branching Ratio Measurements of B_s^0 Decays*, Phys. Rev. **D86** (2012) 014027, arXiv:1204.1735.

[17] K. De Bruyn *et al.*, *Probing New Physics via the $B_s^0 \to \mu^+\mu^-$ Effective Lifetime*, Phys. Rev. Lett. **109** (2012) 041801, arXiv:1204.1737.

[18] A. D. Sakharov, *Violation of CP Invariance, C Asymmetry, and Baryon Asymmetry of the Universe*, Pisma Zh. Eksp. Teor. Fiz. **5** (1967) 32.

[19] J. H. Christenson, J. W. Cronin, V. L. Fitch, and R. Turlay, *Evidence for the 2π Decay of the K_2^0 Meson*, Phys. Rev. Lett. **13** (1964) 138.

[20] N. Cabibbo, *Unitary Symmetry and Leptonic Decays*, Phys. Rev. Lett. **10** (1963) 531.

[21] M. Kobayashi and T. Maskawa, *CP Violation in the Renormalizable Theory of Weak Interaction*, Prog. Theor. Phys. **49** (1973) 652.

[22] ARGUS collaboration, H. Albrecht *et al.*, *Observation of B^0–$\bar{B}^0$ Mixing*, Phys. Lett. **B192** (1987) 245.

[23] BaBar collaboration, B. Aubert *et al.*, *Measurement of Time-Dependent CP Asymmetry in $B^0 \to c\bar{c}K^{(*)0}$ Decays*, Phys. Rev. **D79** (2009) 072009, arXiv:0902.1708.

[24] Belle collaboration, I. Adachi *et al.*, *Precise Measurement of the CP Violation Parameter $\sin 2\phi_1$ in $B^0 \to (c\bar{c})K^0$ Decays*, Phys. Rev. Lett. **108** (2012) 171802, arXiv:1201.4643.

[25] CKMfitter group, J. Charles *et al.*, *Current Status of the Standard Model CKM Fit and Constraints on $\Delta F = 2$ New Physics*, Phys. Rev. **D91** (2015), no. 7 073007, arXiv:1501.05013, Online update: CKM 2014.

[26] UTfit collaboration, A. Bevan *et al.*, *Standard Model Updates and New Physics Analysis with the Unitarity Triangle Fit*, arXiv:1411.7233, Online update: Post Moriond 2014.

[27] DØ collaboration, V. M. Abazov *et al.*, *Measurement of the CP-Violating Phase $\phi_s^{J/\psi\phi}$ using the Flavor-Tagged Decay $B_s^0 \to J/\psi\phi$ in 8 fb^{-1} of $p\bar{p}$ Collisions*, Phys. Rev. **D85** (2012) 032006, arXiv:1109.3166.

[28] CDF collaboration, T. Aaltonen *et al.*, *Measurement of the Bottom-Strange Meson Mixing Phase in the Full CDF Data Set*, Phys. Rev. Lett. **109** (2012) 171802, arXiv:1208.2967.

[29] LHCb collaboration, R. Aaij *et al.*, *Measurement of the CP-violating Phase ϕ_s in $\bar{B}_s^0 \to J/\psi\pi^+\pi^-$ Decays*, Phys. Lett. **B736** (2014) 186, arXiv:1405.4140.

[30] LHCb collaboration, R. Aaij *et al.*, *Precision Measurement of CP Violation in $B_s^0 \to J/\psi K^+K^-$ Decays*, Phys. Rev. Lett. **114** (2015), no. 4 041801, arXiv:1411.3104.

[31] LHCb collaboration, R. Aaij *et al.*, *Angular Analysis of the $B^0 \to K^{*0}\mu^+\mu^-$ Decay*, , LHCb-CONF-2015-002.

[32] LHCb collaboration, R. Aaij *et al.*, *Test of Lepton Universality using $B^+ \to K^+\ell^+\ell^-$ Decays*, Phys. Rev. Lett. **113** (2014) 151601, arXiv:1406.6482.

[33] W. Altmannshofer and D. M. Straub, *Implications of $b \to s$ Measurements*, Proceedings of the 50th Rencontres de Moriond, Electroweak Session (2015) arXiv:1503.06199.

[34] LHCb collaboration, R. Aaij *et al.*, *Implications of LHCb Measurements and Future Prospects*, Eur. Phys. J. **C73** (2013), no. 4 2373, arXiv:1208.3355.

[35] Belle II collaboration, T. Abe *et al.*, *Belle II Technical Design Report*, arXiv:1011.0352.

[36] R. Fleischer, *Extracting γ from $B_{(s/d)} \to J/\psi K_S^0$ and $B_{(d/s)} \to D_{(d/s)}^+ D_{(d/s)}^-$*, Eur. Phys. J. **C10** (1999) 299, arXiv:hep-ph/9903455.

[37] R. Fleischer, *Extracting CKM Phases from Angular Distributions of $B_{(d,s)}$ Decays into Admixtures of CP Eigenstates*, Phys. Rev. **D60** (1999) 073008, arXiv:hep-ph/9903540.

[38] R. Fleischer, *Recent Theoretical Developments in CP violation in the B System*, Nucl. Instrum. Meth. **A446** (2000) 1, arXiv:hep-ph/9908340.

[39] S. Faller, M. Jung, R. Fleischer, and T. Mannel, *The Golden Modes $B^0 \to J/\psi K^0_{S,L}$ in the Era of Precision Flavour Physics*, Phys. Rev. **D79** (2009) 014030, arXiv:0809.0842.

[40] X. Liu, W. Wang, and Y. Xie, *Penguin Pollution in $B \to J/\psi V$ Decays and Impact on the Extraction of the B_s^0–$\bar{B}_s^0$ Mixing Phase*, Phys. Rev. **D89** (2014), no. 9 094010, arXiv:1309.0313.

[41] P. Frings, U. Nierste, and M. Wiebusch, *Penguin Contributions to CP Phases in $B_{d,s}$ Decays to Charmonium*, arXiv:1503.00859.

[42] K. De Bruyn and R. Fleischer, *A Roadmap to Control Penguin Effects in $B^0 \to J/\psi K^0_S$ and $B^0_s \to J/\psi \phi$*, JHEP **1503** (2015) 145, arXiv:1412.6834.

[43] CDF collaboration, T. Aaltonen *et al.*, *Observation of $B_s^0 \to J/\psi K^*(892)^0$ and $B_s^0 \to J/\psi K_S^0$ Decays*, Phys. Rev. **D83** (2011) 052012, arXiv:1102.1961.

[44] LHCb collaboration, R. Aaij *et al.*, *Measurement of the $B_s^0 \to J/\psi K_S^0$ Branching Fraction*, Phys. Lett. **B713** (2012) 172, arXiv:1205.0934.

[45] LHCb collaboration, R. Aaij *et al.*, *Measurement of the Effective $B_s^0 \to J/\psi K_S^0$ Lifetime*, Nucl. Phys. **B873** (2013) 275, arXiv:1304.4500.

[46] LHCb collaboration, R. Aaij *et al.*, *Measurement of the Time-Dependent CP Asymmetries in $B_s^0 \to J/\psi K_S^0$*, JHEP **1506** (2015) 131, arXiv:1503.07055.

[47] D. Griffiths, *Introduction to Elementary Particles*, Physics textbook (John Wiley & Sons, 2008) 1.

[48] G. C. Branco, L. Lavoura, and J. P. Silva, *CP Violation*, International series of monographs on physics **103** (Clarendon Press, 1999) 1.

[49] I. I. Y. Bigi and A. I. Sanda, *CP Violation*, Cambridge monographs on particle physics, nuclear physics, and cosmology **9** (Cambridge University Press, 2000) 1.

[50] M. S. Sozzi, *Discrete Symmetries and CP Violation: From Experiment to Theory*, Oxford Graduate Texts (Oxford University Press, 2008) 1.

[51] A. J. Buras and R. Fleischer, *Quark Mixing, CP Violation and Rare Decays after the Top Quark Discovery*, Adv. Ser. Direct. High Energy Phys. **15** (1998) 65, arXiv:hep-ph/9704376.

[52] R. Fleischer, *CP Violation in the B system and Relations to $K \to \pi\nu\bar{\nu}$ Decays*, Phys. Rept. **370** (2002) 537, arXiv:hep-ph/0207108.

[53] R. Fleischer, *Flavour Physics and CP Violation: Expecting the LHC*, 4th CERN-CLAF School of High-Energy Physics (2008) 105, arXiv:0802.2882.

[54] C. S. Wu *et al.*, *Experimental Test of Parity Conservation in Beta Decay*, Phys. Rev. **105** (1957) 1413.

[55] R. L. Garwin, L. M. Lederman, and M. Weinrich, *Observations of the Failure of Conservation of Parity and Charge Conjugation in Meson Decays: The Magnetic Moment of the Free Muon*, Phys. Rev. **105** (1957) 1415.

[56] F. Englert and R. Brout, *Broken Symmetry and the Mass of Gauge Vector Mesons*, Phys. Rev. Lett. **13** (1964) 321.

[57] P. W. Higgs, *Broken Symmetries and the Masses of Gauge Bosons*, Phys. Rev. Lett. **13** (1964) 508.

[58] J. Goldstone, *Field Theories with Superconductor Solutions*, Nuovo Cim. **19** (1961) 154.

[59] J. Goldstone, A. Salam, and S. Weinberg, *Broken Symmetries*, Phys. Rev. **127** (1962) 965.

[60] S. L. Glashow, J. Iliopoulos, and L. Maiani, *Weak Interactions with Lepton-Hadron Symmetry*, Phys. Rev. **D2** (1970) 1285.

[61] B. Pontecorvo, *Mesonium and Anti-Mesonium*, Sov. Phys. JETP **6** (1957) 429.

[62] Z. Maki, M. Nakagawa, and S. Sakata, *Remarks on the Unified Model of Elementary Particles*, Prog. Theor. Phys. **28** (1962) 870.

[63] B. Pontecorvo, *Neutrino Experiments and the Problem of Conservation of Leptonic Charge*, Sov. Phys. JETP **26** (1968) 984.

[64] Particle Data Group, K. A. Olive *et al.*, *Review of Particle Physics*, Chin. Phys. **C38** (2014) 090001.

[65] L. Wolfenstein, *Parametrization of the Kobayashi-Maskawa Matrix*, Phys. Rev. Lett. **51** (1983) 1945.

[66] A. J. Buras, M. E. Lautenbacher, and G. Ostermaier, *Waiting for the Top Quark Mass, $K^+ \to \pi^+ \nu\bar{\nu}$, B_s^0–$\bar{B}_s^0$ Mixing and CP Asymmetries in B-Decays*, Phys. Rev. **D50** (1994) 3433, arXiv:hep-ph/9403384.

[67] C. Jarlskog, *Commutator of the Quark Mass Matrices in the Standard Electroweak Model and a Measure of Maximal CP Violation*, Phys. Rev. Lett. **55** (1985) 1039.

[68] I. I. Y. Bigi, N. G. Uraltsev, and A. I. Vainshtein, *Nonperturbative corrections to inclusive beauty and charm decays: QCD versus phenomenological models*, Phys. Lett. **B293** (1992) 430, arXiv:hep-ph/9207214.

[69] I. I. Y. Bigi, M. A. Shifman, and N. G. Uraltsev, *Aspects of Heavy Quark Theory*, Ann. Rev. Nucl. Part. Sci. **47** (1997) 591, arXiv:hep-ph/9703290.

[70] D. Benson, I. I. Y. Bigi, T. Mannel, and N. G. Uraltsev, *Imprecated, yet Impeccable: On the Theoretical Evaluation of* $\Gamma(B \to X_c l \nu)$, Nucl. Phys. **B665** (2003) 367, arXiv:hep-ph/0302262.

[71] A. Alberti, P. Gambino, and S. Nandi, *Perturbative Corrections to Power Suppressed Effects in Semileptonic B Decays*, JHEP **1401** (2014) 147, arXiv:1311.7381.

[72] T. Mannel, A. A. Pivovarov, and D. Rosenthal, *Inclusive Semileptonic B Decays from QCD with NLO Accuracy for Power Suppressed Terms*, Phys. Lett. **B741** (2015) 290, arXiv:1405.5072.

[73] Fermilab Lattice & MILC collaborations, J. A. Bailey *et al.*, *$|V_{ub}|$ from $B \to \pi \ell \nu$ Decays and (2+1)-Flavor Lattice QCD*, arXiv:1503.07839.

[74] LHCb collaboration, R. Aaij *et al.*, *Measurement of CP Violation in $B^0 \to J/\psi K^0_S$ Decays*, arXiv:1503.07089.

[75] A. J. Buras, *Weak Hamiltonian, CP Violation and Rare Decays*, arXiv:hep-ph/9806471.

[76] G. Buchalla, A. J. Buras, and M. E. Lautenbacher, *Weak Decays Beyond Leading Logarithms*, Rev. Mod. Phys. **68** (1996) 1125, arXiv:hep-ph/9512380.

[77] E. Fermi, *Tentativo di una Teoria dei Raggi β*, Nuovo Cim. **11** (1934) 1.

[78] K. G. Wilson and W. Zimmermann, *Operator Product Expansions and Composite Field Operators in the General Framework of Quantum Field Theory*, Commun. Math. Phys. **24** (1972) 87.

[79] E. Witten, *Short Distance Analysis of Weak Interactions*, Nucl. Phys. **B122** (1977) 109.

[80] W. A. Bardeen, A. J. Buras, D. W. Duke, and T. Muta, *Deep Inelastic Scattering Beyond the Leading Order in Asymptotically Free Gauge Theories*, Phys. Rev. **D18** (1978) 3998.

[81] M. Bander, D. Silverman, and A. Soni, *CP Non-invariance in the Decays of Heavy Charged Quark Systems*, Phys. Rev. Lett. **43** (1979) 242.

[82] R. Fleischer, *CP Violating Asymmetries in Penguin Induced B Meson Decays Beyond the Leading Logarithmic Approximation*, Z. Phys. **C58** (1993) 483.

[83] R. Fleischer, *Electroweak Penguin Effects Beyond Leading Logarithms in the B Meson Decays $B^- \to K^- \phi$ and $B^- \to \pi^- \bar{K}^0$*, Z. Phys. **C62** (1994) 81.

[84] G. Altarelli, G. Curci, G. Martinelli, and S. Petrarca, *QCD Nonleading Corrections to Weak Decays as an Application of Regularization by Dimensional Reduction*, Nucl. Phys. **B187** (1981) 461.

[85] O. Haan and B. Stech, *Violation of the $\Delta I = 1/2$ Rule in Non-Leptonic Decays*, Nucl. Phys. **B22** (1970) 448.

[86] D. Fakirov and B. Stech, *F and D Decays*, Nucl. Phys. **B133** (1978) 315.

[87] N. Cabibbo and L. Maiani, *Two-Body Decays of Charmed Mesons*, Phys. Lett. **B73** (1978) 418.

[88] M. Wirbel, B. Stech, and M. Bauer, *Exclusive Semileptonic Decays of Heavy Mesons*, Z. Phys. **C29** (1985) 637.

[89] A. J. Buras, J. M. Gerard, and R. Ruckl, *1/n Expansion for Exclusive and Inclusive Charm Decays*, Nucl. Phys. **B268** (1986) 16.

[90] M. Neubert, *Heavy Quark Symmetry*, Phys. Rept. **245** (1994) 259, arXiv:hep-ph/9306320.

[91] M. Beneke, G. Buchalla, M. Neubert, and C. T. Sachrajda, *QCD Factorization for Exclusive, Non-Leptonic B Meson Decays: General Arguments and the Case of Heavy Light Final States*, Nucl. Phys. **B591** (2000) 313, arXiv:hep-ph/0006124.

[92] C. W. Bauer, D. Pirjol, I. Z. Rothstein, and I. W. Stewart, *$B \to M_1 M_2$: Factorization, Charming penguins, Strong Phases, and Polarization*, Phys. Rev. **D70** (2004) 054015, arXiv:hep-ph/0401188.

[93] H.-n. Li, *Applicability of Perturbative QCD to $B \to D$ Decays*, Phys. Rev. **D52** (1995) 3958, arXiv:hep-ph/9412340.

[94] R. Fleischer, N. Serra, and N. Tuning, *Tests of Factorization and $SU(3)$ Relations in B Decays into Heavy-Light Final States*, Phys. Rev. **D83** (2011) 014017, arXiv:1012.2784.

[95] M. J. Dugan and B. Grinstein, *QCD Basis for Factorization in Decays of Heavy Mesons*, Phys. Lett. **B255** (1991) 583.

[96] C. W. Bauer, D. Pirjol, and I. W. Stewart, *A Proof of Factorization for $B \to D\pi$*, Phys. Rev. Lett. **87** (2001) 201806, arXiv:hep-ph/0107002.

[97] M. Beneke, G. Buchalla, M. Neubert, and C. T. Sachrajda, *QCD Factorization for $B \to \pi^+\pi^-$ Decays: Strong Phases and CP Violation in the Heavy Quark Limit*, Phys. Rev. Lett. **83** (1999) 1914, arXiv:hep-ph/9905312.

[98] M. Beneke, G. Buchalla, M. Neubert, and C. T. Sachrajda, *QCD Factorization for $B \to \pi K$ Decays*, arXiv:hep-ph/0007256.

[99] S. Scherer, *Introduction to Chiral Perturbation Theory*, Adv. Nucl. Phys. **27** (2003) 277, arXiv:hep-ph/0210398.

[100] L. N. Cooper, *Bound Electron Pairs in a Degenerate Fermi Gas*, Phys. Rev. **104** (1956) 1189.

[101] Y. Ne'eman, *Derivation of Strong Interactions from a Gauge Invariance*, Nucl. Phys. **26** (1961) 222.

[102] M. Gell-Mann, *A Schematic Model of Baryons and Mesons*, Phys. Lett. **8** (1964) 214.

[103] M. Nagashima, A. Szynkman, and D. London, *U-spin Tests of the Standard Model and New Physics*, Mod. Phys. Lett. **A23** (2008) 1175, arXiv:hep-ph/0701199.

[104] M. Gronau, *U-spin Breaking in CP Asymmetries in B Decays*, Phys. Lett. **B727** (2013) 136, arXiv:1308.3448.

[105] M. Jung and T. Mannel, *General Analysis of U-Spin Breaking in B Decays*, Phys. Rev. **D80** (2009) 116002, arXiv:0907.0117.

[106] M. Gronau, O. F. Hernandez, D. London, and J. L. Rosner, *Broken $SU(3)$ Symmetry in Two-Body B Decays*, Phys. Rev. **D52** (1995) 6356, arXiv:hep-ph/9504326.

[107] M. Gronau and D. London, *Isospin Analysis of CP Asymmetries in B Decays*, Phys. Rev. Lett. **65** (1990) 3381.

[108] A. J. Buras and R. Fleischer, *A General Analysis of γ Determinations from $B \to \pi K$ Decays*, Eur. Phys. J. **C11** (1999) 93, arXiv:hep-ph/9810260.

[109] R. Fleischer, *New Strategies to Extract β and γ from $B^0 \to \pi^+\pi^-$ and $B_s^0 \to K^+K^-$*, Phys. Lett. **B459** (1999) 306, arXiv:hep-ph/9903456.

[110] R. Fleischer and R. Knegjens, *In Pursuit of New Physics with $B_s^0 \to K^+K^-$*, Eur. Phys. J. **C71** (2011) 1532, arXiv:1011.1096.

[111] V. Weisskopf and E. P. Wigner, *Over the Natural Line Width in the Radiation of the Harmonic Oscillator*, Z. Phys. **65** (1930) 18.

[112] V. Weisskopf and E. P. Wigner, *Calculation of the Natural Brightness of Spectral Lines on the Basis of Dirac's Theory*, Z. Phys. **63** (1930) 54.

[113] A. J. Buras, M. Jamin, and P. H. Weisz, *Leading and Next-to-leading QCD Corrections to ϵ Parameter and B^0–$\bar{B}^0$ Mixing in the Presence of a Heavy Top Quark*, Nucl. Phys. **B347** (1990) 491.

[114] Flavour Lattice Averaging Group, S. Aoki *et al.*, *Review of Lattice Results Concerning Low-Energy Particle Physics*, Eur. Phys. J. **C74** (2014), no. 9 2890, arXiv:1310.8555.

[115] T. Inami and C. S. Lim, *Effects of Superheavy Quarks and Leptons in Low-Energy Weak Processes $K_L^0 \to \mu^+\mu^-$, $K^+ \to \pi^+\nu\bar{\nu}$ and $K^0 \leftrightarrow \bar{K}^0$*, Prog. Theor. Phys. **65** (1981) 297.

[116] R. Aleksan *et al.*, *Estimation of $\Delta\Gamma$ for the B_s^0–$\bar{B}_s^0$ System: Exclusive Decays and the Parton Model*, Phys. Lett. **B316** (1993) 567.

[117] E. C. Poggio, H. R. Quinn, and S. Weinberg, *Smearing the Quark Model*, Phys. Rev. **D13** (1976) 1958.

[118] M. A. Shifman, *Quark Hadron Duality*, arXiv:hep-ph/0009131.

[119] A. Lenz and U. Nierste, *Theoretical Update of B_s^0–$\bar{B}_s^0$ Mixing*, JHEP **0706** (2007) 072, arXiv:hep-ph/0612167.

[120] LHCb collaboration, R. Aaij *et al.*, *Measurement of the Flavour-Specific CP-Violating Asymmetry a_{sl}^s in B_s^0 Decays*, Phys. Lett. **B728** (2014) 607, arXiv:1308.1048.

[121] Heavy Flavour Averaging Group, Y. Amhis *et al.*, *Averages of b-Hadron, c-Hadron, and τ-Lepton Properties as of Summer 2014*, arXiv:1412.7515, Online update: Fall 2014.

[122] A. Lenz and U. Nierste, *Numerical Updates of Lifetimes and Mixing Parameters of B Mesons*, Proceedings of the 6th International Workshop on the CKM Unitarity Triangle (2011) arXiv:1102.4274.

[123] A. Lenz, *Lifetimes and HQE*, arXiv:1405.3601.

[124] LHCb collaboration, R. Aaij *et al.*, *Determination of the Sign of the Decay Width Difference in the B_s^0 System*, Phys. Rev. Lett. **108** (2012) 241801, arXiv:1202.4717.

[125] I. Dunietz and J. L. Rosner, *Time-Dependent CP Violation Effects in B^0–$\bar{B}^0$ Systems*, Phys. Rev. **D34** (1986) 1404.

[126] I. Dunietz, *B_s^0–$\bar{B}_s^0$ Mixing, CP Violation and Extraction of CKM Phases from Untagged B_s Data Samples*, Phys. Rev. **D52** (1995) 3048, arXiv:hep-ph/9501287.

[127] R. Fleischer and I. Dunietz, *CP Violation and the CKM Angle γ from Angular Distributions of Untagged B_s Decays Governed by $\bar{b} \to \bar{c}u\bar{s}$*, Phys. Lett. **B387** (1996) 361, arXiv:hep-ph/9605221.

[128] R. Fleischer and R. Knegjens, *Effective Lifetimes of B_s^0 Decays and their Constraints on the B_s^0–$\bar{B}_s^0$ Mixing Parameters*, Eur. Phys. J. **C71** (2011) 1789, arXiv:1109.5115.

[129] K. Hartkorn and H. G. Moser, *A New Method of Measuring $\Delta\Gamma/\Gamma$ in the B_s^0–$\bar{B}_s^0$ System*, Eur. Phys. J. **C8** (1999) 381.

[130] I. Dunietz, R. Fleischer, and U. Nierste, *In Pursuit of New Physics with B_s^0 Decays*, Phys. Rev. **D63** (2001) 114015, arXiv:hep-ph/0012219.

[131] S. Faller, R. Fleischer, and T. Mannel, *Precision Physics with $B_s^0 \to J/\psi\,\phi$ at the LHC: The Quest for New Physics*, Phys. Rev. **D79** (2009) 014005, arXiv:0810.4248.

[132] LHCb collaboration, R. Aaij *et al.*, *Measurement of the $\bar{B}_s^0$ Effective Lifetime in the $J/\psi\, f_0(980)$ Final State*, Phys. Rev. Lett. **109** (2012) 152002, arXiv:1207.0878.

[133] LHCb collaboration, R. Aaij *et al.*, *Measurement of the B_s^0 Meson Lifetime in $D_s^+\pi^-$ Decays*, Phys. Rev. Lett. **113** (2014) 172001, arXiv:1407.5873.

[134] LHCb collaboration, R. Aaij *et al.*, *Effective Lifetime Measurements in the $B_s^0 \to K^+K^-$, $B^0 \to K^+\pi$ and $B_s^0 \to \pi^+K$ Decays*, Phys. Lett. **B736** (2014) 446, arXiv:1406.7204.

[135] R. Fleischer, *Exploring CP Violation and Penguin Effects through $B^0 \to D^+D^-$ and $B_s^0 \to D_s^+D_s^-$*, Eur. Phys. J. **C51** (2007) 849, arXiv:0705.4421.

[136] LHCb collaboration, R. Aaij *et al.*, *Measurement of the $\bar{B}_s^0 \to D_s^-D_s^+$ and $\bar{B}_s^0 \to D^-D_s^+$ Effective Lifetimes*, Phys. Rev. Lett. **112** (2014), no. 11 111802, arXiv:1312.1217.

[137] A. J. Buras, R. Fleischer, J. Girrbach, and R. Knegjens, *Probing New Physics with the $B_s^0 \to \mu^+\mu^-$ Time-Dependent Rate*, JHEP **1307** (2013) 77, arXiv:1303.3820.

[138] M. Ciuchini, M. Pierini, and L. Silvestrini, *The Effect of Penguins in the $B_d \to J/\psi K^0$ CP Asymmetry*, Phys. Rev. Lett. **95** (2005) 221804, arXiv:hep-ph/0507290.

[139] K. De Bruyn, R. Fleischer, and P. Koppenburg, *Extracting γ and Penguin Topologies through CP Violation in $B_s^0 \to J/\psi K_S^0$*, Eur. Phys. J. **C70** (2010) 1025, arXiv:1010.0089.

[140] M. Ciuchini, M. Pierini, and L. Silvestrini, *Theoretical Uncertainty in* $\sin 2\beta$*: An Update*, arXiv:1102.0392.

[141] M. Jung, *Determining Weak Phases from $B \to J/\psi P$ Decays*, Phys. Rev. **D86** (2012) 053008, arXiv:1206.2050.

[142] A. S. Dighe, I. Dunietz, H. J. Lipkin, and J. L. Rosner, *Angular Distributions and Lifetime Differences in $B_s^0 \to J/\psi \phi$ Decays*, Phys. Lett. **B369** (1996) 144, arXiv:hep-ph/9511363.

[143] A. S. Dighe, I. Dunietz, and R. Fleischer, *Extracting CKM Phases and B_s^0–$\bar{B}_s^0$ Mixing Parameters from Angular Distributions of Non-Leptonic B Decays*, Eur. Phys. J. **C6** (1999) 647, arXiv:hep-ph/9804253.

[144] LHCb collaboration, R. Aaij *et al.*, *Measurement of the CP-Violating Phase β in $B^0 \to J/\psi \pi^+\pi^-$ Decays and Limits on Penguin Effects*, Phys. Lett. **B742** (2015) 38, arXiv:1411.1634.

[145] LHCb collaboration, R. Aaij *et al.*, *Measurement of the $B_s^0 \to J/\psi \overline{K}^{*0}$ Branching Fraction and Angular Amplitudes*, Phys. Rev. **D86** (2012) 071102, arXiv:1208.0738.

[146] A. Bharucha, D. M. Straub, and R. Zwicky, *$B \to V\ell^+\ell^-$ in the Standard Model from Light-Cone Sum Rules*, arXiv:1503.05534.

[147] L3 collaboration, M. Acciarri *et al.*, *Search for Exclusive B Decays to J/ψ and η or π^0 with the L3 Detector*, Phys. Lett. **B391** (1997) 481.

[148] LHCb collaboration, R. Aaij *et al.*, *Measurement of Resonant and CP Components in $\bar{B}_s^0 \to J/\psi \pi^+\pi^-$ Decays*, Phys. Rev. **D89** (2014), no. 9 092006, arXiv:1402.6248.

[149] R. Fleischer and T. Mannel, *Constraining the CKM Angle γ and Penguin Contributions through Combined $B \to \pi K$ Branching Ratios*, Phys. Rev. **D57** (1998) 2752, arXiv:hep-ph/9704423.

[150] Belle collaboration, K. Abe *et al.*, *Measurement of Branching Fractions and Charge Asymmetries for Two-Body B Meson Decays with Charmonium*, Phys. Rev. **D67** (2003) 032003, arXiv:hep-ex/0211047.

[151] G. Duplančić and B. Melić, $B_d, B_s \to K$ *Form Factors: An Update of Light-Cone Sum Rule Results*, Phys. Rev. **D78** (2008) 054015, arXiv:0805.4170.

[152] A. Khodjamirian, T. Mannel, A. A. Pivovarov, and Y.-M. Wang, *Charm-Loop Effect in* $B \to K^{(*)}\ell^+\ell^-$ *and* $B \to K^*\gamma$, JHEP **1009** (2010) 089, arXiv:1006.4945.

[153] A. Bharucha, *Two-Loop Corrections to the* $B \to \pi$ *Form Factor from QCD Sum Rules on the Light-Cone and* $|V_{ub}|$, JHEP **1205** (2012) 092, arXiv:1203.1359.

[154] P. Ball, $|V_{ub}|$ *from UT Angles and* $B \to \pi l \nu$, Phys. Lett. **B644** (2007) 38, arXiv:hep-ph/0611108.

[155] C. G. Boyd, B. Grinstein, and R. F. Lebed, *Constraints on Form-Factors for Exclusive Semileptonic Heavy to Light Meson Decays*, Phys. Rev. Lett. **74** (1995) 4603, arXiv:hep-ph/9412324.

[156] C. G. Boyd and M. J. Savage, *Analyticity, Shapes of Semileptonic Form-Factors, and* $\bar{B} \to \pi l \bar{\nu}$, Phys. Rev. **D56** (1997) 303, arXiv:hep-ph/9702300.

[157] Belle collaboration, S. E. Lee *et al.*, *Improved Measurement of Time-Dependent CP Violation in* $B^0 \to J/\psi \pi^0$ *Decays*, Phys. Rev. **D77** (2008) 071101, arXiv:0708.0304.

[158] BaBar collaboration, B. Aubert *et al.*, *Evidence for CP Violation in* $B^0 \to J/\psi \pi^0$ *Decays*, Phys. Rev. Lett. **101** (2008) 021801, arXiv:0804.0896.

[159] LHCb collaboration, R. Aaij *et al.*, *Measurement of the Fragmentation Fraction Ratio* f_s/f_d *and its Dependence on B Meson Kinematics*, JHEP **1304** (2013) 001, arXiv:1301.5286.

[160] LHCb collaboration, *Updated Average* f_s/f_d *b-Hadron Production Fraction Ratio for 7* TeV *pp Collisions*, , LHCb-CONF-2013-011.

[161] J. L. Rosner, *Determination of Pseudoscalar Charmed Meson Decay Constants from B Meson Decays*, Phys. Rev. **D42** (1990) 3732.

[162] G. Kramer and W. F. Palmer, *Branching Ratios and CP Asymmetries in the Decay* $B \to VV$, Phys. Rev. **D45** (1992) 193.

[163] G. Kramer and W. F. Palmer, *Polarization and CP Asymmetries in the Decays* $B \to K^*\psi$, $K^*\omega$ *and* $K^*\rho$, Phys. Lett. **B279** (1992) 181.

[164] G. Kramer, T. Mannel, and W. F. Palmer, *Angular Correlations in the Decays $B \to VV$ using Heavy Quark Symmetry*, Z. Phys. **C55** (1992) 497.

[165] M. Bauer, B. Stech, and M. Wirbel, *Exclusive Non-Leptonic Decays of D, D_s, and B Mesons*, Z. Phys. **C34** (1987) 103.

[166] LHCb collaboration, R. Aaij *et al.*, *Measurement of the Resonant and CP Components in $\bar{B}^0 \to J/\psi \pi^+\pi^-$ Decays*, Phys. Rev. **D90** (2014), no. 1 012003, arXiv:1404.5673.

[167] R. Fleischer, R. Knegjens, and G. Ricciardi, *Anatomy of $B^0_{s,d} \to J/\psi f_0(980)$*, Eur. Phys. J. **C71** (2011) 1832, arXiv:1109.1112.

[168] L. Zhang and S. Stone, *Time-Dependent Dalitz-Plot Formalism for $B^0_q \to J/\psi h^+h^-$*, Phys. Lett. **B719** (2013) 383, arXiv:1212.6434.

[169] A. J. Buras and J. Girrbach, *Towards the Identification of New Physics through Quark Flavour Violating Processes*, Rept. Prog. Phys. **77** (2014) 086201, arXiv:1306.3775.

[170] P. Ball and R. Fleischer, *Probing New Physics through B mixing: Status, Benchmarks and Prospects*, Eur. Phys. J. **C48** (2006) 413, arXiv:hep-ph/0604249.

[171] A. J. Buras and D. Guadagnoli, *Correlations among New CP Violating Effects in $\Delta F = 2$ Observables*, Phys. Rev. **D78** (2008) 033005, arXiv:0805.3887.

[172] LHC study group, P. Lefèvre *et al.*, *The Large Hadron Collider: Conceptual Design*, CERN-AC-95-05-LHC, 1995.

[173] LHCb collaboration, R. Aaij *et al.*, *Measurement of the B^0–$\bar{B}^0$ and B^0_s–$\bar{B}^0_s$ Production Asymmetries in pp Collisions at $\sqrt{s} = 7$ TeV*, Phys. Lett. **B739** (2014) 218, arXiv:1408.0275.

[174] Illustration courtesy of CERN. CDS Record: 1621894.

[175] CDF collaboration, A. Abulencia *et al.*, *Observation of B^0_s–$\bar{B}^0_s$ Oscillations*, Phys. Rev. Lett. **97** (2006) 242003, arXiv:hep-ex/0609040.

[176] L. Evans and P. Bryant, *LHC Machine*, JINST **3** (2008) S08001.

[177] ATLAS collaboration, G. Aad *et al.*, *The ATLAS Experiment at the CERN Large Hadron Collider*, JINST **3** (2008) S08003.

[178] CMS collaboration, S. Chatrchyan *et al.*, *The CMS Experiment at the CERN LHC*, JINST **3** (2008) S08004.

[179] ALICE collaboration, K. Aamodt *et al.*, *The ALICE Experiment at the CERN LHC*, JINST **3** (2008) S08002.

[180] LHCb collaboration, A. A. Alves Jr. *et al.*, *The LHCb Detector at the LHC*, JINST **3** (2008) S08005.

[181] Illustration courtesy of CERN. CDS Record: 1087860.

[182] LHCb collaboration, R. Aaij *et al.*, *LHCb Detector Performance*, Int. J. Mod. Phys. **A30** (2015) 1530022, arXiv:1412.6352.

[183] R. Aaij *et al.*, *The LHCb Trigger and its Performance in 2011*, JINST **8** (2013) P04022, arXiv:1211.3055.

[184] LHCb collaboration, R. Aaij *et al.*, *Measurement of CP Violation and the B_s^0 Meson Decay Width Difference with $B_s^0 \to J/\psi K^+K^-$ and $B_s^0 \to J/\psi \pi^+\pi^-$ Decays*, Phys. Rev. **D87** (2013), no. 11 112010, arXiv:1304.2600.

[185] M. Feindt, *A Neural Bayesian Estimator for Conditional Probability Densities*, arXiv:physics/0402093.

[186] W. D. Hulsbergen, *Decay Chain Fitting with a Kalman Filter*, Nucl. Instrum. Meth. **A552** (2005) 566, arXiv:physics/0503191.

[187] ⟨phi-t⟩, *The NeuroBayes User's Manual*, See the NeuroBayes website, 2010.

[188] M. Pivk and F. R. Le Diberder, *${}_s\mathcal{P}lot$: A Statistical Tool to Unfold Data Distributions*, Nucl. Instrum. Meth. **A555** (2005) 356, arXiv:physics/0402083.

[189] Illustration courtesy of Julian Wishahi.

[190] LHCb collaboration, R. Aaij *et al.*, *Opposite-Side Flavour Tagging of B Mesons at the LHCb Experiment*, Eur. Phys. J. **C72** (2012) 2022, arXiv:1202.4979.

[191] LHCb collaboration, *Optimization and Calibration of the Same-Side Kaon Tagging Algorithm using Hadronic B_s^0 Decays in 2011 Data*, , LHCb-CONF-2012-033.

[192] D. M. Santos and F. Dupertuis, *Mass Distributions Marginalized over Per-Event Errors*, Nucl. Instrum. Meth. **A764** (2014) 150, arXiv:1312.5000.

[193] H. G. Moser and A. Roussarie, *Mathematical Methods for B^0 $\bar{B}^0$ Oscillation Analyses*, Nucl. Instrum. Meth. **A384** (1997) 491.

[194] T. M. Karbach, G. Raven, and M. Schiller, *Decay Time Integrals in Neutral Meson Mixing and their Efficient Evaluation*, arXiv:1407.0748.

[195] LHCb collaboration, R. Aaij *et al.*, *Measurement of the Semileptonic CP Asymmetry in B^0–$\bar{B}^0$ Mixing*, Phys. Rev. Lett. **114** (2015) 041601, arXiv:1409.8586.

[196] BaBar collaboration, B. Aubert *et al.*, *Measurement of Time-Dependent CP Asymmetry in $B^0 \to c\bar{c}K^{(*)0}$ Decays*, Phys. Rev. **D79** (2009) 072009, arXiv:0902.1708.

[197] T. Skwarnicki, *A Study of the Radiative Cascade Transitions between the Upsilon-prime and Upsilon Resonances*, PhD thesis, Institute of Nuclear Physics, Krakow, 1986, DESY-F31-86-02.

[198] G. J. Feldman and R. D. Cousins, *A Unified Approach to the Classical Statistical Analysis of Small Signals*, Phys. Rev. **D57** (1998) 3873, arXiv:physics/9711021.

[199] T. M. Karbach, *Feldman–Cousins Confidence Levels — Toy MC Method*, arXiv:1109.0714.

[200] Illustration courtesy of Kees Huyser/Nikhef.

A Song of Trees and Penguins

Dear reader,
In the next few pages I would like to introduce you to the world I have been living in for the past few years. This world of mine is inhabited by the smallest of things, the elementary particles. Yet, it is everywhere around us, stretching out to the furthest corners of our Universe. It is an incredibly complex world. The deeper we adventure into it, the more hidden mysteries we uncover, and the more we are drawn in by its spells. To you this world might appear difficult to comprehend, but so it does to us too. And yet, it has not stopped us from exploring. Instead, the challenges and questions drive us ever on. Since, like you, I cannot grasp it all, I have dedicated the four years of my PhD study to one special creature inhabiting this world. It lives in the cold and icy part of my world, and is only rarely seen. Yet we know it must be there, and so we set out to search for it ...

The Standard Model

Let us start our journey through the realm of particle physics right on the doorstep of our home. The objects you encounter in everyday life might not always seem spectacular to you, but there is more to them than meets the eye. If we were to zoom in on them, and continued to do so, at some point you would notice that they are made out of billions of smaller building blocks: molecules. In turn, molecules are made out of atoms, which themselves consist of a core of protons and neutrons, surrounded by a cloud of electrons. But this is not yet the end of it, because protons and neutrons can again be decomposed into quarks. Specifically two types: the up and the down quark. Together, the electrons and the quarks form the most basic building blocks of our Universe (that we know of).

Although everything around us is made out of electrons, up and down quarks, we have learned over the past hundred years that there are actually many more elementary particles in Nature. Most of the other fundamental particles, however, are very exotic and short-lived[a], making it more difficult to observe them. In fact, you need large particle accelerators, either man-made or cosmic in origin, to

[a] Neutrinos form an exception. But due to their weak interaction with other matter, they are still very challenging to observe.

reach the energies that are needed to produce them. By studying collisions involving these accelerated particles we have been able to learn a lot about the world of elementary particles. For example, we have so far identified six different quark types. In order of increasing mass, that are the up, down, strange, charm, bottom (or beauty, whatever you prefer) and top. Likewise, we now know of three electron-like particles, the electron, muon and tau. And have found three different ghost-like particles, referred to as neutrinos, that are associated with these electrons, muons and taus. Together, these six particles form the leptons. As if that is not enough, every particle listed above also has a partner, the antiparticle, which functions as its antagonist. Particles and antiparticles have the same mass, but otherwise opposite properties. If, for example, the particle is blue and positively charged, the antiparticle would be anti-blue (or yellow on the colour wheel) and negatively charged. Energy can be used to create a particle–antiparticle pair, and likewise if a particle and its antiparticle meet, they annihilate each other and transform back into energy. Luckily for us, antimatter has become very rare in the Universe, so the annihilation process almost never happens, and especially not on human-size scales. It is nonetheless regularly produced (and exploited by, for example, medical PET scanners), but only in tiny amounts and most of it quickly annihilates again. Studying the relation between particles and their antiparticles forms an important aspect of my research.

Besides the quarks and leptons, we have also discovered a bunch of particles that act as mediators for three of the four fundamental forces of Nature: electromagnetism, and the weak and strong (nuclear) force. The electromagnetic force is responsible for light, electricity and magnetism, and for keeping electrons in orbit around the atom core. Its force carrier is the photon. The strong force acts as glue that keeps the quarks together inside the protons and neutrons, and is mediated by so-called gluons. The weak force is responsible for the decay of unstable particles, for example in radioactivity. Its mediators are the W and Z bosons. The strong and weak force only play a role at the length scale of atoms or smaller, and are therefore less prominently visible in our daily lives. And lastly, in addition to the quarks, leptons and force carriers, there is also the Higgs particle. It is related to the mechanism that is responsible for the masses of the fundamental particles. But truly explaining what it is and how it comes about, goes a bit beyond the purpose of this summary.

To make sense of all these different particles and their behaviour, physicists have come up with a theory describing the elementary particles and their interactions: the *Standard Model*. The only thing missing from this theory is a description of the fourth, and most obvious, fundamental force, gravity. It simply does not fit into the mathematical formulation used to describe the other forces. That is not the only problem we encounter in particle physics. The Standard Model has been (and

continues to be) remarkably successful in describing the experimental data we collected from cosmic ray and accelerator-based experiments, but it cannot explain the origin or nature of some other firmly established experimental observations. Let me illustrate that with a few examples. Cosmological observations contain a lot of information about the content of the Universe and how it evolved from the Big Bang, an enormous explosion of energy that marked the birth of our Universe, to the present day. These observations tell us that the Universe consists for only 4% out of ordinary matter, i.e. atoms and molecules. The remaining 96%, which go under the mysterious names of dark matter and dark energy, are currently unexplained. In addition, the Big Bang created equal amounts of matter and antimatter. Yet in the Universe we observe today, antimatter has largely disappeared. How did that happen? One way to find out more about this puzzling observation is to study the differences in behaviour between particles and their antiparticles.

Because of the shortcomings mentioned above (and others that are more difficult to explain here), physicists consider the Standard Model to be only an approximate theory; a special corner[b] of a more complete, but unknown, theory of particle physics. It is our goal, as a particle physics community, to find evidence for this "grand theory of particle physics", and gain further insight into its properties. To succeed in that, we explore many different possibilities: we search for new fundamental particles, or new types of interactions, or ... All these phenomena go under the general name of *new physics*. So far, we have not yet found clear evidence for new physics effects. That means that the deviations from the Standard Model will be small or hard to find, thus requiring further effort from both the experimental and the theoretical particle physics communities.

The Search for New Physics

Our main instruments for searching for experimental evidence of new physics are high-energy particle accelerators, which accelerate electrons and/or protons to nearly the speed of light before smashing them into each other at pre-defined collision points. Around these collision regions, large particle detectors are built. These detectors act as oversized cameras taking pictures of the collision events, millions of times per second. By analysing these pictures, we hope to learn more about what happens at the smallest length scales, which can eventually lead to new findings that cannot be explained by the Standard Model theory. In the quest for new physics, the accelerators are attaining higher and higher energies in order to access yet unexplored territory, where new fundamental particles might abide. The latest and most powerful accelerator taking up this task is the Large Hadron Collider (LHC), located at CERN in Geneva, Switzerland. It has four interaction

[b] As an example, Newtonian gravity is the (s)low-speed limit of Einstein's General Relativity.

points. The large detectors surrounding each one of them are called Atlas, Alice, CMS and LHCb. Together, they have performed many interesting new measurements, but the biggest highlight of the LHC is undoubtedly the discovery of the Higgs particle by the Atlas and CMS experiments.

In my research, the LHCb detector plays a central role. Complementary to the high energy frontier that is explored by Atlas and CMS, it focuses on high precision measurements of known physical processes related to the decay of particles containing beauty and charm quarks. Through these measurements we hope to find indirect evidence for new physics, manifesting itself as deviations from the Standard Model predictions. Given the current situation, such new physics observations can only be claimed when the theoretical precision on the Standard Model prediction for the measured observables at least matches the experimental uncertainty. We therefore need to have a careful look at the theoretical assumptions linking the experiment measurements with the Standard Model parameters.

The tools we have developed to perform theoretical calculations in particle physics are based on a series expansion, where each new term in the series gives a small correction to the previous one. Thus, the more terms in these series we take into account, the more precise our calculation becomes. But each additional term is also increasingly more difficult to compute. For many experimental measurements we therefore only take into account the first (few) term(s) of this series. With the increased experimental precision that can be reached by the LHCb experiment, this approximation will no longer remain sufficient for some of the key observables measured by LHCb.

About Trees and Penguins

This thesis reports my study on the impact of such higher order corrections for two specific processes. These processes deal with the decay of so-called neutral B mesons. B mesons are heavy particles consisting of a bottom antiquark and either a down (B^0) or a strange (B_s^0) quark. They are unstable, and only live for a very short period of time (a few trillionths of a second), after which they decay into a number of lighter particles. We have found well over 250 different possible combinations of decay products, but of interest for this thesis are the two decay channels $B^0 \to J/\psi\, K_S^0$ (to be pronounced as B-zero-to-jay-psi-K-short) and $B_s^0 \to J/\psi\, \phi$ (B-s-to-jay-psi-fi). In these modes, the B meson decays into a J/ψ particle, consisting of a charm and an anticharm quark, and either a K_S^0 particle, consisting of a strange antiquark and a down quark, or a ϕ particle, consisting of a strange and an antistrange quark. But you may also see it as cryptic code which particle physicists use to talk about certain decay processes.

The leading order process with which the $B^0 \to J/\psi\, K_S^0$ and $B_s^0 \to J/\psi\, \phi$ decays take place, is referred to as the tree amplitude because of the forked graphical rep-

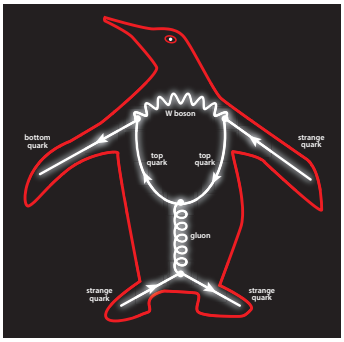

Figure S.1: Graphical illustration of a so-called penguin diagram [200]. Controlling its impact on precision measurements of B meson decays is the main goal of this thesis.

resentation of this mechanism. In addition, the decays can also occur via more complicated decay paths known as penguin diagrams, which are illustrated in Fig. S.1. In the $B^0 \to J/\psi K_S^0$ and $B_s^0 \to J/\psi \phi$ decay channels, the contributions from these penguin diagrams are strongly suppressed compared to the more prominent tree amplitude. Nonetheless, we are reaching experimental precisions on the observables associated with the $B^0 \to J/\psi K_S^0$ and $B_s^0 \to J/\psi \phi$ decays where even these small corrections start to become noticeable, and thus need to be controlled. The main goal of this thesis is to explore methods to do just that.

Because of low-energy strong interactions between the quarks involved in the decay process, direct theoretical calculations of these penguin contributions are difficult. The low-energy dynamics between quarks and gluons cannot be fully described using our standard tools. To nonetheless get a handle on these effects, we need to rely on alternative methods which can estimate them directly from the experimental data. Here symmetries play an important role.

Symmetries and *CP* Violation

The corrections we are after can be determined from observables associated with the difference in behaviour between particles and antiparticles. Particles and their antiparticles are related to each other by simultaneously applying the charge symmetry and parity transformations. The charge symmetry (C) transformation interchanges the positive and negative charges of the fundamental particles, while parity (P) inverts the spatial directions, i.e. it makes the simultaneous transformation $x \to -x$, $y \to -y$ and $z \to -z$. Although the Universe started out CP symmetric, with equal amounts of matter and antimatter, the world around us is now exclusively made out of matter, and antimatter has become very scarce. This can only

be explained if particles do not exactly behave in the same way as antiparticles, i.e. the *CP* symmetry between them is broken. As it turns out, the strong[c] and electromagnetic interactions are invariant under *CP* transformations, but the weak interaction is not. The amount of *CP* violation measured in weak interactions is not sufficient to explain the observed imbalance between matter and antimatter in the Universe. Hence, there must be additional sources of *CP* violation not yet described by the Standard Model. By studying weak decay processes, like $B^0 \to J/\psi\, K_S^0$ and $B_s^0 \to J/\psi\, \phi$, we hope to find new physics that can help us understand all the details regarding *CP* violation in our Universe.

In the Standard Model, *CP* violation is parametrised by complex phases. To avoid a whole introduction into the mathematics of complex numbers, just imagine that for the mathematical formulation of the Standard Model we work with numbers which in addition to their size also acquires a compass direction: a phase. By measuring observables that quantify the (*CP*) asymmetry between the decay process of the B^0 and B_s^0 mesons on the one hand, and the $\bar{B}^0$ and $\bar{B}_s^0$ antimesons on the other, these compass directions can be determined. With the decays $B^0 \to J/\psi\, K_S^0$ and $B_s^0 \to J/\psi\, \phi$ we experimentally measure two of the *CP* violating complex phases, referred to as ϕ_d and ϕ_s. If we ignore the tiny penguin contributions, and assume that these two decays only proceed via the tree diagram, the relation between the measured *CP* asymmetries and the phases ϕ_d and ϕ_s is rather straightforward. But if we also include the penguin effects, the relations get modified and corrections, which we parametrise as shifts $\Delta\phi_d$ and $\Delta\phi_s$ in this thesis, need to be taken into account. These corrections modify the value of the measured *CP* asymmetries, so these asymmetries might also hold the key to controlling the corrections. In $B^0 \to J/\psi\, K_S^0$ and $B_s^0 \to J/\psi\, \phi$ the influence of the penguin amplitudes is small, so the impact on the *CP* asymmetries is difficult to notice. Therefore we search for other decay modes where the effect on the *CP* asymmetries is magnified.

At this point yet another symmetry comes into play: the flavour symmetry of the strong interaction. Assuming the up, down and strange quark are massless, which is an approximation, the strong interaction cannot distinguish between these three quarks. As far as the strong interaction is concerned, these particles then all look the same, and thus behave in the same way. That is an interesting feature to exploit, especially in view of our problems to calculate the low-energy dynamics between quarks and gluons. This symmetry allows us to relate one decay path to another by interchanging up, down or strange quarks, without affecting the low-energy strong dynamics involved in these modes. So instead of performing explicit calculations, we use flavour symmetry to relate the quantities we want to know to similar quantities in other decay modes where they can be constrained

[c] The strong interaction needs not be invariant under *CP* transformations, but experimental measurements suggest that it is. This puzzling situation is known as the strong *CP* problem.

with experimental data. Of course quarks are not massless, so this symmetry is not realised exactly in Nature. But the masses of the up, down and strange quarks are much smaller than the typical energy scale at which strong interaction processes take place, and thus effectively appear massless to them. The flavour symmetry of the strong interaction therefore is an excellent tool in the study of B^0 and B_s^0 meson decays.

Hunting Penguins

Let me illustrate the use of flavour symmetry in a bit more detail. By interchanging all down and strange quarks with one another, the $B^0 \to J/\psi K_S^0$ decay transforms into the $B_s^0 \to J/\psi K_S^0$ decay mode. In the flavour symmetry limit, the strong interaction effects involved in these two decay paths are identical. However, the weak interaction still causes differences between the two decays. As a result the relative contributions of the tree and penguin amplitudes in $B_s^0 \to J/\psi K_S^0$ are different from those in $B^0 \to J/\psi K_S^0$; the penguin amplitudes are enhanced in $B_s^0 \to J/\psi K_S^0$. As a consequence, the $B_s^0 \to J/\psi K_S^0$ decay is much more sensitive to penguin effects, and can in fact be used to constrain their impact in $B^0 \to J/\psi K_S^0$, i.e. to quantify the shift $\Delta\phi_d$.

Our main strategy is as follows: We measure the *CP* asymmetries in $B_s^0 \to J/\psi K_S^0$, and use them to determine the size of the penguin contributions. Then we invoke the flavour symmetry argument to relate the penguin contributions in $B_s^0 \to J/\psi K_S^0$ to those in $B^0 \to J/\psi K_S^0$. With knowledge on the size of the penguin effects in $B^0 \to J/\psi K_S^0$, we can quantify the shift $\Delta\phi_d$, and thus improve the measurement of ϕ_d from the *CP* asymmetries in $B^0 \to J/\psi K_S^0$. That may sound like we have everything under control now, but of course nothing is that simple. The penguin contributions might be enhanced in $B_s^0 \to J/\psi K_S^0$, but the overall decay amplitude is suppressed compared to $B^0 \to J/\psi K_S^0$, making this mode experimentally more challenging to study. At the moment, we do not yet have high precision measurements of the $B_s^0 \to J/\psi K_S^0$ *CP* asymmetries, and therefore cannot yet execute the above described strategy.

Searching for Penguins Footprints

So where does my research come into this game? Well, at two points: it consists both of a theoretical and an experimental part. For the experimental half of my research project, I studied the $B_s^0 \to J/\psi K_S^0$ decay using data collected by the LHCb experiment. This study was performed in three stages, with each new stage adding another layer of complexity to the analysis. In the first stage, my copromotor and I focused on separating the $B_s^0 \to J/\psi K_S^0$ events from the much larger background contribution in the data sample. To do this artificial neural networks were

used. This initial analysis resulted in a measurement of the $B_s^0 \to J/\psi K_S^0$ branching fraction, i.e. the number of times a B_s^0 meson decays into the specific $J/\psi K_S^0$ final state. In the second stage, we also looked at the distribution of decay times of the $B_s^0 \to J/\psi K_S^0$ events and measured their lifetime. In the final stage, the *CP* asymmetries of the $B_s^0 \to J/\psi K_S^0$ decay were measured. Unfortunately, the uncertainties on these parameters are still too large to execute the above described strategy, but it nonetheless offers interesting information regarding the future prospects for this decay channel.

On the theoretical side I explored the flavour symmetry method sketched above to determine the penguin effects in $B^0 \to J/\psi K_S^0$ and $B_s^0 \to J/\psi \phi$. As the necessary information is not yet available for the $B_s^0 \to J/\psi K_S^0$ decay, my promotor and I looked at other decay modes that can also be related by the flavour symmetry to $B^0 \to J/\psi K_S^0$ and $B_s^0 \to J/\psi \phi$. To control the penguin shift $\Delta\phi_d$ affecting $B^0 \to J/\psi K_S^0$, a combined analysis of the $B^0 \to J/\psi K_S^0$, $B_s^0 \to J/\psi K_S^0$, $B^+ \to J/\psi K^+$, $B^+ \to J/\psi \pi^+$ and $B^0 \to J/\psi \pi^0$ modes was performed. All five modes have similar decay dynamics as the $B^0 \to J/\psi K_S^0$ decay, and can thus be used to constrain the penguin contributions affecting the $B^0 \to J/\psi K_S^0$ channel. In addition to the analysis of the currently available data, we also illustrated the potential of the $B_s^0 \to J/\psi K_S^0$ mode for the future LHCb upgrade era using a benchmark scenario, and discussed a strategy to probe corrections to the flavour symmetry method relating the strong interaction dynamics between the $B^0 \to J/\psi K_S^0$ and $B_s^0 \to J/\psi K_S^0$ decays.

The decay channels that can be used to control the penguin shift $\Delta\phi_s$ affecting $B_s^0 \to J/\psi \phi$ are $B^0 \to J/\psi \rho^0$ and $B_s^0 \to J/\psi \overline{K}^{*0}$. Also for these modes we explored the currently available data and determined the resulting constraints on $\Delta\phi_s$. In addition, a new combined analysis was suggested, which would offer interesting information on the corrections to the flavour symmetry method relating the strong interaction dynamics between $B_s^0 \to J/\psi \phi$, $B^0 \to J/\psi \rho^0$ and $B_s^0 \to J/\psi \overline{K}^{*0}$.

Congratulations! You have survived this long and perilous journey through the realm of trees and penguins. I hope you got a brief glimpse of what my research has been about, and what I have been doing for the past four years. At least you now understand why I continue talking about penguins, even though I am not a biologist.

Amsterdam 2015,
Kristof

Een Lied over Bomen en Pinguïns

Beste lezer,
In de volgende pagina's zou ik jou graag meenemen naar de wereld waarin ik de afgelopen jaren geleefd heb. Deze wereld wordt bewoond door de allerkleinste objecten, elementaire deeltjes. Desondanks vinden we deze wereld overal om ons heen, en strekt het zich uit tot in de verste uithoeken van ons Heelal. Het is een ongelooflijk complexe wereld. Hoe meer we ons er in verdiepen, hoe meer verborgen raadsels we ontdekken, en hoe meer we ertoe aangetrokken worden. Deze wereld is voor jou misschien moeilijk te doorgronden, maar dat is het ook voor mij. Dat weerhoudt ons er echter niet van om op ontdekkingstocht te gaan. In tegendeel, de uitdagingen en onbeantwoorde vragen motiveren ons om steeds verder te zoeken. Omdat ik, net als jij, niet alles kan bevatten, heb ik de vier jaar van mijn doctoraat toegewijd aan één speciaal wezentje dat in deze wereld terug te vinden is. Het leeft in de koude en ijzige delen van mijn wereld, en wordt maar zelden gezien. Toch weten we dat het er moet zijn. Laat ons daarom samen op zoek gaan.

Het Standaardmodel

Onze reis door de wondere wereld van de deeltjesfysica vertrekt rechtstreeks vanuit jouw luie zetel. De voorwerpen die je dagdagelijks tegenkomt zijn misschien niet altijd spectaculair, maar ze zijn complexer dan je op het eerste zicht zou denken. Als we er ver genoeg op blijven inzoomen, dan merken we dat ze zijn opgebouwd uit miljarden kleinere bouwstenen: moleculen. Moleculen zijn op hun beurt opgebouwd uit atomen, die zelf weer bestaan uit een kern van protonen en neutronen, met daar omheen een wolk van elektronen. Maar dit is nog steeds niet het einde van het verhaal, want protonen en neutronen kunnen weer opgesplitst worden in quarks. In het bijzonder, twee soorten quarks: de *up* en de *down* quark. Samen vormen de elektronen en quarks de meest elementaire bouwstenen van ons Heelal (voor zover we nu weten).

Hoewel alles om ons heen opgebouwd is uit elektronen, up en down quarks, hebben we de afgelopen honderd jaar geleerd dat er eigenlijk veel meer elementaire deeltjes bestaan in de Natuur. De meeste van deze fundamentele deeltjes zijn

echter exotisch en leven maar heel kort[a], wat het moeilijker maakt om ze waar te nemen. We hebben grote deeltjesversnellers nodig, die of door de mens gebouwd of kosmisch van origine zijn, om de energie niveaus te bereiken die nodig zijn om ze te produceren. Door de botsingen van deze versnelde deeltjes te bestuderen, leren we veel over de wereld van de elementaire deeltjes. Zo hebben we, bijvoorbeeld, zes verschillende soorten quarks geïdentificeren. Gerangschikt naar hun massa zijn dat de *up*, *down*, *strange*, *charm*, *bottom* (of *beauty*, als je wil) en *top*. We kennen nu ook drie op elektronen gelijkende deeltjes: het elektron, het muon en het tau deeltje. En we vonden drie spookachtige deeltjes, ook wel neutrino's genoemd, die gerelateerd zijn met de elektronen, muonen en tau deeltjes. Tezamen noemen we de zes laatst genoemde deeltjes de leptonen. Maar alsof dat nog niet genoeg is, heeft elk van de bovenstaande deeltjes ook nog een partner, het antideeltje, dat als zijn antagonist fungeert. Deeltjes en antideeltjes hebben dezelfde massa, maar verder precies tegenovergestelde eigenschappen. Als het deeltje bijvoorbeeld blauw en positief geladen is, dan zou zijn antideeltje anti-blauw (oftewel geel volgens het kleurenwiel) en negatief geladen zijn. Om een deeltje–antideeltje paar te creëren heb je energie nodig. Omgekeerd, wanneer een deeltje en zijn antideeltje elkaar ontmoeten, annihileren ze elkaar en veranderen ze terug in energie. In ons Heelal is antimaterie zeldzaam geworden. Het annihilatie procedé vindt dus bijna nooit plaats en al helemaal niet op de schaalgrootte van dagdagelijkse voorwerpen. Desondanks wordt antimaterie regelmatig geproduceerd (wat bijvoorbeeld gebruikt wordt in medische PET scanners), maar dat is altijd in kleine hoeveelheden. Het overgrote deel daarvan annihileert bijna onmiddellijk. Het bestuderen van de relatie tussen deeltjes en hun antideeltjes is een belangrijk onderdeel van mijn onderzoek.

Naast de quarks en leptonen ontdekten we ook een groep deeltjes die nodig zijn voor het overdragen van drie van de vier fundamentele krachten in de Natuur: elektromagnetisme, en de sterke en zwakke kernkracht. Elektromagnetisme is verantwoordelijk voor licht, elektriciteit, magnetisme, en houdt de elektronen in een baan om de atoomkern. Het geassocieerde krachtdragende deeltje is het foton. De sterke kernkracht werkt als lijm die de quarks bij elkaar houdt in protonen en neutronen. Het wordt overgedragen door gluonen. De zwakke kernkracht is verantwoordelijk voor het verval van onstabiele deeltjes, zoals bij radioactiviteit. Daarbij worden de W en Z bosonen uitgewisseld. De sterke en zwakke kernkracht spelen alleen een rol op de schaalgrootte van atomen en kleiner. Ze zijn daarom minder prominent aanwezig in ons leven. Als laatste is er naast de quarks, leptonen en krachtdragende deeltjes ook nog het Higgs deeltje. Het heeft te maken met het mechanisme dat verantwoordelijk is voor de massa van de fundamentele deeltjes.

[a]Neutrino's zijn een uitzondering op deze regel. Maar door de zwakke interactie met andere materie, is het nog steeds heel moeilijk om ze waar te nemen.

Maar in detail uitleggen wat dit juist is en waarom het er is, gaat een beetje te ver voor deze samenvatting.

Om inzicht te krijgen in al deze deeltjes en hoe ze zich gedragen, ontwikkelden fysici een theorie die de elementaire deeltjes en hun interacties beschrijft: het *Standaardmodel*. Het enige wat ontbreekt aan deze theorie is een beschrijving van de vierde en meest opvallende fundamentele kracht, de zwaartekracht. Die kan simpelweg niet beschreven worden met dezelfde mathematische formules als de drie andere krachten. Maar dat is niet het enige probleem waar we in de deeltjesfysica tegenaan lopen. Het Standaardmodel is opmerkelijk succesvol in het beschrijven van de data die we verzameld hebben met experimenten die gebruik maken van kosmische straling en deeltjesversnellers, maar het kan de oorsprong en eigenschappen van sommige andere, gevestigde waarnemingen niet verklaren. Ter illustratie, enkele voorbeelden. Kosmologische waarnemingen bevatten een enorme hoeveelheid informatie over de inhoud van ons Heelal en haar evolutie sinds de Oerknal, een gigantische explosie van energie die gezien wordt als de geboorte van ons Heelal. Uit deze waarnemingen concluderen we dat het Heelal maar voor 4% uit gewone materie, dat zijn atomen en moleculen, bestaat. De overige 96%, beschreven met geheimzinnige namen zoals donkere materie en donkere energie, is momenteel onverklaarbaar. Bovendien nemen we aan dat er bij de oerknal evenveel materie als antimaterie werd geproduceerd. Als we het Heelal vandaag de dag bekijken, is de antimaterie echter bijna volledige verdwenen. Hoe kan dat? Om hierop een antwoord te vinden, verdiepen we ons in het verschil in gedrag tussen deeltjes en hun antideeltjes bestuderen.

Omwille van bovenstaande tekortkomingen (en anderen die moeilijker te beschrijven zijn), nemen fysici aan dat het Standaardmodel slechts een goede benadering van de werkelijkheid is; een speciale limiet[b] van een completere, maar nog onbekende theorie over elementaire deeltjes. Het is ons doel, als deeltjesfysici, om een bewijs te vinden voor deze "grootse theorie der elementaire deeltjes", en inzicht te krijgen in haar eigenschappen. Om te slagen in deze missie, onderzoeken we verschillende mogelijkheden: we zoeken naar nieuwe elementaire deeltjes, of naar nieuwe manieren van interactie tussen de deeltjes, of ... Al deze manifestaties van de completere theorie worden omschreven met de algemene naam *nieuwe fysica*. Tot nu toe hebben we nog geen duidelijk bewijs voor nieuwe fysica gevonden. Dat betekent dat afwijkingen van het Standaardmodel klein of moeilijk te detecteren zullen zijn, wat verdere inspanningen van zowel de experimentele als de theoretische deeltjesfysica gemeenschap vraagt.

[b] Denk bijvoorbeeld aan Newtoniaanse zwaartekracht, wat een goede benadering van Einstein's Algemene Relativiteitstheorie is voor voorwerpen met lage snelheid.

De Zoektocht naar Nieuwe Fysica

Onze belangrijkste instrumenten in de zoektocht naar experimenteel bewijs voor nieuwe fysica zijn de hoge energie deeltjesversnellers. Zij versnellen elektronen en/of protonen tot bijna de lichtsnelheid, om ze vervolgens op specifieke plaatsen te laten botsen. Rond deze interactiepunten hebben we grote deeltjesdetectoren gebouwd. Deze detectoren zijn vergelijkbaar met enorme camera's die foto's nemen van de botsingen, maar dan miljoenen keren per seconde. Door de foto's te analyseren, hopen we meer te weten te komen over wat er gebeurt op de allerkleinste lengteschalen. Dat kan dan leiden tot nieuwe resultaten, die niet verklaard kunnen worden door het Standaardmodel. Omwille van deze zoektocht naar nieuwe fysica, bouwen we versnellers die een steeds hogere energie bereiken, zodat nog niet onderzocht gebied toegankelijk wordt. Daar houden nieuwe, fundamentele deeltjes zich mogelijk nog schuil. De nieuwste en meest energetische versneller die deze taak op zich genomen heeft, is de Large Hadron Collider (LHC), terug te vinden bij CERN in Genève, Zwitserland. De LHC heeft vier interactiepunten, waar de grote detectoren genaamd Atlas, Alice, CMS en LHCb zijn gebouwd. Deze detectoren leverden reeds vele interessante resultaten op. Maar *het* hoogtepunt van de LHC is ongetwijfeld de ontdekking van het Higgs deeltje door de Atlas en CMS experimenten.

In mijn onderzoek speelt de LHCb detector een belangrijke rol. Aanvullend op de hoge energie limiet die verkend wordt door Atlas en CMS, focust LHCb zich op precieze metingen van gekende fysische verschijnselen die te maken hebben met het verval van deeltjes die een beauty of charm quark bevatten. Met deze metingen hopen we indirect bewijs te vinden voor nieuwe fysica, wat zich manifesteert als afwijkingen van de voorspellingen die gemaakt worden door het Standaardmodel. Gegeven de huidige situatie kunnen dergelijke observaties van nieuwe fysica alleen gemaakt worden wanneer de theoretische nauwkeurigheid op de voorspellingen voor de gemeten grootheden even precies is als die op de experimenteel gemeten waarden. Met als gevolg dat we de theoretische aannamen die nodig zijn om de experimentele observabelen te koppelen aan de parameteres van het Standaardmodel, herevalueren.

De methodes die we ontwikkeld hebben om theoretische berekeningen uit te voeren in de deeltjesfysica zijn gebaseerd op een reeksontwikkeling. Daarbij vormt elke nieuwe term in de reeks een kleine correctie op de vorige term. Dus, hoe meer termen van de reeks we in acht nemen, hoe nauwkeuriger het resultaat wordt. Echter, elke nieuwe term is ook steeds moeilijker om te berekenen. Voor vele experimentele metingen houden we daarom alleen rekening met de eerste (paar) term(en) van de serie. Door de verbeterde nauwkeurigheid die het LHCb experiment kan bereiken, volstaan deze benaderingen niet meer voor enkele van de belangrijke observabelen die door LHCb gemeten worden.

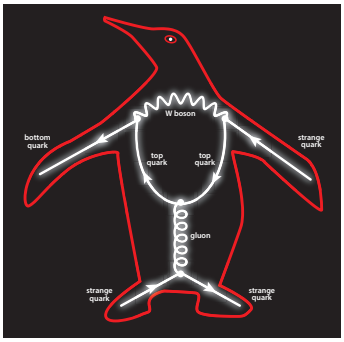

Figure S.1: Grafische illustratie van een zogenaamd pinguïn diagram [200]. Het kwantificeren van de impact van dit diagram op de precisie metingen van B meson vervallen, is het hoofddoel van deze thesis.

Over Bomen en Pinguïns

Deze thesis brengt verslag uit van mijn studie naar de impact van dergelijke hogere orde correcties voor twee zeer specifieke processen. Deze processen hebben te maken met het verval van zogenaamde neutraal geladen B mesonen. B mesonen zijn zware deeltjes die bestaan uit een bottom antiquark en een down (B^0) of een strange (B_s^0) quark. Zij zijn onstabiel, en leven slechts voor een zeer korte periode (enkele miljardsten van een seconde), waarna ze vervallen in lichtere deeltjes. We hebben al meer dan 250 verschillende combinaties van vervalsproducten gevonden, maar voor deze thesis beperken we ons tot de twee vervalskanalen $B^0 \to J/\psi\, K_S^0$ (uit te spreken als B-nul-naar-jee-psaai-K-short) en $B_s^0 \to J/\psi\, \phi$ (B-s-naar-jee-psaai-faai). In deze vervalsmodi vervalt het B meson in een J/ψ deeltje, dat bestaat uit een charm en een anticharm quark, en een K_S^0 deeltje, dat bestaat uit een strange antiquark en een down quark, of een ϕ deeltje, dat een strange en een antistrange omvat. Je mag dit alles ook zien als een raadselachtige code die deeltjesfysici gebruiken om over bepaalde vervalsprocessen te spreken.

De eerste term in de reeksontwikkeling die de $B^0 \to J/\psi\, K_S^0$ en $B_s^0 \to J/\psi\, \phi$ vervallen beschrijft, staat bekend als de boom amplitude omwille van de gevorkte grafische voorstelling van het mechanisme waarmee de vervallen plaatsvinden. Daarnaast kunnen deze vervallen ook plaatsvinden via complexere vervalspaden die bekend staan als pinguïn diagrammen, zoals geïllustreerd in Fig. S.1. In de $B^0 \to J/\psi\, K_S^0$ en $B_s^0 \to J/\psi\, \phi$ vervalskanalen zijn de bijdragen van de pinguïn diagrammen sterk onderdrukt in vergelijking met de meer prominente boom amplitude. Desalniettemin hebben we een experimentele precisie bereikt op de observabelen die geassocieerd worden met de $B^0 \to J/\psi\, K_S^0$ en $B_s^0 \to J/\psi\, \phi$ vervallen waarbij deze kleine correcties merkbaar worden. Ze moeten daarom gekwantificeerd wor-

den. Het is het hoofddoel van deze thesis om methoden te onderzoeken die dit kunnen verwezenlijken.

Omwille van sterke interacties waarbij weinig energie uitgewisseld wordt tussen de quarks die betrokken zijn met het vervalsproces, is het moeilijk om de pinguïn contributies theoretisch te berekenen. De laag energetische dynamica tussen quarks en gluonen kan niet volledig beschreven worden met onze standaard methoden. Om de effecten toch te kwantificeren, grijpen we daarom naar alternatieve methoden die de impact van deze diagrammen afschatten met behulp van experimentele data. Symmetriën spelen daarbij een belangrijke rol.

Symmetriën en *CP* Schending

De correcties die we proberen te kwantificeren, kunnen bepaald worden met behulp van observabelen die het verschil in gedrag tussen deeltjes en antideeltjes parametriseren. Deeltjes en hun antideeltjes zijn aan elkaar gerelateerd door het uitvoeren van zowel de ladingssymmetrie transformatie als de pariteit transformatie. De ladingssymmetrie (C, van het Engelse *charge*) transformatie verwisselt de positieve en negatieve ladingen van de fundamentele deeltjes. Pariteit (P) keert de richtingen die we geven aan de ruimtelijke dimensies om, d.w.z. het maakt de transformaties $x \to -x$, $y \to -y$ en $z \to -z$. Hoewel het Heelal *CP*-symmetrisch begonnen is, met evenveel materie als antimaterie, is de wereld om ons heen nu exclusief uit materie opgebouwd. Antimaterie is zeer schaars geworden. Dit is alleen mogelijk wanneer deeltjes zich niet exact hetzelfde gedragen als antideeltjes, d.w.z. de *CP* symmetrie is gebroken. De sterke[c] en elektromagnetische interacties zijn invariant onder *CP* transformaties, maar de zwakke kernkracht is dat niet. De grootte van de *CP* schending die gemeten wordt in zwakke interacties is echter onvoldoende om de vastgestelde onbalans tussen materie en antimaterie in het Heelal te verklaren. Er moeten dus nog extra bronnen van *CP* schending zijn die niet beschreven worden door het Standaardmodel. Door vervalsprocessen, zoals $B^0 \to J/\psi K_S^0$ en $B_s^0 \to J/\psi \phi$, te bestuderen, hopen we nieuwe fysica te vinden die ons kan helpen om de *CP* schending in het Heelal te begrijpen.

In het Standaardmodel wordt *CP* schending geparametriseerd door complexe fasen. Zonder een uitgebreide introductie in de wiskunde achter complexe getallen te geven, stel je je simpelweg voor dat de wiskundige beschrijving van het Standaardmodel gebruik maakt van getallen die bovenop hun grootte ook nog een kompasrichting hebben: een fase. Door observabelen te meten die de (CP) asymmetrie parametriseren tussen de vervalsprocessen van aan de ene kant B^0 en B_s^0 mesonen, en aan de andere kant $\bar{B}^0$ en $\bar{B}_s^0$ antimesonen, bepalen we deze kompasrichtingen.

[c] De sterke kernkracht hoeft niet invariant te zijn onder *CP* transformaties, maar experimentele waarnemingen suggereren dat dat wel zo is. Deze raadselachtige situatie staat bekend als het sterke *CP* probleem.

Via de $B^0 \to J/\psi K_S^0$ en $B_s^0 \to J/\psi \phi$ vervalskanalen meten we twee van dergelijke *CP*-schendende complexe fasen. Ze worden aangeduid als ϕ_d en ϕ_s. Als we de kleine bijdragen van de pinguïn diagrammen negeren, en dus aannemen dat de twee vervallen alleen via het boom diagram plaatsvinden, dan is de relatie tussen de gemeten *CP* asymmetriën en de fasen ϕ_d en ϕ_s redelijk eenvoudig. Nemen we ook de pinguïn effecten mee, dan wijzigen deze relaties en moeten we rekening houden met correcties, die we in dit doctoraat parametriseren met de verschuivingen $\Delta\phi_d$ en $\Delta\phi_s$. Deze correcties beïnvloeden de waarden van de gemeten *CP* asymmetriën. Bijgevolg kunnen deze asymmetriën ook gebruikt worden om de correcties te beheersen. In $B^0 \to J/\psi K_S^0$ en $B_s^0 \to J/\psi \phi$ is de invloed van de pinguïn amplitudes klein. Hun impact op de *CP* asymmetriën is dus moeilijk waar te nemen. We zoeken daarom andere vervalskanalen waarin het effect op de *CP* asymmetriën is uitvergroot.

Om dit te verwezenlijken hebben we nog een symmetrie nodig: de smaaksymmetrie van de sterke kernkracht. Wanneer we aannemen dat de up, down en strange quark massaloos zijn, wat een benadering van de werkelijkheid is, dan kan de sterke kernkracht de drie quarks niet meer van elkaar onderscheiden. Wat de sterke kernkracht betreft, zien deze deeltjes er precies hetzelfde uit, en gedragen ze zich dus ook op dezelfde manier. Met het oog op de moeilijkheden die we tegenkomen om de laag energetische dynamica tussen quarks en gluonen te berekenen is dat een interessante eigenschap om uit te buiten. Deze symmetrie laat ons toe om vervalskanalen met elkaar te relateren door het verwisselen van up, down en strange quarks, zonder dat daarbij de laag energetische dynamica die deze vervalsmodi beschrijft verandert. Dus in plaats van expliciete berekeningen, gebruiken we de smaaksymmetrie om de parameters die we willen weten te relateren aan soortgelijke parameters uit vervalsmodi waarin deze bepaald kunnen worden met experimentele data. Uiteraard zijn quarks niet massaloos. Deze symmetrie is dan ook niet exact gerealiseerd in de Natuur. Echter, de massa's van de up, down en strange quarks zijn klein in vergelijking met het typische energieniveau waarop sterke interacties plaats vinden. Voor de sterke kernkracht komen ze daarom over als massaloos. De smaaksymmetrie is daarom een uitstekend hulpmiddel in de studies over het verval van B^0 and B_s^0 mesonen.

De Jacht op Pinguïns

Laat mij het gebruik van de smaaksymmetrie in meer detail belichten. Door het met elkaar omwisselen van alle down en strange quarks verandert het $B^0 \to J/\psi K_S^0$ verval in de $B_s^0 \to J/\psi K_S^0$ vervalsmodus. In de limiet waarbij we perfecte smaaksymmetrie hebben, zullen de sterke interacties in deze twee vervalskanalen identiek zijn. De zwakke interacties zorgen echter nog steeds voor verschillen tussen de twee vervalskanalen. Bijgevolg is de relatieve verhouding tussen de boom en pin-

guïn amplitudes in $B_s^0 \to J/\psi K_S^0$ anders dan die in $B^0 \to J/\psi K_S^0$. De pinguïn amplitudes zijn uitvergroot in $B_s^0 \to J/\psi K_S^0$. Derhalve is het $B_s^0 \to J/\psi K_S^0$ verval veel gevoeliger voor pinguïn effecten, en kan het gebruikt worden om hun impact in $B^0 \to J/\psi K_S^0$ te bepalen, d.w.z. om de verschuiving $\Delta\phi_d$ te kwantificeren.

De strategie die we daarvoor gebruiken is de volgende: we meten de *CP* asymmetriën in $B_s^0 \to J/\psi K_S^0$, en gebruiken die om de grootte van de pinguïn bijdragen te bepalen. Dan roepen we de smaaksymmetrie aan om de pinguïn bijdragen in $B_s^0 \to J/\psi K_S^0$ te relateren aan die in $B^0 \to J/\psi K_S^0$. Eens we de grootte van de pinguïn effecten in $B^0 \to J/\psi K_S^0$ kennen, kunnen we de verschuiving $\Delta\phi_d$ kwantificeren. Dat leidt op zijn beurt weer tot een nauwkeurigere bepaling van ϕ_d met behulp van de *CP* asymmetriën in $B^0 \to J/\psi K_S^0$. Het klinkt alsof we alles onder controle hebben, maar zo eenvoudig is het uiteraard niet. De pinguïn bijdragen zijn dan wel uitvergroot in $B_s^0 \to J/\psi K_S^0$, maar de totale vervalsamplitude is veel kleiner dan die in $B^0 \to J/\psi K_S^0$. De $B_s^0 \to J/\psi K_S^0$ vervalsmodus is daarom op experimenteel vlak moeilijker te bestuderen. Als gevolg daarvan hebben we momenteel nog geen precieze metingen van de *CP* asymmetriën in $B_s^0 \to J/\psi K_S^0$, en kunnen we de bovenstaande strategie dus nog niet uitvoeren.

Op Zoek naar Voetsporen van Pinguïns

Waar past mijn onderzoek in dit plaatje? Wel, op twee punten: het bestaat uit zowel een theoretisch als een experimenteel gedeelte. Voor de experimentele helft van mijn onderzoek heb ik het $B_s^0 \to J/\psi K_S^0$ verval bestudeerd met behulp van de data verzameld door de LHCb detector. Deze studie bestond uit drie stappen, waarbij elke nieuwe stap een extra laag in de complexiteit van de analyse toevoegde. In de eerste stap waren mijn copromotor en ik gefocust op het onderscheiden van de $B_s^0 \to J/\psi K_S^0$ vervallen van de veel talrijkere achtergrond gebeurtenissen in de data. Hiervoor maakten we gebruik van artificiële neurale netwerken. Deze eerste analyse resulteerde in een meting van de $B_s^0 \to J/\psi K_S^0$ vertakkingsverhouding, d.w.z. het aantal keren dat een B_s^0 meson vervalt naar de specifieke $J/\psi K_S^0$ eindtoestand. In de tweede stap keken we ook naar de verdeling van de vervalstijden van de $B_s^0 \to J/\psi K_S^0$ gebeurtenissen, en maten we hun gemiddelde levensduur. In de laatste stap zijn dan de *CP* asymmetriën van het $B_s^0 \to J/\psi K_S^0$ verval gemeten. Helaas is de onzekerheid op deze parameters nog te groot om de bovenstaande strategie uit te voeren. Desondanks feeft het interessante informatie over de toekomstmogelijkheden van dit vervalskanaal.

Aan de theoretische zijde heb ik onderzoek gedaan naar de hierboven beschreven methode, die gebaseerd is op de smaaksymmetrie, om de pinguïn effecten in $B^0 \to J/\psi K_S^0$ en $B_s^0 \to J/\psi \phi$ te bepalen. Aangezien in het geval van $B^0 \to J/\psi K_S^0$ de benodigde informatie nog niet beschikbaar is, hebben mijn promotor en ik gekeken naar andere vervalskanalen die ook via de smaaksymmetrie gerelateerd

kunnen worden aan $B^0 \to J/\psi K_S^0$ en $B_s^0 \to J/\psi \phi$. Om de pinguïn verschuiving $\Delta\phi_d$, die we in $B^0 \to J/\psi K_S^0$ tegenkomen, te bepalen, is een gemeenschappelijke analyse van de $B^0 \to J/\psi K_S^0$, $B_s^0 \to J/\psi K_S^0$, $B^+ \to J/\psi K^+$, $B^+ \to J/\psi \pi^+$ en $B^0 \to J/\psi \pi^0$ vervalskanalen uitgevoerd. Alle vijf deze vervalsmodi hebben vervalsdynamica die gelijkaardig zijn aan die in het $B^0 \to J/\psi K_S^0$ verval, en kunnen dus gebruikt worden om de pinguïn bijdrage in $B^0 \to J/\psi K_S^0$ te bepalen. Naast de analyse van de beschikbare data hebben we ook het potentieel van de $B_s^0 \to J/\psi K_S^0$ vervalsmodus voor de toekomstige upgrade van de LHCb detector geïllustreerd aan de hand van een voorbeeld scenario. En we hebben een strategie besproken die kan helpen bij de studie van de correcties op de smaaksymmetrie methode die de sterke interactie dynamica in de $B^0 \to J/\psi K_S^0$ en $B_s^0 \to J/\psi K_S^0$ vervalskanalen met elkaar verbindt.

De vervalskanalen die gebruikt kunnen worden om de pinguïn verschuiving $\Delta\phi_s$ in $B_s^0 \to J/\psi \phi$ te bepalen zijn $B^0 \to J/\psi \rho^0$ en $B_s^0 \to J/\psi \overline{K}^{*0}$. Ook voor deze vervalsmodi hebben we de beschikbare data bestudeerd en de daaruit volgende waarde voor $\Delta\phi_s$ bepaald. Daarnaast hebben we ook een voorstel gedaan voor een nieuwe, gecombineerde analyse van beide vervalskanalen. Deze strategie biedt interessante informatie over de correcties op de smaaksymmetrie methode die de sterke interactie dynamica in de $B_s^0 \to J/\psi \phi$, $B^0 \to J/\psi \rho^0$ en $B_s^0 \to J/\psi \overline{K}^{*0}$ vervalskanalen met elkaar verbindt.

Gefeliciteerd! Je hebt de lange en gevaarlijke tocht door de wereld van bomen en pinguïns overleefd. Ik hoop dat je daarbij een idee gekregen hebt over wat mijn onderzoek nu juist inhield en waar ik de afgelopen vier jaar mee bezig ben geweest. Op zijn minst zou je nu moeten begrijpen waarom ik het steeds over pinguïns heb, terwijl ik toch geen bioloog ben.

Amsterdam 2015,
Kristof

Acknowledgements

In these last two pages, I would like to take the opportunity to thank the people that have helped and supported me throughout all my years at Nikhef.

I would like to start by thanking Marcel Merk. Eight years ago I came to Nikhef for my bachelor project, thinking particle physics would be a fun detour on my path to a masters in meteorology and climate studies. With your enthusiasm and dedication to your students you changed my mind about that, and convinced me to go down the flavour physics road instead. I could always come to you for help, whether that was physics related or not. Thank you for believing in me, already from day one.

My promotor and co-promotor, Robert Fleischer and Patrick Koppenburg. With such high-profile members of the flavour physics community — Robert on all theoretical topics involving B meson decays, and Patrick as the current LHCb physics coordinator — I could not have wished for better support. They were always available for questions and discussions. Whenever I thought I had reached a dead end (or, more rarely, the finish line), talking to you gave me new motivation, inspiration and ideas on how to continue. Thank you for offering me this unique combination of theoretical and experimental particle physics research. It has been a lot of fun to bridge the two worlds. Under your wings, I could explore the potential of the $B_s^0 \to J/\psi K_S^0$ decay, figure out what experimental input was needed to reach that goal, and then go measure those inputs myself. It is a special feeling to be able to perform an analysis completely from A to Z. But the most striking example of this unique situation is undoubtedly that time when a simple question from our internal LHCb referees about a factor 2 led to a complicated theory answer and us writing a high-impact paper about it.

A big thanks also to Nikhef, for all the opportunities they have given me, and for sending me to CERN. Getting submerged into its lively community, and actually seeing the machines producing the data we analyse, was inspiring.

Rob Knegjens, Niels Tuning, Antonio Pellegrino, Lennaert Bel and Mick Mulder. It was wonderful discussing flavour physics with you. I enjoyed working with you on all the different projects.

Florian Kruse, Julian Wishahi, Christoph Cauet and the rest of the group at the TU Dortmund. Although I must admit that at first it felt like you were intruding

my space when you joined the $B_s^0 \to J/\psi K_S^0$ analysis, I could not have succeeded without you guys. I thoroughly enjoyed our collaboration. Thank you also for inviting me twice to come to Dortmund, those visits have been incredibly fruitful for our analysis.

Gerhard Raven, who I could always bother with my problems about RooFit, and was eager to explain things to me when I had yet another problem with my fitter or about statistics, regardless of whether that problem was theory or experiment related.

Manuel Schiller, for explaining me how to properly deal with flavour tagging information in a time-dependent fit, and for all the help with debugging my code. Your dedication to your physics analysis and to LHCb is inspiring.

Sajan Easo, Miriam Gandelman, Ulrik Egede, Yasmine Amhis, Bruno Souze de Paula, Frederic Manchefert, Mirco Dorigo, Alessia Satta, Ronan McNulty, the B2CC working group, the LHCb editorial board, and all others within LHCb who provided comments and questions, or helped to improve the $B_s^0 \to J/\psi K_S^0$ analyses and their papers.

The Nikhef bfys and theory groups for the wonderful and welcoming atmosphere they provided.

Lastly, I would like to thank my family. My parents, for giving me the opportunity to go study in the Netherlands and helping me with all the extra complications that brings, even when I could also have studied (particle) physics thirty minutes cycling from home. You have always been there to help, regardless of the physical distance or the time difference after you moved to Thailand for an adventure of your own. My grandparents and the rest of the family, for helping out wherever possible, and taking care of so many things, allowing me to fully focus on my research. Jan Mariën, for painting the icy landscape that now proudly forms the cover of my thesis.